Paleozoic Transpressional Tectonics in the Beishan Orogenic Collage, Northwest China: Evolution of the Hongliuhe Suture Zone

by

Nathan Cleven

A thesis
presented to the University of Waterloo
in fulfillment of the
thesis requirement for the degree of
Doctor of Philosophy
in
Earth Sciences

Waterloo, Ontario, Canada, 2016

Author's Declaration

I hereby declare that I am the sole author of this thesis. This is a true copy of the thesis, including any required final revisions, as accepted by my examiners.

I understand that my thesis may be made electronically available to the public.

Abstract

The Beishan orogenic collage is a southern, central subset of the Central Asian Orogenic Belt, in Northwest China. It is an accretionary orogen that was active during the early Paleozoic, transitioning to convergent collisional tectonics in the late Paleozoic to early Mesozoic. It comprises two main early Paleozoic arcs built through Precambrian pericratonic fragments, the Hanshan and Dundunshan terranes. Detrital zircon geochronology indicates that they share a similar set of Precambrian ages with the Tarim craton. It also establishes that the Hanshan arc developed with magmatism from the Late Cambrian to Early Devonian, then re-initiated with a minor peak of magmatism in the Carboniferous–Permian. Magmatism in the Dundunshan arc follows an identical pattern, yet offset younger by roughly 50 m.y. in all aspects. We interpret this pattern to indicate a staged collision and accretion event, the docking of the arcs from north to south. The event initiated during a regional magmatic hiatus in the Devonian. Known ophiolite ages of genesis and emplacement respectively bracket the main arc-building magmatic period. This supports conclusions that an ophiolite belt in the Beishan does represent a suture.

Deformation in the Mazongshan terrane, the central Beishan suture and accretionary complex, is due to episodes of early Paleozoic accretion of arcs, oceanic units, and ophiolite emplacement. To further establish the sequence of tectonism we provide an age and tectonic setting of the Hongliuhe ophiolite, one of the oldest that now lies in the suture zone. It comprises cumulate ultramafic to mafic plutonic rocks formed in the Cambrian (520.3 ± 5.8 Ma, U-Pb, Gabbro). Volcaniclastic and arc-marginal sedimentary rocks overlie exposed ductilely deformed lower crustal ophiolitic plutonic rocks. Petrography, lithostratigraphy, and whole rock and mineral chemistry support a conclusion that the ophiolite developed in an extensional arc-marginal supra-subduction tectonic environment. This illustrates how ophiolites can be created during subduction rollback, not necessarily subduction initiation. The emplacement timing of the ophiolite is constrained by an undeformed Early Devonian granite (413.6 ± 3.5 Ma, U-Pb) that intruded through its tilted, folded sedimentary cover sequence.

Paleozoic deformation spanning the Mazongshan terrane can be differentiated into two events: pervasive Silurian–Devonian dextral transpression and Permian–Triassic sinistral transpression. We identify that a protracted regional accretion or collision event produced the early deformation. U-Pb zircon ages define a staged cessation of deformation from five late-syn-kinematic dykes in the Xingxingxia region (436.5 ± 2.6 Ma to 383.1 ± 4.6 Ma, Early Silurian–Middle Devonian). High strain zones distributed throughout the accretionary complex exhibit dextral kinematics, with transpressive fault dynamics. Narrow fault width and high variation of stretching lineation orientations within the foliation plane together correlate to earlier timing of fault cessation. Wide fault zones bounding the accretionary complex have focused lineation orientations and correlate to later cessation. This pattern of fault cessation indicates a progressive increase in localization of strain over time, due to a possible combination of uplift, cooling (cessation of magmatism), and waning tectonism; each of these mechanisms can be characteristically linked to collision. The dextral transpressive event is likely the collision of the northern and southern arc terranes of the Beishan and spanned the Silurian to Middle Devonian. The timing correlates to the emplacement of ophiolites within the suture.

To aid analysis of highly tectonized regions, we present a new detrital geochronology provenance analysis technique dating populations of variably tectonized conglomerate clasts. Bulk samples of clasts are sorted based on their degree of internal deformation into three subsets: undeformed, deformed, and intermediate, or slightly deformed. Zircon from each population is analyzed identically to a standard sandstone detrital geochronology sample. Our application of the method to the Hongliuhe Formation, a Permian syn-orogenic deposit overlying the Mazongshan accretionary units, compares clast and sandstone data sets at three stratigraphic levels. Clast population age spectra include a wider range of ages than sandstone. They indicate a minimal lag time, implying rapid exhumation rates. A dominant Ordovician magmatic peak is present in sandstone data, switching to a dominant Silurian–Devonian peak in clast data, indicating a younging of magmatism towards a proximal provenance. A hiatus of magmatism starts in the Devonian, correlating with the latest age of deformed clasts, interpreted as timing of collisional tectonics. The detailed age spectra provide regional tectonic context and interpretation of processes, as well as more robust provenance interpretation than could be determined from sandstone samples alone.

Acknowledgements

I would like to thank my friends, family and colleagues that have provided me with incredible support and inspiration over the years. It is important to me to acknowledge the help and support of the students and professors from the Institute of Geology and Geophysics, Chinese Academy of Science that have assisted me in my field work, especially Ao Songjian, Tian Zhonghua and Ma Chong for their invaluable help in the field, and Professor Xiao Wenjiao for his generous support of my work. I would like to extend a kind thank you to Professor Brian Windley of the University of Leicester, England, for participating in 2008 field trips. Thank you Joanna Hamlyn for being my field assistant in the summer of 2009 and sticking through it. The comments on my works during the publication process from Dr. John Wakabayashi of California State University, Fresno, and all of the anonymous reviewers are greatly appreciated. My deepest regards go to Dr. John Waldron of the University of Alberta for his extensive comments on my thesis. The guidance of Dr. Don W. Davis in the Jack Satterly Geochronology Laboratory was instrumental to the success of the analytical portions of my work. I would like to acknowledge the dedication and patience shown by my committee members over the years, Drs. Brian Kendall, Mario Coniglio, Chris Yakymchuck, and especially by Drs. Shoufa Lin, Wenjiao Xiao, and Carl Guilmette, my advising team.

Table of Contents

List of Figures

List of Tables

Chapter 1

Introduction

1.1 The Central Asian Orogenic Belt

The Central Asian Orogenic Belt (CAOB), historically referred to as the Altaids (Şengör et al., 1993; Allen et al., 1995; Yakubchuk, 2004; Şengör and Natal'in, 2007), is defined by the interrelated orogens between the Siberia and Baltica cratons (Fig. 1.1). It extends from Kazakhstan, in the west, to eastern Siberia, along the southern margin of the Siberian craton. The southern boundary is marked by the Tarim and North China cratons. The late Neoproterozoic–Paleozoic sialic crustal material sandwiched between these four major cratons formed from the progressive subduction of the Paleo-Asian ocean. Subduction and collision brought about the accretion of intervening arcs, microcontinents, ophiolites, oceanic seamounts and sedimentary rocks (Zhang et al., 1993; Jahn et al., 2001; Buckman and Aitchison, 2004; Xiao et al., 2004a; Windley et al., 2007; Xiao et al., 2009b, 2010). Collisional and post-collisional magmatism modified, reworked, and added volume to the crust at different stages in CAOB development (Pirajno et al., 2002; Xiao et al., 2009a,b). Early work in the CAOB established general terrane domains of oceanic crust, continental crust, island arc crust, and composite crust, as well as the major faults bounding them (Coleman, 1989; Windley et al., 1990; Allen et al., 1992; Şengör et al., 1993). A key finding was the wide geographical distribution of late Paleozoic A-type granites interpreted to represent the final stages of amalgamation.

The Siberian and Baltic cratons are largely considered to be central nuclei around which terranes were accreted. Early models of accretion proposed an idea which involved the progressive strike-slip dismemberment of a single, large, migrating arc called the Kipchak arc (Şengör et al., 1993). The many orogens identified in the present, the Ural, Tianshan, Kazakhstan, Altay, and Mongol-Okhotsk orogens, were interpreted to have been emplaced as offset fragments of the single arc, utilizing a single subduction system. Those purporting this model eventually accepted growing evidence that more than one subduction system was active simultaneously, and attempted to refine the model by increasing the number of arcs involved to three Wang et al. (2003); Yakubchuk (2004); Şengör and Natal'in (2007). The modern island archipelago model, or multiple subduction zone model, was developed from work in the Tianshan orogen (Fig. 1.2) that indicated the Tianshan had evolved with subduction zones under both its north and south margins (Windley et al., 1990; Allen et al., 1992; Gao et al., 1998; Chen et al., 1999; Laurent-Charvet et al., 2002; Xiao et al., 2004b). The model interprets that subduction systems were more prevalent, active contemporaneously, and of various polarities. Each subduction system consumed portions of the Paleo-Asian ocean, thus building arcs and bringing about the inevitable collision and accretion events. Workers have drawn analogues to the tectonic setting of the Indonesian archipelago in the South Pacific (Windley et al., 2007; Xiao et al., 2009b, 2010).

Evidence of subduction and each subduction zone's specific polarity has continually been the focus of debate and controversy in the CAOB. Sedimentology and stratigraphic analysis have been used to identify passive margin and rift sequences, constraining subduction location and timing (Windley et al., 1990; Charvet et al., 2007). Structural vergence in subduction-accretion complexes is commonly used to infer subduction polarity, or the transport direction of the overriding plate, though complications arise due to syn- or post-accretionary back-thrusting and overprinting by both late convergence and strike-slip structures (Laurent-Charvet et al., 2003; Xiao et al., 2003, 2004b; Windley et al., 2007). The identification of suture zones by the presence of quasi-linear belts of ophiolite fragments and high-pressure metamorphic rocks (Gao et al., 1998; Xiao et al., 2014) emplaced along major structural breaks has been a contentious topic for establishing evidence of subduction zones.

Researchers have noted that ophiolite successions in the CAOB are strongly deformed and are commonly incomplete or fragmented sections. They are imbricated with various other lithologies in accretionary complexes, and have highly variable geochemical characteristics (Zhang et al., 1993; Xiao et al., 2008). Their organization along major structural lineaments is considered by some to provide a loose framework for siting consumed ocean basins, debatably as either major oceans or small back-arc/fore-arc basins (Xiao et al., 2008, 2010, 2014). Ophiolite geochemistry in the CAOB largely points to supra-subduction affinities (Hsü, 2003; Xiao et al., 2008). Overall, they provide records of ocean generation and consumption from the Cambrian to Permian (Ao et al., 2012; Mao et al., 2012b).

Accretion and crustal growth in the CAOB occurred in stages from the Neoproterozoic through to the end of the Paleozoic or Early Mesozoic (Windley et al., 2002; Wang et al., 2003; Buckman and Aitchison, 2004; Xiao et al., 2004a; Windley et al., 2007; Xiao et al., 2008, 2009b; Schulmann and Paterson, 2011; Kröner et al., 2014). In modern times the orogenic belt generally trends E-W and youngs southwards. Termination of orogeny is considered to coincide with the collision of the Tarim craton against the southern margin of the Tianshan orogen during the Late Carboniferous–Permian (Allen et al., 1992; Gao et al., 1998; Chen et al., 1999; Laurent-Charvet et al., 2002; Li et al., 2002; Xiao et al., 2004b; Charvet et al., 2007; Xiao et al., 2009a; Xiao and Santosh, 2014). Further east the North China craton collided with the Southern Mongolian accretionary system along the Solonker suture in the Triassic (Xiao et al., 2003; Lehmann et al., 2010). These two major collisions converted the mode of tectonism from localized accretion to regional convergence, causing widespread, distributed deformation, reactivation of inboard fault systems and further orogeny. The region between the two major cratonic sutures is called the Beishan orogenic collage (Figs. 1.1 and 1.2). It offers a prime setting for analysis for both far-field effects of both collisions, as well as deformation episodes preserved from prior tectonic events with less of an overprint than its neighboring regions.

1.2 The Beishan orogenic collage

Development of the tectonostratigraphic architecture of the Beishan orogenic collage (or Beishan) is in its infancy. Until recently researchers have assumed it to be an eastern extension of the Tianshan orogen with a directly analogous tectonic history, albeit less affected by convergence associated with the collision of the Tarim craton. Some researchers promote direct lithotectonic correlations between the two regions (Ma et al., 2014; Shi et al., 2014). Review of its tectonomagmatic framework, metamorphic, structural and accretionary history, indicates some significant differences from, and some similarities to the Tianshan (Xiao et al., 2010). The Beishan has a history of Paleozoic arc magmatism through the early and middle Paleozoic. This is similar to the Tianshan except that magmatism ceased earlier, in the Devonian, instead of the Carboniferous (Li et al., 2001; Hu et al., 2007; Li et al., 2009b; Lei et al., 2011; He et al., 2012; Mao et al., 2012a; Song et al., 2013a,b; Guo et al., 2014; Lei et al., 2014). The Beishan contains two identifiable early Paleozoic arc terranes, the Hanshan and Dundunshan arcs, separated by the Mazongshan accretionary complex (each indicated in Fig. 1.2). These developed from two north dipping subduction zones, as opposed to the bivergent subduction under the Tianshan along the North Tianshan suture and South Central Tianshan suture (indicated in Fig. 1.2) (Gao et al., 1998; Xiao et al., 2010; Qu et al., 2011; Ao et al., 2012; Tian et al., 2014; Cleven et al., 2015). The terranes from the two orogenic systems share interconnecting E-W trending major structural lineaments (Fig. 1.2), yet the magnitudes of strike-slip motion are uncertain, and the faults are known to have been active from early amalgamation to post-orogenic reactivation as late as the Triassic (Wang et al., 2010). The Beishan arc terranes amalgamated in the middle Paleozoic and subsequently accreted against the northern margin of the poorly understood Dunhuang block, which some purport to be an offset block of the Tarim craton (Xiao et al., 2010; Guo et al., 2012; He et al., 2014a; Wang et al., 2014a). A significant similarity between Beishan terranes and the Tianshan is that they all share inherited Precambrian zircon ages, implying they may have co-genetic histories as pericratonic fragments of the Tarim craton (Song et al., 2013c; Ma et al., 2014;

Xia et al., 2014; Chapters 2, 4, and 5).

Many aspects of the Beishan provide opportunities for study of the evolution of accretionary orogenesis in the CAOB. Its position in the south of the CAOB dictates that it should be amongst the youngest terranes, yet it contains some of the earliest records of Cambrian oceanic crust generation in some of its ophiolites (Ao et al., 2012; Chapter 3). Its central early Paleozoic suture, the Hongliuhe suture (Fig. 1.2), contains two generations of ophiolites, from the Cambrian and the Silurian–Devonian (Tian et al., 2014). This phenomenon is not well constrained or understood. The staging of accretion events is an important aspect of subduction zone evolution and the progressive closure of ocean basins. While many researchers have focused on the deformation effects of terminal collision (Wang et al., 2010; Zhang and Cunningham, 2012; Tian et al., 2013; Cleven et al., 2015) some recent metamorphic evidence supports the interpretation of early Paleozoic collision (Qu et al., 2011; He et al., 2014a). Understanding the effects of early amalgamation and the subsequent tectonic staging allows for further refining of the island archipelago accretionary model.

This thesis approaches many topics of controversy in the Beishan. It focuses on the dynamics and periodicity of magma generation, ophiolite generation and emplacement, tectonism, and the regional deformation patterns of the accretionary orogenic collage.

1.2.1 Location and previous work

The region of study spans the Hongliuhe to Xingxingxia area in Northwest China, straddling the border between Gansu province and the Xinjiang Autonomous Region (Fig. 1.2). The mapped area is slightly larger than two (Canadian) 1:50,000 scale map sheets. The area is accessible by train and the national freeway system, though much of the region requires an off-road vehicle to safely traverse the vast networks of dirt roads. There are many small towns in the region with limited availability of goods and supplies. From largest to smallest, towns include: Liuyuan, Xingxingxia, Hongliuhe, Weiya, and Tianhu (Fig. 1.2).

The Chinese portion of the southern Central Asian Orogenic Belt, including the Tianshan and Beishan orogenic collages, have a publicly available 1:1 000 000 scale map produced in 1997 (Anonymous, 1997). Maps of the Beishan produced at a scale of 1:200 000 in the year 1966 exist and are available to Chinese researchers, but are protected from distribution by state secrecy laws. A regional review of available Chinese language literature and survey data summarizing Beishan tectonics was produced by Xiao et al. (2010).

Studies providing isotopic ages and geochemistry of ophiolitic and volcanic rocks in the Hongliuhe region have been published in Chinese (Pan et al., 2008; Zhang and Guo, 2008). Geochemistry and isotopic ages of deformed granitoids and gneisses from the Tianhu and Xingxingxia region have been published, mostly in Chinese, except for the most recent, in English (Hu et al., 2007; Li et al., 2009a; Hu et al., 2010; Lei et al., 2014; Wang et al., 2014b). Late fold-and-thrust belt deformation of Permian sedimentary rocks in the Hongliuhe to Xingxingxia (and further east) have been structurally characterized by Zhang and Cunningham (2012), Tian et al. (2013), and Cleven et al. (2015).

1.3 Thesis objectives

The research objectives of this thesis are to approach regional and local tectonic questions concerning stages, processes and mechanisms of accretionary orogenesis in the Beishan orogenic collage. The Beishan has regional significance in providing a natural laboratory for exploring the concepts behind CAOB Paleozoic tectonics. This is exemplified in the exposure of magmatic rocks indicating staging relationships, well-preserved fault kinematic structures, and the unique relationships between suturing and ophiolite production. The specific, central objectives of this thesis are to investigate:

1. the time spans and nature of Paleozoic magmatic periods throughout the Beishan and how the magmatic architecture relates to tectonism;
2. suturing processes within accretionary complexes and orogens, including staging and structural dynamics;
3. whether ophiolites and ophiolite belts reliably mark suture zones in the Central Asian Orogenic Belt, and to characterize the Hongliuhe ophiolite and its petrogenetic history in the Beishan;
4. links of deformation processes with periods of tectonism from the penetrative ductile strain observable in the central accretionary complex of the Beishan;
5. constraints on the timing of deformation and the dynamics and kinematics of regional shear zones;
6. geochronological and tectonostratigraphic links of preserved Precambrian crust to any affinity with a specific craton;

7. new ideas and methods to approach the problem of establishing previously unknown magnitudes of displacement across terrane and plate boundary faults developed in obliquely convergent tectonic environments.

To approach these questions, my work has included mapping and sampling in the field area, structural analysis, petrographic studies, U-Pb zircon geochronology studies (both LA-ICPMS [Laser Ablation - Inductively Coupled Plasma Mass Spectrometry] and SHRIMP [Sensitive High-Resolution Ion MicroProbe]) of igneous and detrital rocks, and whole-rock and mineral geochemistry. In addition, data and observations have been cited from existing literature.

1.4 Organization of thesis

This thesis is presented as a series of four journal articles. Each following chapter addresses separate questions forming conclusions about the specified topic, intended to be a stand-alone paper. Field data, photographs, geochronological results, interpretations and conclusions are unique to each chapter. Repetitive use of maps, descriptions of regional geology and tectonics, and some discussion points, is necessary. The chapters are ordered to provide a progressive, cohesive understanding of the main ideas and conclusions, occasionally referencing previously stated conclusions. References and appendices for all chapters are collated at the end of the thesis.

The second chapter contains U-Pb igneous and detrital zircon geochronology data to provide a framework of the Paleozoic magmatic periods in the Beishan. The results depict a similar pattern of magmatic peaks between two arc terranes, yet offset by forty million years, interpreted as staged subduction and collision dynamics. The third chapter provides genetic and lithostratigraphic definition to the Hongliuhe ophiolite, characterizing it as a Cambrian supra-subduction ophiolite formed in an extensional arc-marginal environment. Its Devonian geochronological emplacement constraint links to the conclusions of chapter four, which characterizes transpressive deformation within shear zones bounding and cutting through the accretionary complex hosting the ophiolite. Deformed dyke ages allow interpretation that the period spanning the Silurian through Middle Devonian experienced oblique convergence and collision events that caused widespread penetrative dextral deformation. Chapter five offers expanded methodology on detrital geochronology techniques. The variably tectonized conglomerate clast dating technique provides a method for analyzing the magmatic framework of highly tectonized, structurally and magmatically complex regions, such as accretionary orogenic belts. Age populations derived from geochronological analysis of internally deformed and less/undeformed clasts are compared to establish periods of tectonism and infer tectono-magmatic processes that occurred throughout the region's history. The sixth chapter synthesizes the main conclusions of the thesis.

1.4.1 Publication of chapters

In fulfillment of degree requirements chapters of this thesis have been submitted for publication. Chapter 2 has been submitted to an appropriate journal, its acceptance and publication pending peer review. Chapter 3 has been published by the Journal of Asian Earth Sciences in volume 113, part 1, a special issue on Tectonics of the CAOB and its Pacific analogues. Chapter 5 has been accepted for publication in the American Geophysical Union journal Tectonics, and is currently in an editing phase. The coauthors for these publications mainly fulfilled supervisory roles, providing instruction for lab work, comments and critical analysis of the presented ideas, and edits of written work. For chapters 2 and 3 Bill Davis of the Geological Survey of Canada conducted and provided laboratory results for all SHRIMP geochronology analyses presented.

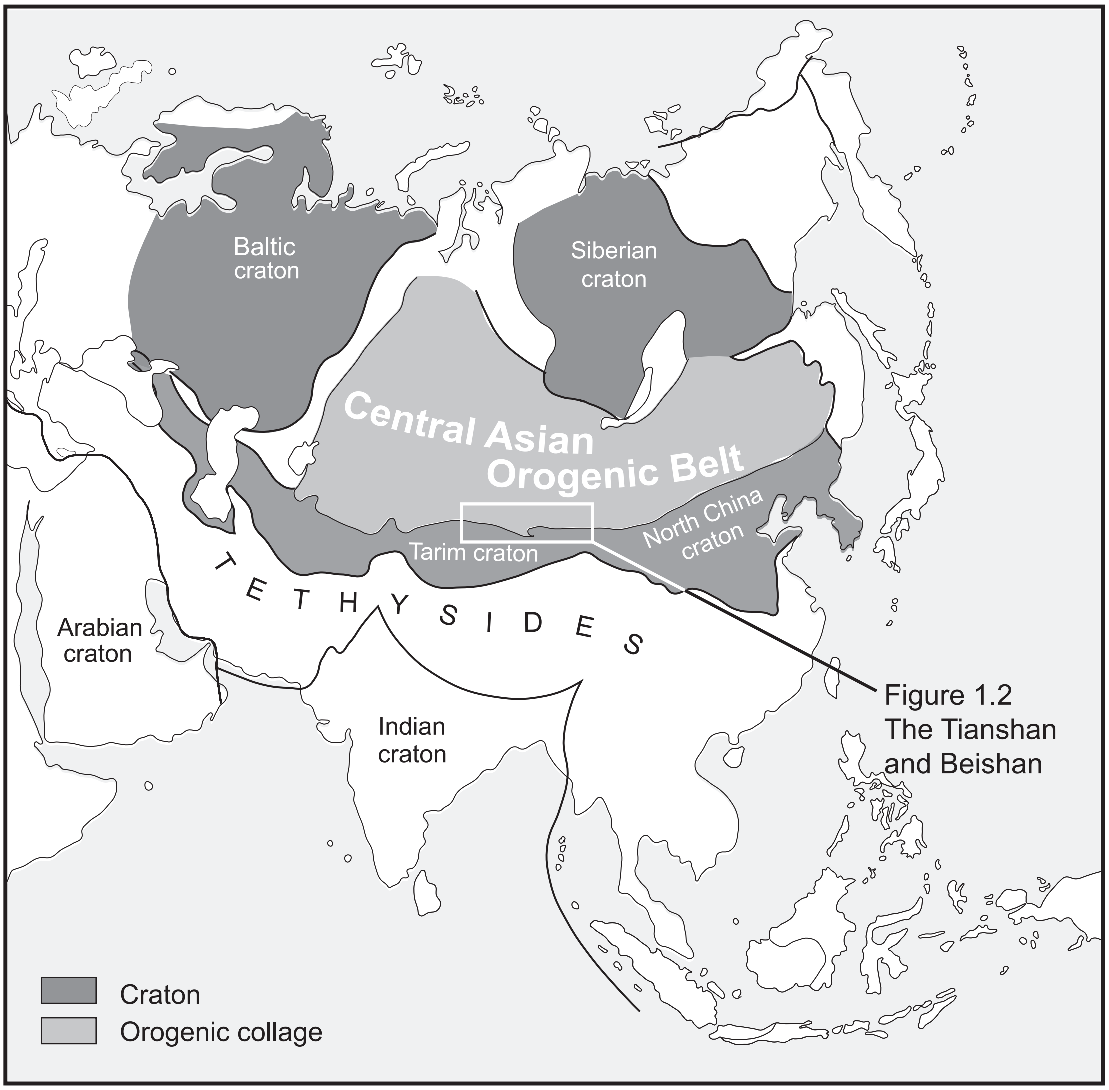

Figure 1.1: Generalized map of the Central Asian Orogenic Belt. Modified from Xiao et al. (2009b).

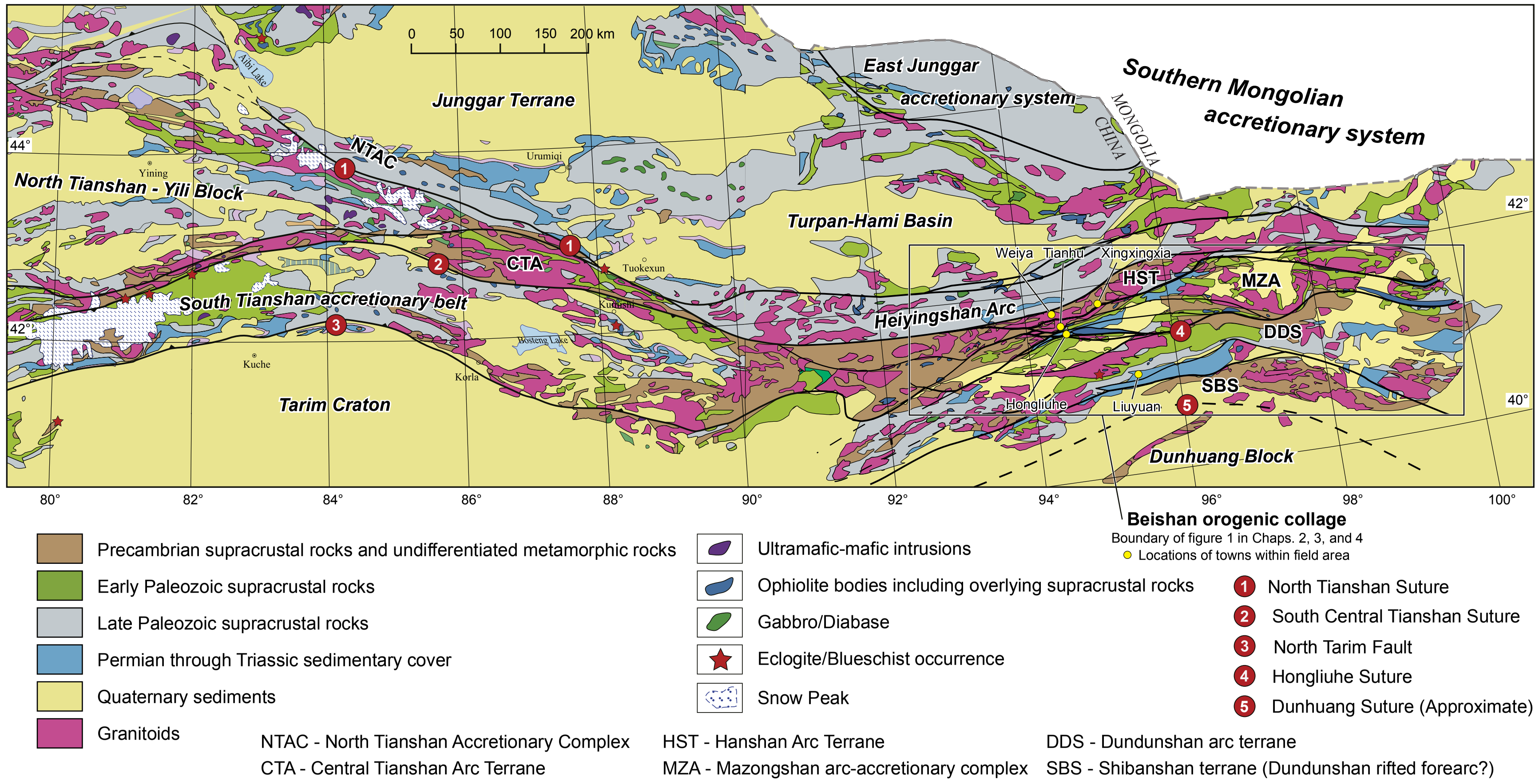

Figure 1.2: Major tectonostratigraphy of the Chinese southern Central Asian Orogenic Belt, including the Tianshan, Junggar, and Beishan orogenic collages. Modified from Gao et al. (2011); Cleven et al. (2015).

Chapter 2

Accretionary tectonic architecture inferred from offset magmatic age signatures between terranes of the southern Central Asian Orogenic Belt: Correlations between U-Pb zircon detrital geochronology, tuff ages and ophiolite generation within suture zones of the Beishan orogenic collage, NW China

2.1 Introduction

The Beishan orogenic collage (or Beishan), a southerly sub-region of the Central Asian Orogenic Belt (CAOB; Fig. 2.1 inset), has many controversial interpretations concerning the location, number and age of its suture zones (Xiao et al., 2010, 2014). As with other regions of the CAOB, and as with other orogens worldwide, many workers in the Beishan have assumed that fragments of ophiolites distributed along structural lineaments directly correlate to suture zones. Potential complications in the Beishan include that it contains three reported ages of Paleozoic ophiolite generation (Cambrian, Devonian, and Carboniferous), and one known age of eclogitic rocks (Ordovician) within only two likely sutures (Qu et al., 2011; Ao et al., 2012; Mao et al., 2012b; Tian et al., 2014; Zheng et al., 2014; Chapter 3). To place these ophiolites and sutures in proper context, the general tectonomagmatic framework of the Beishan requires clarification, in particular concerning Paleozoic tectonic staging and the distribution of magmatic ages within terranes. This article characterizes these aspects of the Beishan, comparing its tectonomagmatic framework to the surrounding regions of the CAOB and shedding light on the processes involved in its suturing and ophiolite generation.

The controversy in accretionary architecture of the Beishan stems in part from the reliance on few, local studies of the stratigraphy and the granitoid geochemistry and chronology. Researchers infer arc to continental magmatism through the early and middle Paleozoic (Li et al., 2001; Hu et al., 2007; Li et al., 2009a; Lei et al., 2011; He et al., 2012; Mao et al., 2012a; Song et al., 2013a,b; Guo et al., 2014; Lei et al., 2014) with orogenic to post-orogenic magmatism in the middle Paleozoic (Zhao et al., 2007; Zhang and Guo, 2008; Li et al., 2009b, 2011) and late Paleozoic (Li et al., 2011; Su et al., 2011; Li et al., 2012; Zhu et al., 2012). Some imply that the whole region contains continental material created during and before the assembly of Rodinia, tenuously linked to the Tarim craton (Li et al., 2009a; Hu et al., 2010; Lei et al., 2011; He et al., 2012; Wang et al., 2014b). Individually, these existing studies provide details of local ages and evidence of specific tectonic processes, but they commonly produce conflicting interpretations. Many studies lack a collective regional view with the fidelity to reliably reconstruct the accretionary history. Terrane-scale correlations are necessary for interpretation of tectonic and amalgamation processes, and are key to understanding regional geodynamics (Xiao and Santosh, 2014).

Age spectra from detrital zircon geochronology of syn-orogenic clastic deposits can be used as a proxy to frame the regional distribution of magmatic bodies and their tectonic staging (Amato and Pavlis, 2010; Ma et al., 2012; Condie, 2014; Xia et al., 2014). The detrital zircon record represents a widely sampled provenance with age distributions proportional to historical volumetric presence (Fedo et al., 2003; Vermeesch, 2004; Moecher and Samson, 2006; Gehrels, 2011; von Eynatten and Dunkl, 2012; Condie, 2014). In this paper we present the results of a U-Pb detrital zircon and tuff geochronological study from the Beishan. We provide field-based structural and petrologic relationships as context for linking detrital age distributions to metamorphic and deformation episodes. Tuff ages determine arc-building periods (Guo et al., 2014) and allow us to constrain the latest accretion event in the central Beishan to the Devonian, earlier than previous Permian interpretation. The tectonomagmatic signatures of the two main Beishan terranes are similar, however, absolute ages relating to staging are different. This implies a shared geodynamic control across individually evolving subduction and collision systems. Our inter-terrane approach correlates existing knowledge to our detrital and igneous geochronology results, enhancing interpretations of the regional structure and metamorphism. Our conclusions further the understanding of accretionary processes active in the Central Asian Orogenic Belt during the Paleozoic, and of the general dynamics of island archipelago accretionary models (Xiao et al., 2010; Kröner et al., 2014; Xiao and Santosh, 2014).

2.2 Regional geologic setting

The CAOB is an E-W trending, generally southward younging orogenic belt. It was built through continental and arc magmatic processes and through accretion of island arc archipelago systems, oceanic units and micro-continents. Accretion occurred in stages against the Siberian and Baltic cratonic margins from the Neoproterozoic through the Paleozoic to early Mesozoic (Windley et al., 2002; Wang et al., 2003; Buckman and Aitchison, 2004; Xiao et al., 2004a; Yakubchuk, 2004; Windley et al., 2007; Xiao et al., 2008, 2009b; Schulmann and Paterson, 2011; Xiao and Santosh, 2014). Researchers consider termination of orogeny to be timed with the collision of the Tarim and North China cratons through the Permian and Triassic periods, respectively (Gao et al., 1998; Chen et al., 1999; Laurent-Charvet et al., 2002; Li et al., 2002; Xiao et al., 2004b; Charvet et al., 2007). The Beishan bridges major suture regions that separate the Tarim craton from the Tianshan orogen to its west, and the North China craton from the Southern Mongolian accretionary system to its east (Fig. 2.1). Some workers promote direct lithotectonic correlations between the Beishan and the Tianshan (Ma et al., 2014; Shi et al., 2014). Late overprinting deformation and poorly constrained crustal-scale strike-slip shear zones severely complicate the along-strike correlation of terranes and structures between the Beishan and the

Tianshan. Late deformation in the Beishan is related to terminal closure and subsequent convergence. Earlier deformation occurred during accretion events, emplacing Cambrian, Devonian and Carboniferous ophiolites and oceanic units (Pan et al., 2008; Ao et al., 2012; Mao et al., 2012b; Zheng et al., 2013; Tian et al., 2014; Chapter 3). In many areas late Paleozoic–early Mesozoic fold-and-thrust belts cover accretion and suture zones, obscuring older structural relationships (Guo et al., 2012; Zhang and Cunningham, 2012; Tian et al., 2013; Cleven et al., 2015). Many workers have cited the impetus for terminal collision as the Dunhuang block. The Dunhuang block is a poorly understood cratonic block south of the southern margin of the Beishan, and is possibly an eastern part of the Tarim. It is reported to have experienced a ca. 400 Ma tectonothermal event (Zhang et al., 2013b; Wang et al., 2014a; He et al., 2014a). Other researchers cite this tectonothermal event, along with early Paleozoic ophiolite emplacement in the central Beishan, as an indication of middle Paleozoic arc-arc collision or arc accretion against the Dunhuang block (Zhao et al., 2007; Zhang and Guo, 2008; Li et al., 2009b, 2011; Qu et al., 2011; Ao et al., 2012; Song et al., 2013b, 2014; Chapters 3 and 4).

2.3 Tectonic framework of the Beishan

The architecture of the Beishan overlies a basement of scarcely preserved Precambrian sialic material. Two E-W trending Precambrian cratonic slivers, which we will refer to as the Hanshan and Huaniushan blocks, were intruded by Paleozoic arc plutons. Despite numerous names in literature for the arcs, we will use the Hanshan and Dundunshan arcs for that which built through the Hanshan and Huaniushan blocks, respectively. Encompassing the respective block, arc, and related supracrustal rocks, we use the Paleozoic namesakes for each respective terrane (their bounds defined in Fig. 2.1). Terrane terminology is used considering their fault-bounded nature and progressive history through multiple tectonic and magmatic episodes. The Mazongshan terrane lies as a wedge between the Hanshan and Dundunshan terranes. Some consider it a protracted forearc accretionary complex to the Hanshan terrane (Song et al., 2013b, 2014). The Hongliuhe shear zone separates the Mazongshan from the Dundunshan terrane and has temporally unconstrained sinistral kinematics. The Xingxingxia shear zone developed as a main structure between the Mazongshan and Hanshan terrane (Fig. 2.1). It is reported to have been active as early as the Silurian in a dextral kinematic sense (Chapter 4), and sinistral as late as the Triassic (Wang et al., 2010). The Heiyingshan arc is a late Paleozoic arc massif that stretches westward along the north margin of the Hanshan terrane and the Tianshan orogen. It is separated from them by the dextral strike-slip Shaquanzi fault, reported to have been active until Permo-Triassic times (Wang et al., 2011) (Fig. 2.1).

The Hanshan terrane contains the remnants of the Hanshan block, ca. 950-800 Ma orthogneisses with a ca. 470-450 Ma tectonothermal overprint (Li et al., 2009a; Hu et al., 2010; Wang et al., 2014b), and Neoproterozoic metasedimentary rocks. Intruding these are Early Paleozoic arc plutonic rocks (Wang et al., 2010; Lei et al., 2011; He et al., 2012), and late Paleozoic syn-tectonic granitoids (Wang et al., 2010; Zhou, 2014). Mesoproterozoic (ca. 1200-1400 Ma) and Paleoproterozoic (ca. 1750-1800 Ma) detrital zircon and inherited cores in magmatic zircon have been reported in many existing geochronological studies of the gneisses (Li et al., 2009a; Lei et al., 2011; He et al., 2012; Zhou, 2014).

The Mazongshan terrane comprises minor arc volcanics, and extensive metasedimentary and (meta)plutonic rocks termed the Beishan complex. The Beishan complex has been interpreted to be a subduction or accretionary complex, with amphibolite to granulite facies metamorphism and a high concentration of deformation (Song et al., 2013a; Tian et al., 2014). Geochemistry and geochronology have recently been used to reinterpret some of its plutonic rocks and orthogneisses as Early Paleozoic volcanic arc rocks, over their original Precambrian age estimations (Hu et al., 2007; Song et al., 2013a,b; Lei et al., 2014). The southern margin of the Mazongshan terrane includes isolated fragments of accreted Cambrian (Zhang and Guo, 2008; Ao et al., 2012; Chapter 3) and Devonian (Tian et al., 2014) ophiolites, along with related supracrustal rocks. Sedimentary rocks of the Permo-Triassic Hongyanjing basin (Fig. 2.1), which includes the Hongliuhe Formation of the Zhesi Group, overlie the oceanic units and metamorphic rocks. The basin developed during late Carboniferous extension then rapidly evolved to a compressional fold-and-thrust belt with large-scale fold superpositioning in Permo-Triassic times (Zhang and Cunningham, 2012; Tian et al., 2013; Cleven et al., 2015).

Studies of Dundunshan plutonic rocks have indicated Early Paleozoic arc-related magmatism (Mao et al., 2012a; Guo et al., 2014) that transitioned to collisional (Li et al., 2011) and intraplate (Zhao et al., 2007; Li et al., 2009a) settings. Late Paleozoic and Early Mesozoic intrusive rocks are reportedly A-type post-collisional granites (Su et al., 2011; Li et al., 2012; Zhu et al., 2012), with some I-type characteristics (Li et al., 2012). The terrane has only rare high-grade metamorphic rocks, but has extensive Paleozoic marginal sediment cover (including the Dundunshan Group) and volcanic rocks. Late Neoproterozoic through Silurian passive margin sediments (the Pingtoushan Formation) compose the northern margin, exhibiting superposed folds. There is an eclogite occurrence in high-grade gneissic rocks at the southern margin (Qu et al., 2011). The existence or boundary of any southern accretionary complex or suture zone is poorly defined. This may be due to late Paleozoic extension that localized along the margin (Su et al., 2011) and produced the Liuyuan complex, a 9 km thick Carboniferous–Permian supra-subduction ophiolitic volcano-sedimentary succession (Mao et al., 2012b). It is in fault contact with Permo-Triassic nearshore sedimentary deposits to the north and south (the Shuangbaotang Formation). Sparse outcrops have been studied in the expanse of desert further south, most attributed to metamorphic rocks of the Dunhuang block (Zhang et al., 2013b; Wang et al., 2014a; He et al., 2014a).

2.4 Field relationships

2.4.1 The Dundunshan terrane

Stratigraphic features and both extensional and compressional structures across the Dundunshan terrane were mapped, providing context for detrital and igneous geochronology (Fig. 2.2). The Shuangbaotang Formation sedimentary successions to the north and south of the Liuyuan complex (Fig. 2.2) are openly to tightly folded successions of active margin nearshore sediments. They exhibit syn-sedimentary deformation and loading structures, including flame structures and convolute bedding (Fig. 2.3 A). Their fold axes plunge very shallowly to the west and the units have an E-W trending, steeply north-dipping axial planar cleavage (Fig. 2.2, stereonet A). The Shuangbaotang Formation sandstones from both basins north and south of the Liuyuan complex were sampled for detrital geochronology (samples 11NC58 and 11NC59; indicated on Fig. 2.2).

Along and near the contact between the Dundunshan Group (Fig. 2.2) and the Shuangbaotang Formation is a distributed series of four small steeply dipping shear zones hosted in the Dundunshan Group metasediments (Figs. 2.4 A and 2.4 B). Ductile stretching lineations are subvertical (Fig. 2.2, stereonet B). The shear zone rocks are highly carbonaceous with a protolith of siltstone or slate and have a very finely spaced mylonitic foliation. Mantled porphyroblasts of quartz, C' fabrics, and folded quartz domains indicate both senses of shear, with a dominant south-over-north sense (Fig. 2.4 B with schematic diagram).

Distributed within the Dundunshan Group metasedimentary rocks are ductile fault zones of meter-scale width with steeply plunging mineral stretching and striation lineations (Fig. 2.2, stereonet B). Some shear zones indicate a kinematic reversal from extension to compression (to south over north) as seen in individual boudins imbricated back over neighboring in-line boudins (Fig. 2.4 C). Most Dundunshan metasedimentary units are tilted to sub-vertical with a slight southern structural vergence, and show an increasing metamorphic grade northward. A graywacke with crystal-lithic tuff layers from the Dundunshan Group was sampled for geochronology (sample 08NC03C; Fig. 2.3 B) along with a quartzite for detrital geochronology (sample 11NC60; Fig. 2.3 C).

Further north, the Late Neoproterozoic Pingtoushan Formation (Fig. 2.2) comprises amphibolite-grade marginal metasedimentary rocks. Its marbles host fine gray layers 4-15 cm thick, interpreted to have originally been ash layers (Fig. 2.3 D). One layer was sampled for geochronology (sample 08NC04A, indicated on Fig. 2.2). The marbles also contain deformed and undeformed dykes providing further evidence of compression after extension; an early mafic dyke exhibits horizontal extension (boudinage) in a weak, shallowly dipping marble layer, with subsequent opposing compressional folding and imbrication of the boudin series (Fig. 2.4 D). An undeformed felsic dyke in the same photo (Fig. 2.4 D cross-cuts the mafic dyke, and was sampled for geochronology (sample 08NC01A) to provide an age constraint on the cessation of all deformation.

At the northern boundary of the Dundunshan terrane sinistral translation across the Hongliuhe shear zone has deformed, folded and imbricated a tract, several kilometers thick, of passive margin sedimentary rocks. Within the cross-section they appear as alternating fault-bounded units of limestone and schist, punctuated with E-W trending mylonitic foliations that are loosely organized into flower-like structures (Fig. 2.2 cross-section and stereonet C). Some slices of gneissic lithologies exist in the strike-slip imbricated stack. Deformation is distributed in many (at least one dozen counted) meter- to decameter-scale high-strain zones commonly hosted in limestone lithologies (Fig. 2.5 A), as well as in schist and basalt units associated with the Mazongshan terrane (Figs. 2.5 B).

2.4.2 The Mazongshan terrane

Accreted oceanic volcano-sedimentary successions and younger overlying sedimentary rocks were mapped within the Mazongshan terrane (Fig. 2.6) to constrain the latest accretion event. The syn-orogenic Hongliuhe Formation is part of the Zhesi Group in the Hongyanjing basin (indicated in Fig. 2.1), and unconformably overlies the early Paleozoic oceanic units. It is Early Permian in age (Li et al., 2006), and contains sections with rhythmic interbedding of sandstone and siltstone and thick basal successions of conglomerate. It contains low-angle south-vergent thrusts and folds with a shallowly plunging fold-axis

(Cleven et al., 2015), except where overprinted by shear folding proximal to the Hongliuhe shear zone. The formation was extensively sampled at three stratigraphic levels for detrital geochronology (samples HLH; indicated in Fig. 2.6).

In the western Hongliuhe region sub-vertically dipping reverse brittle-ductile faults, with a north-over-south sense of shear, imbricated the unconformably underlying oceanic volcanic units, along with their overlying Hongliuhe Formation sedimentary rocks, into a thrust stack. There are three separate thrust slices of volcano-sedimentary successions in the Hongliuhe to Tianhu area. Cross-sectional maps provide detailed structural and stratigraphic relationships (Fig. 2.7; section locations indicated in Fig. 2.6).

The southwest Tianhu volcanic section (section B-B'; Fig. 2.7 A) lies along the Hongliuhe shear zone and previous studies interpret that the volcanics have an ocean island basalt geochemistry (Pan et al., 2008). It is approximately 700 m thick and contains epidote-chlorite-altered massive and pillow basalt flows (Fig. 2.8 A) interlayered with limestone and sandstone. A thick succession of interlayered limestone with thin basalt or basaltic volcaniclastic rocks covers the pillow unit (Fig. 2.8 B) and continues north to the Hongliuhe shear zone. Steeply dipping east-west striking ultramylonites are localized within limestone units and exhibit both north-over-south and south-over-north kinematics.

The northwest Tianhu volcanic section (section C-C'; Fig. 2.7 B) contains similarly epidotized basalt pillow flows with morphologies that indicate a younging direction to the north in the southern unit (Fig. 2.8 C) and younging to the south in the northern unit (Fig. 2.8 D). The southern and northern units are separated by siltstone exhibiting a well-developed cleavage. The units all dip steeply to the north. Hongliuhe Formation conglomerates unconformably overlie the overturned pillows, and the entire volcanic section has been thrust over the Hongliuhe Formation sedimentary rocks in the south (Fig. 2.8 E).

The northeast volcanic-sedimentary section (section D-D'; Fig. 2.7 C) borders metasedimentary rocks of the Mazongshan terrane to its north. They are separated by the Tianhu shear zone (Fig. 2.6). The section is approximately 1200 m thick. It contains a thin series of mafic-ultramafic cumulate intrusive rocks at its northern end which are overlain by basalt and quartz-rich sandstone. The thin peridotite unit has been analyzed petrographically, and shows poikilitic textures of amphibole encasing relict plagioclase and/or pyroxene, and chloritized ?pyroxene encasing relict serpentinized olivine (Fig. 2.9 A). Sandstones upsection contain lithic fragments of plagioclase, K-feldspar, cryptocrystalline quartz, detrital magnetite and volcanic material (Fig. 2.9 B). They were sampled for detrital geochronology (sample 11NC57E). The section continues with basalt, diabase and sandstone units, with the diabase also showing poikilitic textures of amphibole phenocrysts encasing plagioclase grains (Fig. 2.9 C). Sedimentary units fine towards the south end to siltstone (Fig. 2.9 D) and chert (Figs. 2.8 F and 2.9 E). Layers hosted in siltstone comprising coarse fragmental quartz layers centimeters to meters thick are interpreted as crystal-lithic tuff horizons. One tuff horizon was sampled for geochronology (sample 11NC57I). Overlying the chert unit is a unit of pillow basalt that indicates a southerly younging direction, implying the unit is overturned (Fig. 2.8 G).

2.5 Geochronology

Uranium-lead zircon analyses were performed on the samples described above, including three igneous samples, two felsic tuff samples, one amphibolite (metamorphosed ash layer in marble), and four detrital samples. An additional set of detrital samples (sample HLH) were collated from previous work to provide an effective fifth detrital sample. Two separate analytical procedures were used: Sensitive High Resolution Ion MicroProbe (SHRIMP II) analyses on zircon from one tuff sample, the amphibolite, one igneous dyke, and one pillow basalt sample; and laser ablation – inductively coupled plasma mass spectrometry (LA-ICPMS) techniques for the remainder. In all cases zircon grains were separated from pulverized sample material using standard heavy liquid and magnetic separation procedures. Individual grains were selected and hand-picked for favorable characteristics for igneous samples, randomly for detrital samples, then mounted in epoxy, ground to expose their cores and polished for analysis.

2.5.1 Analytical techniques

LA-ICPMS

Mounted and polished zircons were imaged with electron backscatter (BSE) and cathodoluminescence (CL) functions of a JEOL JSM6610-Lv scanning electron microscope (SEM) at the University of Toronto. The U-Pb isotopic analysis was performed on the LA-ICPMS apparatus at the Jack Satterly Geochronology Laboratory in the Department of Earth Sciences at the University of Toronto, Ontario, Canada. The laboratory procedure involves a VG Series 2 Plasmaquad ICPMS used in conjunction with a 75 l/s rotary pump for the expansion chamber (the S-option) for enhanced sensitivity. The laser system is a 213 nm New Wave laser ablation system. Polished zircon crystals were ablated using a beam diameter of 15, 25 or 30 µm at 5 or 10 Hz and 40% power. The He carrier gas was passed through a 25 ml mixing chamber to dampen signal instability from U heterogeneity in the sample. Data collection for chosen elements and isotopes was applied over specific time intervals: ^{88}Sr (10 ms), ^{206}Pb (30 ms), ^{207}Pb (40 ms), ^{232}Th (10 ms) and ^{238}U (20 ms). Sr was measured as a proxy for alteration or inclusions. Analyses with high Sr were rejected. Rastered ablation patterns were lasered onto the surface to remove debris or impurities prior to each target analytical measurement. The 35 second target ablation and analysis was performed after a 10 second establishment of a baseline signal. A washout period of 50 seconds was allowed to elapse between target sample analyses. In-house data reduction software authored and provided by D. W. Davis allowed for practical editing and reduction of data. The analyses did not include a measure of ^{204}Pb, so the reduction and calculation process made no corrections for common lead. Two in-house zircon standards were used in separate analytical runs, the standards DD85-17 (3002 ± 2 Ma) and DD83-10 (2733.0 ± 0.9 Ma). The standard grain analyses were applied as brackets for sets of three or fewer sample measurements.

SHRIMP

Analytical procedures for U-Pb zircon SHRIMP dating were conducted at the Geological Survey of Canada Geochronology Laboratory in Ottawa, Ontario, Canada. The analytical procedures followed the outline of Stern (1997) utilizing the U-Pb calibration methods and zircon standards of Stern and Amelin (2003). Internal zircon zonation and grain structure was imaged with back-scattered scanning electron microscopy utilizing CL in a Cambridge Instruments SEM.

2.5.2 Igneous U-Pb zircon analyses – Dundunshan terrane

All LA-ICPMS single-age analytical results are provided in Table A.1 in the appendix. All SHRIMP single-age analytical results are provided in Table A.2 in the appendix. Backscatter SEM images of select zircons from igneous samples are provided in figure 2.11. Plotted Concordia diagrams are provided in figure 2.12 using the program Isoplot (Ludwig, 2003). All error amounts in Concordia diagrams are reported as 2σ values, or at 95% confidence level, and Concordia ages are calculated with decay-constant errors included.

Sample 08NC05 – LA-ICPMS analysis, Tonalite gneiss

Sample 08NC05 was collected from a tonalite gneiss approximately 20 km south of the Liuyuan Complex. Four concordant data (Fig. 2.12 A) provide a Middle Ordovician Concordia age (Ludwig, 1998) of 467.9 ± 4.0 Ma. This is interpreted to be either the crystallization age of the tonalite or an age of metamorphism.

Sample 08NC03C – SHRIMP analysis, Graywacke with crystal-lithic tuff layers

Sample 08NC03C was collected from a muscovite bearing graywacke with quartz crystal-lithic layers (Figs. 2.3 B and 2.10 C) near the southern margin of the Dundunshan terrane (Fig. 2.2). The zircon population exhibits euhedral to subhedral grains commonly with a low aspect ratio. CL images show that oscillatory zonation is present in most of the grains, and some exhibit sector zonation (Fig. 2.11). Twelve concordant analyses (Fig. 2.12 B) yield a Late Ordovician Concordia age of 449.9 ± 2.9 Ma. This date is interpreted to be the age of volcanism and sedimentation.

Sample 08NC04A – SHRIMP analysis, Metamorphosed ash layer in marble

Sample 08NC04A was collected from a horizon in a marble on the northern margin of the Dundunshan terrane (Figs. 2.2 and 2.3 D). The sampled layer is quartz-amphibole (anthophyllite) schist (Fig. 2.10 E) within a quartz-biotite-cordierite schist host rock (Fig. 2.10 F). The sample is interpreted to be a metamorphosed ash layer and proved to contain abundant zircon. The zircon population contains euhedral to anhedral grains. The edges of grains show partial resorption, creating irregular grain boundaries and embayments. Small inclusions are common, and in many instances form inclusion trails, sometimes along zonation lines. Oscillatory growth and sector zonation is common, and some grains show disrupted patchy or convolute zonation in CL images (Fig. 2.11). Twenty-two concordant data (Fig. 2.12 C) provide a Neoproterozoic Concordia age of 673.2 ± 5.6 Ma. This date is interpreted to be the age of volcanism and sedimentation.

Sample 08NC01A – SHRIMP analysis, Undeformed felsic dyke

Sample 08NC01A was collected from an undeformed felsic dyke crosscutting a foliated marble unit in the northern margin of the Dundunshan terrane (Figs. 2.2 and 2.4 E). It yielded abundant zircon, most of which is euhedral with a lesser population of subhedral grains, and most share a similar long aspect ratio. Inclusions are fairly abundant. Typical igneous oscillatory growth and sector zonation patterns are visible in CL and BSE images (Fig. 2.11). Fourteen concordant data (Fig. 2.12 D) provide a Late Triassic Concordia age of 232.3 ± 2.1 Ma. This date is interpreted to be the age of emplacement of the dyke.

2.5.3 Igneous U-Pb zircon analyses – Mazongshan terrane

Sample 09NC39G – SHRIMP analysis, Pillow basalt

Sample 09NC39G was collected from a non-vesicular portion of a basaltic pillow outcrop in the NW volcanic succession described above (location shown in Fig. 2.6). The small population of zircon exhibits subhedral crystal shapes and CL imagery shows oscillatory growth zonation (Fig. 2.11). The grains are small, all less than 100 µm in diameter. Three concordant data (Fig. 2.12 E) provide an Early Devonian Concordia age of 416.6 ± 15 Ma. This date is interpreted to be the age of eruption of the basalt, which is supported by field relationships and regional correlations (see below).

Sample 11NC57I – LA-ICPMS analysis, Crystal lithic tuff

Sample 11NC57I was collected entirely from a fine grained quartz crystal-lithic horizon inside a siltstone unit, interpreted as a tuff layer, in the northeast volcanic succession described above (Figs. 2.6 and 2.9 D). Zircon is abundant and appears euhedral to anhedral with high aspect ratios, but some are rounded. Inclusions are found in moderate abundance. Oscillatory growth zonation and sector zonation are common. Occasional grains exhibit inherited cores with patchy zonation (Fig. 2.11). A total of 18 grains were analyzed (Fig. 2.12 F). Precambrian ages in the range of 1100, 1400, and 1800 Ma are interpreted to be from detrital or inherited grains. The youngest set of eight concordant data provides a Concordia age of 409.0 ± 2.9 Ma (Early Devonian). This date is interpreted to be the age of volcanism and sedimentation.

2.5.4 U-Pb detrital zircon analyses – Dundunshan terrane

All detrital zircon analyses were performed by LA-ICPMS. The analytical results are provided in Table A.3 in the appendix. The ^{206}Pb/^{238}U ages were used to assemble age spectra. Separate histogram plots for Paleozoic and Precambrian grains are provided due to the lengthy hiatus between their populations and the small number of analyses that prove to be Precambrian. Adaptive kernel density estimates (KDEs) are overlain on all histograms as calculated by the visualization software Density Plotter, which also provides an algorithm for calculation of the labeled component peak ages (Sircombe and Hazelton, 2004; Vermeesch, 2012). Component peak ages and their percentage representation of the population are reported with the respective plot. Radial plots (Galbraith, 1990) were prepared with the software RadialPlotter (Vermeesch, 2009) to visualize the differing precision distributions (σ values) by age, and to display the level of discordance of each grain. Any data that are >10% discordant or >5% reverse discordant were discarded.

Samples 11NC58 and 11NC59 – Sandstones from the Shuangbaotang Formation

Samples 11NC59 and 11NC58 were collected from low metamorphic grade sandstones of the Shuangbaotang Formation, south and north of the Liuyuan complex, respectively (locations indicated on Fig. 2.2). Petrographic images are provided in figures 2.10 A and 2.10 B, respectively. A total of 96 grains from sample 11NC59 and 98 grains from sample 11NC58 fit the concordance criteria. A total of 22 grains from sample 11NC59 and 30 grains from sample 11NC58 yield Precambrian ages, including measurements on six inherited cores from each of the samples.

The Paleozoic age distributions of these two samples are shown in a cumulative probability plot (Gehrels, 2011) in figure 2.13. It illustrates the similarity between the age distributions of the two samples and is accompanied by the results of a Kolmogorov-Smirnov (K-S) test (Sircombe and Hazelton, 2004), a goodness-of-fit statistical test (Fig. 2.13, inset). The spreadsheet macro produced by George Gehrels of the Arizona LaserChron Center was used to produce the cumulative probability plots and make the K-S statistical calculations.

The probabilities (P values) obtained from the K-S test are used to compare potential similarities in the provenance between detrital samples. The P value of 0.476 comparing samples 11NC58 and 11NC59 is considered a high value, well above the threshold of 0.05 that gives a 95% confidence that the differences between the two samples are due to random variation, and not due to a difference in provenance. For comparison, the two samples are each paired with the Hongliuhe Formation sample set (sample HLH, described below) for the same K-S test (Fig. 2.13). The low P-values (0.010 and 0.017) support that the Hongliuhe Formation has a different provenance.

The above statistical analysis shows, with a fair degree of certainty, that the two samples from the Shuangbaotang Formation have statistically identical zircon populations. This supports interpretation that the Shuangbaotang Formation exposed north and south of the Liuyuan Complex is indeed part of the same formation. The zircon age data from the two samples are thus combined in later discussion, together referred to below as the Shuangbaotang sample set.

The Shuangbaotang sample set has a combined total of 142 Paleozoic grains that fit the concordance criteria. The age distribution shows three distinct Paleozoic component peak ages of ca. 280, 370, and 430 Ma (Fig. 2.14 A). A total of 52 grains have Precambrian ages. The Precambrian population has a spread of ages yet shows only two distinct component age peaks of ca. 940 and 1450 Ma.

Sample 11NC60 – quartzite, Dundunshan Group

Sample 11NC60 was collected from a quartz-biotite schist with porphyroclastic plagioclase grains, polycrystalline quartz, cryptocrystalline quartz and volcanic fragments (Fig. 2.10 D) within the Dundunshan Group (location indicated on Fig. 2.2). A total of 108 grains fit the concordance criteria. The age distribution shows a single distinct Paleozoic component peak age of ca. 450 Ma (Fig. 2.15 A). There are no Precambrian ages obtained from this sample.

2.5.5 U-Pb detrital zircon analyses – Mazongshan terrane

Sample 11NC57E – sandstone, Mazongshan accretionary unit

Sample 11NC57E was collected from a low-metamorphic grade sandstone situated within a volcanic succession underlying the Hongliuhe Formation (Figs. 2.6 and 2.9 B). A total of 95 grains fit the concordance criteria. The age distribution shows a single distinct Paleozoic component peak age of ca. 440 Ma (Fig. 2.15 B). The sample yielded no Precambrian ages.

Sample HLH – Hongliuhe Sample Set

The Hongliuhe sample set is a collection of 721 analyses of zircon separates from 408 sampled granitoid conglomerate clasts, and 267 analyses of zircon separates from three sandstone samples, collected from three different stratigraphic levels across a section of the Hongliuhe Formation. Representative petrographic images of Hongliuhe Formation sandstone are provided in figure 2.9 F. Details on their zircon characteristics and the analytical results are presented separately in chapter 5. The data, summarized here in figure 2.14 B for the current purpose, are a compilation of all the clast and sandstone results. They contain component peak ages of ca. 310, 400, and 450 Ma. Precambrian grains are minimal considering the population size, numbering only n=41, five of which are measurements on cores. They show peak component ages of ca. 720, 1030, and 1600 Ma.

2.6 Summary and Discussion

The age spectra of the Late Paleozoic detrital samples presented above show a more diverse age record compared to the middle Paleozoic detrital samples. They depict two distinct signatures, spatially divided between northern and southern regions: the Shuangbaotang sample set in the south, and the Hongliuhe sample set in the north.

The southern Shuangbaotang sample set (Fig. 2.14 A), exhibits two early Paleozoic pulses of magmatism, from 470 to 350 Ma with peaks at 435 and 370 Ma. A graywacke with crystal-lithic tuff layers yields an age of 449.9 ± 2.9 Ma (08NC03C, Fig. 2.12 B) and confirms magmatic activity in the earlier peak. Paleozoic magmatism is followed by a 50 m.y. hiatus then resumed for 40 m.y. peaking at 280 Ma. An age from a metamorphosed, layered anthophyillite cordierite schist, interpreted to have originally been a felsic volcanic ash layer, provides evidence of the earliest magmatic activity, at 673.2 ± 5.6 Ma (08NC04A Fig. 2.12 C). This age is not represented in the detrital record.

The northern Hongliuhe sample set (Fig. 2.14 B) depicts continuous magmatism in its provenance from ca. 500 Ma to 370 Ma with two main peaks at 450 and 400 Ma. A crystal-lithic tuff age of 409 ± 2.9 Ma (11NC57I, Fig. 2.12 F) from a sedimentary succession with negligible lag time (see below, section 2.6.1) confirms arc-related magmatic activity for the latter peak. This magmatism is followed by an approximate 40 m.y. hiatus and a further 40 m.y. of magmatic activity between ca. 330 and 290 Ma, peaking at 310 Ma before complete cessation. The youngest single zircon date at 294 ± 3 Ma conforms with paleontology-based Early Permian deposition timing interpretation (Li et al., 2006).

2.6.1 Paleozoic magmatic periods and detrital provenance

The Early Paleozoic detrital samples from both the Dundunshan terrane (11NC60, Fig. 2.15 A) and the Mazongshan terrane (11NC57E, Fig. 2.15 B) have similar narrow age distributions of 40-50 m.y. peaking at approximately 440-450 Ma. These are not diagnostic of any single terrane in the region (Fig. 2.16). The Th/U ratios of the zircon are typical for igneous rocks and match the signatures compiled from existing data from any of the terranes in the region (Figs. 2.17 A and B, respectively). The lack of inherited Precambrian zircon may characterize the sources as juvenile material. These features, especially with the minimal lag time for 11NC57E deposition (the youngest single zircon age of 402 ± 6 Ma being within the error of its crystal-lithic tuff age of 409 ± 2.9 Ma, 11NC57I), suggest that their magmatic peaks reflect active arc building in the Ordovician–Early Devonian times, and deposition was in an environment proximal to an active arc.

Age spectra of the southern Shuangbaotang sample set (Figs. 2.14 A) match compiled ages reported from central Dundunshan intrusive and volcanic rocks (Fig. 2.16; references given in the caption). The Th/U ratios of the detrital grains also match the fields defined by the same reference data set (Fig. 2.17 C). The youngest single zircon date is 245.5 ± 5.7 Ma and therefore the formation is likely Permo-Triassic. We interpret this data to indicate that the provenance for the Shuangbaotang Formation is entirely in the Dundunshan terrane. The Shuangbaotang Formation is situated at the southern margin of the Dundunshan terrane, and key aspects of its signature are different from Hanshan and Mazongshan terrane reference data (Fig. 2.16).

The northern Hongliuhe sample set (Fig. 2.14 B) closely mimics the age distribution for previously reported Hanshan terrane igneous ages (Fig. 2.16) up to its deposition age in the Early Permian (the youngest single zircon date of 294 ± 3 Ma). The early Paleozoic peak is also consistent with reported Mazongshan terrane ages (Fig. 2.16). Zircon Th/U ratios closely match both Mazongshan and Hanshan terrane reference data, including very low values, especially for a concentration just prior to the 385 Ma start of the hiatus (Fig. 2.17 D). The exception is the most extremes of the increasingly high values in figure 2.17 D from 440 to 380 Ma, likely a reflection of the limits of the Mazongshan reference data, that represents a limited number of granitoids. The very low Th/U ratios are indicative of metamorphic zircon, potentially sourced from the widespread metamorphic rocks in the Mazongshan terrane (Li et al., 2001; Hu et al., 2007; Song et al., 2013a,b; Lei et al., 2014). Based on the above, we interpret that the provenance for the Hongliuhe Formation is in both the Hanshan and Mazongshan terranes.

Paleozoic age distributions and Th/U ratios throughout the Beishan, from both our detrital data and previous studies of magmatic rocks, are distinct from data reported in along-strike terranes such as the Central Tianshan zone (Figs. 2.17 A–D), a location often cited as a western extension of the Hanshan and Mazongshan terranes (Hu et al., 2007; Li et al., 2009a; Hu et al., 2010; Lei et al., 2011; He et al., 2012; Lei et al., 2014; Wang et al., 2014b). Its data show a similar overall Paleozoic magmatic age pattern, though with a less pronounced, much shorter hiatus of approximately 10 m.y., and Th/U ratios (up to 2.7) in the youngest magmatic pulse that far exceed the Beishan detrital data values that are considered a representative sample of their provenance.

2.6.2 Tectonic staging in the Beishan

The Beishan's Precambrian detrital zircon history shows magmatism coincident with known Tarim craton peak magmatic ages (Li et al., 2009a; Hu et al., 2010; Wang et al., 2014b), as the Tianshan's early history does. This is true for both the Mazongshan terrane and Dundunshan terrane signatures. This implies that the Hanshan and Huaniushan Precambrian blocks, basements to the Hanshan and Dundunshan arcs, may share a history as pericratonic fragments of the Tarim. They are the most likely, or merely proximal, source for the ca. 800, 930, 1400, 1700 and 2400 Ma peak magmatic ages documented in both the norther Hongliuhe and the southern Shuangbaotang detrital sample sets.

The northern Hongliuhe and southern Shuangbaotang sample sets have similar patterns of detrital age spectra, except that the southern Shuangbaotang sample set is younger by roughly 30 to 40 m.y. in all respects (Fig. 2.14). For example, in the north magmatism ramps up to full peak magmatic activity starting around 490 Ma, whereas in the south it initiates around 460 Ma (Fig. 2.18 A). This is interpreted to indicate that arc magmatism started earlier in the north than in the south by ca. 30 m.y. Based on the sudden cessation of magmatism after the initial early Paleozoic pulse and the subsequent hiatus in each of the respective detrital records, our interpretation is that the Beishan underwent a significant multi-terrane, staged collision or accretion event in the middle Paleozoic. Magmatism ceased first in the north implying closure of an ocean basin along a Hanshan/Mazongshan terrane to Dundunshan terrane suture by 380 Ma (Fig. 2.18 B). Magmatism then ceased in the south, with closure of another ocean basin along the southern margin of the Dundunshan by approximately 350 Ma (Fig. 2.18 C). This matched dynamic implies that there is a similar process occurring in both systems. The data may also imply that the Dunhuang block (He et al., 2014a) docked with these terranes earlier than the Permian, as some workers purport (Xiao et al., 2010; Tian et al., 2014; Cleven et al., 2015). The resumption of magmatism in the late Paleozoic also started earlier in the north (at ca. 340 Ma) than in the south (at ca. 300 Ma). It was likely related to regional extension and could have been generated by staged slab breakoff following collision/accretion (Fig. 2.18 D).

2.6.3 Latest accretion in the Mazongshan terrane

Previous workers have suggested that ocean closure in the central Hongliuhe suture occurred as late as the Permian (Xiao et al., 2010; Tian et al., 2014). This stemmed from interpretation of late Carboniferous whole-rock Ar-Ar dates from an ocean island basalt (OIB) as the timing of eruption/deposition of volcano-sedimentary successions incorporated in the suture (Pan et al., 2008; Xiao et al., 2010). New U-Pb ages and field data reported in this article are inconsistent with this age interpretation. The crystal-lithic tuff age (11NC57I, 409 ± 2.9 Ma) in the northeast Tianhu volcanic section and synchronous basalt age (09NC39G, 416.6 ± 15.0 Ma) in the northwest section constrain the eruption/deposition of the Hongliuhe–Tianhu volcano-sedimentary successions to the Devonian. This constrains the youngest accretion in the Mazongshan terrane to after the Early Devonian (younger than ca. 410 Ma). This correlates to the 380 Ma (Middle Devonian) start of the hiatus in the detrital signature of the Hongliuhe sample set, interpreted as the time of the accretion (Fig. 2.18 B).

Redefining the tectonic environment of the Hongliuhe–Tianhu volcanic successions

The northwest and northeast Hongliuhe–Tianhu volcano-sedimentary successions were previously interpreted as members of the Permian Hongliuhe Formation (Li et al., 2006). This is inconsistent with our field observations that the successions include isoclinally folded and overturned sections, and that they contributed metamorphosed clastic material to the unconformably overlying Hongliuhe Formation (Cleven et al., 2015). It is also inconsistent with the Devonian U-Pb ages from the volcano-sedimentary successions reported here (samples 11NC57I and 09NC39G). Although one of the ages (sample 09NC39G) relies on limited number of grains from a basalt, a lithology that rarely yields abundant zircon, the two dates are identical within error. It should be noted that the Hongliuhe–Tianhu volcanic successions bear many similarities with the Huoshishan-Niujuanzi ophiolite (see below), which lie eastward along the same structural lineament (Fig. 2.1), and have yielded broadly similar ages (Huoshishan = 410.5 ± 3.7 Ma, Gabbro zircon, and Niujuanzi = 435.0 ± 1.9 Ma, Gabbro zircon).

Petrologic, lithostratigraphic and geochemical details of the Hongliuhe–Tianhu volcanic successions allow for further reinterpretation of their original tectonic setting. Revisiting the original OIB geochemistry interpretation by Pan et al. (2008) of the southwestern block (section B-B', Figs. 2.6 and 2.7), we found that its chemistry is directly comparable to that of the basalt in the Huoshishan-Niujuanzi ophiolite (Tian et al., 2014). The trace element diagrams from both show enriched LREEs with slight Nb and Ta anomalies, indicative of a suprasubduction environment (Fig. 2.19 A). A La/Nb vs. La/Sm plot, normalized to Sun and McDonough (1989) reference values (Fig. 2.19 B), depicts the influence of a subduction zone in the Pan et al. (2008) and Tian et al. (2014) data. It also shows that the Silurian–Devonian ophiolites are not geochemically comparable to the Cambrian ophiolites (the Hongliuhe and Yueyashan-Xichangjing ophiolites) along the same suture (Ao et al., 2012; Chapter 3), except for some island-arc basalt chemistry from the Hongliuhe ophiolite's thick overlying supracrustal succession. Our petrography of peridotite and diabase associated with the Hongliuhe–Tianhu volcanic successions shows poikilitic textures, indicating that amphibole crystallized after plagioclase, consistent with a supra-subduction setting crystallization sequence (Metcalf and Shervais, 2008). In the northeast succession (section D-D', Figs. 2.6 and 2.7) arc- or continentally derived sandstones are deposited only meters above cumulate gabbro and peridotite, suggesting an arc-proximal extensional seafloor environment that exhumed and exposed deeper plutonic rocks. This type of depositional environment is reported in the nearby Hongliuhe ophiolite, relating to subduction rollback at the margin of an existing arc (Chapter 3).

In previous sections we interpret that arc-arc collision occurred between the Hanshan/Mazongshan and Dundunshan terranes in the Early–Middle Devonian, a case supported by other researchers (Ao et al., 2012; Song et al., 2014; Chapter 4). This timing is coincident with our ages for the Hongliuhe–Tianhu volcanic successions as well as those the Huoshishan-Niujuanzi ophiolites (Tian et al., 2014). Collision and ophiolite generation are not necessarily incongruent phenomena. Tracts of un-subducted oceanic crust can remain preserved, post-collision, in continental re-entrant gaps and may roll-back after their adjoining, subducted oceanic-crustal underpinning has been removed due to post-collision slab breakoff. A modern analogue of this may be present in the Mediterranean, where subduction is now occurring and 100 m.y. old ophiolites have been emplaced in the Alpine orogeny.

2.6.4 Suturing between Beishan terranes

The site of suturing between the Dunhuang block and the Dundunshan terrane is a point of contention (Xiao et al., 2010; Guo et al., 2012; Mao et al., 2012b), and our data support an interpretation that it lies at least 30-40 km south of Liuyuan complex (He et al., 2014a). The well-exposed portion of the Dundunshan terrane south margin, north of the Liuyuan complex, lacks a well-defined suture zone with extensive accretionary units or subduction complexes. Fragments of a subduction complex remain, such as eclogite-bearing granulites (Qu et al., 2011). Ductile faulting is limited to small sets of normal faults, later reversed, as seen in fault porphyroblasts (Fig. 2.4 B) and reversed imbricated boudins (Figs. 2.4 C and 2.4 D). This sequence of deformation has only been constrained by extension of the Pingtoushan Formation that occurred later than its Neoproterozoic deposition (673.2 ± 5.6 Ma; 08NC04A, Fig. 2.12 C), and compression earlier than a Triassic crosscutting dyke (232.3 ± 2.1 Ma; 08NC01A, Fig. 2.12 D). There is no obvious deformation zone, large-scale strike-slip fault, or specific suture zone that is comparable in scale to the Hongliuhe shear zone and the deformation seen within the accretionary units of the Mazongshan terrane.

The Shuangbaotang Formation sediments north and south of the Liuyuan complex have previously been suggested to have separate provenances due to their differing geochemistry (Guo et al., 2012). Our statistical K-S test of the two samples indicates they likely share a provenance (Figs. 2.13 and 2.14 A) despite being separated by the Liuyuan complex. The Liuyuan complex is not likely part of a suture zone, as originally proposed (Xiao et al., 2010; Guo et al., 2012; Mao et al., 2012b). The spreading associated with the creation of the Liuyuan complex (Mao et al., 2012b) could reasonably be a late, post-accretion phenomenon that separated fragments of the Dundunshan terrane (Fig. 2.18 D), both containing its magmatic signature. This would have provided similarly aged detritus for both Shuangbaotang Formation basins. Interpreting the Dundunshan terrane–Dunhuang block suture to be further south is supported by: (1) seismic data from Gao et al. (1998) indicating a north-dipping deeply rooted reflector (subducted oceanic crust) intersecting the surface roughly 40 km south of Liuyuan (if following the regional structural trend); (2) our Middle Ordovician age of a mylonitic tonalite gneiss (08NC05, 467.9 ± 4.0 Ma), a granitoid age of 309.4 ± 1.8 Ma by Mao (2008) in the same region, and mylonitic ca. 430 Ma granitoids further south, all consistent with Dundunshan magmatic ages and geochemistry (He et al., 2014b); (3) granulites further south in the Dunhuang region with peak ages of 431 Ma and retrograde amphibolite overprinting at 403 Ma (He et al., 2014a) akin to accretionary or subduction complex rocks (the suture zone).

Late Paleozoic orogeny was facilitated by reactivation of the existing Devonian suture zones. The Hongliuhe Formation exhibits fold-and-thrust belt deformation with southward vergence synthetic to the original north-dipping subduction system (Cleven et al., 2015). Shuangbaotang Formation sediments north of the Liuyuan complex have broad, open south-verging folds (Fig. 2.2). Deformation within the Liuyuan complex is also south vergent (Mao et al., 2012b). Late Paleozoic/early Mesozoic compression forced the Hanshan/Mazongshan terranes to further override the Dundunshan terrane along the preexisting north-dipping early Paleozoic suture, and the Dundunshan terrane to override a north dipping suture to the south, and further impact the Dunhuang block. These conclusions support an interpretation that the Beishan experienced staged arc accretion and orogenesis using at least two north-dipping subduction systems that were active in the Paleozoic (Fig 2.18 B–D).

2.7 Conclusions

The Beishan can be subdivided into three early Paleozoic terranes (the Hanshan, Mazongshan and Dundunshan) with magmatic histories distinct from each other and from the Central Tianshan. The detrital geochronology age spectra of Paleozoic Beishan sedimentary rocks correlate to known regional granitoid ages and zircon Th/U ratios of each interpreted provenance: the Shuangbaotang Formation and Dundunshan Group provenance is in Dundunshan terrane rocks, while the Hongliuhe Formation provenance is in a combination of the Hanshan terrane and its accretionary complex, the Mazongshan terrane. Tuff and amphibolite (metamorphosed ash layer) ages support an interpretation that the Dundunshan terrane was magmatically active during the Neoproterozoic and the Ordovician, and the Mazongshan terrane during the Devonian. The detrital age spectra indicate a similar pattern of magmatic activity developed in both provenances, yet the pattern they exhibit is offset by 50 m.y. older in the northern Hongliuhe Formation sample set (provenance in the Hanshan/Mazongshan terranes) than in the southern Shuangbaotang Formation sample set (provenance in the Dundunshan terrane). Early Paleozoic arc magmatism ramped up in the Cambrian and Ordovician, respectively, and abruptly ceased in the Early and Late Devonian, respectively. After a 40-50 m.y. hiatus in each, small amounts of magmatism began in the Carboniferous in both provenances and continued through the Permian in the former and Triassic in the latter. We attribute the similar but offset pattern in the magmatic activity to protracted, staged collision between all three terranes and an undetermined backstop, likely the Dunhuang block. The Hanshan and Mazongshan terranes shared one north-dipping migrating-arc subduction zone for which the initiation of magmatism correlates to known ages of Cambrian ophiolite generation. As a subduction system, it accreted oceanic units into the Mazongshan terrane as late as the Early Devonian, correlating to both emplacement constraints on Cambrian ophiolites and the initiation of a second generation of ophiolites. During the Carboniferous extensional deformation localized in both suture zones, separating a fragment of the Dundunshan southern suture/margin through production of the Liuyuan basin. The final Permo-Triassic contraction, often cited as terminal collision, caused the Hanshan/Mazongshan terranes to further override the Dundunshan terrane, and the Dundunshan terrane to further impact the Dunhuang block, emplacing the Liuyuan complex and deforming both the Shuangbaotang and Hongliuhe Formations.

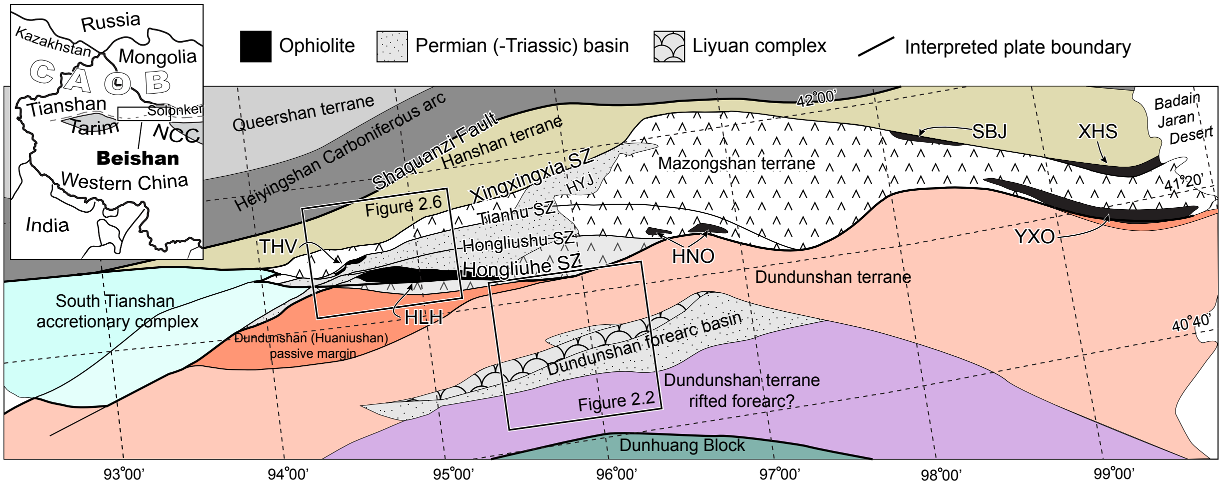

Figure 2.1: Tectonostratigraphic map showing major terranes, structural breaks and faults, ophiolites, and late siliciclastic basins. Colors and fill patterns denote extents of labeled terranes. Areas of figures 2.2 and 2.6 are shown. CAOB: Central Asian Orogenic Belt. NCC: North China Craton. HYJ: Hongyanjing basin. HLH: Hongliuhe ophiolite. THV: Tianhu volcanic successions. HNO: Huoshishan-Niujuanzi ophiolite. YXO: Yueyashan-Xichangjing ophiolite. SBJ: Shibanjing ophiolite. XHO: Xiaohuangshan ophiolite. SZ: shear zone

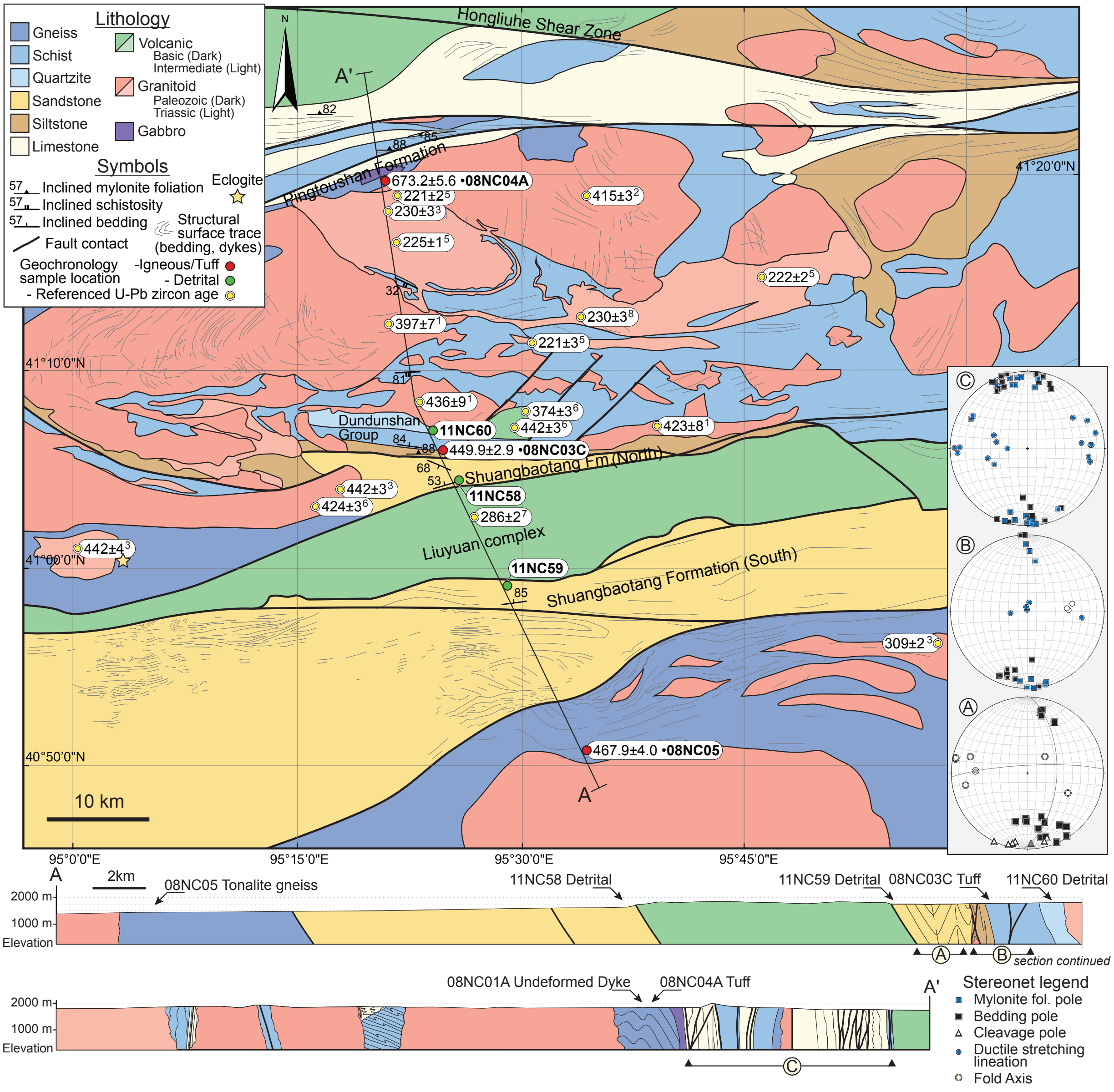

Figure 2.2: Geologic map of the Dundunshan arc in the Liuyuan region, with a cross section and three equal-area lower-hemisphere projections of structural data. Areas covered by the projections are indicated on the section. U-Pb zircon age references: [1]Zhao et al. (2007); [2]Li et al. (2009a); [3]Mao (2008); [4]Qu et al. (2011); [5]Li et al. (2012); [6]Mao et al. (2012a); [7]Mao et al. (2012b); [8]Zhu et al. (2012).

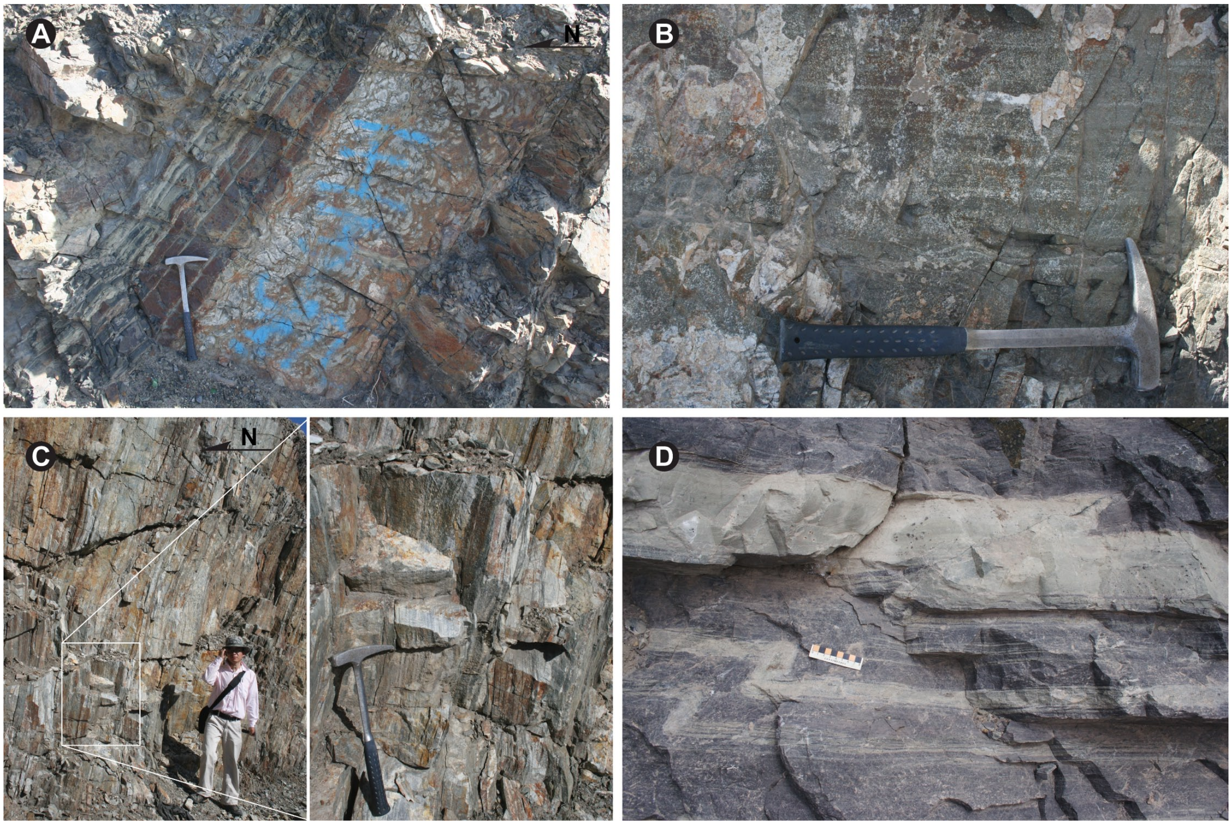

Figure 2.3: Field photos of the sedimentary rocks and geochronology sample sites in the Dundunshan terrane. A) Shuangbaotang Formation sandstone exhibiting convolute bedding (partially covered by blue graffitti) (sample 11NC58). B) Crystal-lithic layers in Dundunshan Group graywacke (sample 08NC03C). C) Dundunshan Group quartzite (sample 11NC60). D) Pingtoushan quartz-biotite chloritoid schist with quartz-amphibole layers (light gray) interpreted to have originally been ash layers (sample 08NC04A). Centimeter scale-card for scale.

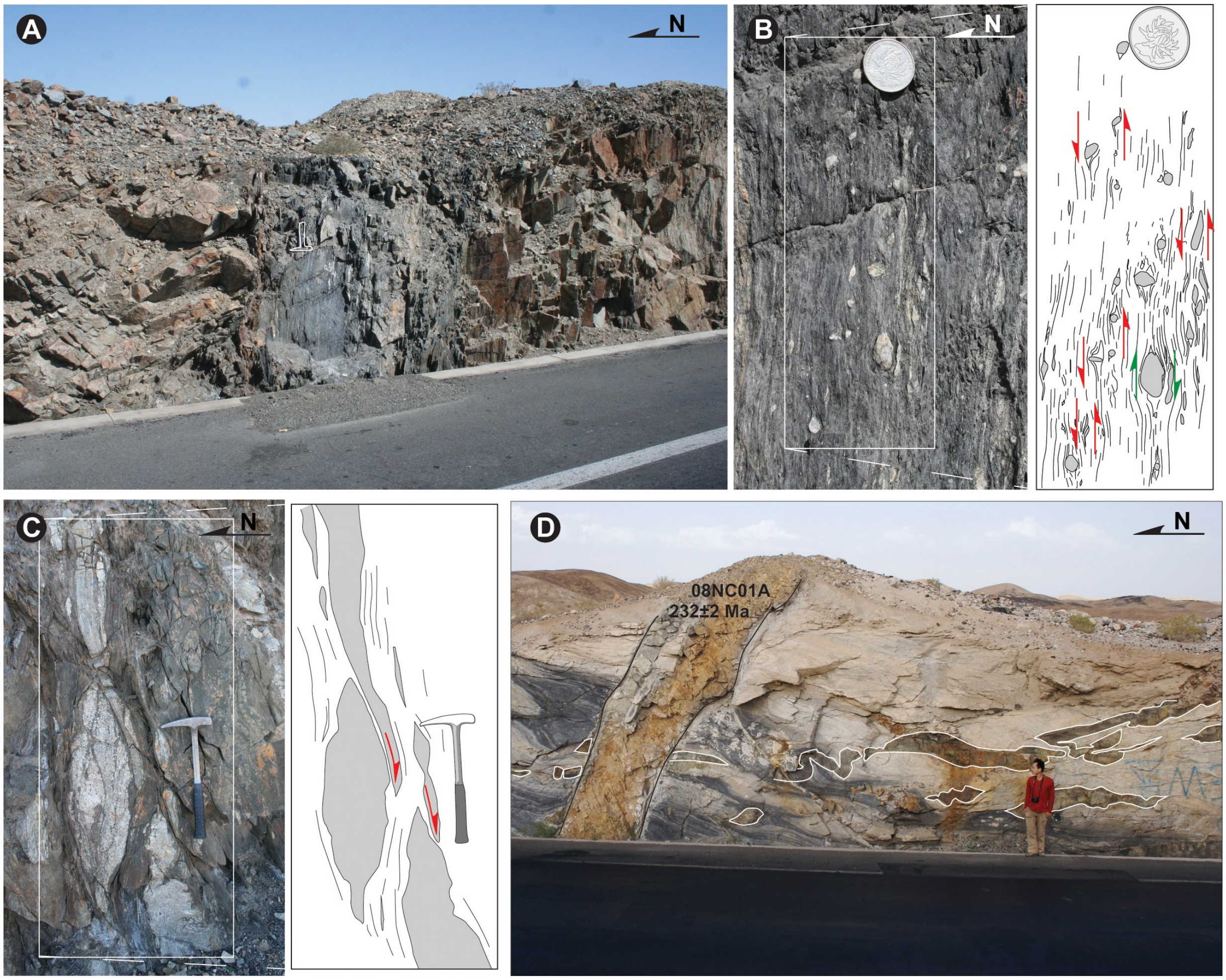

Figure 2.4: Field photos of structure in the Dundunshan terrane. A) One of a set of distributed shear zones marking the boundary between the Devonian Dundunshan Group metasediments and the Permo-Triassic Shuangbaotang Formation. B) Close-up of mylonitic foliation in A), with schematic diagram of asymmetric mantling of porphyroclastic material. Opposing shear senses are present, and the view is reasonably close to the kinematic plane. C) Shear zone deformation within the Dundunshan terrane depicting boudins that have been imbricated back over neighboring in-line boudins, in a post-extension compression event. They appear similar to duplex structures. D) Two phases of dykes cutting Pingtoushan Formation marbles. The older mafic (dark brown) dykes were boudinaged and subsequently folded and imbricated onto itself. The younger felsic dyke (light brown) is undeformed and was sampled for geochronology (sample 08NC01A).

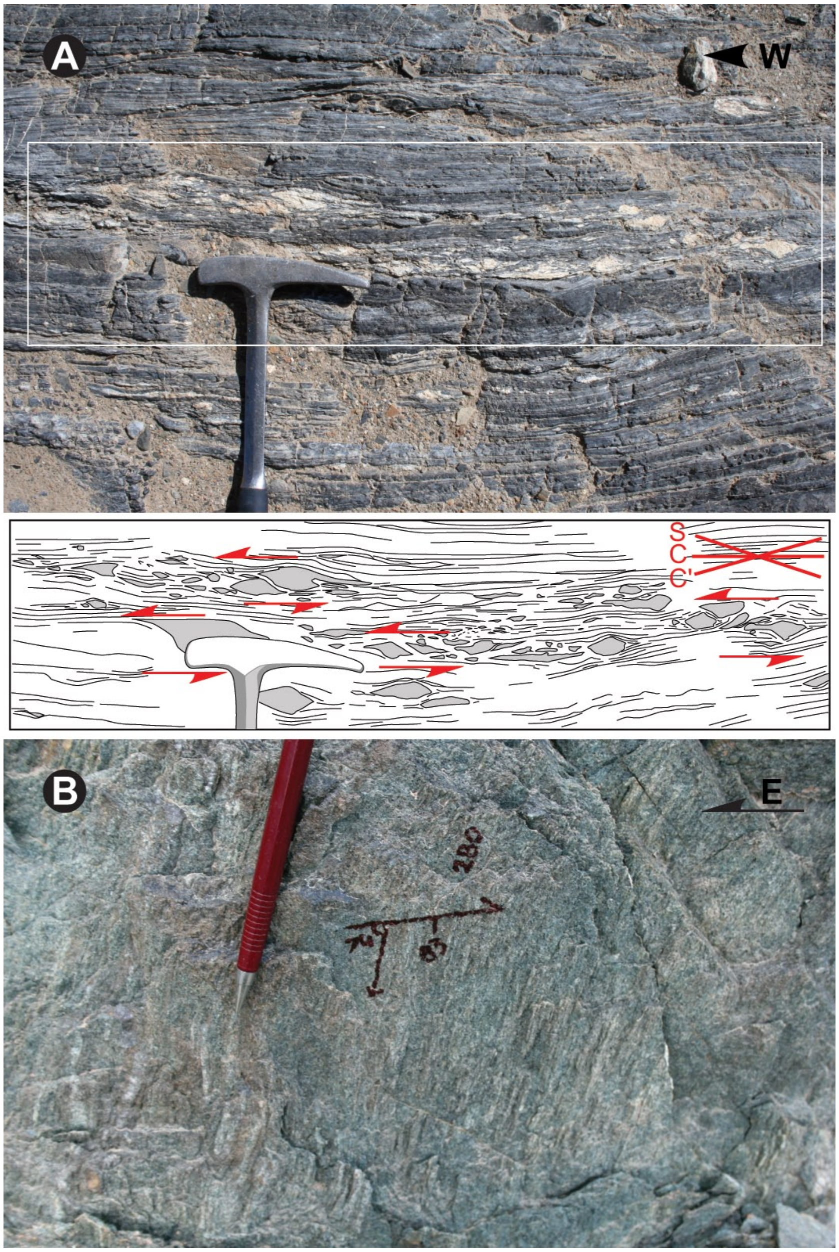

Figure 2.5: Field photos of fault structures in the Hongliuhe shear zone. A) Photo and sketch of C-C' fabric and asymmetric boudins of sandy layers in limestone. B) Steeply plunging ductile striations on a mylonitic foliation plane in a basalt.

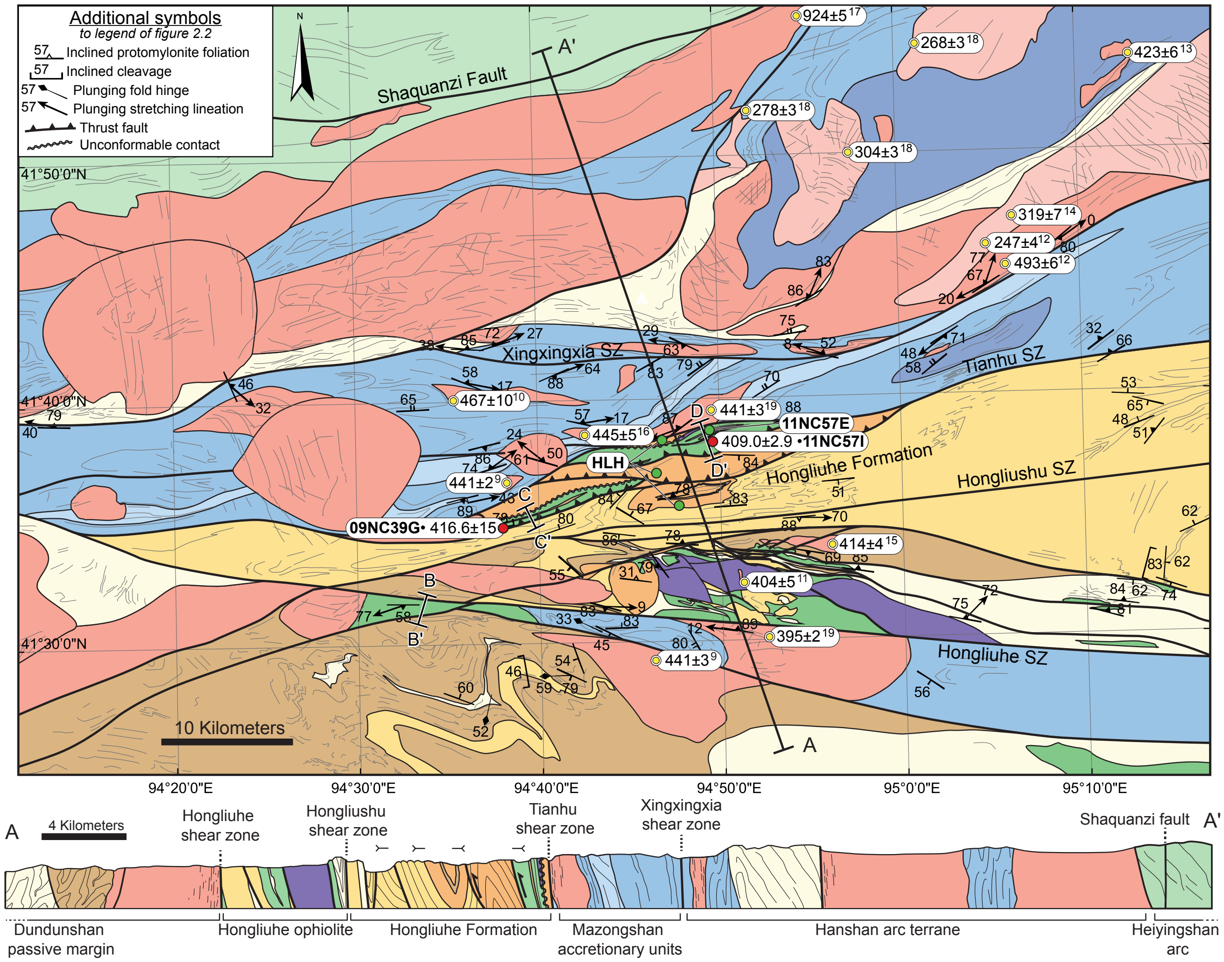

Figure 2.6: Geologic map of the Hanshan and Mazongshan terranes in the Hongliuhe region, with a cross section. Lines B-B', C-C', and D-D' are locations of cross sections shown in Fig. 2.7. SZ: shear zone. U-Pb zircon age references: [9]Li et al. (2001); [10]Hu et al. (2007); [11]Zhang and Guo (2008); [12]Wang et al. (2010); [13]Lei et al. (2011); [14]He et al. (2012); [15]Chapter 3; [16]Lei et al. (2014); [17]Wang et al. (2014b); [18]Zhou (2014); [19]Chapter 4.

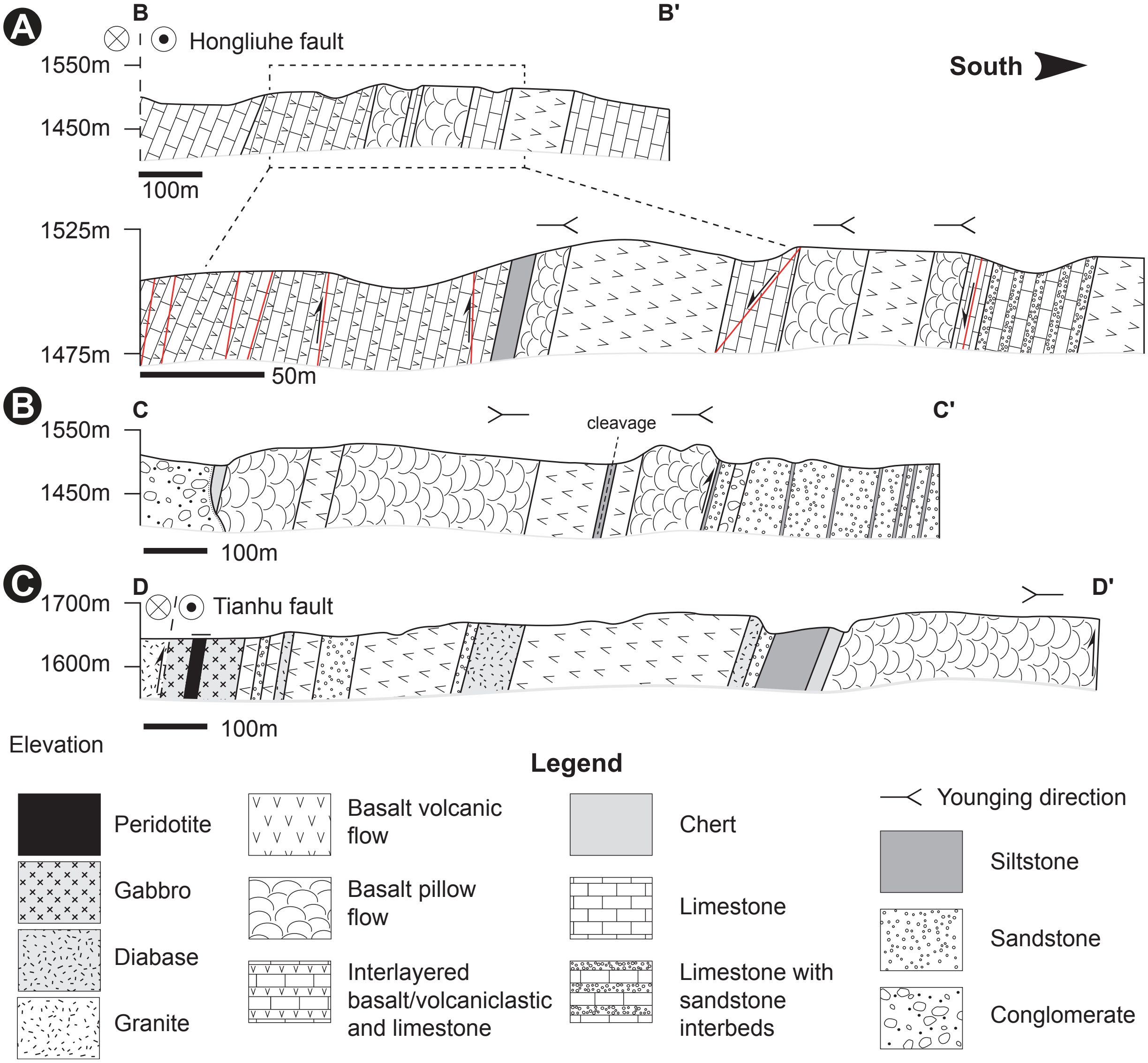

Figure 2.7: Cross-sections of Devonian volcano-sedimentary successions in the Mazongshan terrane. A) Southwest volcanic block along Hongliuhe shear zone. B) Northwest volcanic section near Tianhu. C) Northeast volcanic and sedimentary section near Tianhu. Locations of the sections are shown in Fig. 2.6.

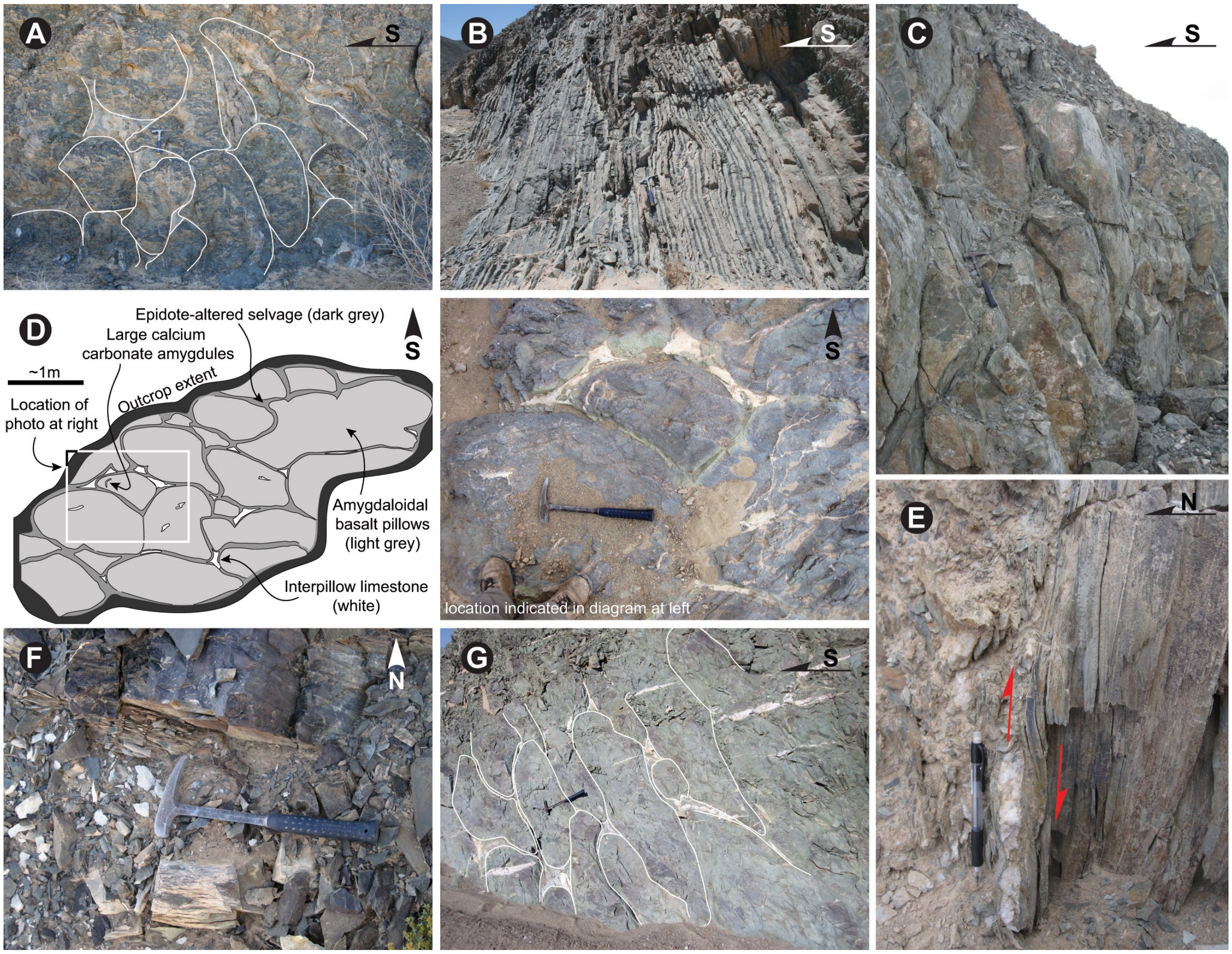

Figure 2.8: Field photos of Devonian pillow basalts and associated sedimentary rocks in the Hongliuhe to Tianhu region. A) Northward younging pillow structures in basalts of the southwest volcanic succession. B) Interbedded limestone and thin basalt/volcaniclastic layers, in the southwest volcanic section. C) Northward younging pillow basalts with cleavage overprint in the northwest volcanic section. D) Schematic diagram with inset photo at right showing pillow basalts younging southward in the northwest volcanic section. E) C-S fabric in sediments underlying the northwest volcanic section indicating a north-over-south sense of motion. F) Crystal-lithic tuff horizon (buff colored fragments by hammer) in chert outcrop in the northeast volcanic section. G) Southward younging overturned pillow basalt in the northeast volcanic section.

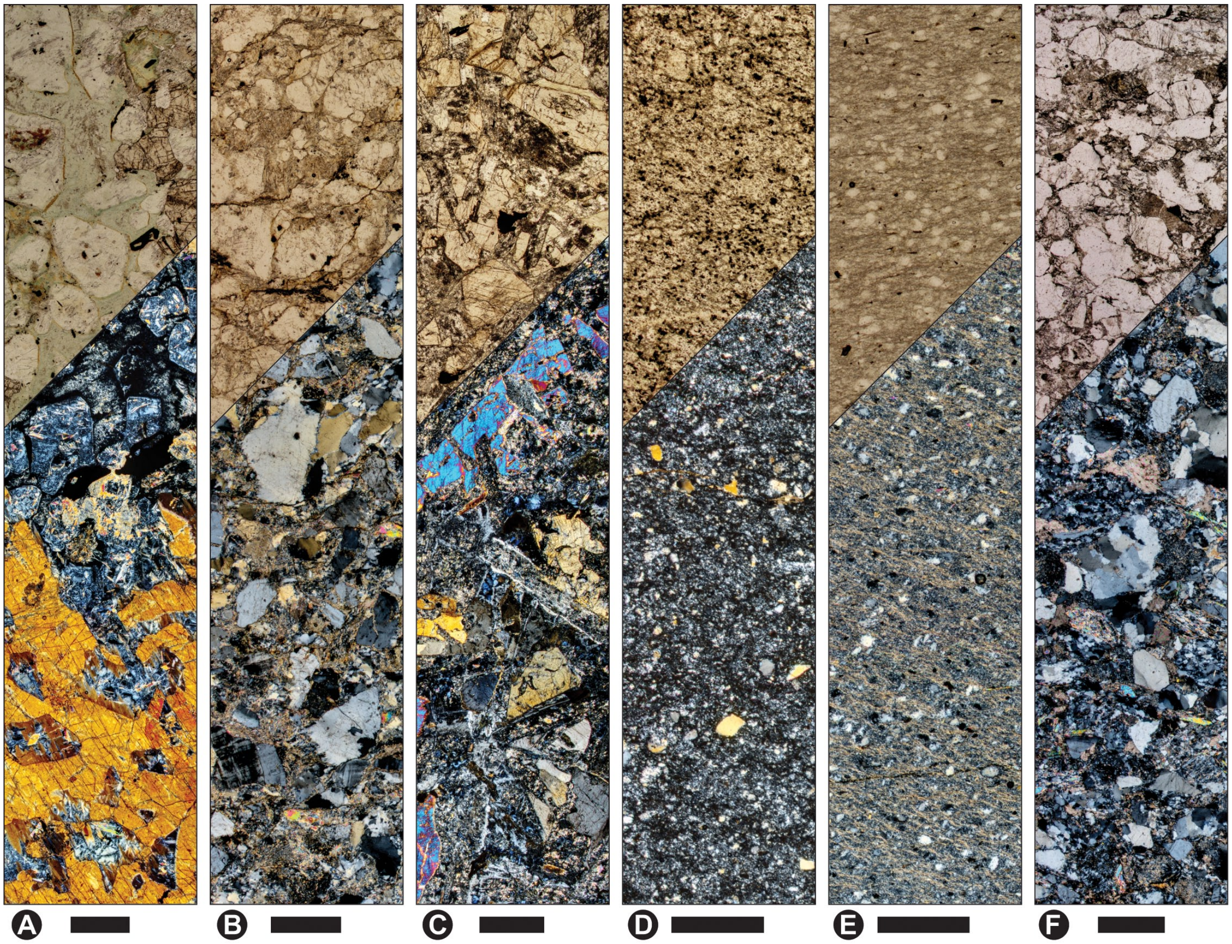

Figure 2.9: Petrography of volcanic and sedimentary samples from the Mazongshan terrane. Photomicrographs in plane polarized light (top) and cross-polarized light (bottom), with 500 µm scale bars at bottom. A) Serpentinized and chloritized olivine cumulate peridotite with poikilitc texture of amphibole encasing sericitized plagioclase or amphibole-altered pyroxene, and chlorite (relict pyroxene?) encasing olivine. B) Coarse sandstone detrital geochronology sample (sample 11NC57E) from within the volcanic succession with lithic fragments of K-feldspar, plagioclase, cryptocrystalline quartz, and volcanic fragments. C) Diabase with poikilitic texture of amphibole encasing plagioclase. D) Fine grained sedimentary rock horizon with lithic magnetite and fragmental quartz, interpreted to be a crystal-lithic tuff (sample 11NC57I). E) Muscovite, detrital magnetite and fragmental quartz bearing chert, pictured in figure 2.8 F. F) Representative sandstone of the Hongliuhe Formation depicting lithic fragments of epidotized volcanic material, cryptocrystalline quartz, plagioclase, K-feldspar and detrital spinel/magnetite.

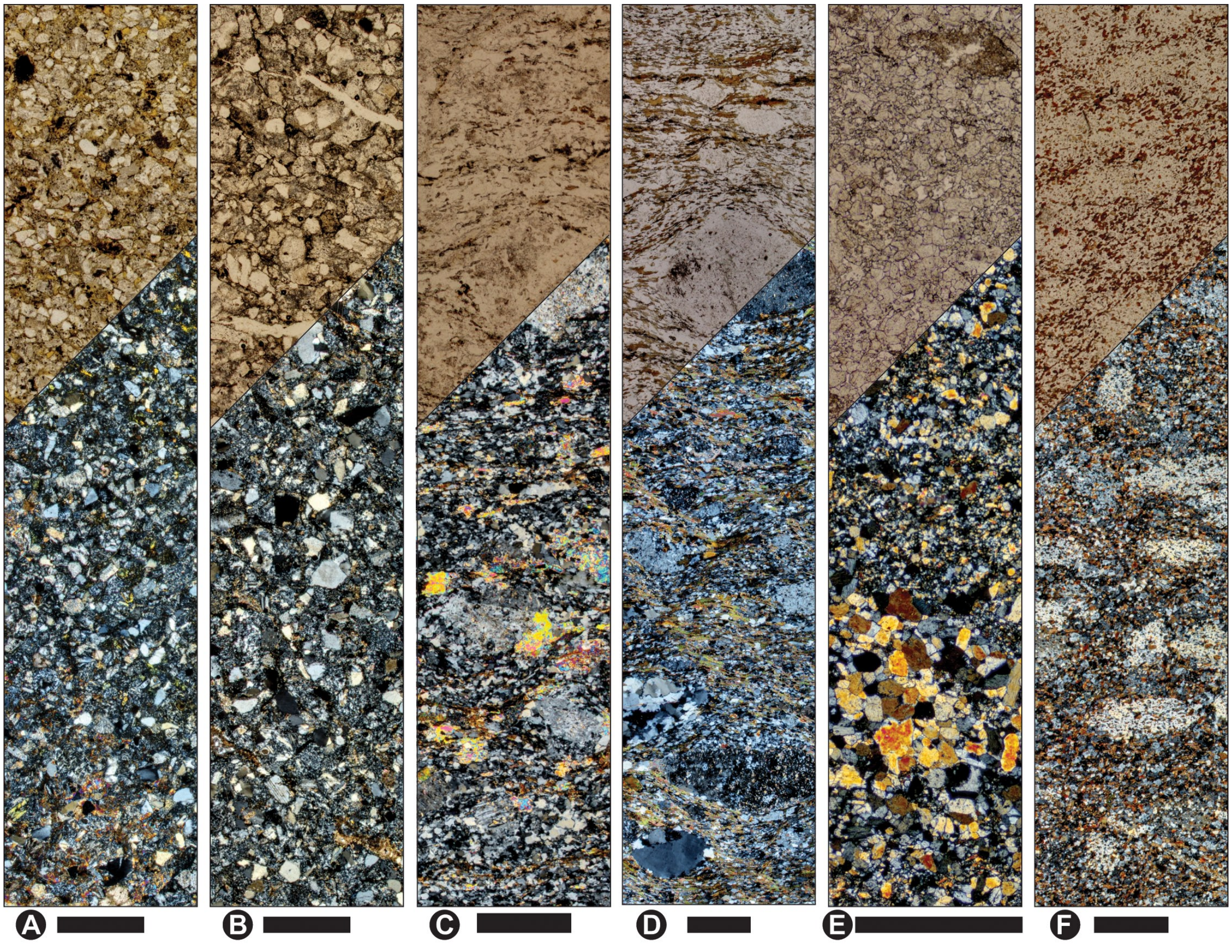

Figure 2.10: Petrography of geochronology samples from the Dundunshan terrane. Photomicrographs in plane polarized light (top) and cross-polarized light (bottom), with 500 µm scale bars at bottom. A) Shuangbaotang Formation sandstone from south of Liuyuan complex (detrital zircon sample 11NC59). B) Shuangbaotang Formation sandstone from north of Liuyuan complex with outcrop pictured in figure 2.3 A (detrital zircon sample 11NC58). C) Plagioclase porphyroclasts in a graywacke with crystal-lithic tuffaceous horizons (sample 08NC03C) from the Dundunshan Group, with outcrop pictured in figure 2.3 B. D) Coarse meta-sandstone from the Dundunshan Group (detrital sample 11NC60) with porphyroclastic volcanic, cryptocrystalline quartz and plagioclase material. Outcrop pictured in figure 2.3 C. E) Amphibolite (anthophyllite bearing) metamorphic rock in association with F), from a sampled metamorphosed ash layer in the Pingtoushan Formation (sample 08NC04A), pictured in figure 2.3 D. F) Cordierite porphyroblasts in quartz biotite schist sampled from the rock hosting the metamorphosed ash layer (this figure, E) pictured in figure 2.3 D.

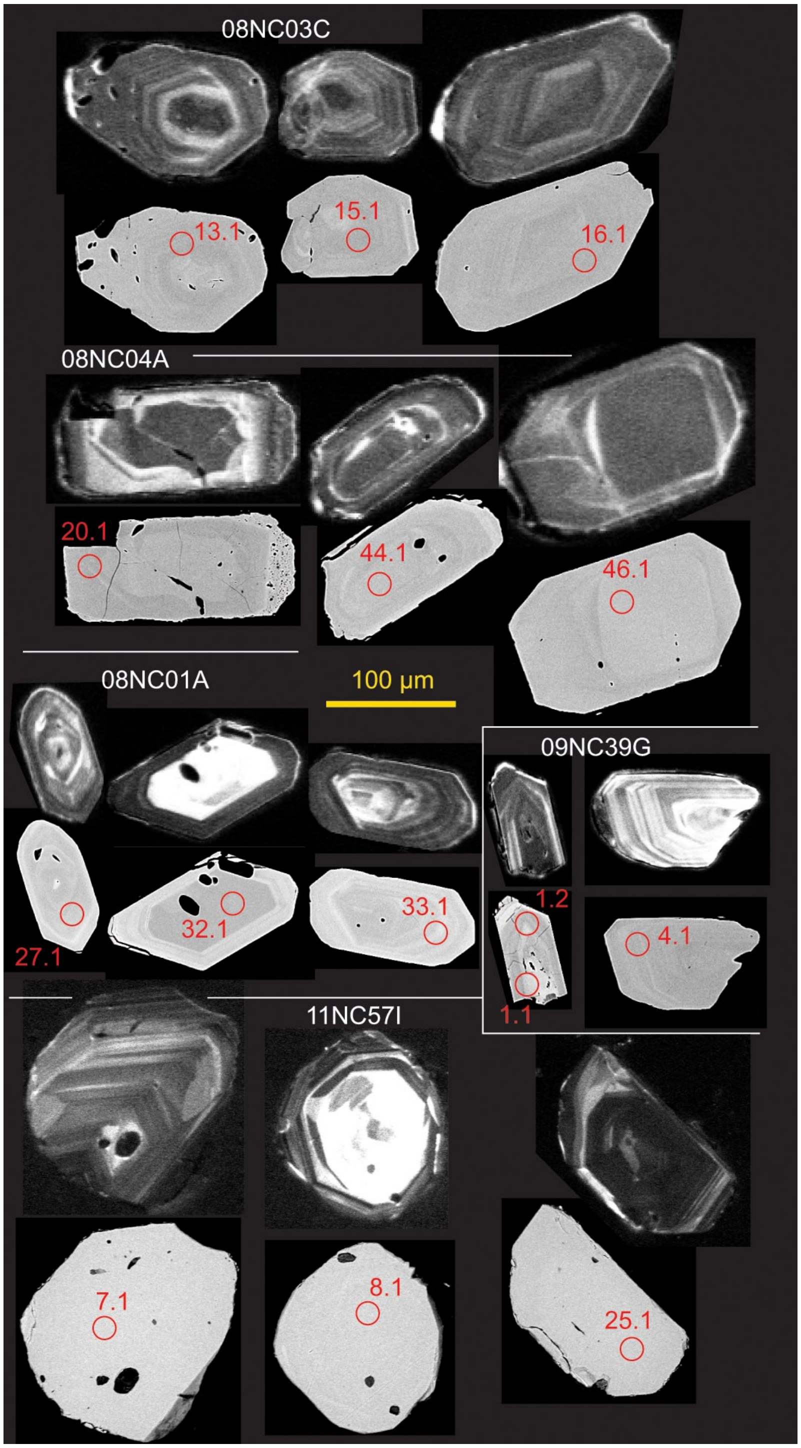

Figure 2.11: SEM and backscatter images of selected analyzed igneous zircon grains. Spot analysis locations and numbers are indicated.

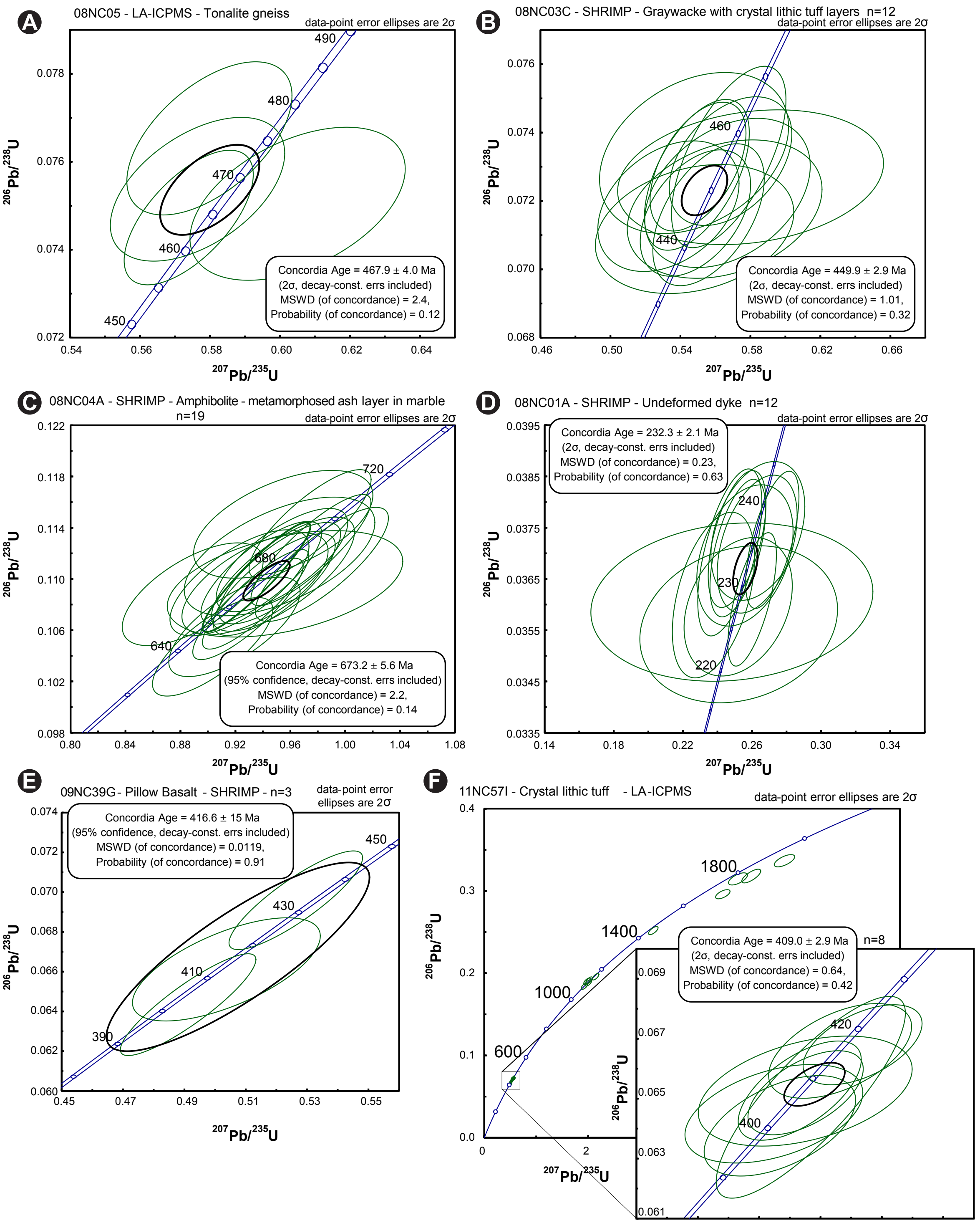

Figure 2.12: Beishan U-Pb zircon geochronology Concordia diagrams for igneous (including tuff) samples. Green ellipses represent error ellipses for individual analyses. Black ellipses represent error ellipses for the calculated Concordia age.

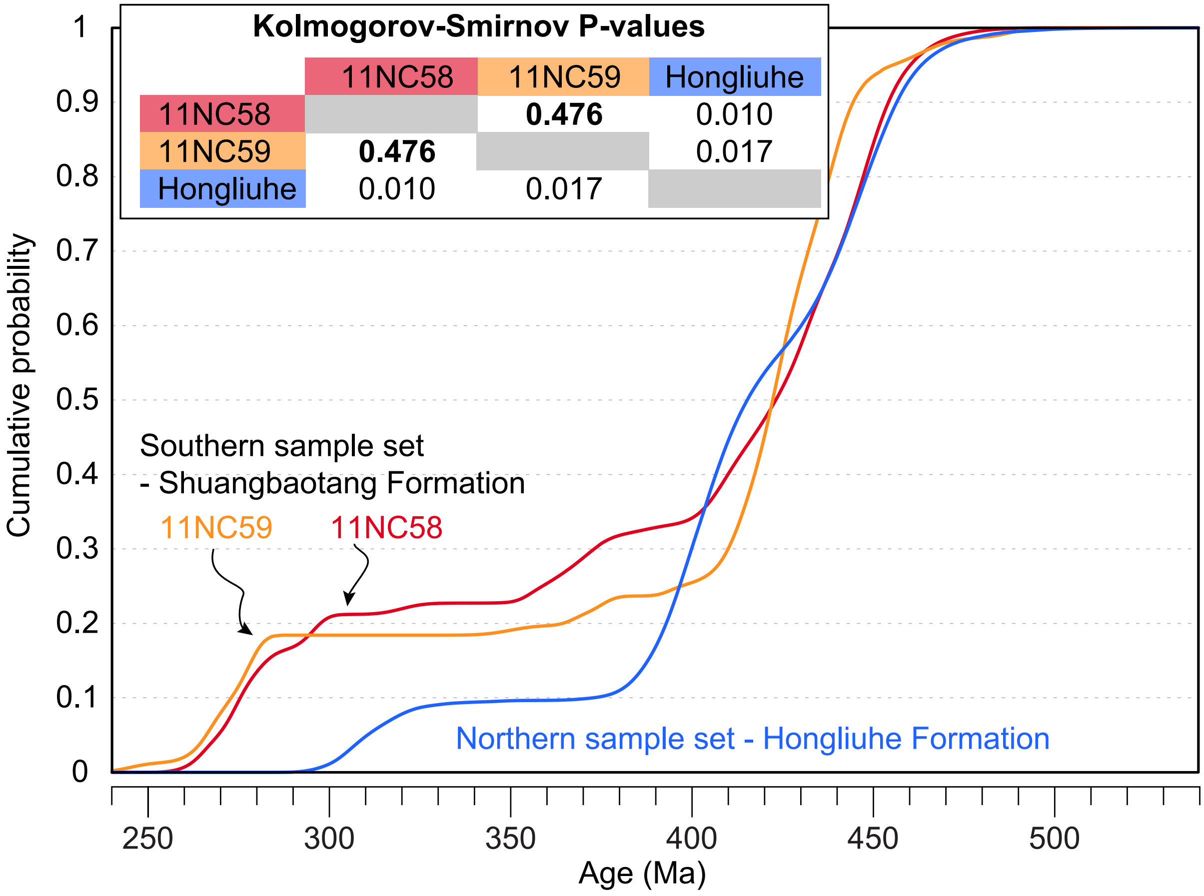

Kolmogorov-Smirnov P-values

	11NC58	11NC59	Hongliuhe
11NC58		**0.476**	0.010
11NC59	**0.476**		0.017
Hongliuhe	0.010	0.017	

Figure 2.13: Cumulative probability plot (Gehrels, 2011) of late Paleozoic/early Mesozoic units. Inset gives the results of a Kolmogorov-Smirnov (K-S) test (Sircombe and Hazelton, 2004). The probabilities (P-values) compare each permutation of pairs amongst the three samples. Bold results indicate that they are above the threshold of 0.05 and the sample pair has a statistically identical provenance.

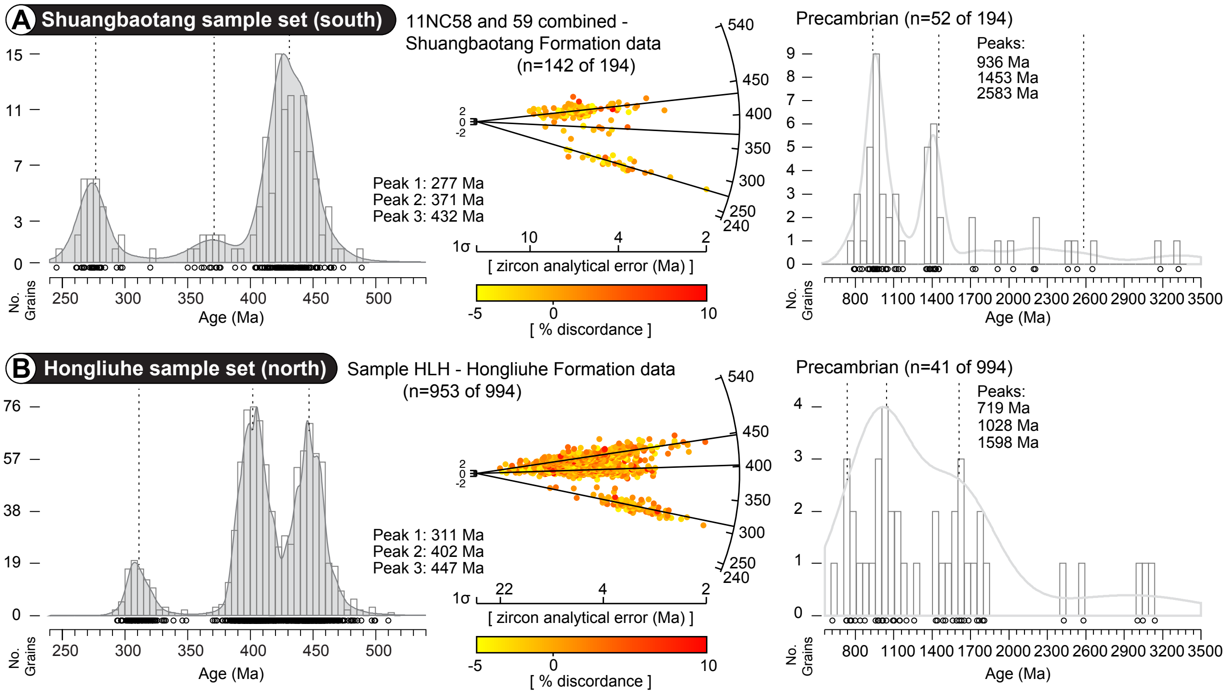

Figure 2.14: Beishan U-Pb zircon detrital geochronology histograms with overlain kernel density estimate (KDE) curves (Sircombe and Hazelton, 2004; Vermeesch, 2012) of late Paleozoic/early Mesozoic units. Included are radial plots (Galbraith, 1990) of analytical error values and separate histograms/KDE plots of Precambrian analyses.

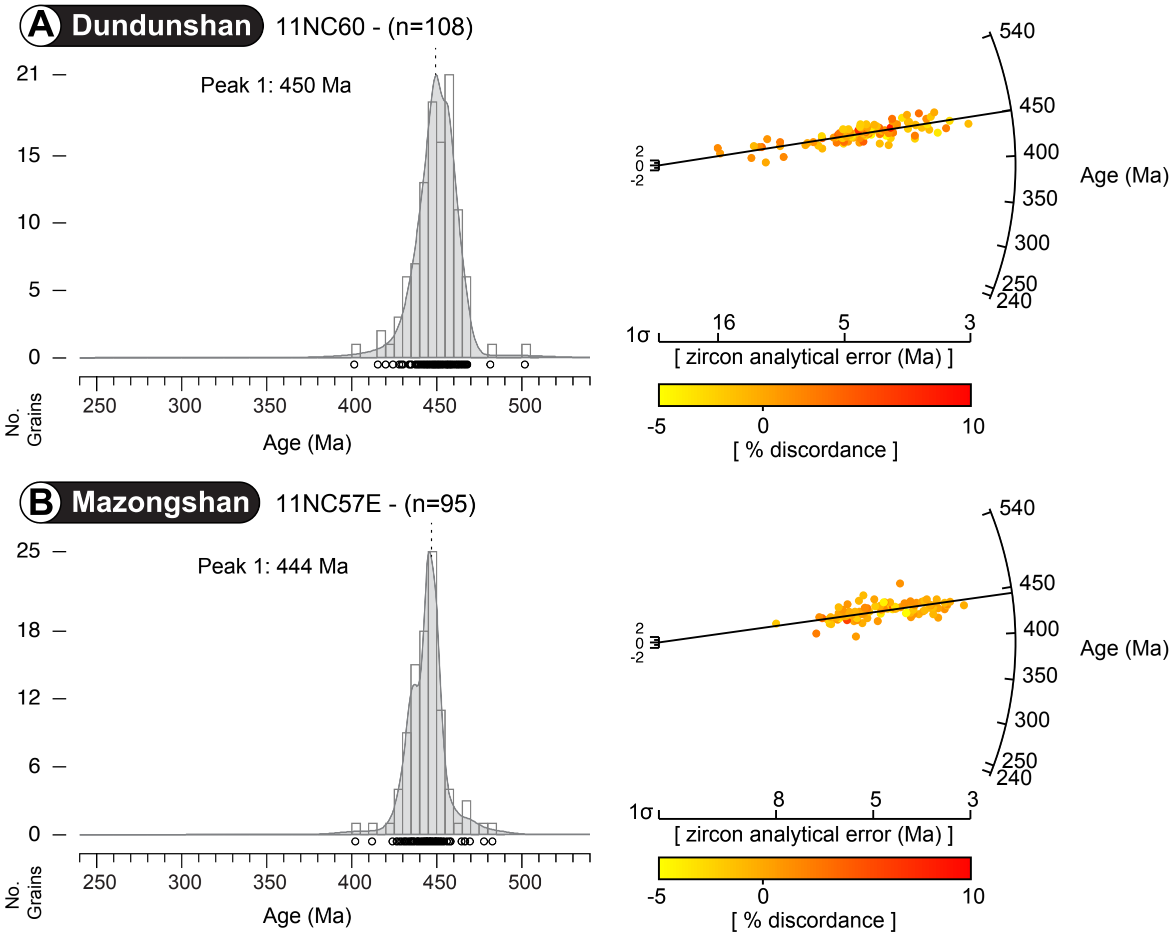

Figure 2.15: Beishan U-Pb zircon detrital geochronology histograms with overlain kernel density estimate (KDE) curves (Sircombe and Hazelton, 2004; Vermeesch, 2012) of early Paleozoic units. Included are radial plots (Galbraith, 1990) of analytical error values.

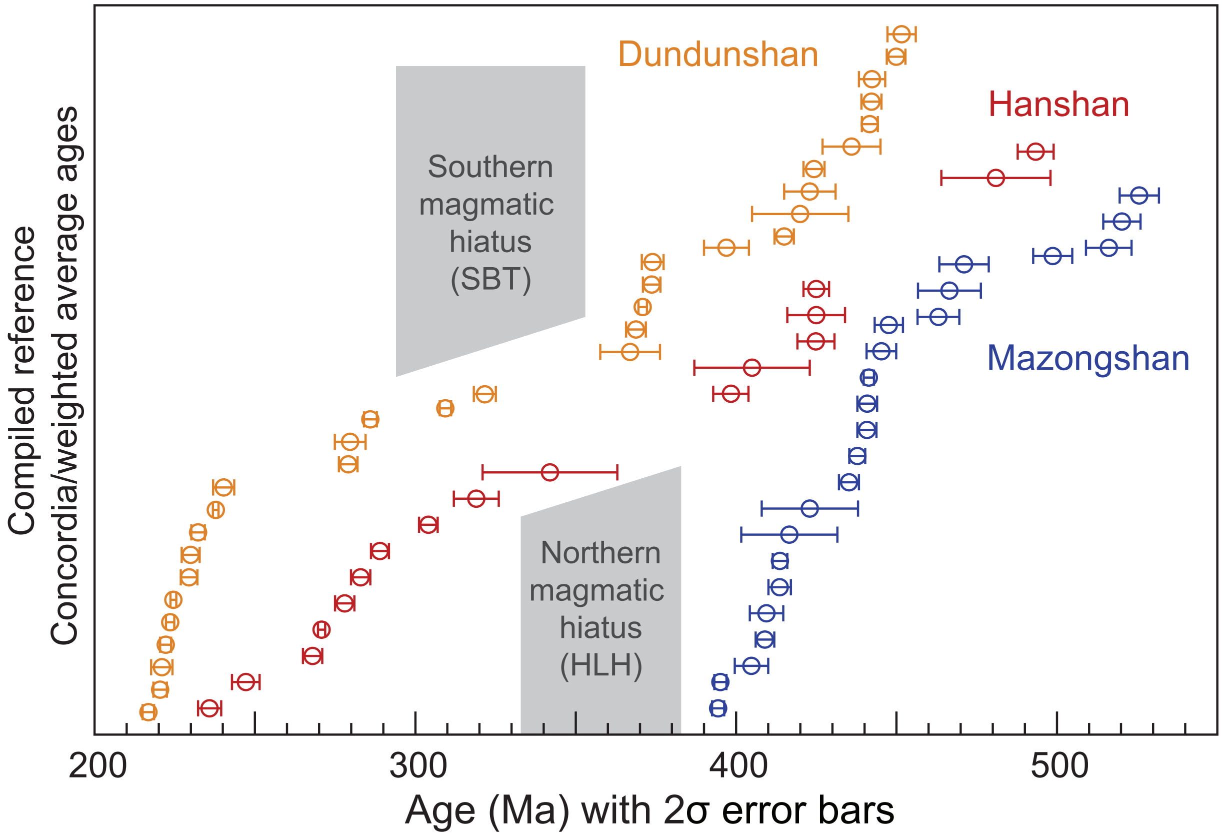

Figure 2.16: Compilation of available Concordia and weighted average ages of igneous rocks from Beishan literature. Magmatic hiatus shown in the detrital samples from the Shuangbaotang sample set (SBT) in the south and the Hongliuhe sample set (HLH) in the north are shown for comparison. Error bars are 2σ values. Ages are grouped by terrane, as indicated. Data compiled from: Hanshan: Li et al. (2009a); Hu et al. (2010); Wang et al. (2010); Lei et al. (2011); He et al. (2012); Zhou (2014); Mazongshan Hu et al. (2007); Song et al. (2013a,b); Lei et al. (2014); Song et al. (2014); Chapter 4; Dundunshan: Li et al. (2001); Zhao et al. (2007); Li et al. (2009b, 2011); Mao (2008); Su et al. (2011); Li et al. (2012); Mao et al. (2012a,b); Zhu et al. (2012); Guo et al. (2014). Central Tianshan: Shi et al. (2014)

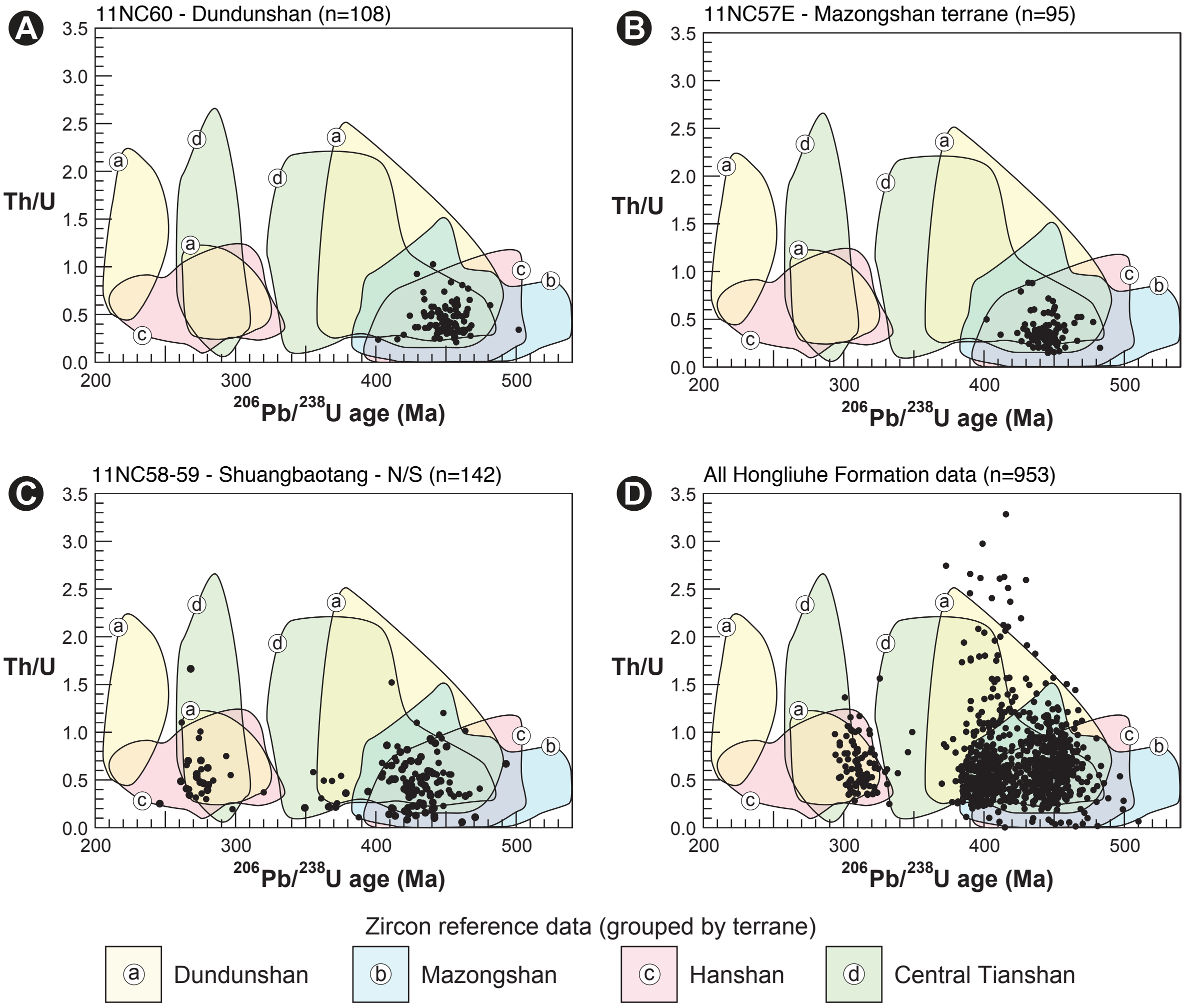

Figure 2.17: Plots of Th/U ratios of detrital samples compared to reference data, by terrane. Sources of data are the same as for Fig. 2.16, with additional data from Shi et al. (2014) for the Central Tianshan.

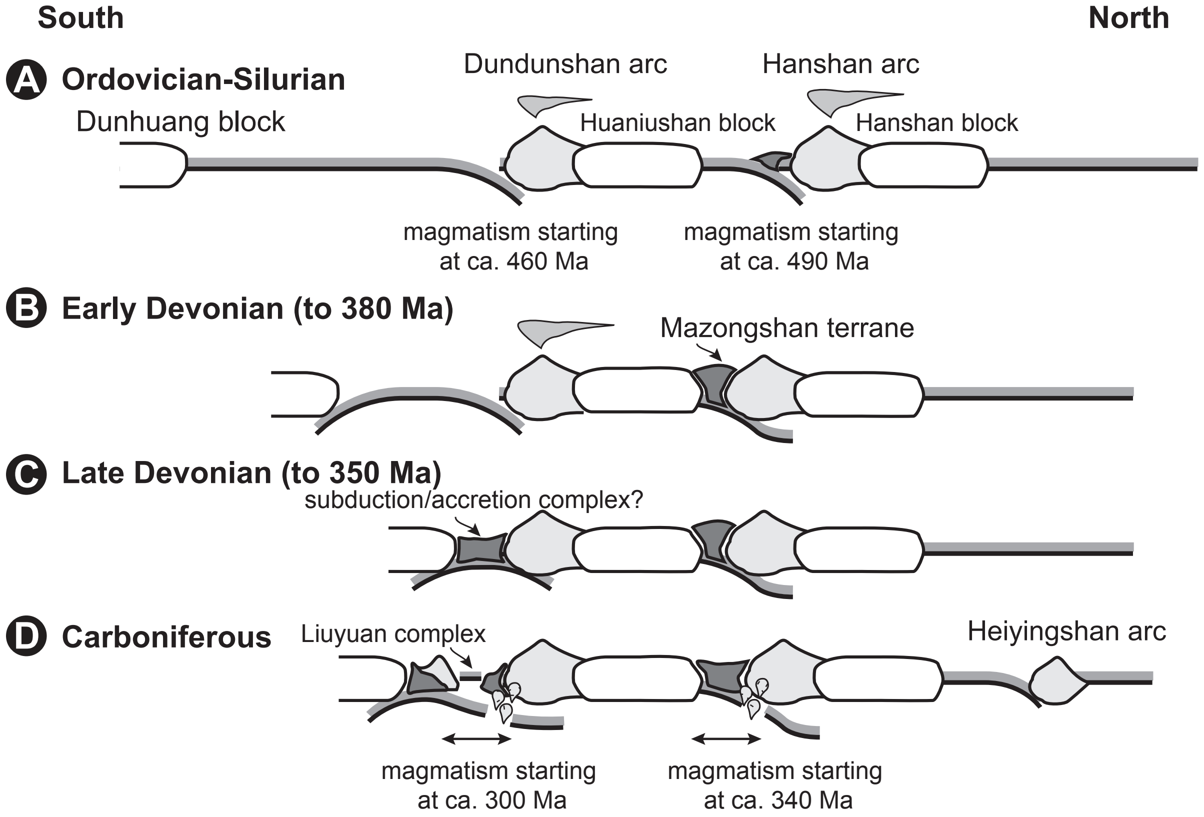

Figure 2.18: Cartoon showing the Beishan's tectonic staging and assembly.

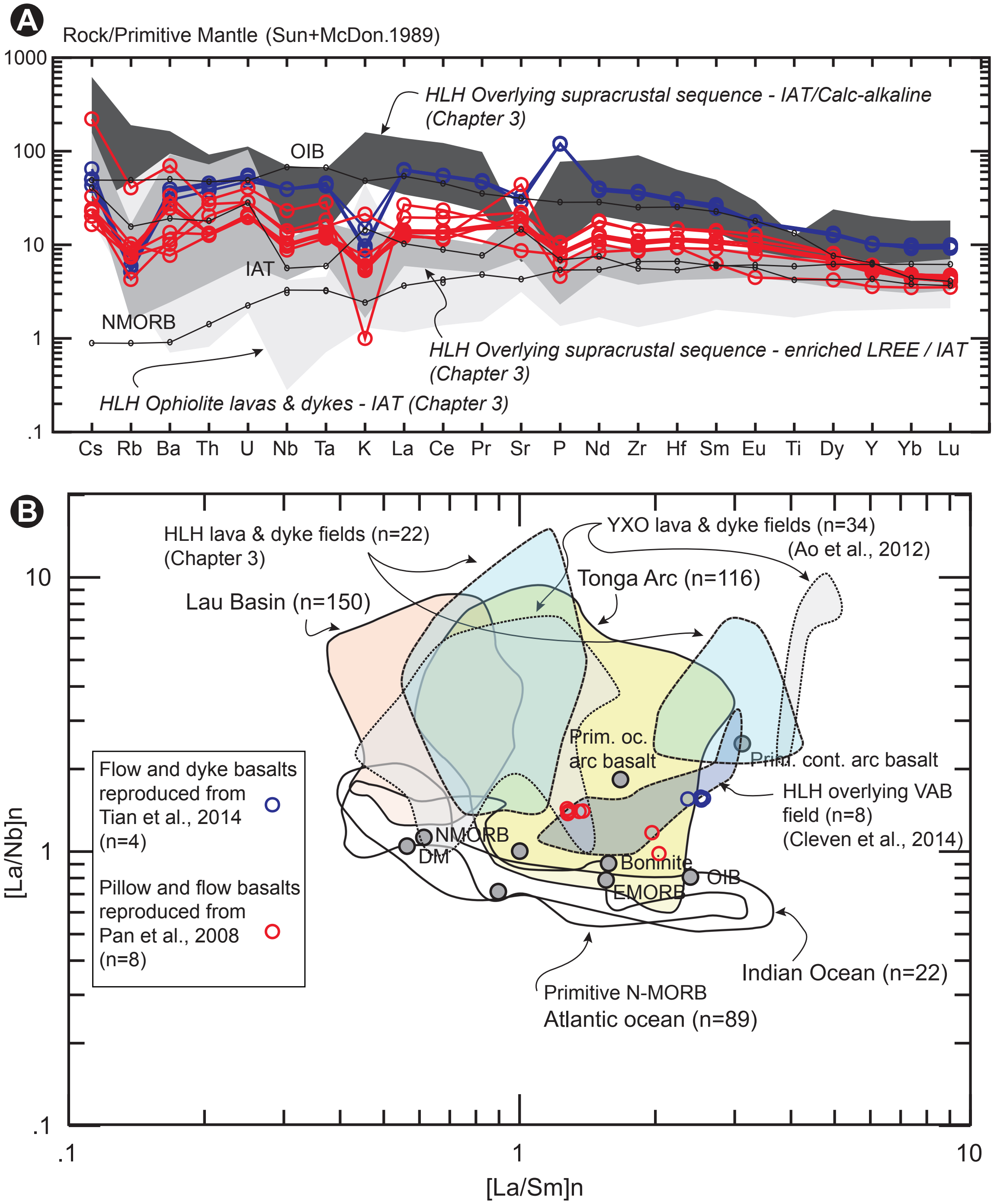

Figure 2.19: Geochemical discrimination diagrams for the southwest Tianhu volcanic succession and Huoshishan-Niujuanzi ophiolites compiled from Pan et al. (2008) and Tian et al. (2014), respectively. A) Spider diagram normalized to the primitive mantle values of Sun and McDonough (1989). B) Geochemical discrimination plot of La/Nb versus La/Sm normalized to the primitive mantle values of Sun and McDonough (1989). Modified from Guilmette et al. (2009), with references therein.

Chapter 3

Petrogenesis and implications for tectonic setting of Cambrian suprasubduction ophiolitic rocks in the central Beishan orogenic collage, Northwest China

3.1 Introduction

The Beishan orogenic collage contains multiple series of ophiolite fragments imbricated into potentially disparate and laterally dismembered accretionary complexes. They offer a prime opportunity to establish both the characteristics of Paleozoic seafloor and subduction-related processes as well as along-strike correlations within suture zones (Fig. 3.1). Research focused on the geochemistry of the Beishan ophiolites has inferred most to be supra-subduction zone (SSZ) in their nature (Wang et al., 2011; Mao et al., 2012b; Zheng et al., 2013; Tian et al., 2014), and the interpretations that follow have furthered the argument for multiple, contemporaneous subduction, obduction and accretion events that may have had varying subduction polarity.

One can see the Beishan as a proxy, in miniature, for the evolution of the broader Central Asian Orogenic Belt (CAOB), of which it is a subset. The magmatic record of the Beishan holds information of Early Cambrian, Silurian-Devonian and Carboniferous seafloor spreading, with diachronous Paleozoic arc- and collision-related magmatism. Complications arise considering that all have been transpressionally packaged between island arc accretionary complexes (Qu et al., 2011; Xiao et al., 2010; Song et al., 2013a) and cratonic margins to the north and south during the Silurian (He et al., 2014a) through Permian (Mao et al., 2012b; Cunningham, 2013; Tian et al., 2013). Analogues have been found for the Beishan, and the CAOB as a whole, within the Lachlan orogen in Australia (Spaggiari et al., 2004; Schulmann and Paterson, 2011) or with modern (pre-collision) scenarios such as the southwestern Pacific archipelago with its collection of variously sized island arcs and complex arrays of subduction zones (Hsü et al., 1994; Hsü, 2003; Safonova et al., 2011; Xiao et al., 2010).

There are common characteristics shared between the Hongliuhe ophiolite (indicated in Fig. 3.1), the subject of this study, and other ophiolite fragments 420 km to the east, the contemporaneous Yueyashan-Xichangjing ophiolites (Ao et al., 2012). They have petrologic similarities in cumulate ultramafic and mafic plutonic rocks, similar trace element patterns in dual-signature volcanic suites, and have volcaniclastic cover. Looking worldwide, many useful corollaries can be drawn from other volcanic arc/forearc/backarc (VA-FA-BA) suprasubduction zone ophiolites, and their supracrustal cover succesions. Extensive compilations of data with type-example interpretations exist for ophiolites around the globe (Dilek and Furnes, 2009, 2011; Hébert et al., 2012), but specific examples of ophiolites similar to the Hongliuhe ophiolite include (but are not limited to): the Betts Cove ophiolite (Bédard, 1999; Cousineau and Bédard, 2000) and the Thetford Mines ophiolite complex

(Schroetter et al., 2003; Pagé et al., 2008, 2009) in Canada, and the Kizildag ophiolite in Turkey (Dilek and Thy, 2009). Among them they exhibit similar island-arc patterns of volcanic geochemistry, extension-related structures with staged igneous activity, and overlying margin-related sediment successions. The similarities indicate that a specific tectonic process created a tendency to preserve its resulting oceanic lithostratigraphy, and they are therefore important for study. Subduction rollback processes are inferred to initiate extension and attenuation of pre-existing oceanic crust in VA-FA-BA ophiolites, and create distinct complexes of multi-stage magmatism through suprasubduction refertilization of depleted mantle. To illustrate this in the Beishan we utilize whole-rock geochemistry, mineral chemistry, petrographic and structural analyses of the Hongliuhe ophiolite lithostratigraphy. Volcaniclastic facies analysis and nearshore supracrustal coverings correlate to interpreted marginal seafloor arc-generation processes; our constraints on the tectonic setting provide further context for the earlier Paleozoic tectonostratigraphy of the Beishan.

3.2 Geologic setting

The Beishan orogen lies in the southern region of the CAOB (Fig. 3.1 inset). Orogeny in the CAOB generally youngs southward, with peaks of magmatism initiated as early as the Neoproterozoic, then spanning the Ordovician, Silurian–Devonian and Late Carboniferous–Early Permian (Şengör et al., 1993; Windley et al., 2002; Laurent-Charvet et al., 2003; Buckman and Aitchison, 2004; Xiao et al., 2004a,b; Wang et al., 2006; Xiao et al., 2008, 2009b). The Beishan models in miniature these sialic crust-building episodes in its much smaller system of three central composite arc terranes (Fig. 3.1) (Xiao et al., 2010). Their internal tectonic architectures resemble fragments of arcs, thinned and tectonically eroded. The main structural boundaries generally trend east-west, as gently arcuate strike-slip fault arrays.

The Mazongshan terrane, central to the Beishan, includes magmatic rocks aged Ordovician-Silurian. It is lenticular-shaped and interpreted to be the forearc accretionary complex of the Hanshan terrane, and to contain juvenile plutonic suites from migrating arc magmatsim (Xiao et al., 2010; Song et al., 2013b, 2014). In the north and west it comprises units of the Beishan complex, also called the Gongpoquan schists, collections of paragneisses and foliated granitoids of middle Paleozoic subduction complex or arc-related affinity (Song et al., 2013b). Lower-grade arc-marginal sedimentary units and arc-related volcanic units occupy the east. Metamorphic rocks are under-studied in the Beishan, but some purport that the surrounding Hanshan and Dundunshan terranes have Precambrian rifted slivers that acted as nuclei for Paleozoic subduction (Xiao et al., 2010; Song et al., 2013a). The Silurian-Devonian Hanshan arc terrane (north of the Mazongshan, Fig. 3.1) consists of mostly calc-alkaline plutons and high-grade metamorphic rocks of poorly understood origin, with the Carboniferous Heiyingshan arc intruded through its northern margin. The Carboniferous age of the Xiaohuangshan ophiolite (Zheng et al., 2013) provides the only constraint for its timing of (final) suturing to the Dundunshan terrane. The Dundunshan arc terrane modified its Precambrian core with magmatic activity spanning the Ordovician to Permian in a southerly migrating arc (Qu et al., 2011; Mao et al., 2012a; Guo et al., 2014). A large swath of sedimentary rocks that resemble a cohesive block of passive margin sediments line sections of the northern margin of the Dundunshan (indicated on Fig. 3.1). They are a succession of Cambrian through Silurian nearshore platformal sedimentary rocks, polydeformed during its protracted history. This study confirms an existing geochronological constraint that the Hanshan and Mazongshan terranes had been sutured to the Dundunshan, roughly by the Silurian-Devonian boundary (Ao et al., 2012). The only other absolute age relating to collision in this time period is an interpretation of collisional orogenic processes in the Dunhuang block (He et al., 2014a).

3.3 Tectonic setting

The three ophiolite belts in the Beishan contain early Cambrian, Silurian-Devonian and Carboniferous seafloor spreading records (Fig. 3.1), each preceding arc-building. Each belt comprises at least one block or tectonic slice of ophiolitic material, commonly grouped with other tectonic slices of units from an oceanic domain, all connected along a structural lineament; the oceanic units are not consistent or continuous along strike. The Hongliuhe ophiolite has conflicting age interpretations of Silurian and Cambrian (Zhang and Guo, 2008; Xiao et al., 2010), with no contemporary geochemical understanding. It outcrops near a small town of its namesake, and spatially is close to the convergence of the Xingxingxia and Hongliuhe shear zones (each indicated on Fig. 3.1). Both are dominantly strike-slip faults with unknown displacement and >100 km strike lengths. They demarcate the north and south boundaries, respectively, of the Mazongshan terrane (Fig. 3.1). The Xingxingxia shear zone is considered to have been active in at least one segment until the Triassic (Wang et al., 2010). The Hongliuhe suture, the focus of this study, is defined here as the quasi-linear belt that contains the Hongliuhe, Huoshishan-Niujuanzi (HNO) and Yueyashan-Xichangjing (YXO) ophiolites, each with a set of tectonically concomitant units sourced from possibly exotic oceanic domains. They have been mapped as intermittent lenses, collections of fault-bounded kilometer to deca-kilometer scale slices and blocks of early to middle Paleozoic marginal and oceanic units. Some portions occur as either block-in-matrix accretionary complexes or as tectonic imbricate slices.

In the Hongliuhe area the narrow region between the Xingxingxia and Hongliuhe shear zones contains isoclinally folded quartzites, garnetiferous metapelites, and marbles in the north. These may belong to the Beishan complex. Their immediate relationship to the Hongliuhe ophiolite package is obscured by the structurally overlying Permo-Triassic Hongyangjing basin fold-and-thrust belt (Zhang and Cunningham, 2012; Cleven et al., 2015; Tian et al., 2013). The Hongliuhe oceanic domainal units comprises the ophiolite, internally folded blocks of metasedimentary rocks, offscraped slices of pillow basalts with arc or SSZ geochemical affinity (Pan et al., 2008; Ch. 2) and interlayered volcaniclastic and nearshore oceanic sediments. They lie in fault contact with each other, centered about the Hongliuhe shear zone. Locally south of the Hongliuhe shear zone lies the expanse of Cambrian–Silurian polydeformed passive margin.

The two easterly sets of ophiolite fragments in the Hongliuhe suture, the HNO and YXO, lie 200 km and 420 km to the east, respectively. Their lithological sequences are very similar, with cumulate ultramafic and gabbroic rocks and overlying pillow basalts, chert and pyroclastic/volcaniclastic material (Ao et al., 2012; Tian et al., 2014). The YXO also exhibits a dual-signature volcanic suite, all yielding a definitive island-arc or SSZ geochemical signature. Their interpreted tectonic emplacement histories differ, the HNO being a block-in-matrix accretionary ophiolite, and the YXO a coherent sequence set in a larger scale tectonic imbrication. The YXO is reported as the elder, with a Cambrian seafloor genesis and a minimum Silurian emplacement timing constraint (Ao et al., 2012), whereas the HNO has Silurian genesis and Carboniferous emplacement (Tian et al., 2014).

3.4 Field observations

3.4.1 Lithostratigraphy of the ophiolite and associated rocks

The Hongliuhe ophiolite has a preserved approximate thickness of 4-7 km in most sections. It is a 30-40 km long set of coherent blocks of oceanic lithostratigraphy that lie tilted near vertical (Fig. 3.2), though the small westernmost block may be partially rotated with respect to the rest. The ophiolite package, including up to a 10 km thickness of cover strata, is fault-bounded to the north and south, pinching out to the east and west forming a large sigmoidally shaped tectonic slice. Faulting has juxtaposed it against the much younger Permian Hongliuhe Formation to the north, and against a tectonic slice of Ordovician metasedimentary rocks to the south.

The peridotites of the mantle section (unit 1 in Fig. 3.2 inset schematic diagram) have common cumulate textures and igneous layering. Dunites exist in rarity, with more common pyroxenites. Both lherzolites and harzburgites make up the bulk, and interlayer with cumulate leucogabbro (Fig. 3.3 A). The ultramafic lithologies exist throughout, even proximal to volcanic lithologies. The body also hosts numerous intrusions of finer basic to intermediate dykes, sills, and lavas. Gabbroic rocks are common throughout the ophiolite sequence, typically plagioclase-bearing mesocratic/leucocratic gabbro, with occasional hornblende megacrystic gabbro and plagioclase cumulate layering (Fig. 3.3 B). Amphibole-bearing gabbros are most common, and quartz-bearing gabbros are rare. Olivine- or pyroxene-bearing gabbros are also rare. Amphibolites, or hornblendites exist in intermittent zones that offer no indication of any regularity or spatial relationships. Diabase outcrops were mapped yet there is no obvious pattern or significant abundance to consider the Hongliuhe ophiolite as having a sheeted-dyke complex. Final stages of plutonic emplacement most likely represent the limited plagiogranites, capping the system within the volcanic carapace.

Eruptive volcanic rocks are not voluminous as primary cover of the ophiolite. They are most concentrated as a subconformable set of units on the north side of the ultramafic and plutonic sequence (unit 2 in Fig. 3.2 inset schematic diagram). They comprise extrusive volcanic and volcaniclastic rocks deposited in an oceanic environment. The volcanic packages are of variable thickness (0-800 m), mostly basic to intermediate lavas. They also host sporadic gabbro and thin diabase and basaltic intrusions (less than 0.6 m wide). Volcanic flow deposits infilled paleo-topography, in some cases directly on exposed utlramafic cumulates. Lenses and horizons of abyssal oceanic sedimentary rocks such as red (hematite bearing) chert and limestone are interspersed within the uppermost layers of volcanics (Fig. 3.3 D). They are draped by and include interlayers of volcaniclastic deposits with incorporated pyroclastic material and terrestrially-sourced sandy material. Coarse autoclastic basaltic conglomerates with moderate rounding of clasts (Fig. 3.3 C) imply proximity to growing vents or active fault scarps. Plagiogranite material also exists as boulder-sized conglomeratic clast material, proximal to outcrops of in situ plagiogranite. Normally graded basal traction deposits (graded at the 5-10 cm scale) of volcaniclastic turbidites overlie sandy material and contain fragmental and rounded red chert, black chert, plagiogranite, and basaltic clasts (Fig. 3.3 E).

The ophiolitic volcanic-related rocks are succeeded by limestone, white banded chert, and black chert (up to ten meters), overlapping in different locations in the west, and mixed-source volcaniclastic sandstones and limestone (with occasional chert lenses) in the east. Sandstone units are up to 200 m thick, commonly deposited directly on volcanic units, and contain interlayers of volcaniclastic conglomerates (Fig. 3.2).

Upsection, the Hongliuhe ophiolite has nearshore oceanic sediments comprising an overlying package of supracrustal rocks (unit 4a in Fig. 3.2 inset schematic diagram). They comprise sandstones and limestones that are variably mixed with volcaniclastic and pyroclastic input (Fig. 3.3 F). Basalts are interlayered with the sediments (Fig. 3.3 G). None of these lithologies indicate a higher degree of metamorphism than low greenschist facies. South of the ophiolite body are fault-bounded sections of supracrustal rocks that contain volcanic successions (unit 4b in Fig. 3.2 schematic diagram), yet their relationships and thicknesses are largely interpretive in Fig. 3.2, due to the poor amount and quality of outcrop in the southerly region. They are interpreted to be sections of the overlying supracrustal sequence, including limestone, volcaniclastic sandstone, siltstone and basalts, which are tectonically strike-slip imbricated to now lie structurally beneath the ophiolite.

Younger granitoid bodies have intruded through the suture. In the ophiolite rare plutonic bodies incorporate xenoliths of basic rocks, and appear less deformed and altered than the basic rocks hosting them. The few bodies vary in composition from granitic to tonalitic. There is also a large pluton 15 km in length and 2-4 km in thickness that has intruded the overlying sediments (unit 5 in Fig. 3.2 inset schematic diagram). It shows no ductile deformation, metamorphism or alteration, and cross-cuts the tilted strata of the sedimentary country rock, post-dating most deformation. This pluton, within the overlying sediments, was sampled for U-Pb zircon geochronology to establish a minimum age constraint for the formation and emplacement of the ophiolite, including the deposition of the overlying supracrustal sequence, and their collective deformation.

3.4.2 Structure in the ophiolite

There is a disparity between deformation styles within the plutonic sequence and within the overlying supracrustal cover due to the staged development and modification of the ophiolite. Generally, most structures are subvertically dipping and trend west to northwest (Fig. 3.2 inset stereonet). This provides an approximate cross-sectional view of the ophiolite and cover strata lithostratigraphy in the geologic map (Fig. 3.2). Ductile shearing within the mantle section involves high temperature grain-scale ductility, more suited to an oceanic crustal setting, yet deformation in the volcanic and sedimentary rocks above is dominantly folding and brittle faulting. As described above, fragments of the overlying supracrustal package have been strike-slip imbricated to now structurally underlie the ophiolite (Fig. 3.2).

The ductile shear zone between the western and central blocks of the ophiolite trends NNW, an orientation inconsistent and antithetical to all other major shear zones in the region (Fig. 3.2). It is expressed as a strong steeply west-dipping mylonitic foliation in gabbroic rocks (Fig. 3.4 A), comprising a zone approximately 200 m wide. A mineral alignment and stretching lineation (Fig. 3.4 B) consistently plunges subvertically to steeply towards the northwest (Fig. 3.4 D). Sigmoidal porphyroclastic structures and C-C' fabrics show a sinistral sense of motion in the mylonitic rocks (Fig. 3.4 C). There is a parallel overprint of a narrow, brittle fault zone with local serpentinization of ultramafic wall rock. Ductile strain is localized in many other zones in the plutonic section, but is not pervasive. It is observed largely in gabbroic rocks, pyroxenites and some peridotites.

The northwestern tip of the ophiolite is a fault-bound zone of intense folding, disaggregation and imbrication of units manifested as localized block-in-matrix texture (unit 3 in Fig. 3.2 inset schematic diagram). All lithological units within it are fragments of units that exist within the ophiolite or the material directly overlying. A complicated set of faults, folds and penetrative deformation have produced the complex structural pattern, and have juxtaposed units normally not in contact. There are lens-shaped meter- to decameter-scale fragmented blocks of ultramafic units mixed with limestones, sandstones, and volcanic units, all separated from each other by zones of foliated serpentinite group minerals, mafic chlorite-talc schists and remobilized calcium carbonate.

The supracrustal covering dips subvertically with a slight southward vergence to faulting and folding, consistent with the overall structure of the ophiolite. Faulting has disrupted the continuity of some portions of the volcanics in the north and the overlying supracrustal sequence, especially in the west of the map area. Folding is associated with shear zones that punctuate the upsection stratigraphy. Anastamosing, relatively bedding-parallel ductile shear zones are localized in both limestone and sandstone lithologies, especially within their interfaces with basalt flows. Shearing kinematics are dominantly sinistral, with a late dextral brittle-ductile kinking overprint.

3.5 Petrography

3.5.1 Primary plutonic textures

Cumulate textures dominate the primary ultramafic lithologies in the Hongliuhe ophiolite. Dunites and pyroxenites are sporadic. Poikilitic textures are common in both lherzolites and harzburgites (Fig. 3.5 A). Spinel is observed as disseminated euhedral to subhedral grains and vermicular textured clusters of grains. Gabbroic rocks have common cumulate textures as well (Fig. 3.3 B), mostly nesophitic (Fig. 3.5 B), largely due to the scarcity of pyroxene in the gabbros; amphibole is the most common mafic mineral. Amphibole appears to be the final crystallization phase in most gabbroic rocks, and can be oikocrysts containing chadacrysts of euhedral plagioclase (Fig. 3.5 C). Primary amphiboles are green and strongly pleochroic in thin section. The plagiogranites are largely plagioclase and contain rare amphiboles. Grain-scale fracturing and cataclastic textures are common in them. The full crystallization sequence in the Hongliuhe ophiolite is summarized:

$$Spinel \Rightarrow olivine \Rightarrow \frac{orthopyroxene/clinopyroxene}{plagioclase} \Rightarrow plagioclase \Rightarrow amphibole$$

3.5.2 Metasomatism and ductility in the plutonic sequence

The mitigating effects of metasomatic alteration on the competency of ultramafic and plutonic lithologies is evident within the ophiolite body, a factor in their concession to ductile strain localization. Serpentinite minerals are the most common alteration product; there is a small active mining operation centered in the ophiolite that processes magnetite out of the serpentinite for iron ore. In partially serpentinized ultramafic cumulate rocks serpentine commonly forms a matrix or forms complete pseudomorphs of olivine and pyroxene (Fig. 3.5 E). It also commonly fills protoclastic transgranular fractures in olivine as retiporo-alteromorphs (Fig. 3.5 G). Serpentine forms veins throughout the ultramafic body, commonly with dustings of disseminated magnetite. Pyroxene grains are regularly weathered along cleavages and commonly show the effects of hydration as amphibole septo-altermorphs (Fig. 3.5 F). Secondary amphibole is colorless in thin section. Further degradation of pyroxene grains is common, reducing them to dark masses of barely recognizable brown to black glomero-alteromorphs (Fig. 3.5 H). Chloritization of mafic phases is also common, to a low degree. In plagioclase-bearing rocks, sericite and/or gibbsite, and leucoxene commonly make near complete glomero-alteromorphs of plagioclase. Irregular calcium carbonate replacement and infiltration is also common throughout the plutonic sequence, especially within the block-in-matrix deformation zone.

Alteration and recrystallization textures are more common than primary igneous textures. Many peridotites and gabbros show a significant reduction in grain size with developed dynamic recrystallization; porphyroclastic material remains to varying degrees. Subgrain rotation recrystallization of pyroxene and amphibole indicates a range of high temperatures associated with deformation. Metasomatic breakdown of pyroxene to amphibole may have been enabled through dynamic recrystallization processes in presence of water. Fine-grained, amphibole mylonites (Figs. 3.5 G and 3.5 H) are common along the southern fault contact of the main gabbroic and ultramafic body where it has been structurally juxtaposed against slivers of the supracrustal cover that are now to the south, as well as along the southern fault contact of the block-in-matrix deformation zone. Cataclastic textures occur locally within some lithologies, even in competent pyroxenites.

3.5.3 Volcanic and volcaniclastic microtextures

Many textures exist at the thin section scale that imply subaqueous eruption of volcanics in the Hongliuhe ophiolite. Hand samples of radially jointed vesicular basalt were found in desert regolith, yet pillow structures were never identified. Vesicularity ranges widely, but in some volcanic rock samples close to the paleo-seafloor it can be as high as 15-20% (Fig. 3.6 A). Calcite, silica, zeolite and epidote commonly form the amygdules that fill vesicles. Vitriclastic textures exist with associated devitrification and irregular vesiculation textures (Fig. 3.6 A). The volcanic rocks are less commonly aphanitic and more typically pyroxene or amphibole-phyric, and many are coarse enough to resemble a diabase or microgabbro. Plagioclase commonly forms euhedral laths and amphibole phases fill interstices. The amphiboles are commonly partially chloritized. Pyroxenes in volcanic flow rocks are less common, and show textures that imply they would have formed first in the crystallization sequence (Fig. 3.6 B). Some volcanic samples exhibit foliations that may be related to primary magmatic processes, but they do not show the same degree of high-temperature secondary ductile grain-scale deformation that is found in the plutonic sequence.

Microscopic textures in the volcaniclastic rocks indicate proximal phreatic or phreatomagmatic processes. Volcaniclastic turbidite basal traction deposits are heterolithic with fragmental to rounded clasts of plagiogranite, black chert, and chloritized angular to delicately cuspate basaltic glass, tephra and hyaloclastite fragments, with lithic euhedral spinel and pyroxene grains, in a mud-sized matrix (Fig. 3.6 C). They also contain lenses of quartzofeldspathic sand, and limey material. The sandstones they are associated with are of a mixed provenance, containing up to 50% volcaniclastic material and the remainder quartzofeldspathic fine sand (Figs. 3.6 D and 3.6 E). They contain fine sand-sized grains of quartz and plagioclase (<20%). Polycrystalline quartz is occasionally seen, in accessory amounts. This clastic material is extremely well sorted, commonly very angular, never rounded, and may be fragmental pyroclastic material. The lithic content of detrital spinel/magnetite, chlorite, aphanitic volcanic fragments, euhedral weathered-out plagioclase microphenocrysts and pyrite implies a secondary source, likely volcaniclastic material from the ophiolite; lithic content can compose up to forty percent of the rock. Pyroclastic material may be difficult to distinguish amongst the sandy material, though it forms discrete layers in limestones within the overlying supracrustal package (Fig. 3.6 F).

The black chert, otherwise massive, contains microscopic spherical structures that resemble radiolaria, or possibly spherulites that originated as pyroclastic glassy material (Figs. 3.7 A and 3.7 B). Most of these structures show quartz recrystallization textures within the spheres, though many show an internal concentric structure typical of the radiolaria. White chert overlies the black chert. The white chert is compositionally banded at the sub-centimeter scale, with gray to black bands that, in some samples, are composed of fine fragmental pyroclastic material.

3.6 Ophiolite geochemistry

Forty-three whole-rock chemistry analyses were performed by Actlabs in Ancaster, Ontario, Canada with their 4LithoRes option, a lithium metaborate/tetraborate fusion ICP for major oxides and trace element analysis run on a Perkin Elmer Sciex ELAN ICP/MS. The run was preceded by blanks and controls and with both laboratory duplicates and two duplicates of ours. Sixteen whole rock chemistry analyses were performed by Geoscience Laboratories in Sudbury, Ontario with their XRF-M01 option for major oxides and IMC-100 option utilizing an ICP-MS for trace elements. Analytical data for all whole-rock analyses are provided in Table B.4 in the appendix. Eight peridotite samples and one volcaniclastic sandstone (containing detrital spinel) were selected for microprobe analysis of spinel with olivine, orthopyroxene and clinopyroxene where present. Mineral chemistry performed at the University of Western Ontario, Earth and Planetary Materials Analysis (EPMA) Laboratory used a JEOL 8530F Hyperprobe instrument. Analysis conditions include a 15 keV accelerating voltage and 20 nA beam current. Counting times ranged from 20 to 40 seconds on both peak and background positions. Mineral chemistry performed at Université Laval, Sainte-Foy, Québec, was completed on a Cameca SX-100 electron microprobe. Analysis conditions include a 15keV accelerating voltage and 20 nA beam current with 10 second counting times. Table 3.1 provides a breakdown of the samples analyzed, including lithology, a brief textural description, which minerals were analyzed and on which microprobe. Spinel mineral chemistry analytical results are provided in Table B.1 in the appendix. Olivine mineral chemistry analytical results are provided in Table B.2 in the appendix. All pyroxene mineral chemistry analytical results are provided in Table B.3 in the appendix.

3.6.1 Mineral chemistry

Mineral chemistry of chromium spinel

Mineral chemistries of primary chromium spinel were analyzed from eight ultramafic rock thin sections that bear modal amounts of <1-2%, and a single sample of a volcaniclastic sandstone that contains detrital grains. Table 3.1 summarizes relevant lithologies, textural features of the rocks and the mineral grains. The detrital spinel has small chromium rich cores with large euhedral coronae of magnetite. Granular spinel grains are rounded, anhedral to euhedral crystals with iron-rich coronae of varying thicknesses and chromium-rich cores. Vermicular spinel grains have only very thin iron-rich coronae and are collections of grains tabular to amoeboid in shape. The vermicular spinel grains form a fairly homogeneous population, with Cr# ($\frac{\mathrm{Cr}}{\mathrm{Cr+Al}} \times 100$, from mol% values) ranging from 68 to 82, and with Mg# ($\frac{\mathrm{Mg}}{\mathrm{Mg+Fe^{2+}}} \times 100$, from mol% values) ranging from 35 to 50 (Fig. 3.8, appendix Table B.1). Their coronae are largely magnetite, with median Mg# of 1. The vermicular population has a distinctly low TiO_2 content (<<0.1 wt%). The granular spinel is different, with Cr# ranging from 36 to 73 and Mg# ranging from 8 to 46 (with a median of 28). In comparison to the vermicular spinel, the granular have a 12 wt% higher median FeO^{total} content yet only a 3 wt% lower median MgO. They also have a median TiO_2 content of 0.57 wt%. Their coronae are mostly chromian magnetite, with a Cr_2O_3 range of 6 to 37 wt% and a median content of 31 wt% oxide. They are also titaniferous, with a median TiO_2 amount of 1.7 wt%. The detrital spinel compositions have the largest spread in signature, Cr# ranging 47 to 66 and Mg# from 4 to 61. They have a large range in TiO_2 content, from 0.12 to 3.19 wt%. Their coronae are magnetite.

The vermicular population clusters within the general field for forearc peridotite spinel (Dick and Bullen, 1984) on a Cr# versus Mg# plot (Fig. 3.8 A). The granular population occupies the edge of the same field and trends to lower Mg# contents within the same range of Cr#. The subdivided fields where this population lies are fields of metasomatic and thermal alteration commonly attributed to magmatic intrusions (Constantin et al., 1995). The detrital spinel population occupies a similar region and trend as the granular population, yet with a wider range of higher Mg#. Vermicular spinel grains fall within a distinct forearc region on a Fe_2O_3 versus TiO_2/Cr# plot (Fig. 3.8 B). Granular spinel exhibits a correlation between increasing ferric iron content and TiO_2/Cr#, positively trending along the island-arc tholeiite field on the aforementioned plot. The detrital spinel occupies a wide range but shows two trends; one small population mimics the granular spinel trend in the IAT field, and the remainder span the alkali or within-plate basalt region.

Mineral chemistry of olivine and pyroxenes

Olivine analysis reveals two populations, one defined by a single sample (HLH-042A) with an Mg# ranging from 76 to 78, the other population ranging Mg# 85 to 95, with a median of 87. Figure 3.9 A plots Mg# versus NiO, showing that both populations are compatible with a fractional crystallization trend (Constantin, 1999) indicated by the arrow. The higher Mg# population is generally associated with forearc peridotites (Constantin et al., 1995; Hébert et al., 2003). The whole olivine set has a narrow range of NiO values, from 0.17 to 0.57 wt%. Both clusters may indicate interactions between gabbro and peridotite, from the closest fields to the data clusters.

Pyroxene chemistries show a set of signatures arguably related to a forearc tectonic setting. The orthopyroxene grains measured are largely enstatite in composition, with values of En_{86-92}. Consequently, their Mg# is similarly high and consistent, but their alumina varies between 0.7 and 1.9 wt%. In a plot of Al_2O_3 versus Mg# they have a pattern similar to the shape of the forearc peridotite field yet with a wider range of Mg#, spanning the edge of the boninite field along the fractionation trend (Fig. 3.9 B); they are far from being aluminous enough to be genetically related to abyssal peridotites. Clinopyroxene chemistry shows wide range in Mg# (83 to 100) and spans most reference fields in an Mg# versus Cr_2O_3 variation diagram (Fig. 3.9 C). The low chrome sample HLH-104C is the closest to the forearc peridotite field. Similarly, on a plot of $Mg/(Mg+Fe^{2+}+Fe^{3+})$ versus TiO_2 (Fig. 3.9 D) the same sample (104C) has a similar TiO_2 range as the forearc peridotite field, yet along with the rest of the points, defines a trend within the abyssal peridotite field. Clinopyroxenes are commonly very altered in these rocks, which may be reflected in the data; they define a trend away from a forearc affinity, largely within the field of abyssal peridotites.

3.6.2 Whole-rock geochemistry

Spider plots of basic and ultrabasic intrusive rocks

Peridotites in the Hongliuhe ophiolite have a range of Mg# from 84 to 94. They are very low in K_2O and their Al_2O_3 content ranges from 0 to 8 wt%. Their loss on ignition (LOI) ranges between 2 and 22 wt%, likely a result of the variable serpentinization. Pyroxenites have a range in Mg# from 75 to 80. Gabbros are more variable, from 41 to 89 Mg#. Their CaO content ranges from 9 to 24%. LOI for gabbro samples is almost entirely within the 1 to 4 wt% range, with one exception of an intensely altered sample at 9.5 wt%.

Considering trace elements, the intrusive rocks have three distinct signatures in REE spider variability plots, normalized to the primitive mantle of Sun and McDonough (1989). Analyzing trace elements, one set of peridotites and gabbros has a distinct flat REE pattern (Fig. 3.10 A) and another shows depletion in the LILE's (Fig. 3.10 B). In both populations some samples are more depleted of trace elements than primitive mantle, indicating they may be residues from previous melt extractions. These samples show only a refertilization of the most extremely incompatible LILE's, namely Cs, Rb, and Ba. Most samples, especially gabbros and pyroxenites, have positive anomalies of uranium, potassium and strontium. Many of the gabbros have positive europium anomalies correlating with their plagioclase content. All of the gabbro samples, except one with a calc-alkaline signature (in Fig. 3.10 E), and most peridotites fall into these two subdivisions. There is a third population of peridotite samples that are ultra-depleted in REE's, to the point that the analyses fall below detection limits for many of the elements (Fig. 3.10 C). Their signatures exhibit extreme depletion of the HFSE's and REE's, and a refertilization of LILE's creating a reversed slope in the normalized spider plot.

Geochemistry of the lavas and dykes

Major and trace element-based classification of the extrusive and dyke rocks show a range of the majority from tholeiitic basalt to andesite (Figs. 3.11 A and 3.11 B); the single high-silica content andesite sample is not volcanic, but largely pyroclastic material with some volcaniclastic input from the ophiolite lithologies (Fig. 3.6 E). Silica contents of the volcanic rocks range from 47 to 67 wt%. TiO_2 varies between 0.4 and 2.5 wt%, and has a limited covariance with SiO_2 that supports a fractional crystallization interpretation. The spread that the extrusive suite shows in silica and titanium compositions is largely similar to those found for a typical mid-ocean spreading center, back-arc or fore-arc region (Dilek and Furnes, 2011).

Classification of Hongliuhe ophiolite basalts using major element geochemistry indicates a transitional tholeiitic to calc-alkaline nature, ranging from more primitive chemistry to more evolved (Fig. 3.11 A). Figure 3.11 shows that there are multiple different fractionation trends in the eruptive rocks: pyroxene phenocryst accumulation affected some samples giving them a high chrome/low titanium signature; low chrome/high titanium rocks trend along the calc-alkaline line. Many samples skirt the field for boninite, but only one sample, a <1% orthopyroxene phenocrystic basaltic andesite, has > 8 wt% MgO and > 52 wt% SiO_2.

Trace element discrimination identifies two distinct populations. Their signatures have been differentiated into LILE (and to an extent, HFSE) depleted rocks (Fig. 3.10 D), interpreted to be island arc tholeiites, and LILE and LREE enriched rocks (Fig. 3.10 E). These loosely resemble both island arc tholeiites and calc-alkaline rocks. All show distinct negative Nb and Ta anomalies. They have anomalous peaks of uranium, potassium and strontium, and few samples have positive europium anomalies. They are enriched only in the most incompatible elements, Cs, Rb, and Ba. There is no spatial association between the members of each of the two populations, depleted or enriched. All lavas and dykes are concentrated on the north side of the ophiolite.

Geochemistry of units within the overlying supracrustal sequence

The volcanic rocks within the overlying supracrustal package have similar chemistry to the lavas and dykes of the ophiolite. Their major element chemistry differs little from the ophiolitic rocks. It is a smaller sample population, and it exhibits a narrower range of silica contents, from 47 to 58 wt%. The differentiation trend in figure 3.11 A shows that they contain some barely primitive basalts, and evolved along a borderline calc-alkaline/tholeiitic trend.

Their spider diagrams show two distinct REE patterns. One population (Fig. 3.10 F) is relatively similar to the island arc tholeiites from the ophiolite (of Fig. 3.10 D), with a less pronounced niobium and tantalum anomonly, a negative potassium anomaly, and chaotic enrichment of the most incompatible LILE's. The other population 3.10 G) exhibits a similar signature as the IAT/calc-alkaline group (of Fig. 3.10 E), two of the three samples having the characteristic Nb and Ta anomalies.

3.7 Geochronology

3.7.1 Analytical procedures

Sample crushing and analytical work were performed at the Geological Survey of Canada Geochronology Laboratory in Ottawa, Ontario, Canada using standard mineral separation techniques including heavy-liquid and magnetic separation. Zircons were dated using the Sensitive High-Resolution Ion MicroProbe (SHRIMP II). Analytical procedures followed the outline of Stern (1997), using standards and U-Pb calibration methods of Stern and Amelin (2003). Internal zircon structure was imaged utilizing both back-scattered electrons and cathodoluminescence in a Cambridge Instruments scanning electron microscope. Analytical data are given in Table B.5 in the appendix.

3.7.2 Gabbro and tonalite U-Pb zircon geochronology

A megacrystic, possibly pegmatitic, plagioclase-pyroxene gabbro was sampled for geochronology from approximately the boundary between the mantle section and the northern volcanic rocks. The gabbro has a depleted LREE whole-rock geochemistry (Fig. 3.10 B). The sample location is indicated on figure 3.2, in the west. A large sample yielded approximately 120 zircons. Zircons exhibit concentric and sector zoning textures, many with euhedral to slightly rounded prismatic morphologies, consistent with a magmatic origin. Nine analyses from nine grains yield a Concordia age of 520.3 ± 5.8 Ma, (Cambrian; MSWD of concordance = 4.6 and probability of concordance = 0.033) (Fig. 3.12 A). This age is interpreted as the crystallization age of the gabbro.

The second date presented here is from a tonalite body hosted in the sedimentary package overlying the ophiolite main body. The sample location is also indicated on figure 3.2, in the northeast. Separation yielded abundant zircons. The zircons exhibit concentric zonation, most with euhedral, prismatic morphologies, implying a magmatic origin. Twenty analyses from 20 grains yield a Concordia age of 413.6 ± 3.5 Ma (Early Devonian; MSWD of concordance = 4.2 and probability of concordance = 0.041) (Fig. 3.12 B). This age is interpreted as the crystallization age of the tonalite.

3.8 Discussion

3.8.1 A seafloor genesis for the Hongliuhe ophiolite

Many facets of the Hongliuhe ophiolite indicate a seafloor genesis, analogous to volcanic-arc/forearc type examples such as the Betts Cove ophiolite (Bédard, 1999; Cousineau and Bédard, 2000), the Thetford Mines ophiolite complex (Schroetter et al., 2003; Pagé et al., 2008, 2009) and the Kizildag ophiolite in Turkey (Dilek and Thy, 2009); it is a section of marginal oceanic crust generated and modified close to an arc with cumulate ultramafic and mafic sequences, mixed volcanic and volcaniclastic layers, and a related overlying supracrustal sequence kilometers thick. The younging direction of its coherent sections of lithostratigraphy is interpreted to be northward. Plutonic rocks in the Hongliuhe ophiolite are dominated by cumulate lithologies with pervasive oikocrystic textures in the peridotites and gabbros showing that the main igneous body represents crystallization sequences formed at the uppermost mantle or lower crustal depths. Ductile deformation recorded within the gabbros and peridotites indicates that high temperature grain-scale dynamic recrystallization of mafic mineralogy was taking place in localized shear zones. Such deformation temperatures are consistent with high-temperature oceanic crust transform or normal faulting. The very thin crustal section and the exposure of upper mantle rocks to immediate supracrustal covering support interpretations involving a magma starved setting or thinning of the oceanic lithosphere along intraoceanic detachments (Bédard, 1999; Pagé et al., 2008). Faulting within the ophiolite does not fit the regional structural pattern and could represent such fossilized detachments, primarily offsetting upper mantle ultramafic and plutonic rocks and overlain by relatively undeformed volcanics. The overlying supracrustal package is much less competent and does not exhibit high-temperature ductile deformation, indicating that the deformation in the ophiolite predated the volcanic effusions and some intrusions. Despite it not exhibiting seafloor eruptive features such as pillow basalts or a sheeted dyke complex it does exhibit volcanic deposits with interlayers and lenses of red chert; they may be vented hydrothermal precipitates, or abyssal siliceous deposits, both related to seafloor processes. Vesicle contents in basalts indicate a moderately shallow seafloor setting (Kokelaar, 1986), as do vitriclastic calcite and epidote-filled amygdules. Geochemically, uranium, strontium and potassium metasomatic enrichment (and some stripping) is fairly consistent with seafloor alteration processes and is seen throughout the petrologic record (Harper, 2003; Dilek et al., 2008). The volcaniclastic conglomerates indicate developing fault scarps or proximity to a growing dome or vent, and in conjunction with the coarse volcaniclastic turbidites, both proximal and distal facies, they indicate the topographic relief was below wave base (Cousineau and Bédard, 2000; Kessler and Bédard, 2000). The fragmental and hyaloclastite materials found in the basalt traction deposits require phreatomagmatic brecciation. The volcaniclastic sandy deposits include detrital spinel input from the ophiolite and an alkalic volcanic source (Fig. 3.8 B) mixed with well-sorted quartzofeldspathic sand; this may point towards a rapid obduction event or a proximal oceanic arc or continent. The overlap sequence from extremely angular volcaniclastic sandy deposits to abyssal limestones and (interbedded) black and white cherts upsection is consistent with the development of a trench. The thickness, 10 m, of indurated chert could be deposited in as little as five million years. The overlying supracrustal package, with increased sandy contributions, indicates a transition to a nearshore environment with intermittent island-arc related volcanism; pyroclastic input into siltstones and limestones imply proximity to an active arc.

3.8.2 Arc-related geochemical nature

The most direct geochemical evidence that the ophiolite formed in a supra-subduction setting, marginal to an arc, is the identification of two distinct geochemical signatures for the volcanic and dyke rocks (Figs. 3.10 D and 3.10 E). The two signatures of the whole-rock geochemistry exhibit increased levels of geochemical differentiation of the LILE's and light rare earth elements, except for Nb and Ta, characteristic of slab devolitilization under a SSZ setting. They match reference chemistries of island arc tholeiites (Fig. 3.10 D) and calc-alkaline rocks (Fig. 3.10 E). There may be only a single boninitic sample, yet it is at the edge of an array skirting the boninite field; the volcanic data array may be interpreted as a derivation from large melt fractions of a previously depleted mantle (Dilek and Thy, 2009; Pagé et al., 2009). The subduction influence dominating over mid-ocean ridge processes is exemplified by a bivariate comparison of La/Nb versus La/Sm (normalized to their primitive mantle values of Sun and McDonough (1989), Fig. 3.13 A). It depicts the IAT population trending vertically away from the MORB array with its large range of La to Nb ratios, showing the increased subduction-component influence (Kamenetsky et al., 1997; Guilmette et al., 2009). The IAT/calc alkaline population depicts the distinct signature of Nb conservation and refertilization of La from the downgoing slab source, occupying a more differentiated or arc-like region of the plot. It has a tighter cluster than the IAT population due to the low variation of Nb. The overlying supracrustal basalts occupy a region between the two ophiolite populations, more towards the enriched portion of the MORB array.

The suite also depicts a crystallization sequence typical of SSZ rocks (Metcalf and Shervais, 2008). Crystallization of late primary phases in hydrous conditions is evident, such as the prevalence of amphibole in gabbros and basic volcanics. The hydrated environment for the localized shearing in the plutons, including incongruent dynamic recrystallization of primary phases to amphiboles, is not solely related to SSZ hydration or hydrative melting; such features are common near ridges and transform faults (Constantin, 1999).

Ultramafic and mafic plutonic rocks provide less conclusive evidence in whole-rock analysis. Most exhibit geochemical depletion signatures resembling typical oceanic crusts modified by seafloor alteration and enrichment in only the lightest LILE's (Figs. 3.10 A and 3.10 B). Few examples exhibit extreme depletion with refertilization of most LILE components, providing a limited example of a SSZ signature in the ultramafics (Fig. 3.10 C); most LILE analyses in the set approach detection limits. Mineral chemistry from the ultramafic rocks allows for more definitive interpretation. The bimodal aspect to the spinel populations is attributable to textural characteristics. Vermicular spinel records the most definitive SSZ signature, confined to the intersection of forearc peridotite and IAT fields in an Mg# versus Cr# diagram (Fig. 3.8 A) (Barnes and Roeder, 2001; Kamenetsky et al., 2001; Hébert et al., 2003). The vermicular texture may be related to melting processes (Mercier and Nicolas, 1975; Hébert et al., 2003; Pagé et al., 2008). It is considered to have originally equilibrated with primary mineral phases, yet the original textural relationships were destroyed in the serpentinization process. All other primary granular spinel was analyzed from tectonized or altered rocks and has a geochemical signature that indicates re-equilibration under high-temperature metasomatic conditions associated with deformation or nearby intrusions (Constantin et al., 1995; Constantin, 1999). Their high TiO_2 content and its relationship to Fe_2O_3 (Fig. 3.8 B) shows a similarity to island-arc tholeiite and back-arc basin spinels, yet they are from ultramafic rocks. This may indicate that a magmatic stage in the evolution of the ophiolite was a potential reservoir for re-equilibration, such as either the IAT or calc-alkaline melts (Arai, 1992; Constantin et al., 1995; Constantin, 1999). The olivine population is less diagnostic, and may have been complicated by the cumulate nature. Those with high nickel content and Mg# are refractory mineral compositions, whose presence is consistent with the spinel-based interpretation of a forearc origin that had a stage of high-temperature re-equilibration, metasomatic or magmatic related, to a more iron rich nature. The orthopyroxenes analyzed are low in Al_2O_3, supporting a forearc peridotite interpretation. Clinopyroxene compositions of the tectonized sample (HLH-104C) also roughly correlate to forearc chemistry (Hébert et al., 2003; Pagé et al., 2008), implying that re-equilibrations during dynamic recrystallization were in a marginal or forearc SSZ setting. The remainder of the clinopyroxene analyses trend through lower Mg# compositions and increasing TiO_2 through fields associated with abyssal peridotites, a possible effect of re-equilibration; such a titanium trend is also seen in the spinel data.

3.8.3 Tectonic setting in the context of the Beishan

The Cambrian age of the gabbro dated in this study reveals what is likely a late stage of oceanic crust magmatism. Many studies link ophiolite genesis to subduction initiation (Bédard, 1999; Metzger et al., 2002; Harper, 2003; Stern and De Wit, 2003; Dilek et al., 2008; Dilek and Furnes, 2009; Dilek and Thy, 2009; Pearce and Robinson, 2010; Ao et al., 2012) yet this study shows dual-signature volcanism with a strong island arc affinity and a slightly less refractory nature than typical boninitic lavas. This leads to the interpretation that temperatures of volcanism within the extending forearc were not as high as models of subduction inception imply (Dilek and Furnes, 2009; Dilek and Thy, 2009); our interpretation of tectonic setting is based strictly on the presence of extensional structures, high-temperature deformation zones with hydrous conditions, the volcaniclastic facies and immediate quartzofeldspathic sedimentary cover. The setting of a margin of an arc, pre-emergent, intraoceanic or otherwise, still requires a mechanism such as subduction rollback to provide the syn-magmatic crustal extension required to create the relationships reported here (Fig. 3.14). The island arc tholeiite and calc-alkaline geochemical natures of the two volcanic populations are also consistent with such an interpretation. Well constrained magmatic ages are not extensively reported for the Beishan, but literature generally reports the start of magmatism as Ordovician (Xiao et al., 2010). The Hanshan/Mazongshan terranes are, combined, possibly the arc in question, yet strike-slip motion along the suture boundaries is unconstrained in magnitude. It is possible the ophiolite is exotic with respect to the surrounding arc terranes.

Our data are consistent with an interpretation that the Hongliuhe ophiolite is genetically related to some components of the Yueyashan-Xichangjing ophiolites. They have a similar lithostratigraphic sequence, similar Cambrian gabbro zircon ages, and dual-signature volcanic suites that show similar geochemical characteristics (fields labeled in Figs. 3.10, 3.11, and 3.13) (Ao et al., 2012). The Huoshishan-Niujuanzi ophiolites, lying between the two, exhibits lithological similarities yet is considerably younger (Tian et al., 2014). Its genesis age is similar to our second age, an undeformed granitoid yielding an age of ca. 414 Ma (Fig. 3.12) interpreted as a younger age constraint on emplacement of the Hongliuhe ophiolite. Suture zones are considered crustal weaknesses and the central

Beishan could reasonably have localized spreading at this time, accommodating growth of the HNO. This would imply that the emplacement of the Hongliuhe ophiolite would have been within the 100 m.y. timespan before the constraint, perhaps in the Silurian towards the end of reported magmatism in the Mazongshan.

For the evolution of the Beishan, the Hongliuhe ophiolite offers an along-strike correlation to known Cambrian seafloor spreading and SSZ ophiolite generation 400 km to the east, in the YXO. This tentative link provides a scale to the size of the margin along which arc inception and generation was occurring in the early Paleozoic Beishan. It cements the interpretation of a suture zone, despite the dismembered nature of the incorporated oceanic units. In conjunction with the high density of sutures in the region it supports the archipelago model of orogeny and accretion in the Beishan (Windley et al., 2007; Xiao et al., 2010; Chapter 2).

3.9 Conclusion

The Hongliuhe ophiolite is a fragment of early Cambrian oceanic crust. It comprises cumulate layered, pervasively altered, intermittently deformed, plutonic lithologies attenuated to expose lower crustal rocks subsequently overlain by extrusive sub-aqueous volcanic rocks. Mineral chemistry of peridotite-hosted spinel, olivine, and pyroxenes indicate primary crystallization in a forearc/island-arc setting, and may imply multi-stage plutonic emplacement; spinel populations are related to a forearc setting, but also contain an iron-enrichment trend along a range indicative of re-equilibration with melt intrusions. Multi-stage or -source volcanism is observed in the dual-signature whole-rock geochemical populations of basic lavas and dykes, which depict an evolution from island-arc tholeiites to a distinct group more calc-alkaline in composition. They have characteristic Nb-Ta anomalies indicating influences from melt or metasomatic fluids derived from a subducting slab; it is a SSZ ophiolite. The intermediate to basic volcanic rocks are interlayered with coarse fragmental volcaniclastic debris deposits showing turbidite sequences. Active-arc-related pyroclastic input may have been responsible for the common siliceous interlayering in the mostly hemipelagic limestone, basalt and sandstone overlying succession. We conclude that the tectonic setting is a fore-arc (possibly back-arc?) region of an emergent or mature arc; the most probable relationship is to the Hanshan and Mazongshan terranes to the north and east. Emplacement may have involved a considerable strike-slip component, that cast the body into a sigmoidal shape, chaotically deformed the northwestern tip into a block-in-matrix structured deformation zone, and caused interspersed localized thrusting and strike-slip imbrication. This collision was completed by the Early Devonian, but is otherwise unconstrained. The Hongliuhe ophiolite bears petrogenetic links to the Yueyashan-Xichangjing ophiolite and, together, these ophiolites offer evidence of subduction rollback effects along a wide margin in the early Paleozoic. The history of the Hongliuhe ophiolite suggests that the Beishan experienced multiple phases and polarities of subduction, of which the ophiolite represents just one, and is an example for the archipelago type of accretion and orogeny in the southern Central Asian Orogenic Belt.

				Grain Textures (– indicates no analyses)			
Sample	Probe	Lithology	Rock Textures	Spinel	Olivine	Cpx	Opx
HLH-075A	Laval	Peridotite	Alt.-Chl, Am, Srp	Granular	Relict cum.	–	–
HLH-067C	UWO	Lherzolite	Serpentinized	–	–	Part. recr.	–
HLH-067C	Laval	Lherzolite	Serpentinized	Granular	–	–	–
HLH-077A	UWO	Lherzolite	Primary	–	Cumulate	Poikilitic	Poikilitic
HLH-077A	Laval	Lherzolite	Primary	Granular	–	–	–
HLH-042A	UWO	Lherzolite	Tectonized	–	Part. serpent.	–	–
HLH-042A	Laval	Lherzolite	Tectonized	Granular	–	–	–
HLH-104C	Laval	Lherzolite	Tectonized	Granular	Part. serpent.	Subgrains	Part. recr.
HLH-051E	Laval	Serpentinite	Magnetite veining	Vermicular	Cumulate	–	–
HLH-046B	Laval	Serpentinite	Magnetite veining	Vermicular	–	–	–
HLH-074C	Laval	Serpentinite	Magnetite veining	Granular	–	–	–
HLH-036F	Laval	Sandstone	Detrital spinel $< 5\%$	Mag corona	–	–	–

Table 3.1: Mineral chemistry sample and analyses information.

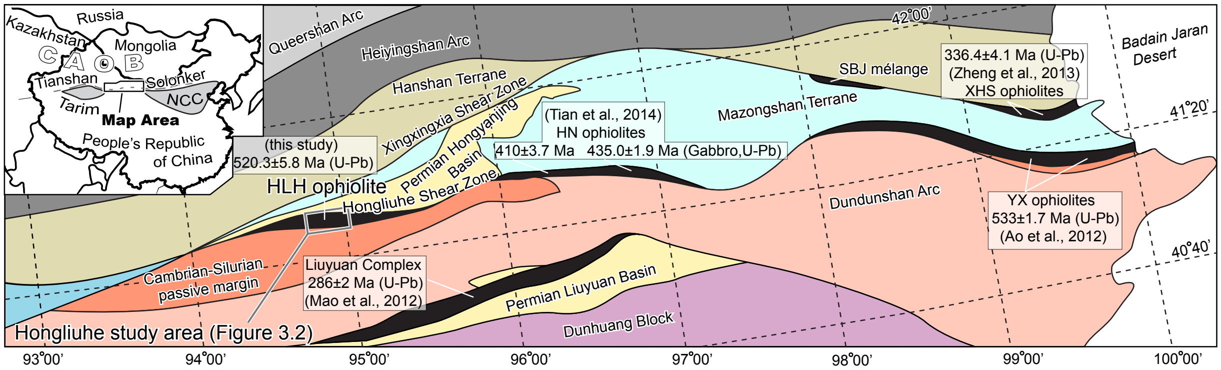

Figure 3.1: Tectonostratigraphic map of the Beishan. HLH: Hongliuhe ophiolite; HN(O): Huoshishan-Niujuanzi ophiolites (Tian et al., 2014); SBJ: Shibanjing ophiolite; XHS: Xiaohuangshan ophiolite (Zheng et al., 2013); YX(O): Yueyashan-Xichangjing ophiolites (Ao et al., 2012). Abbreviations used in inset map: CAOB: Central Asian Orogenic Belt; NCC: North China Craton. Colors denote individual terrane extents, with light brown used to highlight the youngest, Permian sedimentary deposits. Black infill denotes the collections of fault-bound tectonic slices of likely exotic oceanic units centered about a suture zone.

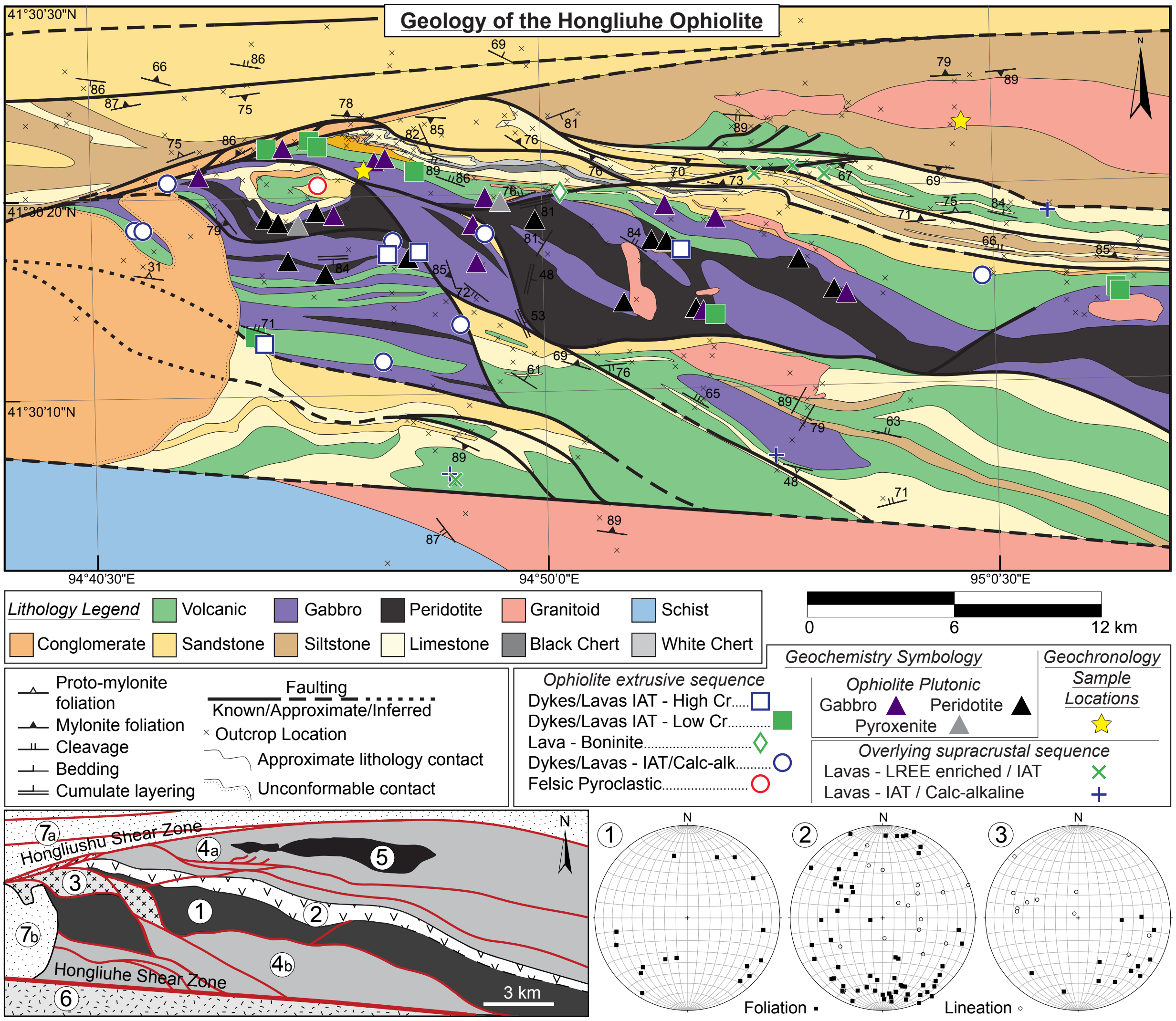

Figure 3.2: Geological map of the Hongliuhe region, centered on the ophiolite. The large symbols denote geochemistry and geochronology sample locations, with a symbol key identical to further geochemistry figures. The inset map at bottom denotes the lithostratigraphic sequences identified in this study and shows a slightly larger region than the above geological map. Red lines denote faults, and equal-area stereographic projections at bottom right contain structural information of the respective numbered domain. Divisions: 1) The plutonic and ultramafic sequence 2) Seafloor interface volcanic and volcaniclastic rocks 3) Block-in-matrix deformation zone 4a) Overlying supracrustal sequence 4b) Overlying supracrustal sequence, tectonically strike-slip imbricated beneath the ophiolite 5) Post-emplacement granitoid dated in this study (413 Ma) 6) Tectonic slices of metasedimentary and plutonic 7a) The Permian Hongliuhe Formation in fault contact 7b) The Hongliuhe Formation unconformably overlying the ophiolite.

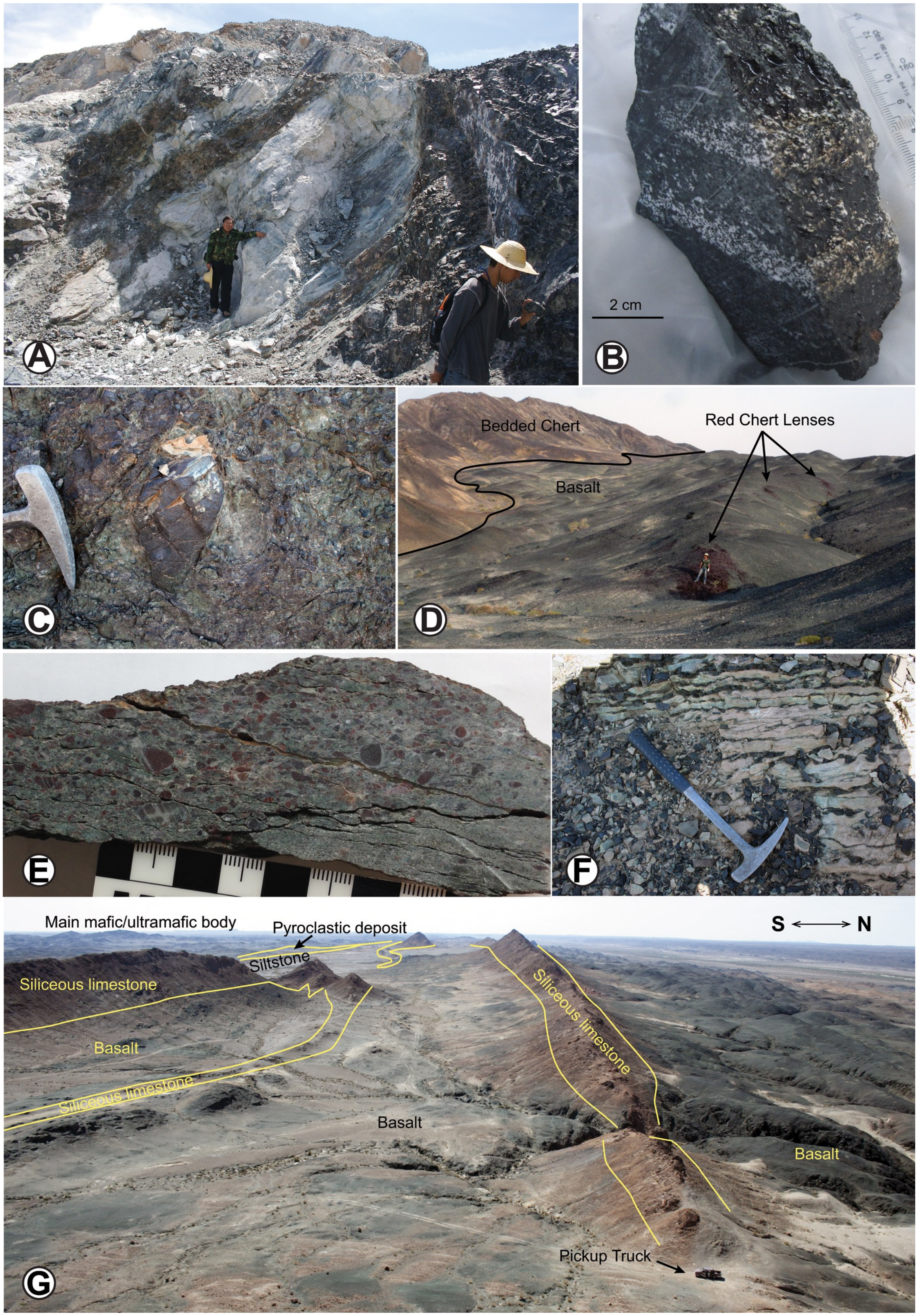
A
2 cm
B
C
Bedded Chert
Red Chert Lenses
Basalt
D
E
F
Main mafic/ultramafic body
Pyroclastic deposit
Siltstone
S
N
Siliceous limestone
Basalt
Siliceous limestone
Siliceous limestone
Basalt
Basalt
Pickup Truck
G

Figure 3.3 *(preceding page)*: A) Photograph of cumulate textures in outcrop: a quarry pit exhibiting layered intrusive rocks characteristic of the lower structural levels. The dark green rock is serpentinized peridotite, the white layers are an altered leucogabbro. B) Plagioclase cumulate textures in gabbroic rocks of the main ophiolite body. C) Autoclastic congomerate of basalt, with large sub-rounded clast beside hammer head surrounded by numerous pebble-sized clasts. D) Lensoidal outcrops of red chert within basalts of the seafloor interface. Scientist standing on red chert outcrop for scale. E) Heterolithic volcaniclastic conglomerate exhibiting grading, interpreted to be the traction base of a turbidite deposit. F) Interlayered limestone and basaltic tuff or volcaniclastic material, deposited on top of basaltic flows, within the overlying sedimentary sequence. G) View of the interlayered siliceous limestones and basalts of the overlying sedimentary sequences. Pickup truck for scale.

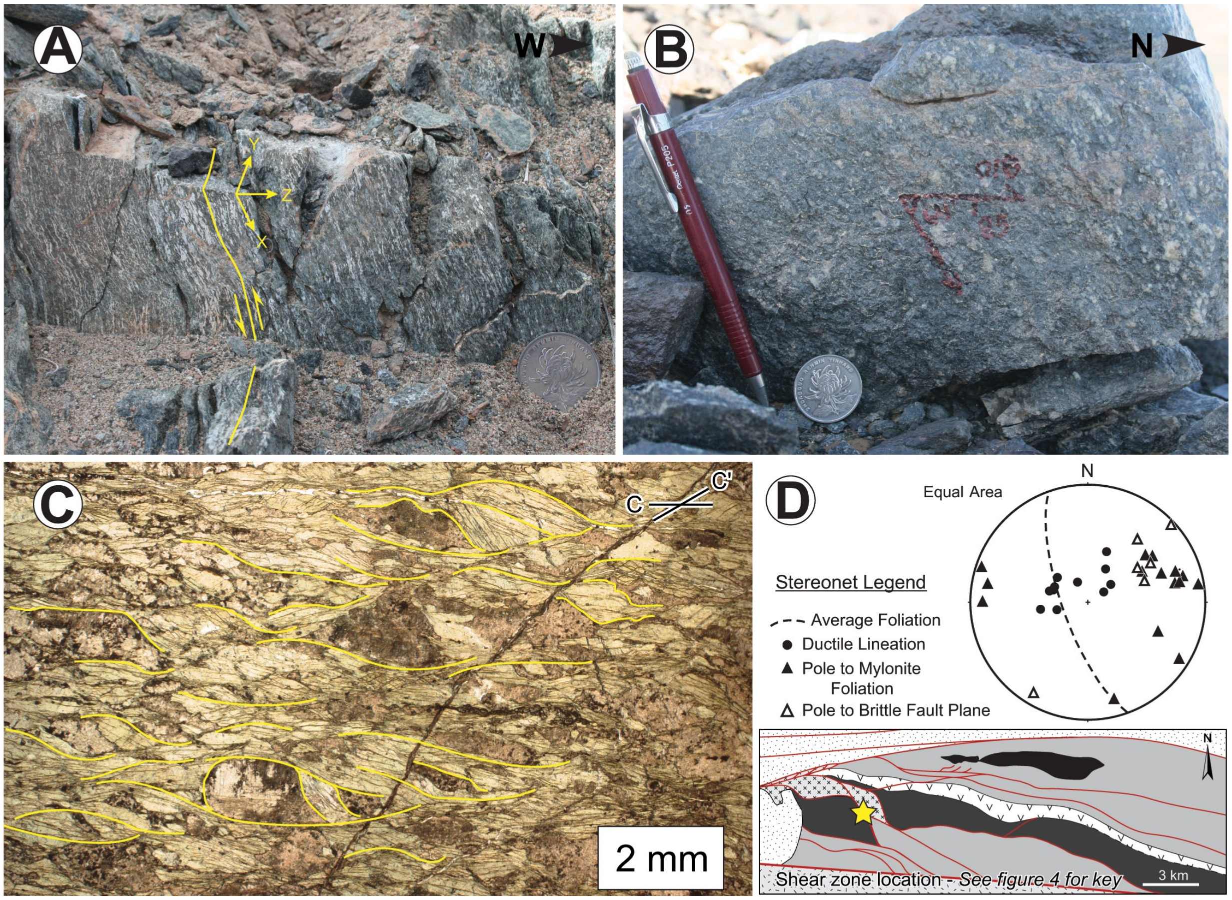

Figure 3.4: High-temperature gabbroic ductile shear zone with structural analysis. Inset map for location: A) Outcrop photo facing south showing the strongly foliated gabbro mylonite. Differentiated layers of white plagioclase visually define the steeply west-dipping foliation. One foliation trace is annotated, with principal strain axes and sense of shear indicated. B) Mineral stretching and ductile striation lineation from an outcrop of sheared gabbro. The white plagioclase grains exhibit alignment and stretching parallel to the pencil and the pitch orientation indicated on the rock surface. C) Photomicrograph under plane-polarized light of high-temperature sinistral C' fabric defined by amphiboles in gabbro mylonite. D) Stereonet of NNE-trending shear deformation within the main ophiolite body. Sinistral kinematics correlate to the west block largely moving up, east side down, in current reference frame. Considering the general steep northerly dip of the ophiolite lithostratigraphy this loosely correlates to transform motion in a paleohorizontal reference frame.

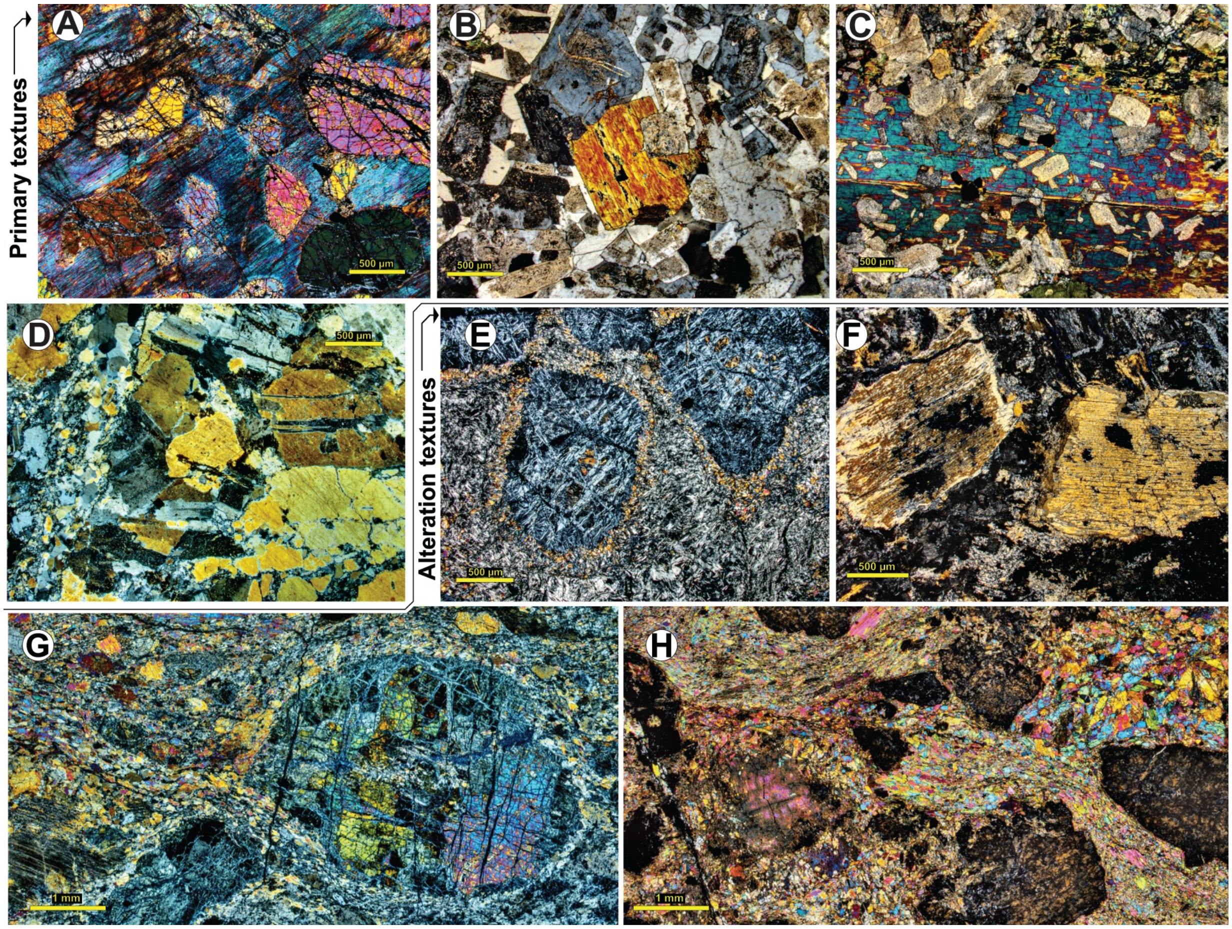

Figure 3.5: Photomicrographs depicting the crystallization sequences in plutonic sequence rocks. All images captured under crossed-polarized light. Primary textures: A) Poikilitic texture in lherzolite: sub-rounded, anhedral olivine chadacrysts encased in clinopyroxene oikocrysts. B) Nesophitic texture in gabbro, with a euhedral pyroxene grain that grew contemporaneously as the plagioclase grain it encases, yet is encased by later plagioclase. C) Gabbroic primary amphibole oikocryst encasing euhedral plagioclase grains and filling the interstices. D) Plagiogranite/anorthosite with near entirely plagioclase mineralogy. Alteration textures: E) Serpentinite, with first-order blue birefringence, pseudomorphing olivine or pyroxene, with granular amphibole rims, clusters of amphibole inclusions, in a matrix of first-order gray serpentinite. F) Thin amphibole replacement rims around pyroxene in serpentinized matrix. G) Rounded, mantled olivine porphyroclast in matrix of dynamically recrystallized amphibole, serpentinite and possibly olivine. H) Chemically weathered pyroxene (black to brown large grains) with matrix of either dynamically recrystallized amphibole, or intrusions of microgabbro-hornblendite.

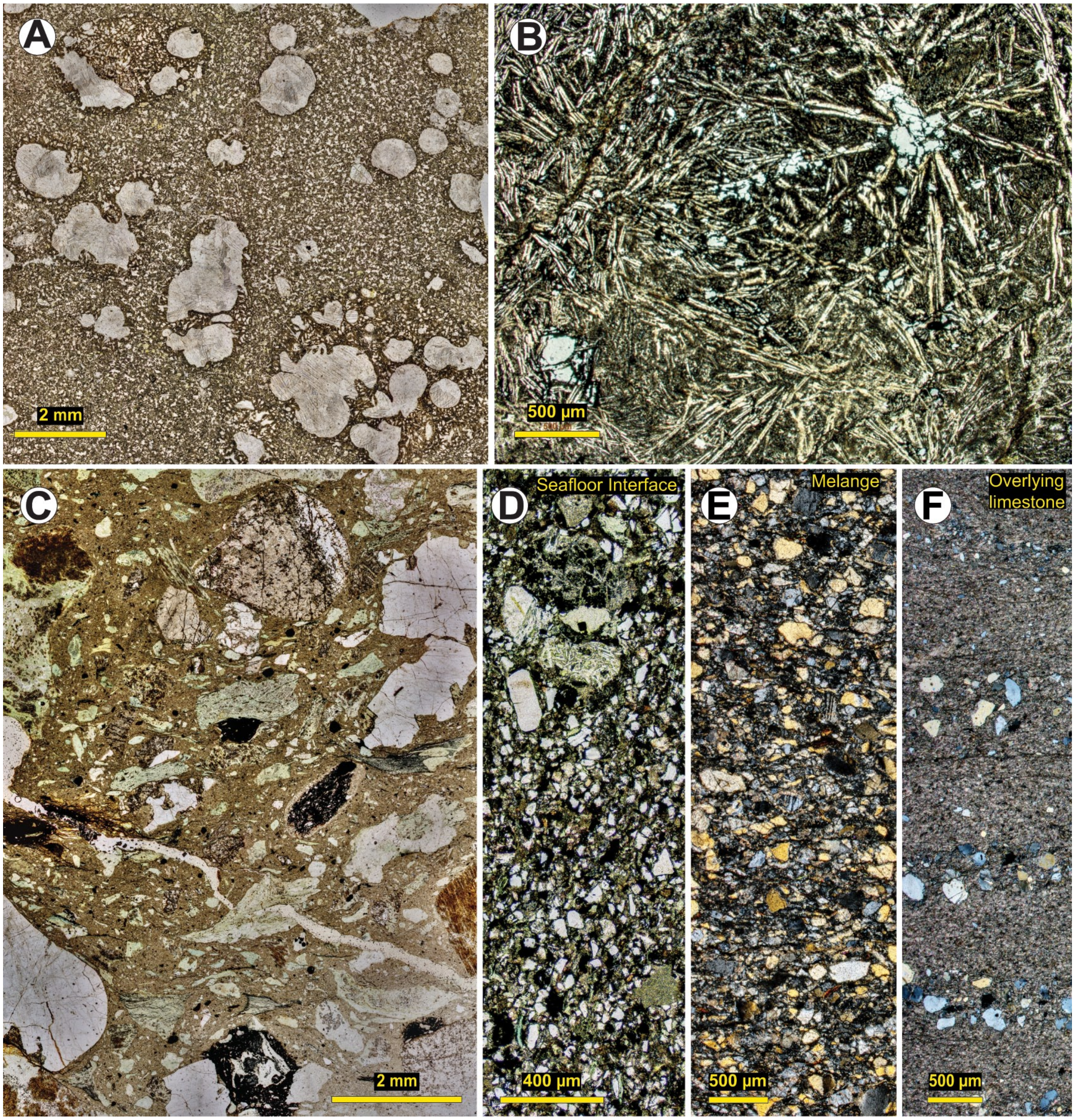

Figure 3.6: Photomicrographs of volcanic, volcaniclastic, and sedimentary textures. A) Vitriclastic texture: amoeboid shaped amygdules of calcite formed in exsolution cavities within juvenile magmatic clasts (darker brown, egg shaped) contained in the hosting basalt lithology. (PPL) B) Basalt with radial plagioclase growth off of pyroxene phenocrysts in a glassy matrix. (PPL) C) Basal traction deposit of purely volcaniclastic turbidite flow: contains rounded fragments of plagiogranite, black chert, chloritized angular to delicately cuspate basaltic glass or hyaloclastite fragments, with spinel and pyroxene grains, in a mud-sized matrix. (PPL) D) Mixed source volcaniclastic/arc-related sandstone with high volcaniclastic detrital spinel content, detrital …

figure caption continued on next page

Figure 3.6: *(continued from last page):* . . . chlorite and basalt fragments, weathered-out volcanic plagioclase phenocrysts, with well-sorted angular quartz and minor plagioclase fine sand. (PPL) E) Similar mixed-source sandstone, with less volcaniclastic material. This sample was found in the block-in-matrix deformation zone, a fragment of preserved seafloor interface unit juxtaposed against plutonic section units. (XPL) F) Limestone with fine (<1 mm) interlayers of angular sand sized material, possibly pyroclastic in origin or deposited as rhythmic sets of microturbidites. (XPL)

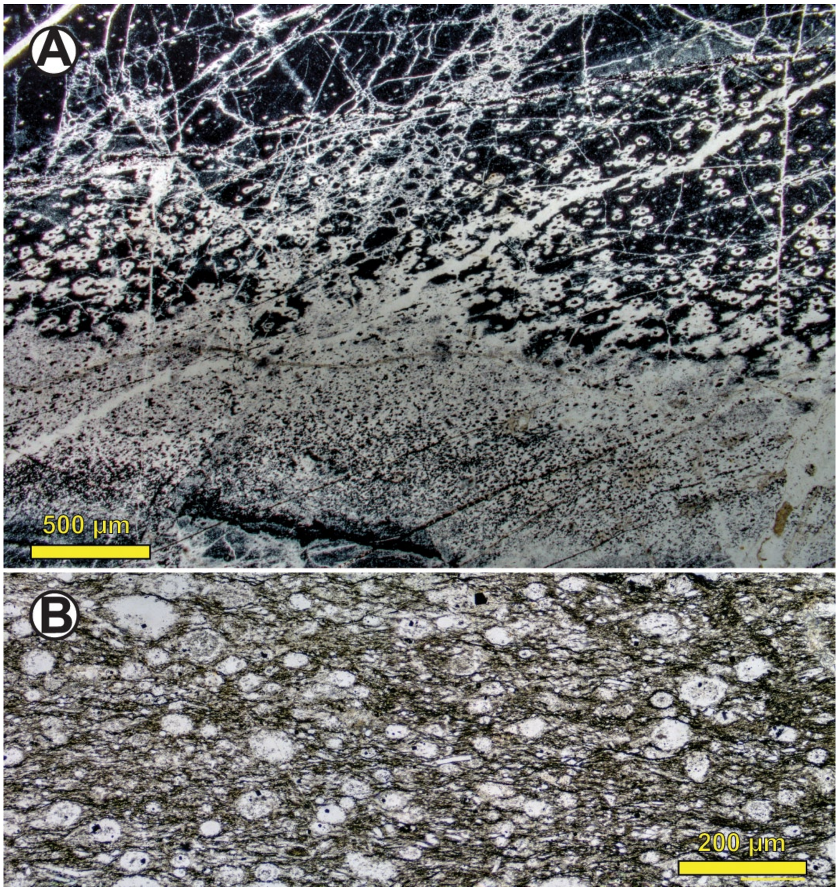

Figure 3.7: Photomicrographs of micro scale textures in chert. Both photomicrographs taken under plane polarized light. A) Black, carbonaceous chert with quartz veining and radiolaria structures, slightly ovoid in shape consisting of recrystallized quartz with dots of opaque primary material at their center. B) Magnified view of a banded white chert sample with diagenetic foliation showing round to ovoid cryptocrystalline quartz material with concentric spherical internal structures that resemble radiolaria.

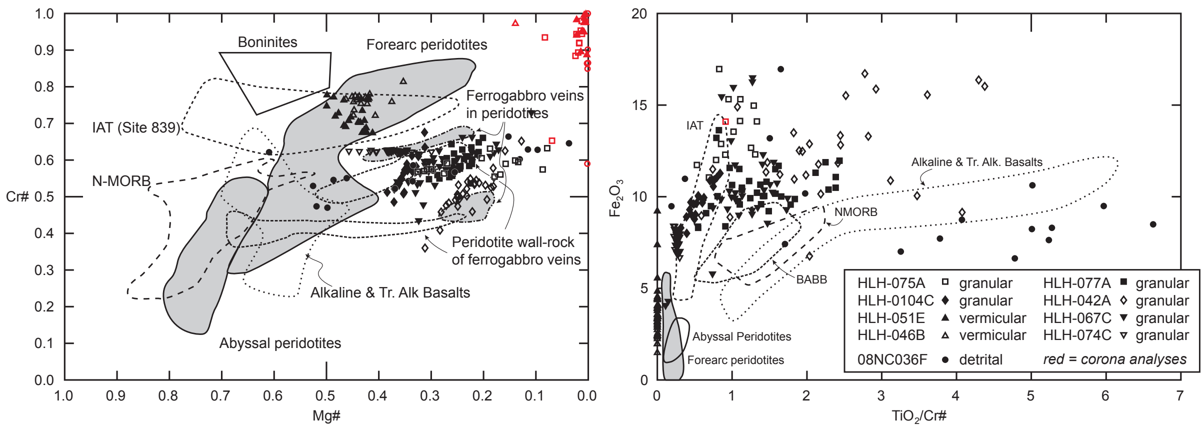

Figure 3.8: Spinel mineral chemistry. The fields are from data compiled by (Hébert et al., 2003) with references found therein.

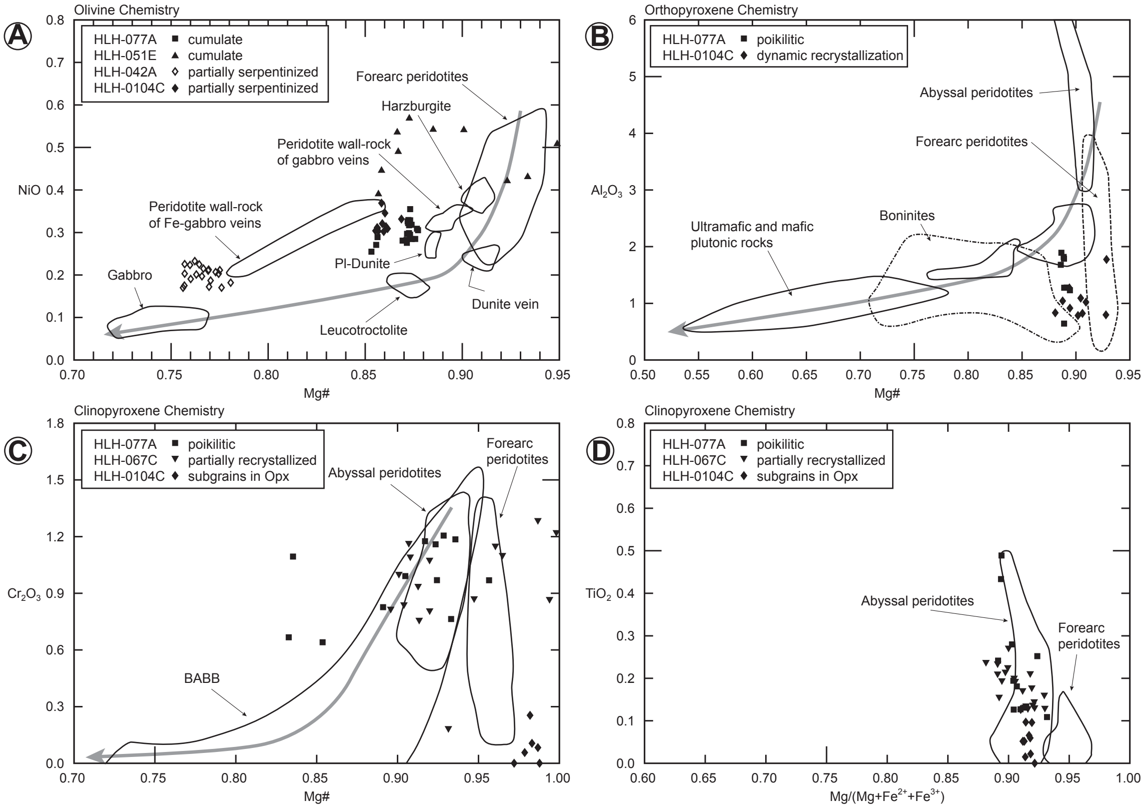

Figure 3.9: Olivine, orthopyroxene and clinopyroxene mineral chemistry. The fields are from data compiled by (Hébert et al., 2003) with references found therein.

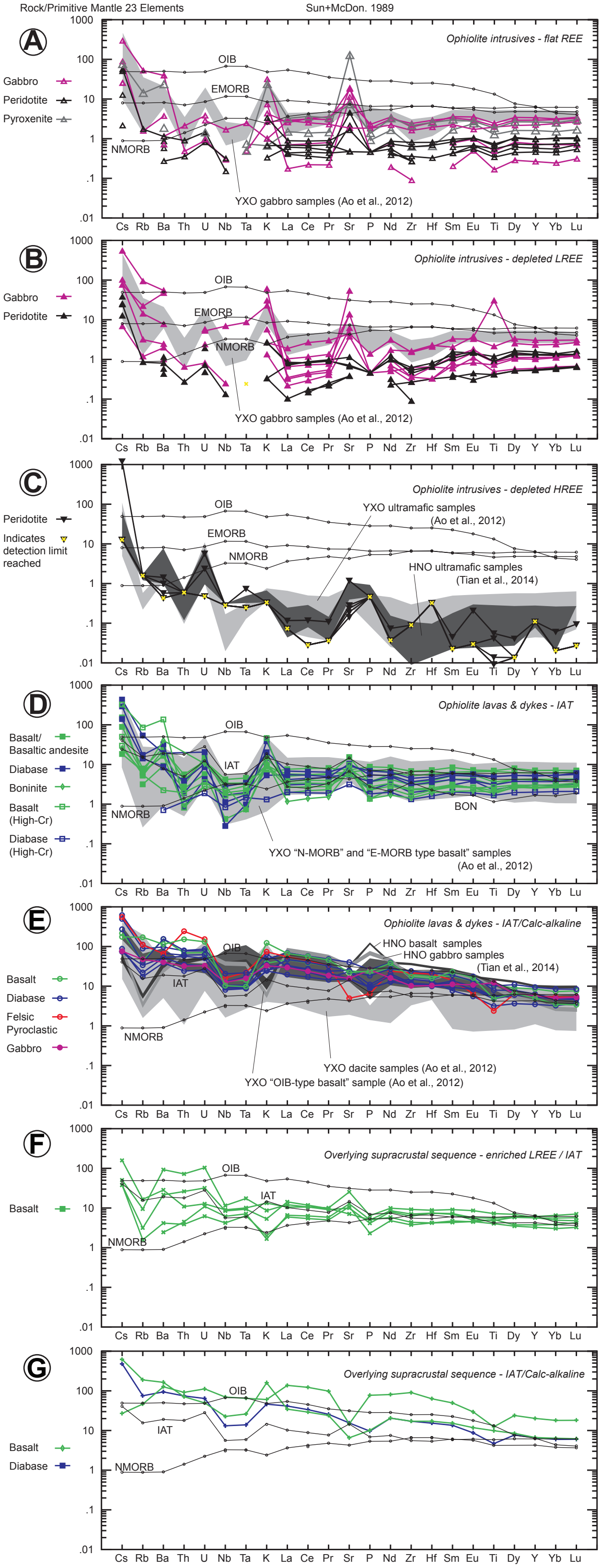

Figure 3.10: Geochemical spider diagrams of the ophiolitic basic and ultrabasic intrusive rocks. Rocks normalized to primitive mantle of Sun and McDonough (1989). NMORB (normal mid-ocean ridge basalt), EMORB (enriched mid-ocean ridge basalt) and OIB (ocean island basalt) reference lines from Sun and McDonough (1989). IAT (island arc tholeiite) and BON (boninite) reference line from Kelemen et al. (2003).

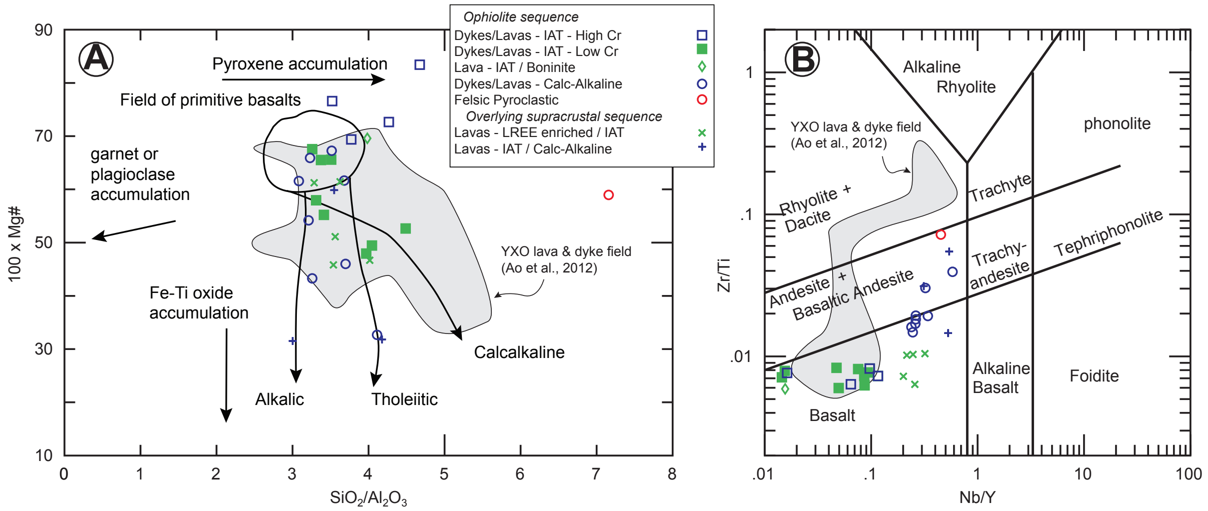

Figure 3.11: Geochemical basaltic rock type classification diagrams: A) Major element classification of basalts from Le Bas; B) Trace element classification of basalts from Pearce (1996).

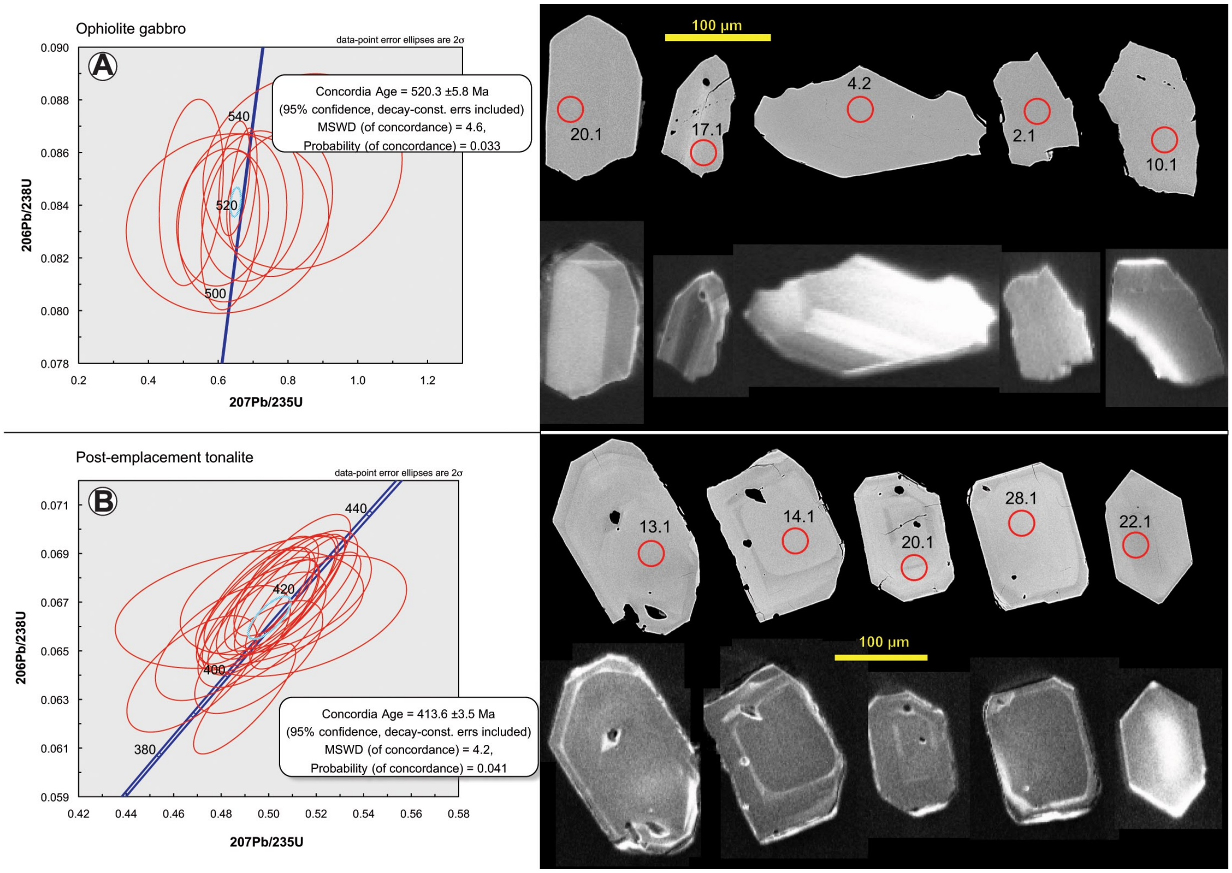

Figure 3.12: Geochronological Concordia plots and zircon images. A) Gabbro from the northwest of the ophiolite body. B) Tonalite body intruded through the overlying supracrustal sequence, in the northeast.

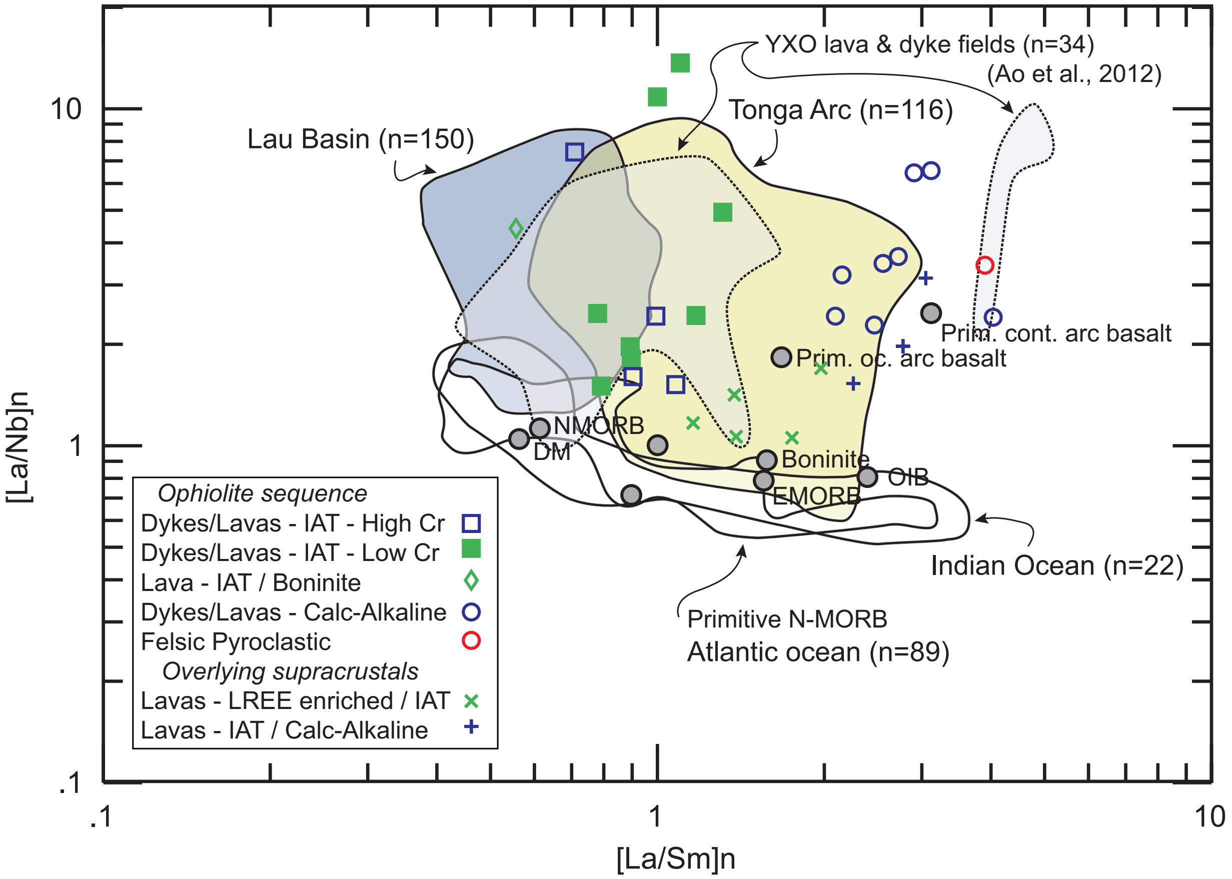

Figure 3.13: Geochemical discrimination plot of La/Nb versus La/Sm normalized to the primitive mantle values of Sun and McDonough (1989). The data show a similarity in differentiation to primitive arcs. Modified from Guilmette et al. (2009).

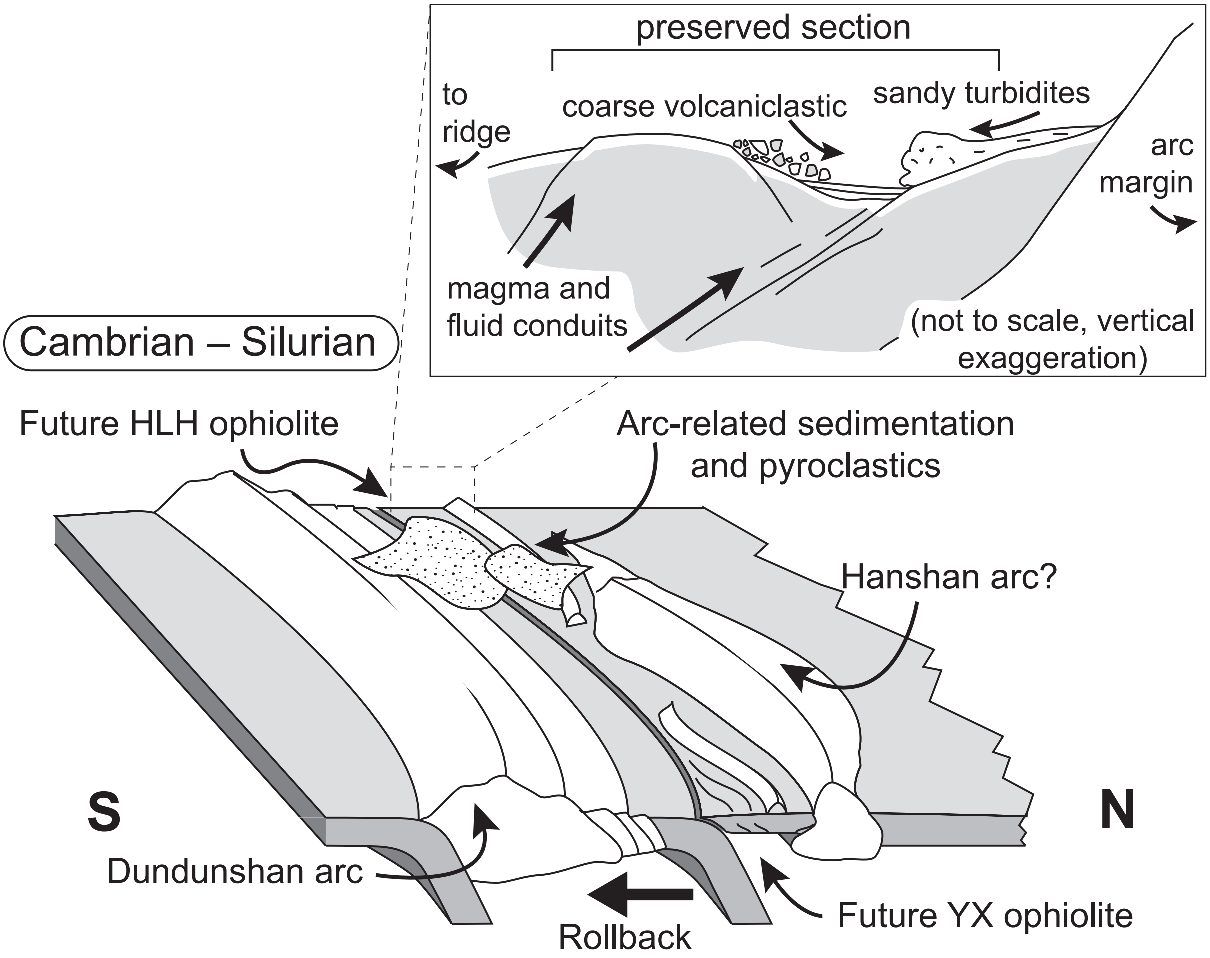

Figure 3.14: Tectonic model of the Hongliuhe suture zone. The time of amalgamation is constrained by the undeformed granitoid age of ca. 414 Ma.

Chapter 4

Kinematics and geochronology of transpressive shear zones in the central Beishan orogenic collage, Northwest China: Progressive strain localization during middle Paleozoic arc-arc collision

4.1 Introduction

The southern region of the Central Asian Orogenic Belt (CAOB, Fig. 4.1 inset) includes the Beishan orogenic collage and its western neighbor, the Tianshan arc. This region accumulated and preserved continental and juvenile crust during the Paleozoic. This occurred in two main fashions: through lateral accretion of arc terranes and oceanic units (Buckman and Aitchison, 2004; Kröner et al., 2007; Xiao et al., 2010), and through late Paleozoic underplating of mantle derived magmas (Pirajno et al., 2002; Dong et al., 2011; Su et al., 2011; Li et al., 2012; Zhu et al., 2012). However, the region transitioned to convergent collisional tectonics in the late Paleozoic to Early Mesozoic (Charvet et al., 2007; Xiao et al., 2010, 2013; Xiao and Santosh, 2014). Study of early Paleozoic collision and accretion events is complicated by the late convergent overprint, and by the potential of large magnitude translation, which at most plate and terrane boundaries remains unconstrained. Most studies to date have focused on either the late strike-slip overprinting deformation (Shu et al., 1999; Laurent-Charvet et al., 2003; Wang et al., 2010) or the folding and thrusting associated with terminal closure (Zheng et al., 1996; Yang et al., 2007; Tian et al., 2013; Zhang and Cunningham, 2012; Cleven et al., 2015). The Beishan orogenic collage exhibits evidence of at least one widespread early Paleozoic tectonic event responsible for developing penetrative distributed strain and for initiating enduring terrane-bounding strike-slip shear zones. Our study provides reliable temporal constraints and structural characterization of this early Paleozoic event.

Preserved crustal material in accretionary orogenic belts is likely to exhibit penetrative transpressive deformation related to oblique convergence during subduction, collision or accretion (Kusky et al., 1997; Wang et al., 2009; Jiang et al., 1998; Jiang, 2007). The strain distribution within the affected region and the kinematics of structures can be used to quantify and constrain the tectonic history (Choulet et al., 2012; Liu et al., 2015). Our analysis integrates evidence of both strike-slip and compressive components of deformation, focusing on transpressional shear zone development within a heterogeneous accretionary complex (Lin et al., 1998; Czeck and Hudleston, 2003, 2004; Jiang, 2007; Kuiper et al., 2011; Jiang, 2012, 2014). The temporal progression of strain localization within a series of shear zones across the accretionary complex is evaluated from zircon U-Pb dates of late-syn-tectonic dykes (Zhang et al., 2009). From their progressive cessation, we interpret a protracted Silurian-Middle Devonian arc-arc collision or arc accretion event.

4.2 Geologic background: framework of the Beishan

The CAOB (Fig. 4.1 inset) has been described as the largest Phanerozoic accretionary orogen on Earth (Windley et al., 2007; Xiao et al., 2009a,b). Accretion of island arcs and oceanic units against the Siberian craton margin, and possibly the Tarim craton margin, preserved both juvenile and reworked Precambrian crust (Kröner et al., 2007; Xiao et al., 2009b; Kröner et al., 2014). Arc building episodes range in age from the Neoproterozoic (Xiao et al., 2009b; Rojas-Agramonte et al., 2011; Song et al., 2013c) through to late Paleozoic (Jian et al., 2010; Mao et al., 2012a; Guo et al., 2014), with orogenic ages from middle Paleozoic to early Cenozoic (Coleman, 1989; Wang et al., 2006; Su et al., 2011; Li et al., 2012; Zhu et al., 2012). The Beishan orogenic collage is the southernmost subset of the CAOB. It is situated east of the suture in the Carboniferous–Permian South Tianshan accretionary complex (Allen et al., 1992; Shu et al., 1999; Xiao et al., 2013) and west of the Triassic Solonker suture (Xiao et al., 2003; Lehmann et al., 2010; Eizenhöfer et al., 2014), though where these sutures intersect the Beishan is poorly defined.

The Beishan provides an excellent research proxy, as a subset, for study of the evolution of the CAOB. Zircon inheritance ages from both the Beishan and the Tianshan imply that their Paleozoic arcs built through an array of pericratonic fragments, likely related to the Tarim craton (Rojas-Agramonte et al., 2011; Ma et al., 2012; Song et al., 2013c; Shi et al., 2014; Wang et al., 2014b; Chapter 2). These terranes amalgamated in stages throughout the Paleozoic until the terminal closure in the Early to Middle Permian (Xiao et al., 2010). Two Paleozoic arc-related terranes containing remnants of their Precambrian metamorphic basement were preserved in the Beishan. The northern Hanshan terrane (Fig. 4.1) comprises Ordovician to Silurian magmatic rocks built through a sliver of ca. 1400 Ma to 950 Ma calc-alkaline orthogneisses and Late Neoproterozoic metasedimentary rocks (Wang et al., 2010; Xiao et al., 2010; He et al., 2012; Wang et al., 2014b). The southern Dundunshan terrane (Fig. 4.1) contains a poorly preserved Precambrian basement intruded by an Ordovician through Devonian migrating arc (Mao et al., 2012a; Guo et al., 2014). Its magmatism transitioned to late Paleozoic collision-related and intraplate granitoid suites (Zhao et al., 2007; Li et al., 2009a, 2011). Its southern margin contains high-grade gneissic rocks that include an eclogite occurrence (Qu et al., 2011). South of the Dundunshan terrane lies the Dunhuang block, and modern sediments largely obscure their poorly defined suture (estimated to lie within the Shibanshan terrane, Fig. 4.1).

The Mazongshan terrane, an accretionary complex situated between the Hanshan and Dundunshan terranes, is the focus of this study (Fig. 4.1). It is a composite of partially juvenile island arc plutonic and volcanic rocks (Song et al., 2013b), built through variably metamorphosed Precambrian to Paleozoic marginal sedimentary rocks (Song et al., 2013c). It also contains accreted oceanic volcano-sedimentary successions and suprasubduction ophiolites (Ao et al., 2012; Song et al., 2013b; Tian et al., 2014; Chapter 3). The Hongyanjing basin sedimentary rocks (Fig. 4.1), a Permian syn-orogenic fold-and-thrust belt, unconformably cover much of the western half of the Mazongshan terrane (Cunningham, 2013; Tian et al., 2013; Cleven et al., 2015).

4.3 Tectonic setting: sutures, accretion and collision in the Beishan

Structures created during an early collision or accretion event in the Beishan were largely localized into the central, heterogeneous, and relatively less competent Mazongshan accretionary complex terrane. The Mazongshan terrane is bounded by two long, E-W to NE-SW trending strike-slip shear zones: the Xingxingxia shear zone to the north and the Hongliuhe shear zone to the south (Figs. 4.1 and 4.2). The region around the Hongliuhe shear zone is the closest representation of a suture zone between the Hanshan and Dundunshan terranes. The earliest Paleozoic age records in the Beishan are early Cambrian gabbroic U-Pb zircon ages from both the Hongliuhe and the Yueyashan-Xichangjing ophiolites (Ao et al., 2012; Chapter 3) (Fig. 4.1). In the Hongliuhe region a ca. 414 Ma undeformed granitoid post-dates tilting of supracrustal cover of the ophiolite (Chapter 3). Overlying the incoherent Yueyashan-Xichangjing ophiolites are coherent fossiliferous Late Ordovician–early Silurian sedimentary rocks (Ao et al., 2012). These constrain ophiolite emplacement to the early Paleozoic. The Hongliuhe ophiolite forms a lensoidal tectonic slice, bounded at its north by the Hongliushu shear zone (Fig. 4.2). Further north of the Hongliushu shear zone, tectonic slices of accreted Devonian oceanic volcanic and ophiolitic sections are preserved and unconformably covered by Hongyanjing basin Permian sedimentary rocks (extent indicated in Fig. 4.1). Below the unconformity, U-Pb zircon dating in the Tianhu volcano-sedimentary successions (Fig. 4.1) has yielded an age from basalt of 416.6 ± 15.0 Ma, and a crystal-lithic tuff age of ca. 409.0 ± 2.9 Ma (Chapter 2). The Huoshishan-Niujuanzi ophiolites (Fig. 4.1) have reported gabbro zircon ages ranging from ca. 435 Ma (Niujuanzi) to 411 Ma (Huoshishan) (Tian et al., 2014). These provide a maximum age for the accretion of units, constraining their accretion to later. The Beishan complex, east of the map area (north of the Niujuanzi region), contains paragneissic and orthogneissic rocks with Ordovician and Silurian metamorphic zircon and is considered an arc-related subduction complex (Song et al., 2013a,b). Detrital zircon analyses of late Paleozoic Hongyanjing basin sedimentary rocks indicate that the source, likely a combination of Hanshan and Mazongshan terrane rocks, has a 40-50 m.y. hiatus from magmatism starting at ca. 385 Ma, after prolonged Ordovician through Silurian magmatism (Chapter 2). This evidence supports interpretation that an accretion or collision event halted subduction and magma production in approximately the Middle Devonian.

The southern margin of the Dundunshan contains evidence for an early Paleozoic accretion or collision event. An eclogite occurrence within a high-grade gneiss complex yielded a late Silurian age of retrograde metamorphism (Qu et al., 2011). Mafic granulites near the suture with the Dunhuang block yielded a late Silurian peak or late-stage metamorphic zircon age, from a subduction environment, and Early Devonian retrograde amphibolite ages (He et al., 2014a). Detrital zircon analyses of Permo-Triassic Shuangbaotang formation sandstones indicate that magmatic rocks from their source, the Dundunshan terrane, experienced a 50 m.y. hiatus, later than the northern suture, starting at 355 Ma (Chapter 2). These studies imply that the tectonic event affecting the Mazongshan accretionary complex was pervasive, and likely involved both suture zones in the Beishan.

4.4 Structure of the western Mazongshan terrane

The Hongliuhe–Xingxingxia region spanning the western Mazongshan terrane was mapped for lithology and structure, with greatest detail in shear zones (Fig. 4.2, location indicated in Fig. 4.1). Five main shear zones were recognized; some apparently evolved coevally as subsidiary shear zones, networks, or splays. The shear zones, from south to north, are as follows (Fig. 4.2): the (1) Hongliuhe dextral/sinistral shear zone, (2) Yushishan sinistral shear zone array, (3) Hongliushu dextral shear zone, (4) Tianhu dextral shear zone, and (5) Xingxingxia dextral shear zone. Dextral shear zones dominantly strike east-west, with subordinate northeast-southwest orientated jogs. Sinistral shear zones dominantly strike west-northwest to east-southeast with subordinate northwest-southeast oriented jogs. Less concentrated penetrative deformation is hosted in 20-40 km wide tracts around shear zones, and map patterns exhibit large-scale dextral or sinistral sigmoidal structures within individual tectonic slices (Fig. 4.3).

The lithologies in the Mazongshan terrane are a mix of oceanic volcanic, sedimentary, and metasedimentary units, though the region is punctuated by pre- and syn-tectonic plutons. These commonly abut shear zones and provided rheological contrast. Specific plutons along shear zones were analyzed across their strain gradient for kinematic and textural features, and foliation and lineation orientations. Permian sedimentary rocks in the region exhibit less pervasive ductile deformation than the earlier metamorphic rocks and therefore post-date older deformation. There is evidence for later stage brittle faulting across most of the shear zones described below.

Each of the five shear zones exhibits a unique combination of kinematics, ductile stretching orientations and strain distributions. These characteristics will be examined in the five shear zones, referring to their respective lineation and foliation data in equal area stereonet plots (Fig. 4.3). A brief interpretation of their regional significance follows the description of each shear zone below.

4.4.1 The Hongliuhe shear zone

The Hongliuhe shear zone has a consistently straight, very slightly arcuate surface trace. The foliation near the center of the shear zone consistently strikes west-northwest and has a vertical dip (Fig. 4.3 F). In the shear zone margins the foliation varies between C- and S-orientations (Fig. 4.3 E). Rocks south of the shear zone exhibit higher strain than to the north. Within the map region, mylonitized units in the shear zone include a granitic pluton (Figs. 4.4 A–D), folded metasedimentary rocks, pillow basalt and massive flows intercalated with limestone. The shear zone has up to a 400 m half-width.

In the Hongliuhe shear zone S-C fabrics are found throughout the strain gradient (Figs. 4.4 A and 4.4 C), and C' fabrics are found towards the shear zone margin (Fig. 4.4 A). Ductile striation, mineral orientation and stretching lineations of quartz and biotite (Fig. 4.4 B) form a tight cluster that plunges approximately 10° to the west (Fig. 4.3 F). The lineation orientation is consistent across the entire strain gradient within the one mapped plutonic body. In other lithologies along strike in the west, lineation measurements are spread along the northwestern hemisphere of the S-foliation (Fig. 4.3 E). Tight folds in metasedimentary units along the shear zone have a fold axis, calculated as the pole to the profile plane, plunging approximately 35° northwest (Fig. 4.3 E). Hinge measurements vary from subvertical to parallel to the calculated fold axis.

A transect across the granitic pluton on the south side of the Hongliuhe shear zone reveals a decrease in grain size of dynamically recrystallized material towards the center, and an increase in porphyroclast preservation and biotite content towards the margin.

The deformed granitic pluton is mylonitized along its northern boundary with subgrain-rotation recrystallization of quartz and bulging recrystallization of plagioclase (Fig. 4.4 D). Feldspar porphyroclasts are asymmetrically mantled with a sinistral sense, and show deformation twinning. The shear zone has consistent sinistral kinematic indicators (Passchier and Simpson, 1986; Trouw et al., 2009) throughout its strain gradient, except for rare dextral indicators in the margins. A dextrally folded dyke in the extreme margin of the shear zone (Fig. 4.5 A), and the granitic body hosting it, were sampled for geochronology (samples 11NC49B and 11NC50, respectively). Dextral C' fabrics in less competent limestone lithologies have been observed as well (Fig. 4.5 B), yet no direct overprinting relationship has been observed between sinistral and dextral kinematic indicators.

Hongliuhe shear zone regional tectonic interpretation

The width, linearity and terrane-scale length of the Hongliuhe shear zone imply that large-scale plate motions with a high magnitude of translation controlled the dynamics of the boundary it represents. The consistently sub-horizontal lineations in the analyzed pluton indicate dominantly strike-slip motion (Fig. 4.3 F). This lineation pattern is found in outcrops that consistently exhibit sinistral kinematics (Figs. 4.4 A, 4.4 C and 4.4 D). The lineations in more heterogeneous along-strike units (Fig. 4.3 E) indicate a minor vertical stretching component, within the dominantly strike-slip regime. The folding at the shear zone margins appears to be related to both compression and shearing, with fold hinges varying from the calculated axis to subvertical (Fig. 4.3 E). Dextral deformation at the margins may be earlier, preserved after a narrower zone of late sinistral deformation overprinted an existing shear zone.

4.4.2 The Yushishan shear zone arrray

The Yushishan shear zone array is a subsidiary or splay of the Hongliuhe shear zone with which it intersects at its southeastern tip. It comprises several thin shear zones varying from 5 m to 40 m wide, anastamosing through and across weak supracrustal strata within the Hongliuhe ophiolite cover succession. The ophiolite cover is up to 10 km thick, including interbedded sandstone, limestone, tuff, and basalt. The interfaces between basalt and limestone or basalt and sandstone are common sites for strain localization. Ultra-mylonitized limestones show little structural information due to their rheologic weakness and highly recrystallized nature, though occasional sandy material provides kinematic information.

Kinematic indicators are most developed on horizontal surfaces. Mantled porphyroclastic quartz aggregate material and C-S fabrics are consistently sinistral (Fig. 4.6 A). There is widespread chaotic outcrop scale folding, which varies from tight folds to isoclinal rootless folds indicating lateral sinistral motion (Fig. 4.6 B). Mafic volcanic units are mylonitized near the center of the shear zones and show sinistral kinematics in porphyroclastic plagioclase phenocrysts that are asymmetrically mantled by chlorite and recrystallized carbonate material. They have also been observed with coevally developed conjugate C' fabrics (Fig. 4.6 C).

The average foliation dips steeply south, and strikes between east-west (C-orientation) and northwest-southeast (S-orientation), and rarely northeast-southwest (C'-orientation) (Figs. 4.3 G and 4.7). Lineations are spread within the C-foliation, dominantly from near vertical to the eastern hemisphere (Fig. 4.3 G). No lineation plunges less than 20°. There is a minor spatial correlation to outcrops with similar lineation orientations. Grouped spatially, in clusters from the west and east in the map area (Figs. 4.7 C and D), lineation data occupy opposing hemispheres, highlighting the jigsaw nature of stretching and faulting within and between units.

Yushishan shear zone array regional tectonic interpretation

The Yushishan shear zone array accommodated strain internal to the supracrustal sequence in the Hongliuhe ophiolite succession. The short strike-length and highly sinuous traces indicate it is a low-strain shear zone network. We interpret the Yushishan shear zone array as a system of transpressive shear zones with only a weak strike-slip component (Tikoff and Greene, 1997; Angen et al., 2014). The concentration of steep lineations with a minor spread around the foliation plane, in narrow shear zones with evidence of lateral motion, is consistent with a low ratio of simple shear to pure shear components of strain (Jiang and Williams, 1998; Lin et al., 1998; Lin and Jiang, 2001; Czeck and Hudleston, 2003; Kuiper and Jiang, 2010). The lack of near-horizontal lineations reinforces the interpretation that a greater degree of strain was accumulated through vertical stretching than shearing (Jiang, 2014). This pattern is also exhibited in the Tianhu shear zone (see below). East-west, orogen parallel stretching at the formation scale is interpreted from competent siliceous limestone layers that are necked and boudinaged (Fig. 4.7), and from microstructural conjugate C' structures (Fig. 4.6 C). If the shear zone developed contemporaneously with sinistral deformation in the Hongliuhe shear zone, they may together be considered distributed sinistral transpression; the Yushishan shear zone array resembles a sigmoidal shaped flower structure alongside the Hongliuhe shear zone.

4.4.3 The Hongliushu shear zone

Mostly obscured from study by modern river sediments, the Hongliushu shear zone has an approximate 300-600 m half-width, and strikes E-W to NE-SW. Proto-mylonitic foliations in Permian Hongliuhe Formation sedimentary rocks indicate late reactivation, but the few exposures of older mylonitic rocks are too weathered to sample. Deformation within supracrustal successions of the Hongliuhe ophiolite include asymmetrically mantled sheared conglomerate clasts that indicate dextral kinematics (Fig. 4.6 D). Dextral C' fabrics are visible in basaltic units within the northern (upper) sections of the ophiolite. Shear folding of sedimentary strata is consistent with a dextral kinematic sense (NW corner of Fig. 4.7). A folded black chert unit overlying the ophiolite exhibits subvertical fold hinge orientations spread slightly along a NW trending plane, and bedding measurements spread around the primitive circle (Fig. 4.7 A). Sandstone and shale lithologies that structurally overlie the chert contain outcrop-scale shear folds, including decimeter scale sheath folds. Two clusters of fold hinges are apparent within this unit (Fig. 4.7 B), one orientation plunging moderately east, another plunging moderately west.

Hongliushu shear zone regional tectonic interpretation

The Hongliushu shear zone is interpreted to mark the northern boundary between the Hongliuhe ophiolite package and Mazongshan metasedimentary rocks, at depth (below the overlying Permian sediments). Evidence indicates dextral shear zone kinematics (Figs. 4.6 D, 4.7 A and 4.7 B). Its trace converges with the Hongliuhe shear zone 40 km west. Similarly oriented faulting 150 km along strike to the east continues through the Niujuanzi region and again converges with the Hongliuhe shear zone (Fig. 4.1). This implies that the Hongliushu shear zone and the Hongliuhe shear zones bound a tectonic slice including the Hongliuhe ophiolite, which is possibly exotic relative to the remainder of the Mazongshan terrane.

4.4.4 The Tianhu shear zone

The Tianhu shear zone separates Mazongshan metasedimentary rocks from the succession of Devonian oceanic units with overlying Permian Hongliuhe Formation sediments.

It has multiple branches and is slightly more sinuous, with wider jogs, than the nearby Xingxingxia shear zone. It has a half-width of approximately 125 m. It exhibits mylonitic textures in granite (Figs. 4.8 A and 4.8 B), tonalite (Fig. 4.8 C), quartzite, marble, orthogneiss, and garnet-quartz-mica schist. The average C-foliation generally dips subvertical and strikes NE-SW (Fig. 4.3 D), and is parallel to the Xingxingxia shear zone S-foliation (Fig. 4.3 C). Mineral alignment lineations spread around the C-foliation plane, except for a small cluster of C'-associated lineations that plunge shallowly east (Fig. 4.3 D). No lineations plunge less than 20°. No spatial correlations or systematic variations across the strain gradient exist between lineation orientations.

The Tianhu shear zone microstructures include mylonitic textures with subgrain rotation recrystallization of quartz (Figs. 4.9 A and 4.9 B), bulging recrystallization of plagioclase (Fig. 4.9 B), and C' fabrics in biotite and chlorite domains. Mantled porphyroclasts can be fairly symmetric in all strain orientations, despite strong lineations in hosting rocks. Rare samples indicate dextral kinematics with grain preferred-orientations (Fig. 4.9 A), asymmetrically mantled feldspar porphyroclasts, C-S and C' fabrics, and bookshelf rotation of fractured porphyroclasts (Figs. 4.9 B). Transgranular fracturing of porphyroclasts is common, consistent with extension parallel to the lineation (Fig. 4.9 B). Tonalite dykes exhibit necking and boudinage within the shear zone, deformed less than the mylonitized host granite (Figs. 4.8 D–F). Some indicate dextral kinematics (Figs. 4.8 E). These dykes and the host pluton were sampled for geochronology (11NC06B, 11NC27, and 11NC28 respectively). Isolated sinistral kinematic indicators were found in a late (estimated Permian) pluton along the shear zone. In this pluton thin mylonitic bands that are less than 10 m wide contain C-S fabrics and asymmetrically mantled feldspar porphyroclasts (Fig. 4.9 C). Stretched mafic xenoliths in the pluton, outside the mylonitic bands, indicate minor flattening throughout the pluton (Fig. 4.8 C).

Tianhu shear zone regional tectonic interpretation

The Tianhu shear zone delineates a boundary separating different accreted units. Further east than the Niujuanzi region the Tianhu shear zone trace converges with the Hongliuhe shear zone (Fig. 4.1). This implies the Tianhu shear zone and Hongliushu shear zone border a tectonic slice that includes Devonian oceanic volcano-sedimentary successions in the Hongliuhe-Tianhu region, and the Niujuanzi ophiolites farther east (Tian et al., 2014). We interpret that the Tianhu shear zone kinematics are dominantly dextral, with only local late sinistral overprints. The Tianhu shear zone exhibits a low-strain transpressive shear zone lineation pattern, interpreted similarly to the Yushishan shear zone array (see section 4.4.2) except in a dextral kinematic sense. The Tianhu shear zone also lacks near-horizontal lineations, consistent with a greater degree of strain having been accumulated through vertical stretching than shearing.

4.4.5 The Xingxingxia shear zone

The Xingxingxia shear zone has the most intense strain along its E-W section in the north of the map area, where it has a 500-700 m half-width. Mylonitic foliations (Fig. 4.10 A) dip slightly north consistently along its length. The most prominent orientation of the C-foliation is E-W, and jogs and S-foliations strike ENE to NE (Figs. 4.3 A–C). Strong stretching lineations (Fig. 4.10 B) can be found in mylonitized tonalite, garnet-staurolite-mica-quartz schist, quartzite, phyllonite, and carbonaceous-siliceous marble lithologies along the shear zone. A detailed transect of a deformed pluton along the shear zone indicates that lineations cluster within the western hemisphere of a C-surface foliation (Fig. 4.3 B). From the shear zone center northward there is a general increase in the maximum plunge of lineations. They transition from sub-horizontal to sub-vertical, though there are narrow discrete zones of localized slip within the margins with shallow lineation orientations. Lineations in NE oriented sections are spread throughout C-foliation planes. Outcrop-scale isoclinal shear folding is common in isolated zones, often in the margins of the shear zone (Fig. 4.10 C). Fold axis measurements plunge shallowly to the east, and lie within the C-foliation (Fig. 4.3 B). Necked and boudinaged dykes were observed, two of which were sampled for geochronology (11NC39G, Fig. 4.10 D; 11NC45, Fig. 4.10 E). In many locations considerable networks of fractures and veins are present implying a late brittle faulting overprint.

Microstructures of the deformed pluton indicate there is an increased degree of dynamic recrystallization and concentration of oxide material correlating to proximity to the shear zone center. Similarly, towards the shear zone center porphyroclastic material is reduced in size and preserved less (Figs. 4.11 A–C, distance from shear zone center in z-direction indicated). Bookshelf structures in feldspar porphyroclasts, asymmetrically mantled rounded porphyroclasts, S-C and C' fabrics indicate dextral kinematics. Kinematic indicators are most developed on horizontal surfaces. Dextral kinematic indicators are also found in the NE-trending eastern jog (Fig. 4.11 D). The asymmetrically mantled feldspar porphyroclasts in mylonites of this orientation commonly exhibit transgranular fracturing and disaggregation, comparable to similarly oriented mylonites in the Tianhu shear zone.

Xingxingxia shear zone regional tectonic interpretation

We consider the Xingxingxia shear zone to be a major terrane-bounding shear zone comparable, but possibly subordinate, to the Hongliuhe shear zone. Its characteristics and location are consistent with it being a result of slip-partitioning localized at the boundary between the forearc region (Mazongshan terrane) and a backstop of the arc (Hanshan terrane) along an oblique-convergent margin. Along its dominant E-W orientation, its lineation pattern is interpreted in a similar way to the Yushishan shear zone array (section 4.4.2), yet as a transpressive shear zone with a strong strike-slip component (Tikoff and Greene, 1997; Angen et al., 2014). The concentration of shallow lineations with a minor spread to vertical around the foliation plane, in a wide shear zone with evidence of lateral motion, is consistent with a moderate to high ratio of simple shear to pure shear components of strain (Jiang and Williams, 1998; Lin et al., 1998; Lin and Jiang, 2001; Czeck and Hudleston, 2003; Kuiper and Jiang, 2010). The small degree of near-vertical lineations reinforces the interpretation that a small degree of strain was accumulated through vertical stretching while shearing (Jiang, 2014).

4.5 U-Pb zircon geochronology

The U-Pb zircon geochronology presented here focuses on dating dykes deformed in the above described shear zones. In some cases the dykes intruded strongly mylonitized rocks yet only exhibit weak mylonitic foliations or other low-strain structures such as folding, necking or boudinage. These are interpreted to be late-syn-tectonic dykes. In total, five late-syn-tectonic dykes were sampled, along with two of their hosting plutons. One undeformed dyke was sampled. Zircon grains were separated from crushed and pulverized samples utilizing standard heavy liquid and magnetic separation techniques. Grains were subsequently handpicked for favorable characteristics, mounted in an epoxy puck and polished to expose their cores.

4.5.1 Analytical techniques

Mounted zircon were imaged with cathodoluminescence (CL) and electron backscatter (BSE) scanning electron microscopy (SEM), using a JEOL JSM6610-Lv SEM at the University of Toronto Department of Earth Sciences. U-Pb isotopic analysis was completed using the LA-ICPMS apparatus at the Jack Satterly Geochronology Laboratory at the

University of Toronto. The lab utilizes a VG Series 2 Plasmaquad ICPMS in conjunction with a 75 l/s rotary pump on the expansion chamber (S-option) that enhances sensitivity, and a 213 nm New Wave laser ablation system. Zircon material was ablated using a beam diameter of 15, 25 or 30 μm at 5 or 10 Hz and 40% power. Instability in the signal was dampened through the in-line application of He to the carrier gas. Data were collected for the following elements over the indicated analytical intervals: ^{88}Sr (10 ms), ^{206}Pb (30 ms), ^{207}Pb (40 ms), ^{232}Th (10 ms) and ^{238}U (20 ms). Prior to every measurement a rastering ablation pattern was applied to remove any surface debris or polishing impurities. A 10 second period of baseline accumulation was measured and followed by the 35 second target ablation and analysis. A 50 second washout period was used between samples. Custom data reduction software for the procedure, written by D. W. Davis, was used to edit and reduce the data collected. The analyses did not include a measure of ^{204}Pb, so the reduction and calculation process did not correct for common lead. Analyzed spot data were rejected if strontium levels spiked, which was interpreted as sampling of inclusions or possibly alteration along cracks. The zircon standard used throughout the analytical run was DD85-17, from quartz diorite from northern Ontario, Canada, has an established age of 3002 ± 2 Ma (Tomlinson et al., 2003). Analyses of standard grains bracketed sets of three sample measurements. The analytical results are provided in appendix Table C.1. CL images are provided in figure 4.12. Plotted Concordia diagrams (Ludwig, 1998) are provided in figures 4.13 and 4.14 using the program Isoplot (Ludwig, 2003). All Concordia age calculations take into account decay constant error. All zircon analysis and Concordia error amounts are reported using 2σ values, or 95% confidence margins. A histogram compiling all 14 Precambrian grains measured in this study is provided in figure 4.15.

4.5.2 Results of U-Pb zircon analyses

Dates of Hongliuhe shear zone associated rocks

Sample 11NC49B is from a dextrally folded dyke crosscutting the tectonic foliation at the margins of the Hongliuhe shear zone (Fig. 4.5 A). The zircon grains are mostly clear and colorless, with some grains exhibiting a patchy brown coloration, and are mostly subhedral to euhedral. They commonly have high aspect ratios. CL images show clear oscillatory zonation and some sector zonation (Fig. 4.12 A). A single inherited core was measured, yielding a ^{206}Pb/^{238}U date of ca. 1754 Ma. Six highly discordant grain measurements were discarded, and the concordant population of eleven grains yields a Concordia age of 394.4

± 1.9 Ma (Early Devonian; Fig. 4.13 A), interpreted as the age of emplacement of the dyke.

Sample 11NC50 is from the hosting pluton for the above dyke (sample 11NC49B), situated along the south side of the Hongliuhe shear zone. The zircon grains are clear and colorless, mostly euhedral, with common inclusions. They contain more inclusions and inherited cores than 11NC49B, and their aspect ratios are generally smaller. The CL imagery depicts mostly magmatic oscillatory zonation, with some patchy and sector zonation, and occasional inherited cores with metamorphic textured convolute zonation (Fig. 4.12 B). Four Precambrian inherited grains or cores were analyzed, yielding ^{206}Pb/^{238}U dates of ca. 603 Ma, 621 Ma (discordant), 1335 Ma, and 1641 Ma. Of eighteen concordant Paleozoic grains the fourteen youngest provide a Concordia age of 394.9 ± 1.9 Ma (Early Devonian; Fig. 4.13 B). The remaining four together yield a Concordia age of 410.7 ± 3.6 Ma, interpreted as the age of crystallization of the pluton.

Dates of Tianhu shear zone associated rocks

Sample 11NC06B is from a 1 m wide tonalite dyke exhibiting necking deformation (Fig. 4.8 D). The dyke crosscuts the mylonitic foliation in the margins of the Tianhu shear zone, within a megacrystic K-feldspar granite body. The zircon grains are largely subhedral, with small low aspect ratio sub-rounded grains, exhibiting mostly oscillatory zonation with some patchy zonation, as seen in Cl images (Fig. 4.12 C). Three inherited cores and grains were analyzed, yielding (^{206}Pb/^{238}U dates of ca. 560 Ma, 1501 Ma (discordant), and 1746 Ma. Of twenty concordant grains, the youngest eighteen have a Concordia age of 436.5 ± 2.6 Ma (early Silurian; Fig. 4.14 A), interpreted as the age of emplacement of the dyke.

Sample 11NC27 is from a narrow, 15 cm wide tonalite dyke that crosscuts the mylonitic foliation in the shear zone center, within the same pluton as 11NC06B. It exhibits dextral boudinage (Figs. 4.8 E and 4.8 F). The zircon grains are small, ranging from anhedral to euhedral, and many show a slight patchy brown coloration. They mostly have high aspect ratios. Inclusions are moderately common. The CL images depict magmatic oscillatory zonation in the majority of grains, with patchy and uneven zonation in rare inherited cores (Fig. 4.12 D). A single core was measured, yielding a ^{206}Pb/^{238}U date of ca. 1053 Ma. The remaining twenty-one analyses are all concordant, yielding a Concordia age of 437.9 ± 2.4 Ma (early Silurian; Fig. 4.14 B). The eleven youngest zircon grains, while overlapping the error margins of the ten older, form a fairly self-consistent and distinct population with a Concordia age of 432.5 ± 3.2 Ma, is interpreted as the age of emplacement of the dyke.

Sample 11NC28 is from the megacrystic K-feldspar granite pluton deformed along the Tianhu shear zone. It hosts samples 11NC06B and 11NC27 (Figs. 4.8 A and 4.8 B). The zircon are largely clear and colorless, euhedral, with uncommon patchy brown coloration and rare inclusions. The grains are large in comparison to zircon in the dated dykes, and have aspect ratios intermediate between the stubby grains of 11NC06B and tabular grains of 11NC27. Magmatic oscillatory and sector zonation is most common in CL and BSE images (Fig. 4.12 E). No Precambrian inherited grains or cores were observed. Of twenty-three analyzed grains, four are distinctly older and discordant. The nineteen youngest grains form a population with a Concordia age of 446.2 ± 1.9 Ma (Late Ordovician; Fig. 4.14 C), interpreted to be the age of crystallization of the pluton.

Dates of Xingxingxia shear zone associated rocks

Sample 11NC39G is from a late-syn-tectonic tonalite dyke that intruded the Xingxingxia shear zone hangingwall (Fig. 4.10 D). The sample yielded some round and irregularly shaped zircon, but most are high aspect ratio, fractured grains with brown discoloration. Inclusions are common. Their CL and BSE imagery exhibit standard igneous sector and oscillatory growth zonation (Fig. 4.12 F). The zircon analyses are largely discordant, falling along a discordia line connected to the origin, implying lead loss. The three oldest grains are concordant and provide a Concordia age of 398.4 ± 5.6 Ma (Early Devonian; Fig. 4.14 D), interpreted to be the age of emplacement of the dyke.

Sample 11NC45 is from a tonalite dyke that exhibits necking, emplaced within mylonitic rocks of the footwall (Fig. 4.10 E). The zircon grains have assorted shapes and are mostly euhedral to subhedral. Their CL images commonly depict oscillatory zonation, minor patchy zonation, and rare inherited cores (Fig. 4.12 G). Five inherited Precambrian cores or grains were analyzed, and their discordance increases with age. Their ^{206}Pb/^{238}U dates are ca. 605 Ma, 716 Ma, 1039 Ma, 1381 Ma, and 2503 Ma. Of the twenty-four Paleozoic grains, five are highly discordant. The four youngest form a distinct group, with a Concordia age of 383.1 ± 4.6 Ma (Middle Devonian; Fig. 4.14 E). The thirteen next youngest zircon grains also form a distinct population, with a Concordia age of 411.9 ± 3.0 Ma (Early Devonian; Fig. 4.14 E). The age of emplacement of the dyke is interpreted to be ca. 383 Ma. The Early Devonian age population likely represents inheritance from assimilated material or a period of magma residency.

Sample 11NC41 is from an undeformed dyke sampled within the margins of the Xingxingxia shear zone hangingwall. The zircon population is generally subhedral, contains common inclusions, and has many grains with a high aspect ratio. Their CL and BSE images show standard magmatic sector and oscillatory zonation (Fig. 4.12 C). Eighteen concordant zircon analyses provide a Concordia age of 270.8 ± 1.1 Ma (Middle Permian; Fig. 4.14 F), interpreted as the age of emplacement of the dyke.

4.6 Discussion

4.6.1 Deformation chronology and the interpretation of collision

Our interpretation of the timing of arc-arc collision develops from the pattern of ages and the spatial relationships between multiple dated late-syn-tectonic dykes. These dykes conform to situations of dextral kinematics in their respective hosting shear zones. They are from three of the analyzed shear zones. The dates span roughly 55 m.y., bridging the Silurian–Devonian boundary. The Tianhu shear zone late-syn-kinematic dykes have emplacement ages ca. 433 and 437 Ma (Figs. 4.14 A and 4.14 B). The hosting granite is clearly older at ca. 446 Ma (Fig. 4.14 C), yet may have been syn-tectonic; the initiation of deformation in the host granite remains temporally unconstrained. We interpret that deformation in the Tianhu shear zone ceased ca. 435 Ma. The folded dyke sampled at the extreme margins of the sinistral Hongliuhe shear zone was emplaced ca. 394 Ma (Fig. 4.13 A). The dyke age is within error of the hosting granite age, ca. 395 Ma (Fig. 4.13 B). We interpret that dextral deformation in the Hongliuhe shear zone ceased ca. 395 Ma, and that plutonism was syn-tectonic. The late-syn-kinematic dykes from the Xingxingxia shear zone were emplaced ca. 383 Ma in the footwall (Fig. 4.14 E), and ca. 398 Ma in the hangingwall (Fig. 4.14 D). The completely undeformed dyke constrains deformation to earlier than ca. 271 Ma. We interpret that dextral deformation in the Xingxingxia shear zone ceased ca. 385-395 Ma. To summarize, the oldest dyke ages are in the narrower, lower-strain Tianhu shear zone and indicate deformation occurred in the Early Silurian. Younger dyke ages in the larger, higher-strain Xingxingxia and Hongliuhe shear zones indicate cessation of deformation bridging the Early–Middle Devonian. This correlation indicates that tectonism during the Silurian and Devonian was either one protracted event, or two events separated by up to 40 m.y. Deformation ultimately ceased by the Middle Devonian.

The progressive cessation of shearing is consistent with the terminating tectonic event being a collision or staged accretion event. The cessation of minor, central shear zones earlier than the larger bounding shear zones is consistent with a progressive localization of strain with time. This is likely due to a combination of three main contributing factors: 1) uplift, from folding, thrusting or orogeny; 2) cooling, from the termination of magmatism, or implicitly, subduction; 3) waning tectonism or momentum due to subduction termination or interlocking of the terranes involved. Each of these plausible factors is a mechanism that can result from arc or continental collision, or staged accretion, at an active margin.

Implications of dating late-syn-tectonic dykes

Our approach using late-syn-tectonic dykes to constrain timing of the cessation of deformation attempts to allay any controversy by using multiple dykes that correlate amongst each other in a reasonable fashion. Most of the dykes cut strongly mylonitic rocks and their contrast in deformation cannot be explained by competency contrast between them and their host plutons. Our analyses of the shear zones, across the full strain gradients, preclude the possibility of later deformation happening in an isolated zone that includes the dyke. Where possible, we have shown that dykes have deformed in a synthetic fashion to the kinematic sense in question.

4.6.2 Characterizing transpressive deformation at different shear zone scales

Our study purports that pervasive dextral transpressive deformation exists in the western Mazongshan terrane due to a prolonged period of oblique convergence, collision or accretion, and suturing. The evidence we have presented from the map area locally reflects arc-arc collision, yet at the orogen scale the event, or events, may be considered arc accretion against an unknown margin, possibly that of the Dunhuang block. This tectonism was active throughout the Silurian with complete cessation of deformation by the Middle Devonian (Fig. 4.16 A). The collision most likely involved the Hanshan terrane overriding the Dundunshan terrane, with the Mazongshan accretionary complex terrane intervening. The Hongliuhe shear zone represents the plate boundary between the Hanshan and Dundunshan terranes. The Xingxingxia shear zone developed as a main inboard slip-partitioning response localized at the boundary between the Hanshan terrane and likely its accretionary complex, the Mazongshan terrane. The accretionary complex has distributed subordinate shear zone arrays (the Tianhu and Hongliushu) developed at major lithotectonic boundaries separating accreted units.

A low angle of convergence (convergence towards the west northwest in modern coordinates) during Silurian–Devonian oblique subduction and collision would be consistent with the structures reported from this set of shear zones (Fig. 4.16 A). The Xingxingxia, Tianhu, and Hongliushu shear zones are all dextral, and their E-W-striking segments exhibit the most intense deformation. Their NE-SW-trending segments display less common dextral kinematic indicators and contain common fractured and disaggregated porphyroclasts (Figs. 4.9 A–B and 4.11 D). We interpret that under the same convergence regime the NE-SW-striking segments of shear zones had a higher orthogonal convergence component producing more flattening strain and reduced shearing in comparison to the E-W-striking segments of the shear zones. This can be seen as lineations spread throughout the C-foliation plane. The main E-W striking segment of the Xingxingxia shear zone has lineations that are confined to the western hemisphere of its C-foliation and are mostly shallowly plunging. This illustrates the greater accumulation of E-W shear strain over vertical stretching in the transpressive shear zone, and its nature as a slip-partitioning response between the Hanshan arc and the Mazongshan accretionary complex.

Our analysis also indicates a later sinistral deformation event (Fig. 4.16 B). The second event was also transpressional, yet deformation partitioned into strike-slip motion along the Hongliuhe shear zone, and vertical and orogen-parallel stretching (with minor lateral shearing) along the Yushishan shear zone array. Dextral kinematic indicators found at the margins of the Hongliuhe shear zone may imply that sinistral deformation overprinted a wider, existing dextral shear zone. Interbedded sandstones and siltstones overlying the Hongliuhe ophiolite show two distinct groupings of fold hinges, and their relationship supports interpretation that sinistral deformation overprints dextral (Fig. 4.7 B). One cluster, or generation, appears folded and spread away from an eastward plunge, originally parallel to folding in the Xingxingxia shear zone (Fig. 4.3 B). The second generation plunges moderately westward, parallel to the fold axis in the Hongliuhe shear zone folds (Fig. 4.3 E). Late sinistral shearing (ca. 240-250 Ma, ^{39}Ar/^{40}Ar, Wang et al., 2010) has been reported along the NE-striking segment of the Xingxingxia shear zone near the town of Xingxingxia, contrary to the kinematics we report here. The sinistral shearing is focused in young plutonic rocks, similar to the situation we report in a single instance of sinistral kinematics within a young pluton along the Tianhu shear zone (Fig. 4.9 C). We agree with the Wang et al. (2010) interpretation that a regional sinistral deformation event occurred in Permo-Triassic times.

4.6.3 Implications for the tectonic evolution of the Beishan

Our interpretation of progressive cessation of dextral tectonism from the Silurian through to the Middle Devonian in the Mazongshan terrane can be integrated with similar existing interpretations from literature. Detrital geochronology of the Permian Hongliuhe Formation indicates the initiation of a magmatic hiatus ca. 385 Ma (Chapter 2). All accreted units west of the Niujuanzi region are older than our youngest age of deformation, including the Cambrian Hongliuhe ophiolite (Chapter 3), the early Silurian–Early Devonian Huoshishan–Niujuanzi ophiolites (Tian et al., 2014), and the Early Devonian Tianhu volcano-sedimentary sequences (Chapter 2). An undeformed granitoid constraining emplacement of the Hongliuhe ophiolite package (ca. 414 Ma) is consistent with our data. This 410 Ma age range of granitoid is also seen as inherited populations in some of our dated samples across the region (11NC50, Fig. 4.13 B; 11NC45, Fig. 4.14 E), possibly a widespread period of magma production related to slab breakoff or orogeny. Syntectonic granitoids were emplaced in subduction complexes in the eastern Mazongshan terrane during the Silurian (Song et al., 2013a,b). The Mazongshan terrane Silurian–Devonian tectonic event could be akin to tectono-thermal and orogenic events identified at the southern margin of the Dundunshan terrane (Zhao et al., 2007; Li et al., 2009a; Qu et al., 2011; He et al., 2014a), supporting a multi-arc accretion interpretation.

In support of our interpretation that the Hanshan and Mazongshan terranes overrode the Dundunshan terrane, we note a particularity about four of the fourteen Precambrian grains analyzed in this study, aged between 550 and 700 Ma (Fig. 4.15). This age is aberrant, almost completely absent from all regional studies of magmatic and metamorphic rocks, and current detrital zircon studies for both the Mazongshan terrane and southern Dundunshan terrane (Song et al., 2013b,c; Tian et al., 2013, 2014; Chapter 2). The sole zircon U-Pb age in the region from this time period is an age of ca. 673 Ma from a metamorphosed ash layer sampled from the northern passive margin of the Dundunshan terrane (Chapter 2). This supports interpretation that the northern passive margin of the Dundunshan terrane was overridden, and supplied this age of zircon for Devonian orogenic granitoids emplaced in the Hanshan terrane.

4.7 Conclusions

Analysis of shear zones in the central Beishan reveals that their development was controlled by either regional structural trends or by local, within-unit characteristics. Our conclusions are based on analysis of mylonitization along shear zones, lineation patterns, and geochronology of late-syn-kinematic deformed dykes. Our conclusions are that:

1. Late-syn-tectonically deformed dykes in dextral shear zones yield ages in the range of ca. 435 Ma to 385 Ma, with progressively younger ages in wider regional shear zones. This progressive localization of strain with time is possibly due to a combination of uplift (from orogeny), cooling (from cessation of magmatism or subduction), and waning tectonism (from the interlocking of terranes). These mechanisms indicate that oblique convergence and collision, involving the Hanshan terrane overriding the Dundunshan terrane, occurred from the Silurian to Middle Devonian. The Hongliuhe shear zone represents the plate boundary for this suture. The Xingxingxia shear zone formed from localized inboard slip-partitioning in a trench-parallel transpressional deformation zone.

2. The combination of dextral kinematics with coeval vertical stretching in the Xingxingxia and Tianhu shear zones indicates widespread transpression. The ratio of shear strain to vertical stretching components, as interpreted from lineation patterns, correlates to the width of shear zone and its orientation. The main sections of the Xingxingxia shear zone are more than 1 km wide and oriented E-W, correlating to pronounced shear structures and focused stretching orientations. The Tianhu shear zone, and jogs of the Xingxingxia shear zone, are oriented NE-SW and less than 500 m wide. This correlates to less pronounced shear structures and stretching directions that vary throughout the foliation plane.

3. The Hongliuhe shear zone exhibits dominantly sinistral deformation, with rare dextral deformation at its extreme margins. We conclude that late Paleozoic to early Mesozoic sinistral deformation likely overprinted Silurian–Devonian dextral deformation. Sinistral deformation is observed throughout the Hongliuhe ophiolite package, with a concentration of deformation along the Yushishan shear zone array. Its lineations are spread throughout the C-foliation plane indicating a low degree of shear strain. Vertical and orogen parallel E-W stretching, coeval with shearing is interpreted in this case. This implies that sinistral deformation was transpressional as well, though partitioned.

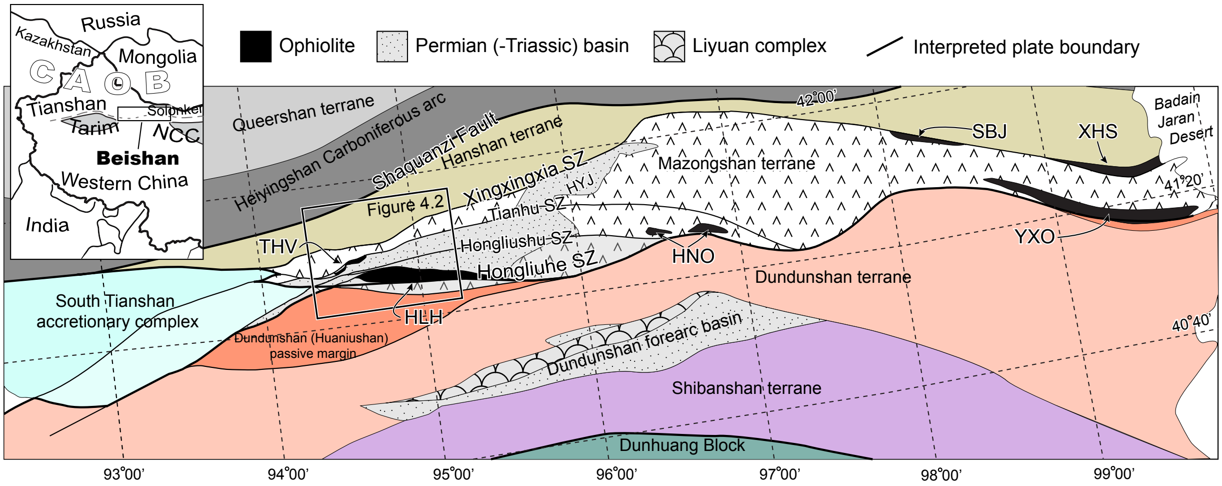

Figure 4.1: Tectonostratigraphic map depicting the major Beishan terranes and the major shear zones related to the Mazongshan terrane. Also shown are ophiolites and late siliciclastic basins. The area of figure 4.2 is indicated. CAOB: Central Asian Orogenic Belt. NCC: North China Craton. HYJ: Hongyanjing basin HLH: Hongliuhe ophiolite. HNO: Huoshishan-Niujuanzi ophiolite. THV: Tianhu volcano-sedimentary successions. YXO: Yueyashan-Xichangjing ophiolite. SBJ: Shibanjing ophiolite. XHS: Xiaohuangshan ophiolite. SZ: shear zone.

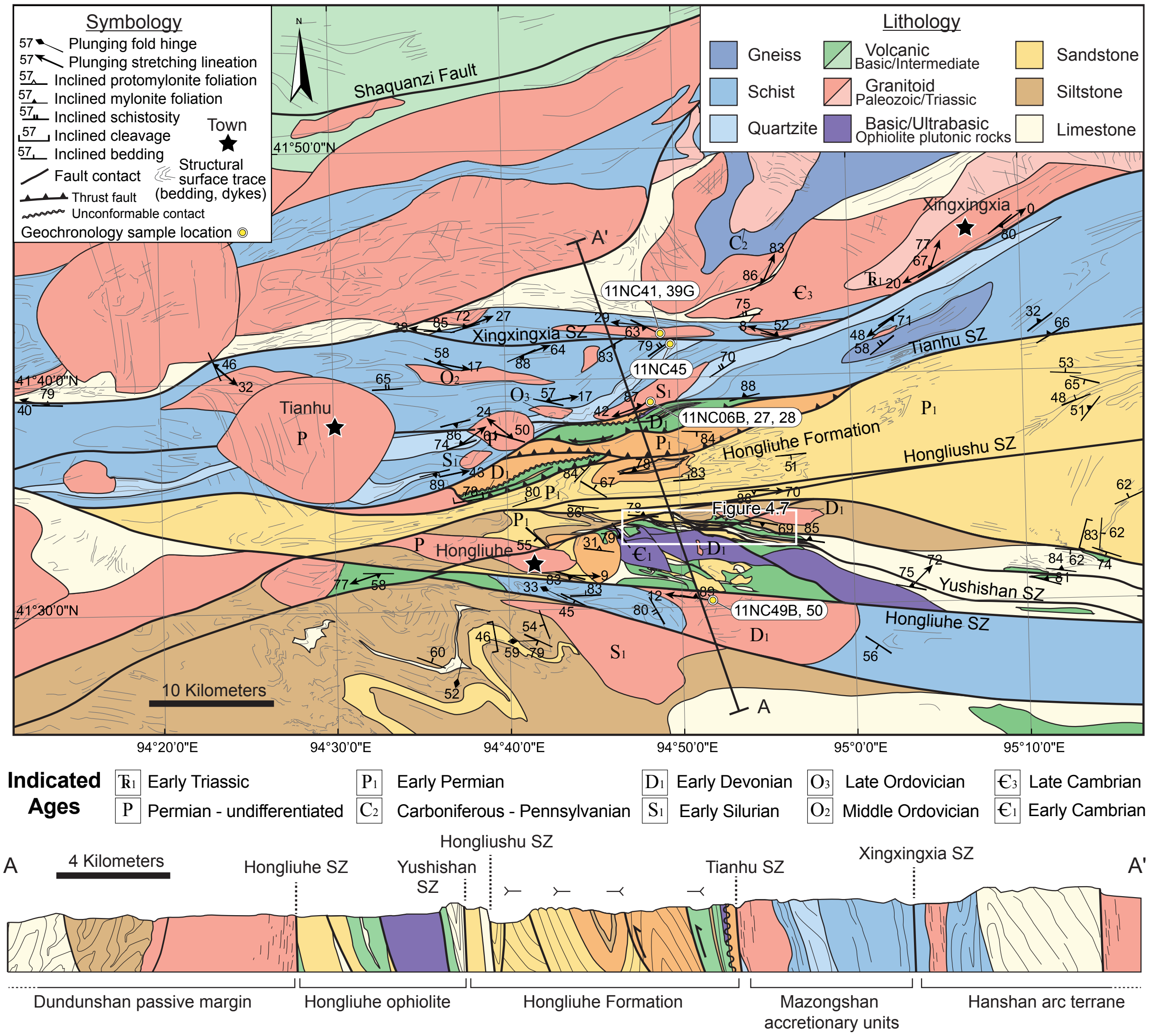

Figure 4.2: Geologic map and cross section of the Hongliuhe to Xingxingxia study area showing lithology and structure. Locations of geochronology samples are shown. The area of figure 4.7 is indicated. SZ: shear zone.

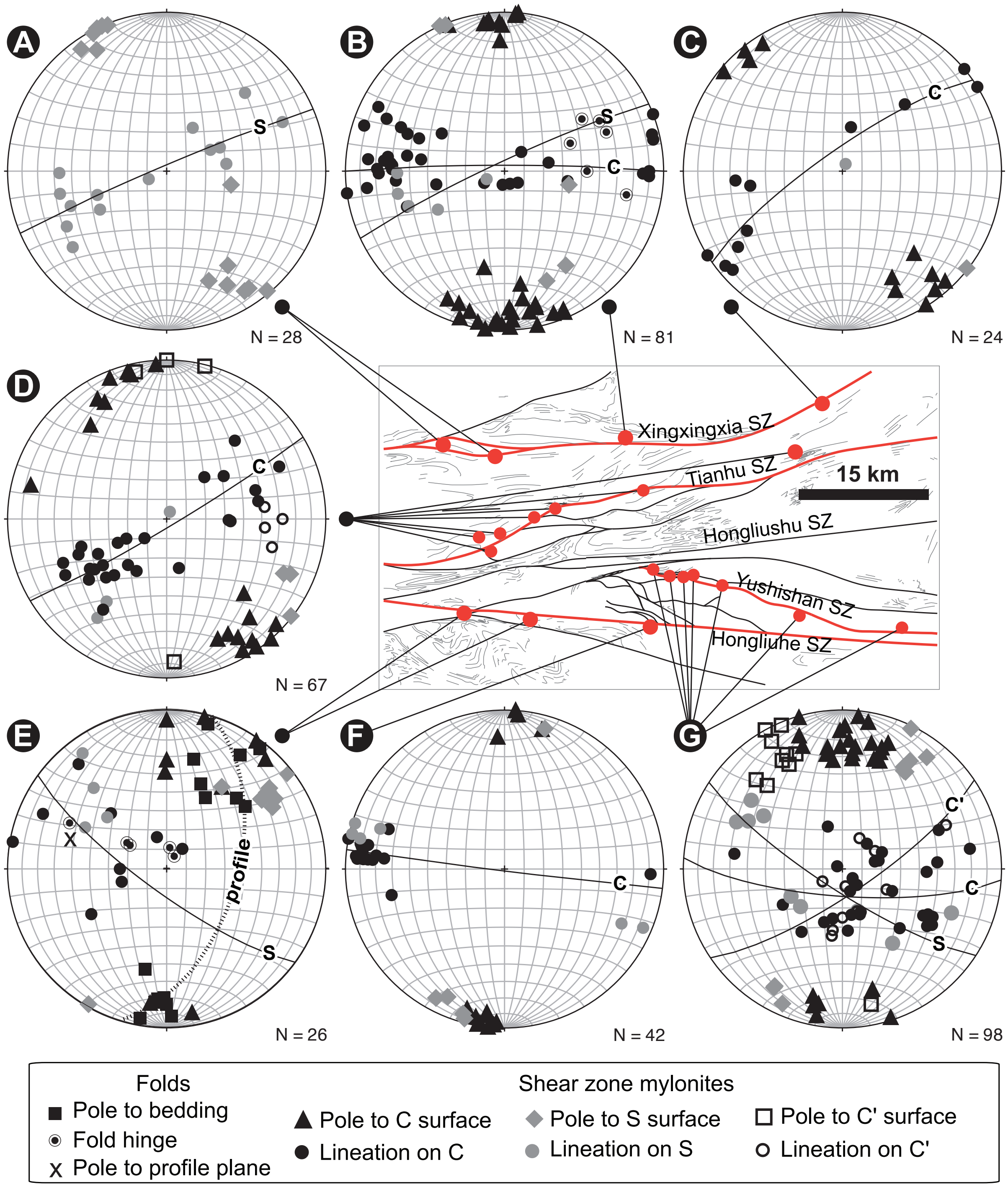

Figure 4.3: Stereonet plots of foliation and lineation data in shear zones with related folding patterns: A) The western, branched, NE-striking segments of the Xingxingxia shear zone. B) The main E-W striking segment of the Xingxingxia … *figure caption continued on next page*

Figure 4.3: *(continued from last page):* . . . shear zone. C) The eastern NE-striking segment of the Xingxingxia shear zone. D) A compilation of all data over the Tianhu shear zone. E) Miscellaneous data from the Hongliuhe shear zone margins. F) Data across a plutonic body within the Hongliuhe shear zone. G) A compilation of all data over the Yushishan shear zone array.

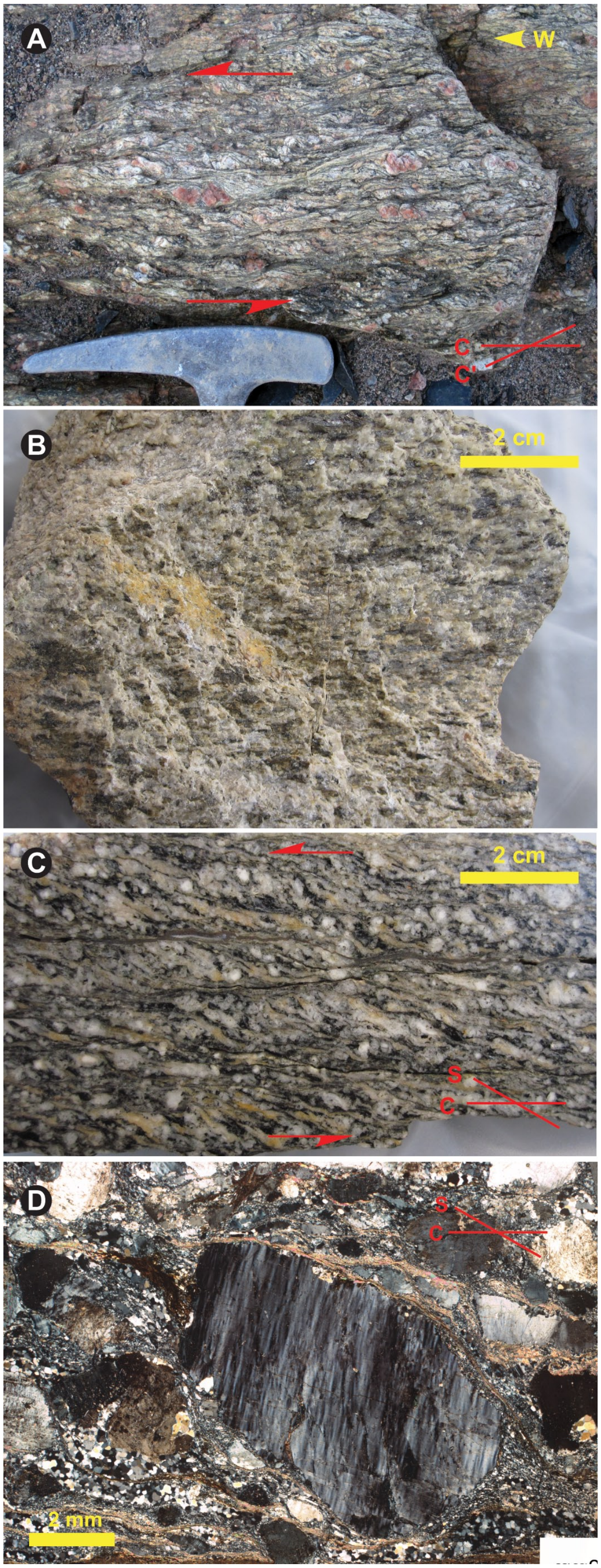

Figure 4.4: Field photographs and a photomicrograph of textures in the Hongliuhe shear zone: A) Mylonite foliation in granitic rock with a C' fabric that indicates sinistral kinematics. B) Subhorizontal ductile striation lineation on a C surface from the granite body depicted in A). C) Polished slab viewing the kinematic plane of a granite sample, from the same granite body as A), showing a strong mylonitic C-S fabric that indicates sinistral kinematics. D) Photomicrograph from a mylonitized granite with a mantled plagioclase porphyroclast indicating sinistral kinematics.

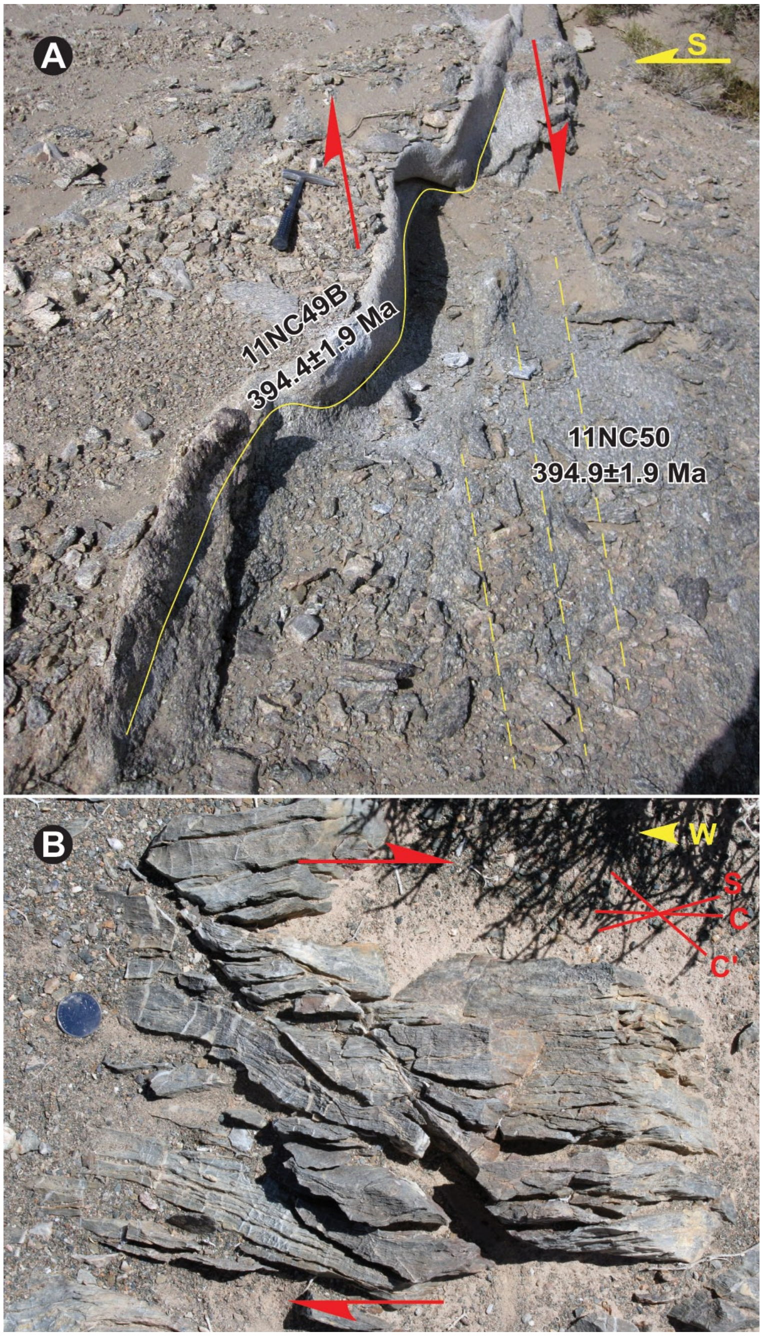

Figure 4.5: Field photographs from the Hongliuhe shear zone: A) A folded dyke intruding the extreme margins of the shear zone, within the granite pluton depicted in Figs. 4.4 A–C. The folding is consistent with dextral kinematics. Both the dyke and pluton were sampled for geochronology (samples 11NC49B and 11NC50, respectively). B) Mylonitic limestone with an S-C' fabric that indicates dextral kinematics, from within volcano-sedimentary units in the marginal domain.

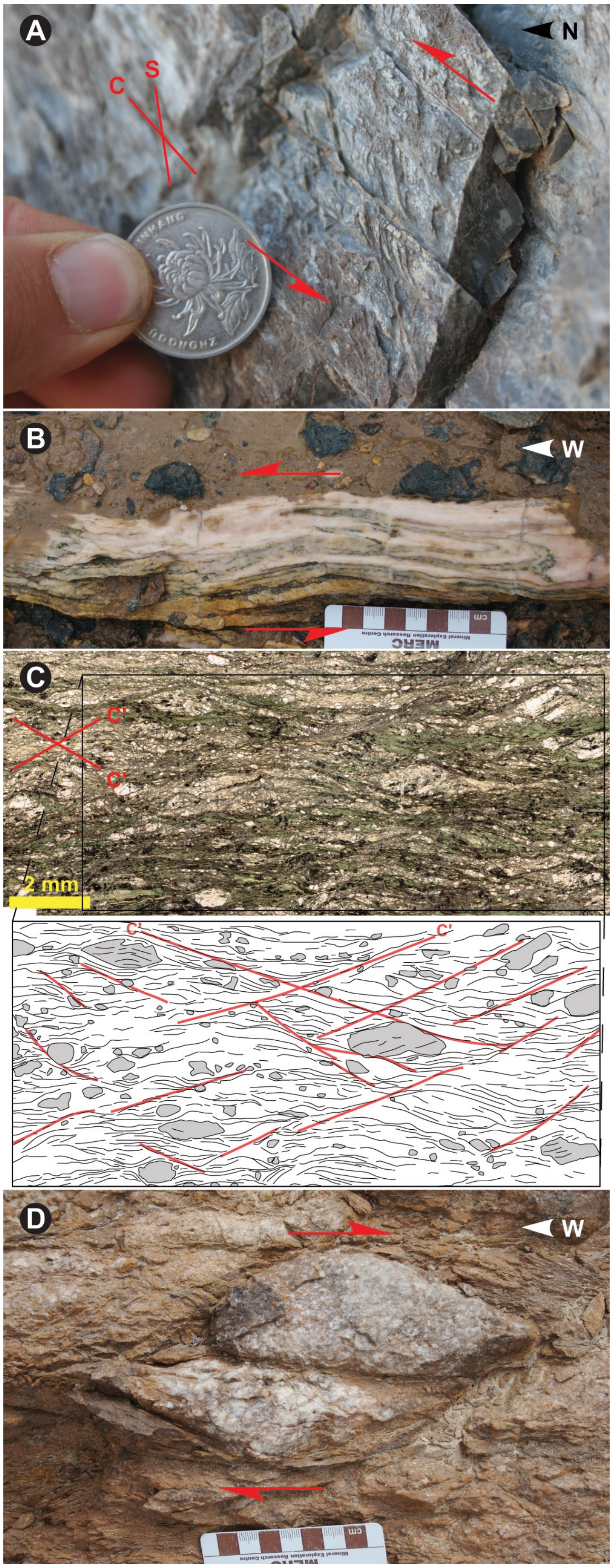

Figure 4.6: Field photographs and a photomicrograph of textures in the Yushishan shear zone array and the Hongliushu shear zone (locations indicated in figure 4.7): A) A mylonitized limestone from within the Yushishan shear zone array exhibiting an S-C fabric with sinistral kinematics. B) Isoclinally folded layers of limestone and chloritized volcaniclastic detritus produced from sinistral shear in the Yushishan shear zone array. C) Mylonitized basalt or volcaniclastic rock in the Yushishan shear zone array that shows conjugate C' foliations. Their implication is that E-W extension was accommodated in the Yushishan shear zone array. D) Asymmetrically mantled boulder-sized clast that indicates dextral kinematics, from mylonitic rocks of the Hongliushu shear zone.

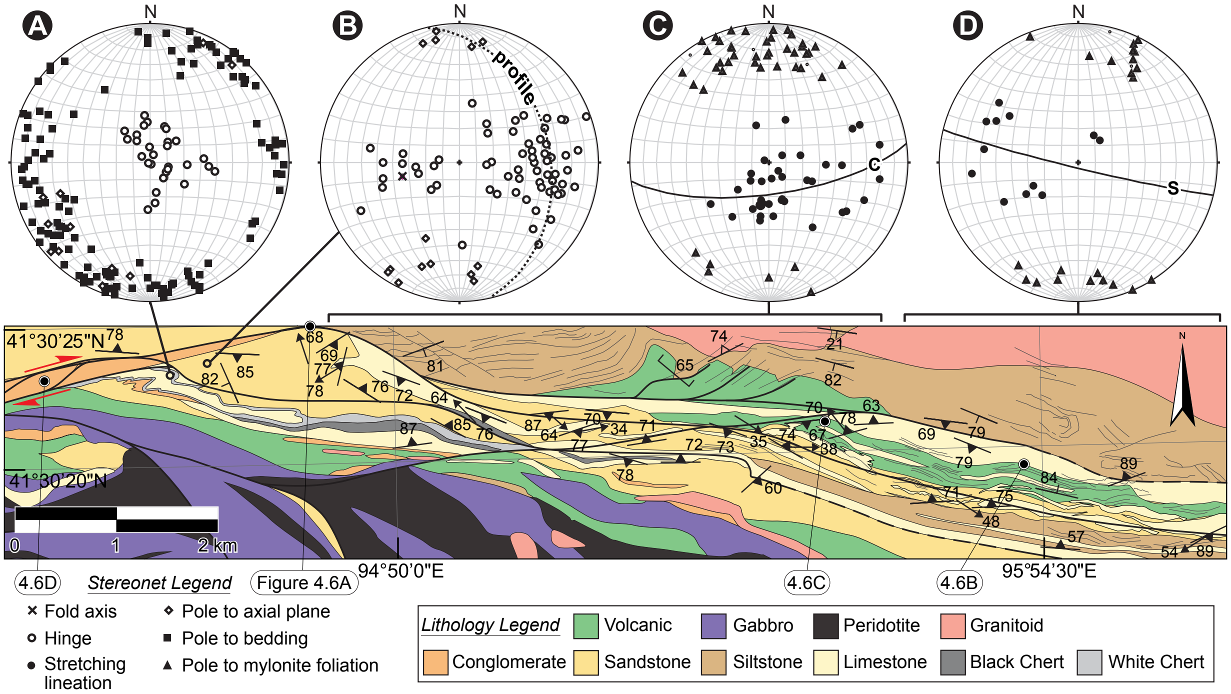

Figure 4.7: Detailed geological map of the Yushishan fault array in the supracrustal sequence overlying the Hongliuhe ophiolite. A small segment of the Hongliushu fault is included in the northwest corner. The locations of figures 4.6 A–D are indicated. Stereonet plots display fault foliation and lineation data and folding patterns: A) Data from folded black chert beds proximal to the Hongliushu fault. B) Data from folded sandstone stratigraphy. C) Fault foliation and lineation data of the western Yushishan fault array. D) Fault foliation and lineation data for the central portion of the Yushishan fault array.

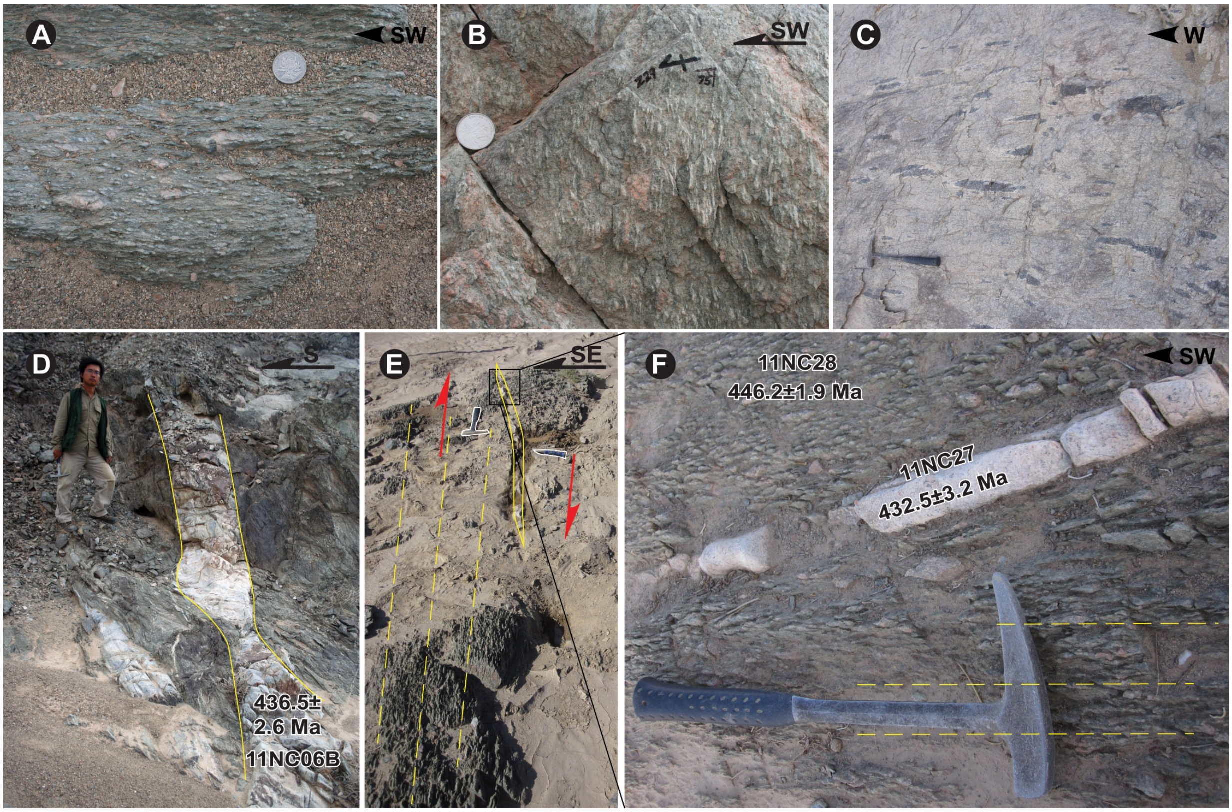

Figure 4.8: Field photographs of deformation in the Tianhu shear zone: A) Mylonitic foliation in a K-feldspar megacrystic granite. This pluton was sampled for geochronology (sample 11NC28). It is also pictured hosting the dykes in photographs D), E) and F). B) Mineral lineation associated with the foliation in A). C) Flattened mafic xenoliths in a tonalite body along the northwestern segment. D) Tonalite dyke exhibiting necking, which crosscuts the mylonitic foliation in the marginal domain. This dyke was sampled for geochronology (sample 11NC06B). E) Thin, boudinaged tonalite dyke obliquely crosscutting the mylonitic foliation in the central domain. This dyke was sampled for geochronology (sample 11NC27). F) Close up view of the sampling location for E).

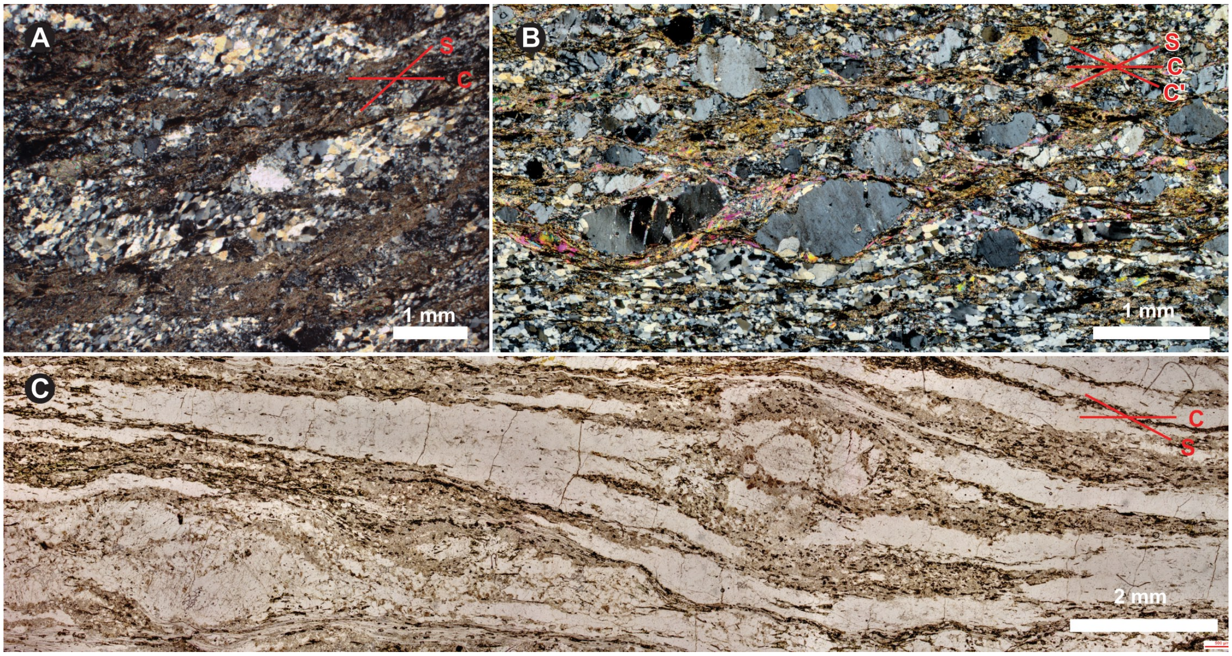

Figure 4.9: Photomicrographs of mylonitic textures from the Tianhu shear zone: A) Preferred orientation in dynamically recrystallized quartz indicating dextral kinematics. B) Mylonitized granite with an S-C' fabric indicating dextral kinematics. C) Mylonitic late (estimated Permian) granitoid with a C-S fabric indicating sinistral kinematics.

Figure 4.10: Field photographs of textures and structures in the Xingxingxia shear zone: A) Mylonitic foliation in a deformed tonalite body. B) Stretching and mineral lineation associated with the foliation in A). C) Folds in quartzite depicting the changing orientation and folding of fold hinges from shearing. Yellow arrow annotations highlight the fold hinges. Coin for scale. D) Weakly foliated tonalite dyke in the central domain of the Xingxingxia shear zone hangingwall. This dyke was sampled for geochronology (sample 11NC39G). The close up view is of the contact, which is annotated in yellow solid line with the mylonitic foliation trace in the host rock in dashed yellow line. The pen used for scale is outlined in white. E) Slightly foliated and necked dyke in the footwall cutting the mylonitic foliation in the latter. This dyke was sampled for geochronology (sample 11NC45).

Figure 4.11: Photomicrographs of mylonitic textures from within the Xingxingxia shear zone. A) through C) A sequence from the main E-W trending segment showing samples of increasing distance north (z values indicated in photomicrographs) from the shear zone center. Each depicts textures of a granodioritic to tonalitic mylonite, and with increasing distance textures appear closer to the protolith. Sheared mantled porphyroclasts of feldspar, and C' fabrics, provide the dextral kinematic sense. D) Mylonitic textures of deformed granitoid within the eastern segment of the Xingxingxia shear zone, where it trends NE-SW. Mantled porphyroclasts of fractured and disaggregated feldspar, and a C' fabric, indicate dextral kinematics.

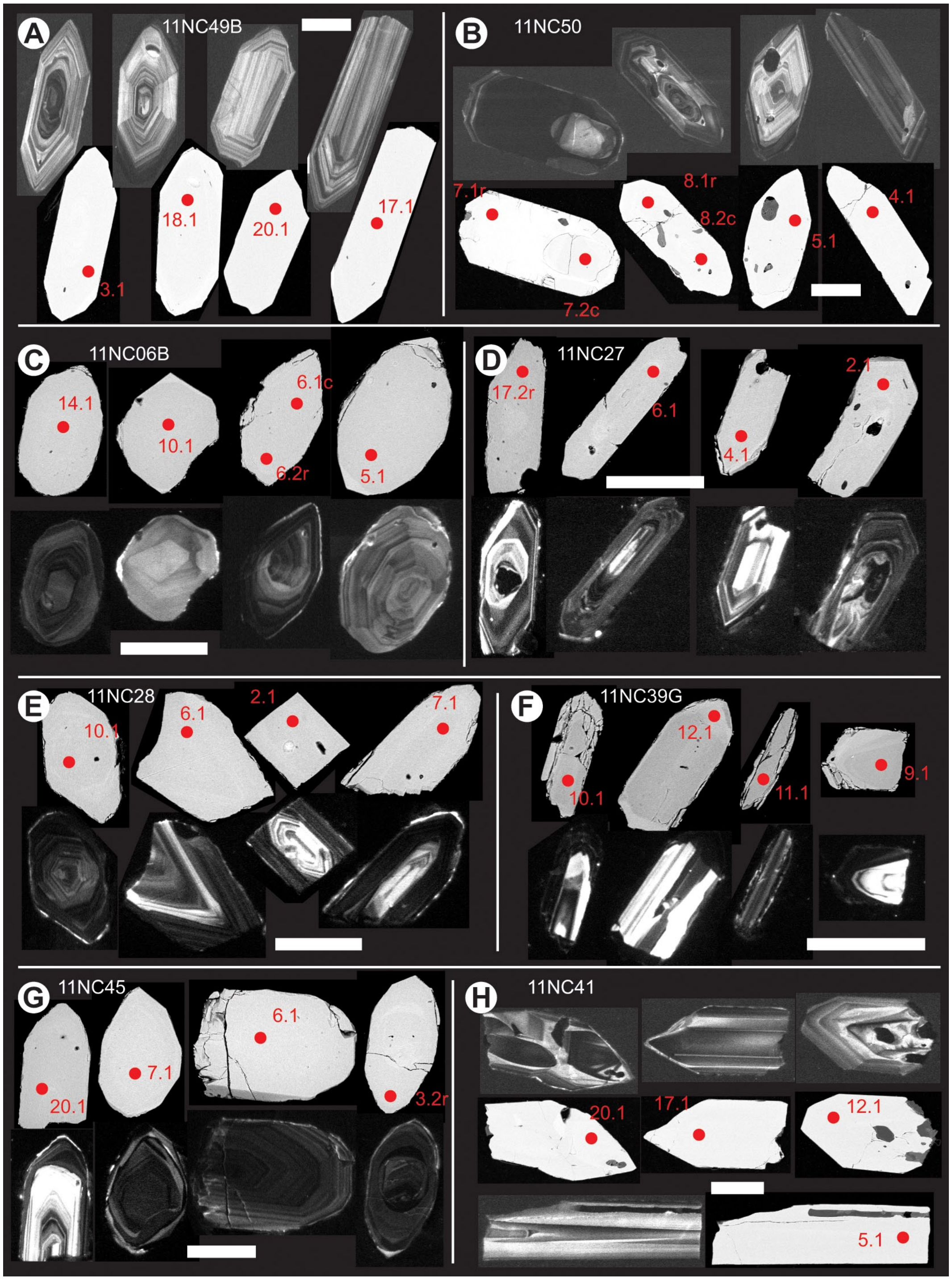

Figure 4.12: Examples of zircon grain textures from each sample, as indicated. Images included are SEM backscatter emission and cathodoluminescence for each, with spot analysis locations indicated with red dots.

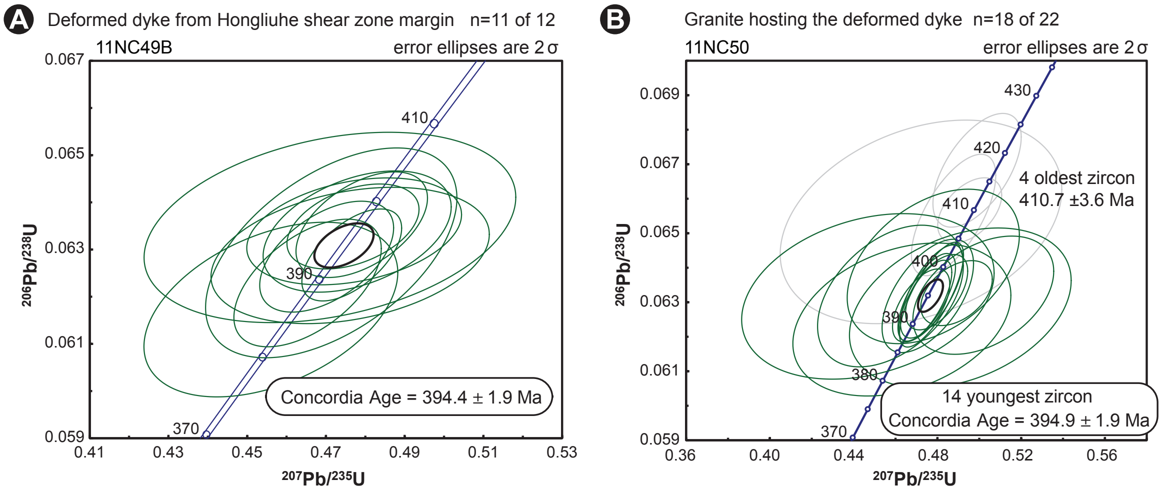

Figure 4.13: Concordia plots of U-Pb zircon data from a deformed dyke (A) and the hosting pluton (B) from the Hongliuhe shear zone. Green ellipses represent data from individual zircon. Gray ellipses represent data not included in age calculation. Black ellipses represent the calculated Concordia age.

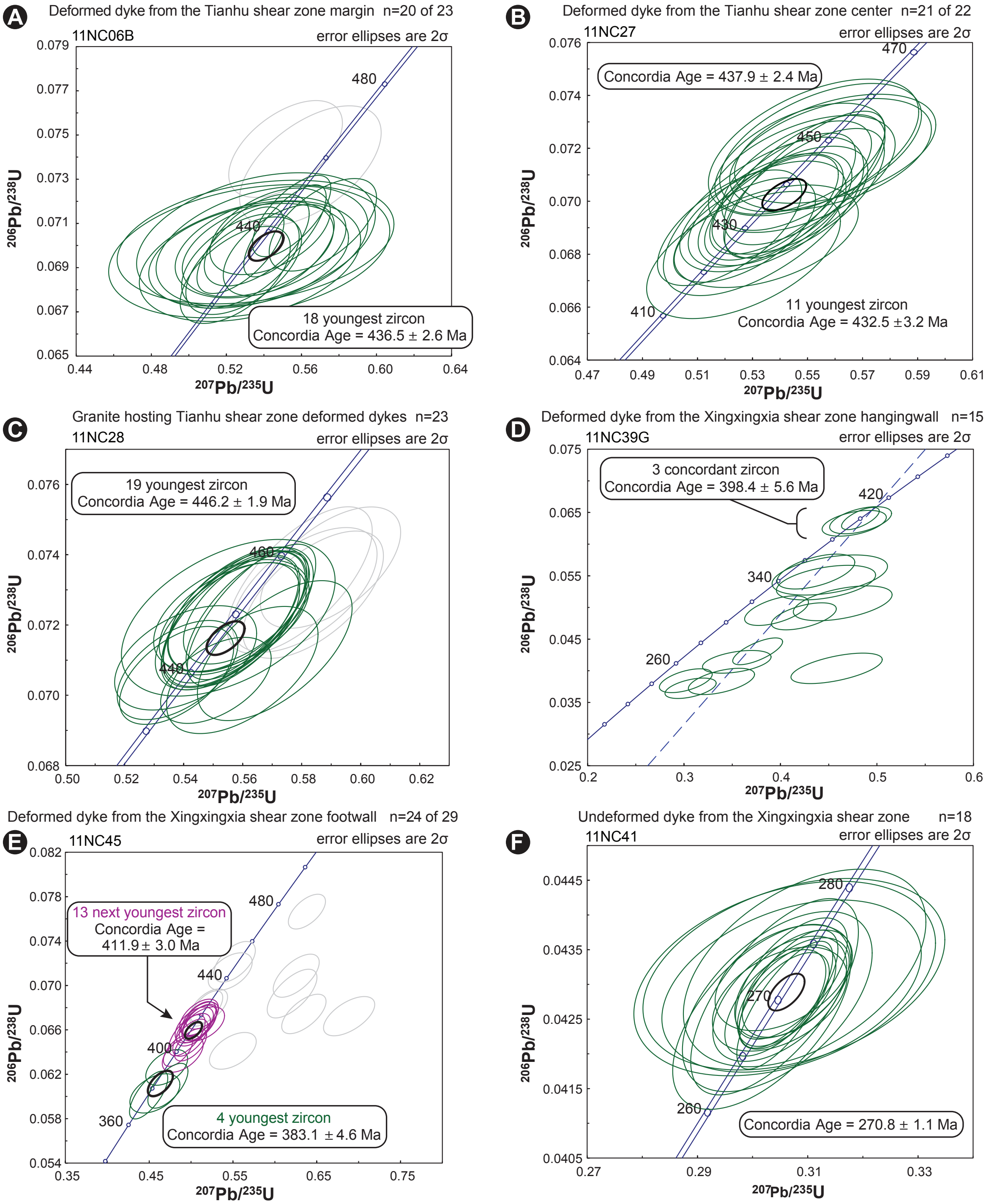

Figure 4.14: Concordia plots of U-Pb zircon data from deformed dykes (A and B) in the Tianhu shear zone, the granite hosting them (C), and deformed dykes (D and E) and one undeformed dyke (F) in the Xingxingxia shear zone. Green and violet ellipses represent data from individual zircon. Gray ellipses represent data not included in age calculation. Black ellipses represent the calculated Concordia age.

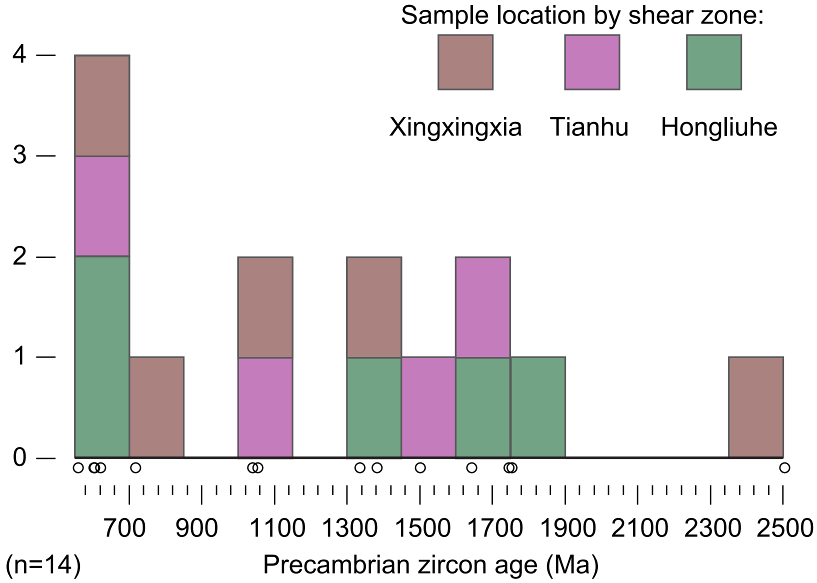

Figure 4.15: Histogram of all Precambrian zircon ages from this study. Color denotes the shear zone from which the respective analysis originates.

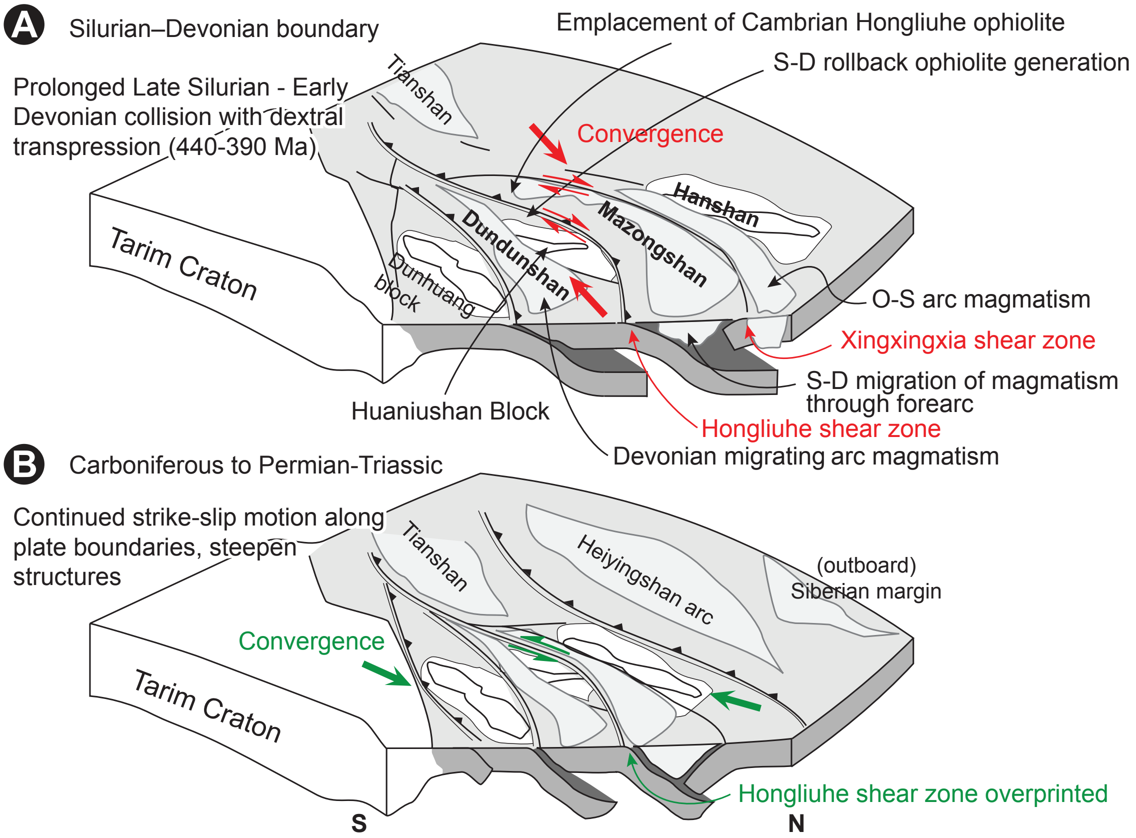

Figure 4.16: Schematic diagram showing a generalized model for the middle Paleozoic tectonic amalgamation of the Beishan during A) Silurian through Devonian, with widespread dextral transpression. B) Carboniferous through Permian–Triassic, with sinistral translation along the major plate boundaries (e.g. the Hongliuhe shear zone).

Chapter 5

Elucidating tectonic events and processes from variably tectonized conglomerate clast detrital geochronology: examples from the Hongliuhe Formation in the southern Central Asian Orogenic Belt, NW China

5.1 Introduction

Detrital zircon geochronology of sampled sandstone or siliciclastic sediments is a powerful method used to establish age distributions of magmatism within an orogenic belt, often pertinent to provenance analysis. It can be used to constrain depositional timing, using the youngest grain as a constraining factor(Fedo et al., 2003), or provide information on lag time, the time between the youngest zircon and an established deposition age. Both are used to interpret the tectonic environment of the provenance (Bernet et al., 2001; Andersen, 2005; Cawood et al., 2012; von Eynatten and Dunkl, 2012). The age spectra represent a collective profile of the provenance, including all contributing zircon-bearing rock sources from various catchment regions (Fig. 5.1).

In this paper we introduce the variably tectonized conglomerate clast detrital geochronology method. It expands upon the traditional sandstone detrital zircon geochronology and involves bulk samples of granitoid clasts, sorted based on the degree of internal ductile deformation (undeformed, slightly deformed, and deformed). Analyzing clast ages provides advantages over traditional sandstone detrital geochronology, as conglomerate clasts provide an identifiable lithology that can help constrain the source within a potential source region (Van Staal et al., 1998; Dunkl et al., 2009). More importantly, the method introduced here relates detrital age spectra from U-Pb zircon analyses to tectonism-related textures found within conglomerate clast populations (Fig. 5.1) and allows us to differentiate between U-Pb zircon age distributions of a region's magmatic rocks that have or have not experienced tectonic deformation. Correlating age spectra to degrees of tectonization may greatly improve provenance analysis in regions that contain strain gradients or major structural breaks, such as shear zones (Fig. 5.1). Comparison of tectonism-related clast age spectra to sandstone age spectra also yields extensive benefits. It expands upon the base deposition constraints (youngest zircon, lag time) and provides a comparison of the source magmatic ages and characteristics based on sediment transport distance. This is depicted by the respective sandstone and conglomerate drainage systems in figure 5.1. Analysis based on provenance proximity may be more relevant in complex accretionary orogenic systems, where high rates of sediment recycling occur, and processes including migrating arc magmatism and high-magnitude strike-slip translation commonly complicate analysis.

Our goal is to provide a geochronological tool for provenance analysis of syn-orogenic sedimentary deposits in highly tectonized regions. Providing more than absolute age information, our method gives an array of age spectra that can correlate with regional-scale lithotectonic reference information. It can also establish connections to, or implications of, ubiquitous magmatic, orogenic, and tectonic processes (Fig. 5.1). A simple example is that the youngest zircon of a deformed granitoid clast population may provide a constraint on the youngest age of tectonization in the provenance. A case study analyzing conglomerates and sandstones from the Permian syn-orogenic Hongliuhe Formation (Fig. 5.2) in the Beishan is presented to illustrate the method and potential applications of the variably tectonized conglomerate clast detrital geochronology method.

5.2 Geologic setting of the Beishan orogenic collage

5.2.1 General background

Reconstruction of tectonic histories of the CAOB has been a main, yet highly contentious, topic of research among scientists. Their interpretations affect the progression of studies into geodynamics, accretionary orogenesis and mineral deposit exploration. Existing studies of granitoids focus on age, geochemical composition and tectonic setting, and in some cases their structural history. These provide an immediately local view for interpretation of the complex and protracted tectonic history that involves collisions between multiple cratons, island arc systems, and accreted oceanic units. A further complication is that suture zones and terrane boundaries host large-scale strike-slip shear zones, repeatedly reactivated, even well past terminal collision. Unconstrained translational shear zone displacements pose a daunting problem for tectonic reconstruction.

The Beishan orogenic collage is a southerly subset of the CAOB (Fig. 5.3, inset). It comprises Precambrian continental nuclei, Paleozoic arc terranes, and intervening accretionary complexes. It lies east of the Tianshan arc, part of the last set of terranes to accrete against the Siberian margin prior to terminal collision, which zippered across the CAOB from west to east. Terminal collision in the CAOB, the final consumption of intervening ocean basins, initiated as the Tarim block collided against the Tianshan starting in the Late Carboniferous–Early Permian (Coleman, 1989; Gao et al., 1998; Chen et al., 1999; Laurent-Charvet et al., 2002; Li et al., 2002; Charvet et al., 2007; Xiao et al., 2009a; Gao et al., 2011; Zhang et al., 2013a), then (debatably) continued with the Dunhuang block colliding against the Beishan in the Late Permian (Xiao et al., 2010; Mao et al., 2012b; Tian et al., 2013; Zhang and Cunningham, 2012; Zhang et al., 2013b). Researchers interpret that the larger North China Craton, further east, collided against the Southern Mongolian accretionary system in the Late Permian–Early Triassic (Xiao et al., 2003; Jian et al., 2008; Chen et al., 2009; Jian et al., 2010; Eizenhöfer et al., 2014). In most cases, the tectonothermal events related to this final closure overprinted and reactivated many orogenic belt-wide structures. Deformation commonly localized into weak, pre-existing sutures, obscuring evidence of previous collisions and accretion events (Wang et al., 2010; Zhang and Cunningham, 2012; Tian et al., 2013; Cleven et al., 2015). The distributed effects of contraction forced some inboard terranes to override others, creating late orogeny, rapid uplift, and sedimentation (Su et al., 2011; Li et al., 2012; Zhu et al., 2012; Zhou, 2014). Some terranes were eroded to the point where their orogenic plutonic roots are now exposed. This is evident in geologic maps, as distributed Carboniferous–Permian plutons, and as Permian syn-orogenic clastic deposits (Fig. 5.3). The Hongliuhe Formation, the focus of this study, is such a deposit. It is described in more detail below.

Four main Paleozoic terranes comprise the Beishan (Fig. 5.3), three of which contain arc-related magmatic rocks aged Ordovician through Devonian. Early Paleozoic arc magmatism developed through two separate Precambrian crustal slivers, defining the Hanshan and Dundunshan terranes (Fig. 5.3). The spans of reported magmatic activity in each terrane, compiled from literature, are graphically compared at the top of figure 5.3. The Mazongshan terrane partially intervenes between the Hanshan and Dundunshan terranes and is considered as a forearc accretionary complex of the Hanshan (Ao et al., 2012; Tian et al., 2014; Song et al., 2014). The Hanshan and Mazongshan terranes are separated from each other by the Xingxingxia dextral strike-slip shear zone (Wang et al., 2010). They are separated from the Dundunshan terrane by the Hongliuhe suture, at surface exhibiting as a kilometer wide ductile sinistral shear zone (Chapter 4). Some workers have concluded from structural and metamorphic studies that the timing of collision between the three terranes, or possibly their accretion to the Dunhuang block to the south, is Early Devonian (Qu et al., 2011; He et al., 2014a; Chapters 2 and 4). This coincides with timing constraints on the emplacement of the Hongliuhe and Yueyashan-Xichangjing ophiolites (Ao et al., 2012; Chapter 3). The consistent southward vergence of collision- or accretion-related transpressive structures (Tian et al., 2013; Song et al., 2014; Cleven et al., 2015) provide convincing evidence of north dipping subduction systems under the Hanshan and Dundunshan terranes. This interpretation is supported by north-dipping deep reflectors seen in a seismic profile (Gao et al., 1998). The seismic profile indicates that the subduction systems intersect the surface along both the Hongliuhe suture and the Beishan–Dunhuang block suture (the southern margin of the Dundunshan terrane; Figure 5.3). The magnitude of late strike-slip displacement across the plate and terrane boundaries remains unconstrained.

5.2.2 The Permian Hongliuhe Formation

The Hongliuhe Formation, the focus of this study, is situated in Gansu province, Northwest China. During Permo-Triassic orogeny the northerly Hanshan terrane overrode the Dundunshan terrane. The late orogeny occurred as an inboard response to outboard collision, after the initial Silurian-Devonian suturing and a short-lived period of reportedly widespread extensional tectonics in the Carboniferous (Su et al., 2011; Mao et al., 2012b; Zheng et al., 2013, 2014). It utilized the existing plate boundary to create new structures in the same southward vergence as the initial Silurian-Devonian suture. Syn-orogenic deposition, of which the Hongliuhe Formation is a part, started to unconformably cover the suture zone in the early Early Permian (Li et al., 2006). Details of the Hongliuhe Formation fold-and-thrust belt deformation associated with the late orogenic event, and its structural reconstruction can be found in Cleven et al. (2015).

The east-west striking Hongliuhe Formation is fault bounded to the north and south, adding to its complexity and obscuring any direct relation to a provenance. It has been interpreted to unconformably overlie obducted or accreted Cambrian and Devonian oceanic volcanic and ophiolitic units hosted within the Mazongshan accretionary complex terrane (Chapters 2 and 3) (Fig. 5.4). It lies at the western taper of the Mazongshan terrane (extent indicated in Figure 5.3), between where the Hongliuhe shear zone nearly converges with the Xingxingxia shear zone.

The Hongliuhe Formation is a prime example to explore how orogenic-related sedimentation can contain a record of previous tectonic events. Granitoid clasts with various degrees of pre-depositional deformation are ubiquitous in outcrops at multiple stratigraphic levels in the syn-orogenic clastic deposit. Their distributions of compositions and degrees of deformation change across stratigraphy (Figs. 5.2 A and 5.2 B). Conglomerates are present in multiple thick successions towards the base of the deposit, commonly punctuated with sandy and silty interbeds and horizons (Fig. 5.5). Thick sequences of rhythmically interbedded sandstones and siltstones occupy the middle section of the deposit, overlain by more conglomerates. The presence of siltstone increases upsection, along with an introduction of some limestone strata. Sandstones are moderately immature, with lithic fragments of k-feldspar, plagioclase, epidotized and fresh volcanic fragments (with textures consistent with underlying rocks), rare magnetite or spinel, and common polycrystalline quartz or quartzite fragments. Conglomerates are polymictic at the base, with clast lithotypes of granitoids, sedimentary rocks, metasedimentary rocks of various grades, and tectonites. Upsection, limestone clasts are introduced and the abundance of tectonites and higher-grade metamorphic rocks decreases. There is also a higher concentration of fresh granitoid and volcanic clasts.

5.3 U-Pb geochronology of variably tectonized conglomerate clasts and sandstones

5.3.1 Variably tectonized conglomerate clast population dating

This section provides an overview of our prescribed methodology for variably tectonized conglomerate clast population dating. Multiple large outcrops (Fig. 5.2) are required for the bulk sampling of an appropriate statistical number of clasts (417 granitoid clasts were sampled for the case study below). All clasts, once sampled, are trimmed to a comparable size to avoid bias due to clast size. Separation into populations based on their individual, pre-deposition degree of internal, ductile deformation, can be field-based (as is the case here) or lab-based, or a combination of the two. Our suggested divisions are three populations including clasts that are observed as foliated (tectonized, or deformed), non-foliated or lineated (undeformed), or intermediate (slightly deformed) (Fig. 5.6). The slightly deformed population is necessary to reduce ambiguity, and includes clasts that lack a strong or consistent foliation or lineation, but contain subtle or patchy deformation textures such as reduced grain size, a degree of mineral alignment, or the rounding of porphyroclastic grains. Care must be taken to exclude clasts exhibiting magmatic mineral alignment textures. The separation into these populations relies on the experience of the sampler with identifying deformation textures in hand sample. Microscopic determination of textures using thin section may be used to aid the process and establish more precise criteria. After sorting, each of the three populations is processed for zircon separation and analysis in an identical manner as a sandstone detrital sample.

5.3.2 Sample framework for the Hongliuhe Formation

Three stratigraphic levels of the Hongliuhe Formation were sampled, referred to as basal, middle, and upper (Fig. 5.5). Sampling was performed in accordance with the method outlined in section 3.1, and full details of the procedure and strategy developed for this study is outlined in the appendix. Representative examples exhibiting the textural criteria used for each population are provided as field-based photographs and thin-section photomicrographs in figure 5.6. A total of 116 clasts were sampled from the basal stratigraphic level, 141 clasts from the middle stratigraphic level, and 151 clasts from the upper stratigraphic level. Clasts were separated into populations of deformed, slightly deformed, and undeformed clasts, the distribution of which is shown by stratigraphic level in figure 5.7. A further breakdown by granitoid composition of each of these populations is provided in Table 5.1. Textural differences noted in the table include (where present) variations in grain size, mafic mineral content and type, phenocrysts, alteration, and type of foliation. In general, the granitoid clasts are mostly tonalitic in composition at the basal (Fig. 5.2 A) and upper stratigraphic levels, and granitic at the middle stratigraphic level (Fig. 5.2 B). Deformed clasts decrease in population upsection, and undeformed clasts are rare at the base.

Sandstone detrital geochronology samples were also collected from the same outcrops as the clasts, at each stratigraphic level, from interbeds in conglomerate or from locations within meters up or down section of the sampled conglomerates. The result is a total of twelve samples, three clast samples (deformed, slightly deformed, and undeformed) and one sandstone sample from each of the basal, middle and upper stratigraphic levels.

5.3.3 LA-ICPMS zircon geochronology and data

For each of the twelve samples approximately 120 zircon grains were mounted in epoxy for dating using a laser ablation, inductively coupled plasma mass spectrometry (LA-ICPMS) techniques at the Jack Satterly Geochronology Laboratory in the University of Toronto, Ontario, Canada. The procedures for the geochronology techniques are described in the appendix. Analytical data are reported in appendix Table D.1 for sandstone samples, and appendix Table D.2 for all clast samples.

Ages of Paleozoic zircon from the sandstone samples are displayed, by stratigraphic level, in figure 5.8 as histograms, with overlain kernel density estimates (Sircombe and Hazelton, 2004; Vermeesch, 2012); component peak ages are indicated. Sandstone samples, in total, include analyses of $n = 290$ grains. Ages of Paleozoic zircon from the clast samples are displayed in a similar graphical fashion in figure 5.9, but as an array, by stratigraphic level (basal, middle and upper) in the vertical direction and by intensity of deformation (deformed, slightly deformed and undeformed) in the horizontal direction. Clast samples, in total, include analyses of $n = 833$ grains. Error (as 1σ values) and discordance values (as %, by color tone) for each Paleozoic grain are plotted versus grain age, as radial plots (Galbraith, 1990), with all samples combined (sandstone and clast) per stratigraphic level, in figure 5.10. The program RadialPlotter was used to create all plots and to calculate component ages (Vermeesch, 2009). The small number of Precambrian grains that were analyzed was sourced from the basal stratigraphic level, and is graphically displayed in figure 5.11, with their respective sample indicated.

5.4 Interpretation and Discussion

The clast and sandstone data together provide standard detrital geochronological information. This includes the youngest single zircon age of 294 ± 3 Ma, from a slightly deformed clast, and age spectra showing three main peaks of Paleozoic magmatic activity (Fig. 5.12). The peaks are at roughly 450, 400 and 310 Ma and there is a hiatus from magmatism during 380-340 Ma. The youngest zircon age correlates well with the Li et al. (2006) palynology- and paleontology-based depositional age interpretation of (early) Early Permian; such a close correlation implies rapid exhumation and sedimentation (Carter and Bristow, 2000). It is interesting that the youngest peak (ca. 310 Ma) is not present in any sandstone detrital sample. The youngest single zircon from the sandstone samples is 384 ± 3 Ma. This means that sandstone samples alone would indicate roughly 90 m.y. of lag time from crystallization of the youngest dated zircon in their provenance to deposition. With the consistency of the sandstone age distributions as major peaks through the Ordovician and into the Silurian it is reasonable to infer that the provenance was dominated by a large source of magmatic arc material. Their age spans correlate to the ages of known arc-related magmatic rocks in both the Hanshan terrane and Mazongshan accretionary complex terrane (Chapter 2, and references therein). The 90 m.y. sandstone-based lag time, however, is not typical of an active arc-related depositional setting, supporting the syn-orogenic (post-arc) nature of the deposit (Cawood et al., 2012). The magmatic rocks contributing to the young age peak (310 Ma), which provides the minimal clast-based lag time, may have been sourced from orogenic granitoids situated in higher crustal levels in the eroded provenance (Fig. 5.13), as this age is found only in the basal stratigraphic level. Similarly aged orogenic granitoids have been recognized further south in the Dundunshan terrane (Su et al., 2011; Li et al., 2012).

5.4.1 Constraining the tectonic framework using clast data

The variably tectonized clast age spectra provide additional information concerning the regional tectonomagmatic framework. The youngest near concordant single zircon age from any deformed (foliated) clast sample is 385 ± 4 Ma. This timing is coincident with the start of the 40 m.y. hiatus from magmatic activity. Both of these correlating attributes are consistent with terrane-scale arc-arc collision or arc accretion to a continent in the Early Devonian. As no deformed clasts yield younger ages, the tectonic events after this period must have been minor, creating little to no ductile deformation in plutonic rocks. This supports the interpretation that the Permian orogenic response related to deposition of the Hongliuhe Formation was an inboard reactivation of an existing suture, caused by the outboard terminal collision (Qu et al., 2011; He et al., 2014a; Song et al., 2014; Chapters 2 and 4).

A comparison of collated sandstone and clast data shows that magmatism is fairly continuous through the Ordovician to Devonian for both sets (Fig. 5.12). The age distributions during this period contain two significant peaks for both the sandstone and clast data sets at approximately 400 and 450 Ma. In the sandstone data there is a large relative abundance of zircon ages centered on the 450 Ma peak and a low abundance at the 400 Ma peak. In contrast, the opposite is observed in the clast data (Fig. 5.12). If transport distance is the major factor differentiating the two sediment grain sizes this could indicate that the provenance includes a proximal, younger source and a distal older source. This would be consistent with plutonism migrating from the distal, arc-related source sampled by the sandstone, towards the proximal forearc region of the deposition site over the course of the Ordovician to Devonian. As a correlating detail, the sandstone age spectra analyzed by stratigraphic level (Fig. 5.8) also show an upsection shift towards younger ages for the major component peak, from 456 to 436 Ma. Correlating the deposition sequence to unroofing of the provenance, this would imply a younging trend with depth (Fig. 5.13), possibly due to a waning heat source with the southerly migration of plutonism. This interpretation illustrates the potential benefits of cross-stratigraphy sampling and correlation.

5.4.2 Using clast data to characterize provenance

The clast age spectra can be broken down into four main age components spanning specific time periods, each potentially linked to specific source regions in the surrounding terranes. Figure 5.13 provides a schematic cross-sectional view of the terranes surrounding the sample region. It illustrates the interpretive potential settings for plutonic bodies from each of the main age components at different crustal levels that were eroded as sedimentation progressed. The four main age components and their provenance interpretations are outlined below.

(1) The 290-320 Ma age component, peaking at 310 Ma, is the most obvious example. It is represented only in the basal level undeformed and slightly deformed clasts, and not in any sandstone sample, suggesting proximity to the deposition site (Fig. 5.13). This age correlates to reported Hanshan terrane ages (Fig. 5.3), yet the literature is limited in this respect. Chinese geologic maps indicate plutons of this age in the Tianhu region, part of the Mazongshan terrane, indicated in figure 5.4 as 'Permian – undifferentiated'.

(2) The 390-410 Ma age component, peaking at 400 Ma, is common in the clast data and is not diagnostic of a certain terrane. Plutons of this age are locally present in the Mazongshan terrane. The proportion of zircon grains of this age component in all data is significant in the middle and upper sections, at 65% and 60% respectively (see statistics in figure 5.10), but drops to 20% in the basal stratigraphic level. This younger, possibly orogenic or post-orogenic, plutonic suite is interpreted to be more deeply seated in the source region (Fig. 5.13). Plutons of this age are highly potassic in the Hongliuhe region, but have no geochemical studies to date.

(3) The 410-430 Ma age component, peaking at 425 Ma, is consistent with ages reported from both the Hanshan and Mazongshan terranes. Geochemical studies of similarly aged granitoids in the region point towards mixed volcanic arc granitoids, and syn-collisional granites (Li et al., 2011; Song et al., 2013b). This age component is not present in sandstone age spectra.

(4) The 430-470 Ma age component, peaking at 450 Ma, can only represent a combination of both the Mazongshan and Hanshan reported ages. The basal and upper stratigraphic level clast populations develop an increase of this age component with increasing deformation (449 and 442 Ma, respectively). This aspect is unique to Mazongshan deformed granite ages (Song et al., 2013a,b). It is also the dominant age component of the sandstone data. Together, these observations may indicate that the erodibility of deformed granitoids contributes to the heavy representation of this age component in sand sized clastic material (Moecher and Samson, 2006).

Correlations between existing studies of deformed granitoid bodies in the Beishan and the deformed clast geochronology data provide for better provenance interpretation. Despite the fault bounded nature of the Hongliuhe Formation and its proximity to major shear zones, the provenance analysis from our method is entirely consistent with Hanshan terrane and Mazongshan terrane mixed sources. No other prospective terrane in the region, or far along strike, fits the profile, including the Dundunshan arc with its later hiatus and almost no record of syntectonic plutonism. The South Tianshan accretionary complex has a plutonic record that is similar but 50 m.y. younger in all respects (Shi et al., 2014). This implies that the magnitude of strike-slip displacement across the Xingxingxia shear zone, or its subsidiaries, does not exceed the scale of the terranes.

5.4.3 Clast age spectra and tectonic processes

Analyzing changes of age spectra of variably deformed clasts across stratigraphic levels, or changes of age components among deformation types (deformed to undeformed) at the same stratigraphic level, may provide additional constraints on tectonic processes. For example, the mid stratigraphic level clast age distribution exhibits predominantly the 390-410 Ma age component in all clast populations. It also exhibits a minor 430-470 Ma age component that increases from slightly deformed to undeformed clasts. This indicates that in the source area, deformed granitoid plutons are younger (390-410 Ma), whereas older (430-470 Ma) plutons are undeformed, which seems unusual. There is no compositional difference between younger and older clasts, indicating that this cannot be explained by any such difference. A possible interpretation is that the younger magmatism was synchronous with significant crustal deformation and the deformed granitoid plutons intruded into active shear zones and were thus deformed during the process. In contrast, at the upper stratigraphic level of the Hongliuhe Formation, corresponding to the deepest eroded provenance, the deformed clast age spectra exhibit all age components, which is consistent with what would be expected at lower crustal conditions where deformation is more homogeneously distributed.

Interestingly, no deformed clasts show inherited Precambrian zircon, pointing towards a juvenile magmatic source. In general there is a scarcity of Precambrian zircon in the data set, none in the middle and upper stratigraphic levels. This may be an indication that juvenile magma production and preservation was ubiquitous in the Beishan accretionary orogen.

5.5 Concluding remarks

Determining the age distributions of variably tectonized granitoid clasts sampled from syn-orogenic conglomerates offers an extra dimension of information over standard sandstone detrital geochronology techniques. It has proved useful for provenance analysis and tectonic reconstructions, especially when used in conjunction with sandstone detrital geochronology. If the two sediment types represent different transport distances, age spectra of clasts can reflect proximal sources while those of sandstones reflect distal sources. Isolating granitoid clasts based on degree of deformation provides further insight into the temporal evolution of plutonic, tectonic and accretionary processes. Analysis of multiple sets of samples across stratigraphy builds a profile of the unroofed source terrane, or terranes.

This study applies the method to three stratigraphic levels of the Permian Hongliuhe Formation in the Beishan orogenic collage in northwestern China. The results lead to: (1) the recognition of a significant young igneous event at ca. 310 Ma that is absent in the sandstone detrital geochronology; (2) the characterization of source lithologies respective to tectonization, such as an increasing abundance of Ordovician ages that correlates with increasing intensity of deformation; (3) an improved provenance interpretation based on age spectra respective of transport distance, which in turn leads to the conclusion that the movement along regional shear zones is not significant; (4) the an interpretation of a Middle Devonian end to significant, regional ductile deformation processes, at the crustal levels of the provenance represented in the sediment package, based on the youngest deformed (foliated) clast age; and (5) the interpretation that 390-400 Ma magmatism was syn-tectonic, with the latent heat of plutonism a possible rheological explanation for localization of strain into plutons of this age of pluton over older ones.

How this method can help in an individual study will depend on the specific situation and the geological setting. It may prove to be especially helpful for reconnaissance work in an orogen where little data is available. Linking age distributions to lithology and degree of deformation could provide insight into natural bias introduced from variable zircon fertility in source rocks, or from sediment grain size differences. Used in conjunction with other geochronological or thermochronological techniques, such as detrital fission track dating, may allow further enhanced provenance analysis and characterization. Hafnium isotopic studies may provide a detailed exposé of crustal recycling, or juvenile crust production and preservation, in either accretionary or collisional orogenic belts.

Clast composition	Basal	Mid	Upper	No. textures
U – tonalite	10	0	46	4
U – granodiorite	0	0	0	–
U – granite	0	64	1	6
S – tonalite	39	1	54	4
S – granodiorite	0	1	2	1
S – granite	0	29	4	3
D – tonalite	62	5	44	6
D – granodiorite	0	0	0	–
D – granite	5	41	0	3

Table 5.1: Granitoid composition statistics of clasts. U = undeformed, S = slightly deformed, D = deformed.

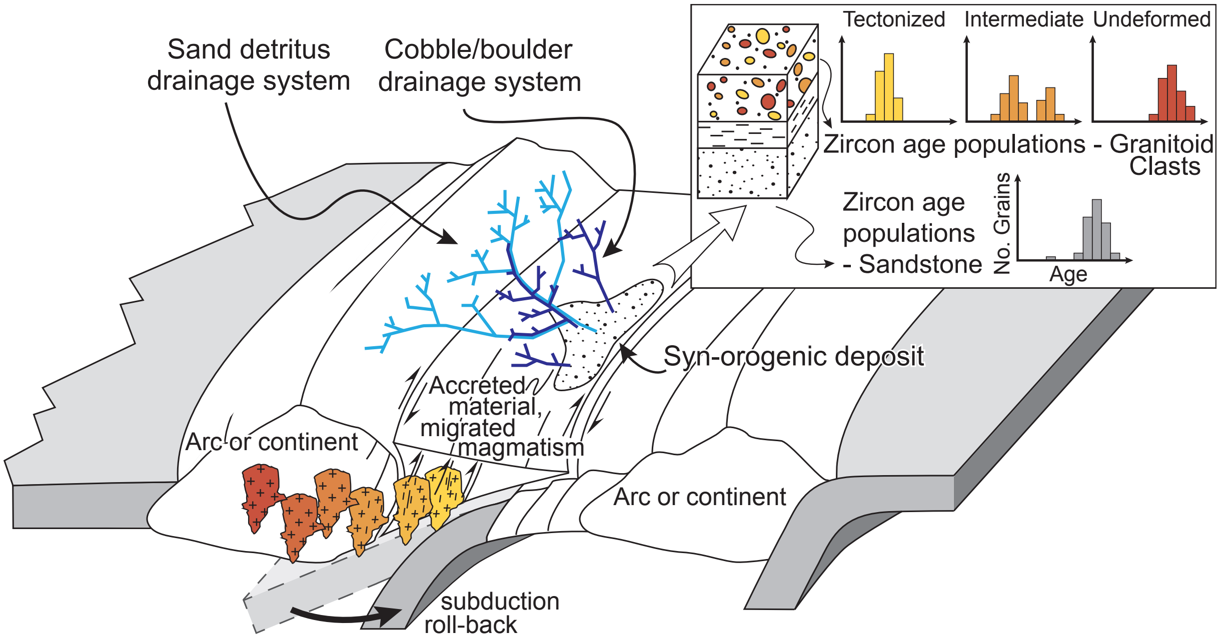

Figure 5.1: Schematic diagram of the variably tectonized clast detrital geochronology concept and sampling strategy. The method compares age spectra of standard sandstone detrital samples with age spectra of variably tectonized conglomerate clasts. Targeting the syn-orogenic deposit (center), a sandstone sample reflects more distal provenances from a wider drainage system (light blue), and a clast sample represents more proximal provenances (dark blue). Separation of bulk-sampled granitoid clasts into populations based on internal degree of deformation or tectonization (inset), prior to U-Pb zircon geochronological analysis, provides extensive information about the regional tectonomagmatic framework. The mock tectonic situation depicted here reflects accretionary dynamics considered in the case study. The timelines of staged orogenesis, migrating arc magmatism, and syn-tectonic plutonism can be recognized in the tectonized clast age spectra.

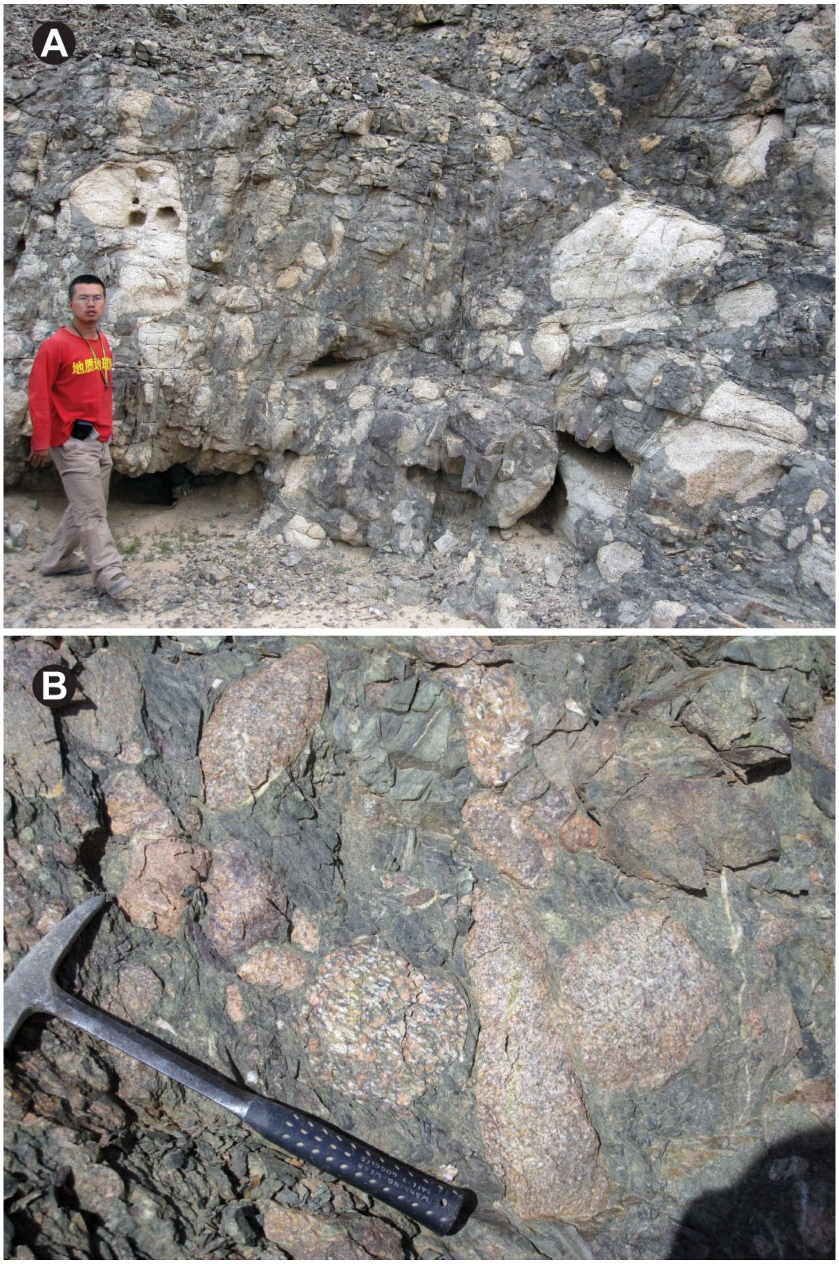

Figure 5.2: Coarse, poorly sorted conglomerate outcrops of the Hongliuhe Formation were sampled for variably tectonized granitoid clasts to be analyzed in a similar manner to detrital zircon geochronological methods. A) Large tonalite boulders in outcrop at the basal stratigraphic level. Scientist for scale. B) Granite clasts in conglomerate at the middle stratigraphic level. Hammer for scale.

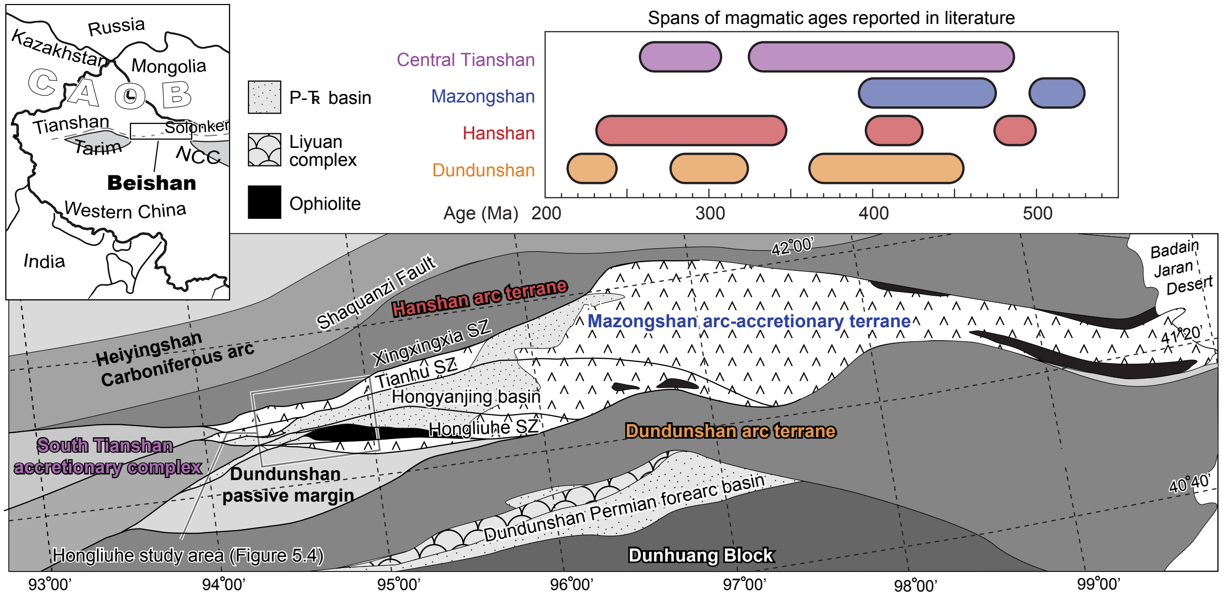

Figure 5.3: Tectonostratigraphic map showing major geologic units and their respective ages, as well as the major shear zones separating the terranes. Fill patterns denote extents of labeled terranes. SZ: shear zone. Included is a summary of magmatic age spans compiled from existing literature (Chapter 2 and references therein).

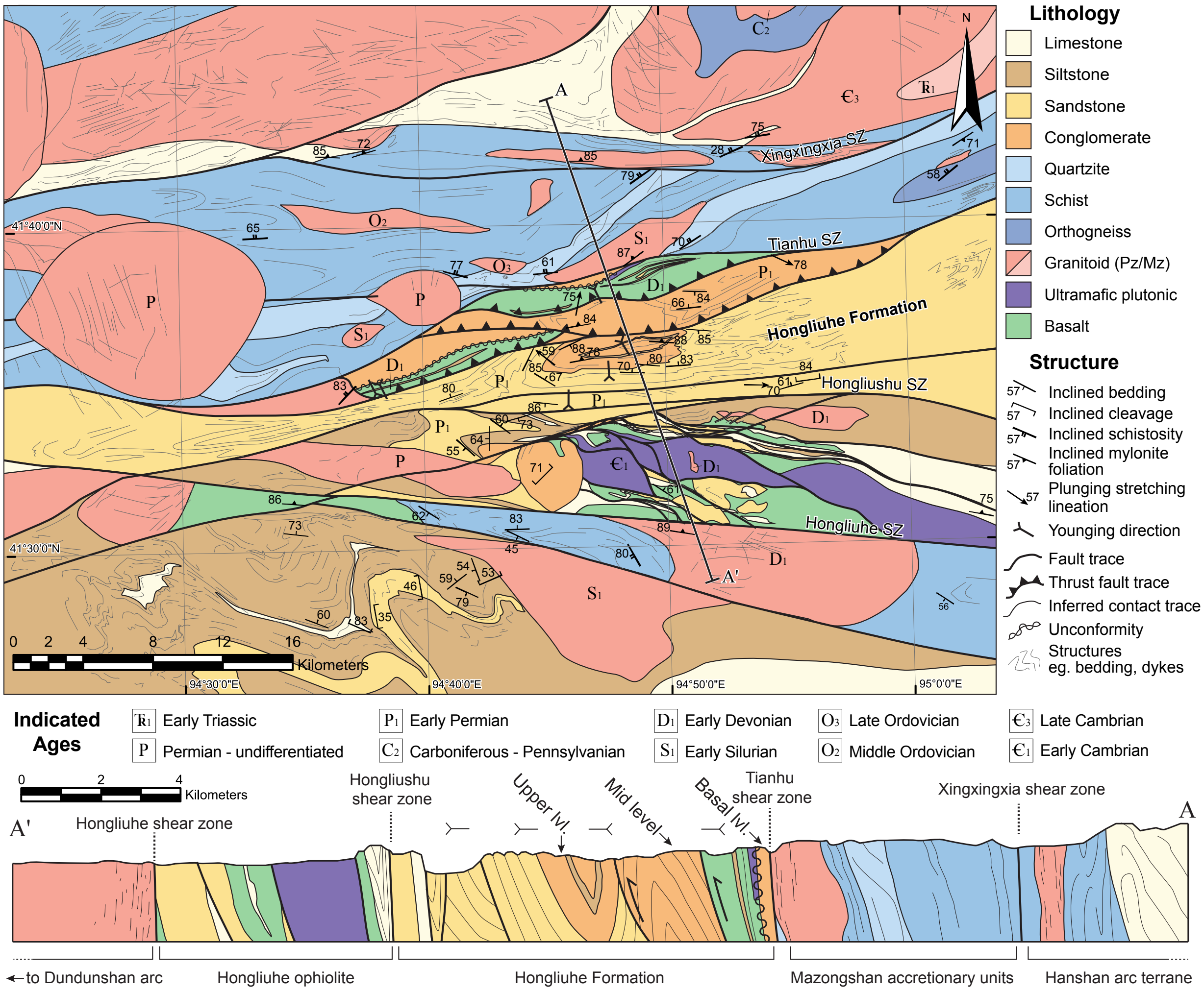

Figure 5.4: Hongliuhe region geological map with cross section. SZ: shear zone.

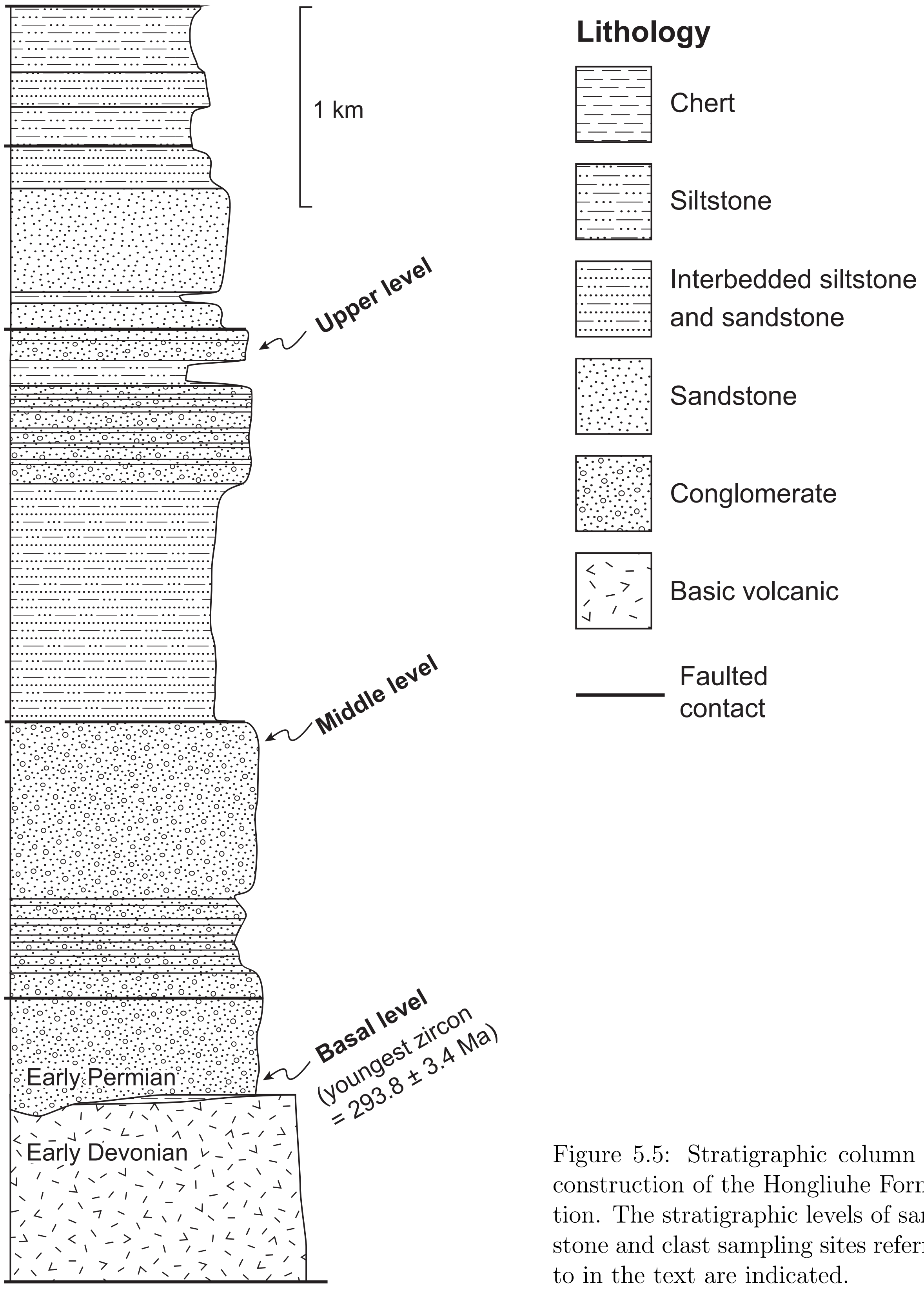

Figure 5.5: Stratigraphic column reconstruction of the Hongliuhe Formation. The stratigraphic levels of sandstone and clast sampling sites referred to in the text are indicated.

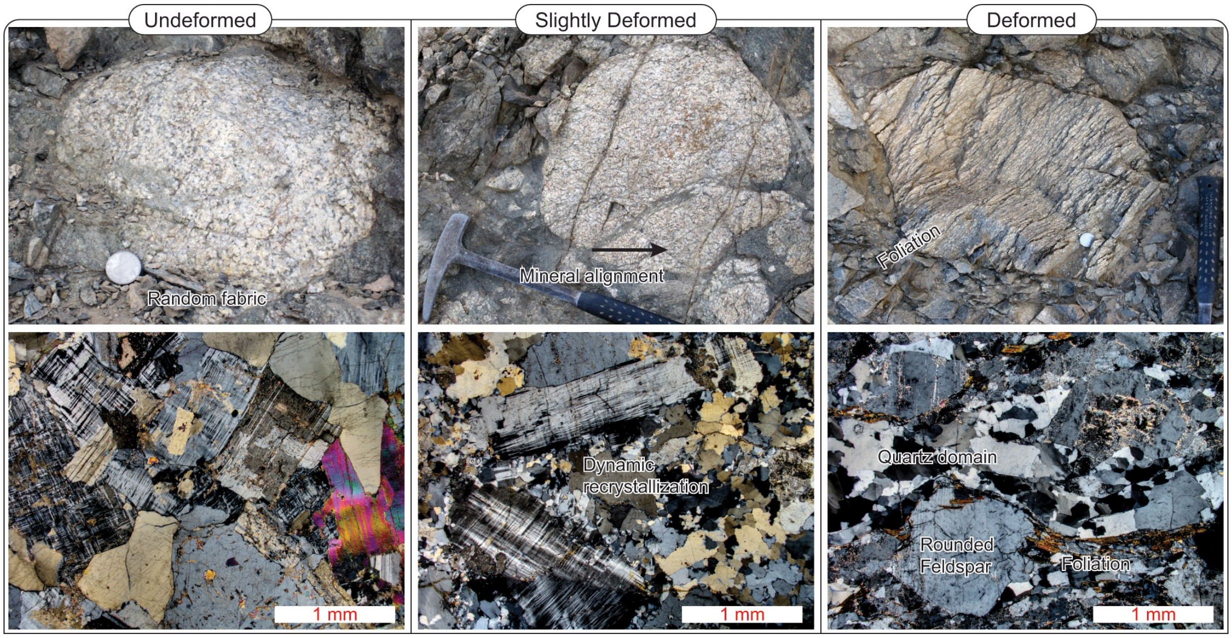

Figure 5.6: Sampled clasts are divided into populations of deformed, slightly deformed and undeformed, prior to mineral separation. Outcrop photos of clasts and thin section photomicrographs depict the textures used to classify the clast tectonization types.

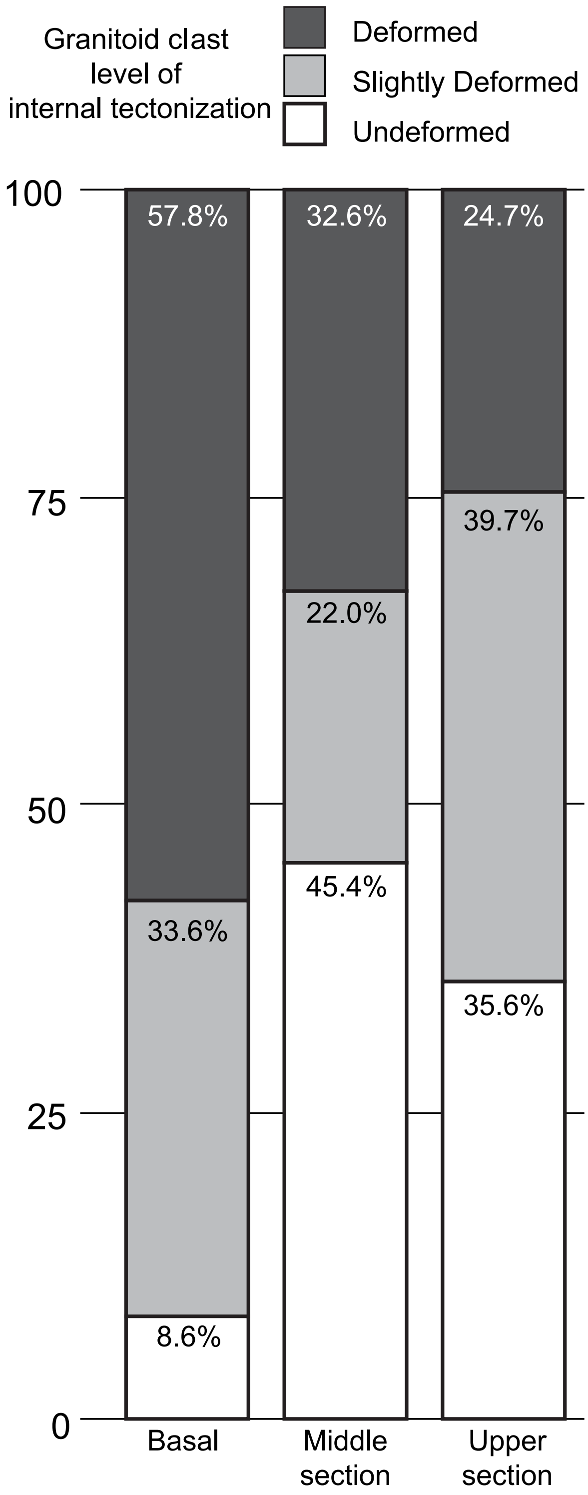

Figure 5.7: Distribution of clast types at each stratigraphic level.

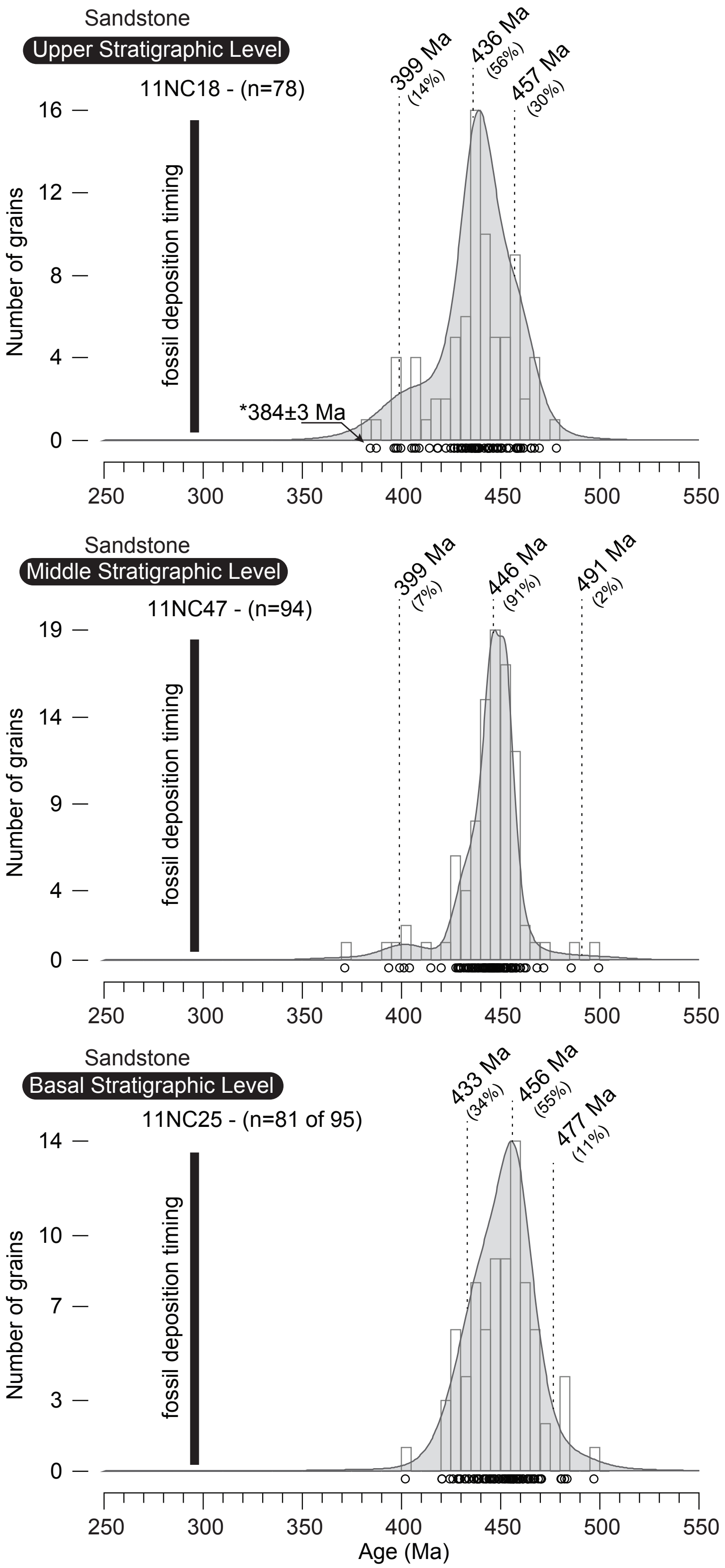

Figure 5.8: Paleozoic sandstone detrital geochronology data kernel density estimate (KDE) (Sircombe and Hazelton, 2004) and histogram plots from across the Hongliuhe Formation stratigraphy. [*]Indicates youngest near-concordant zircon age.

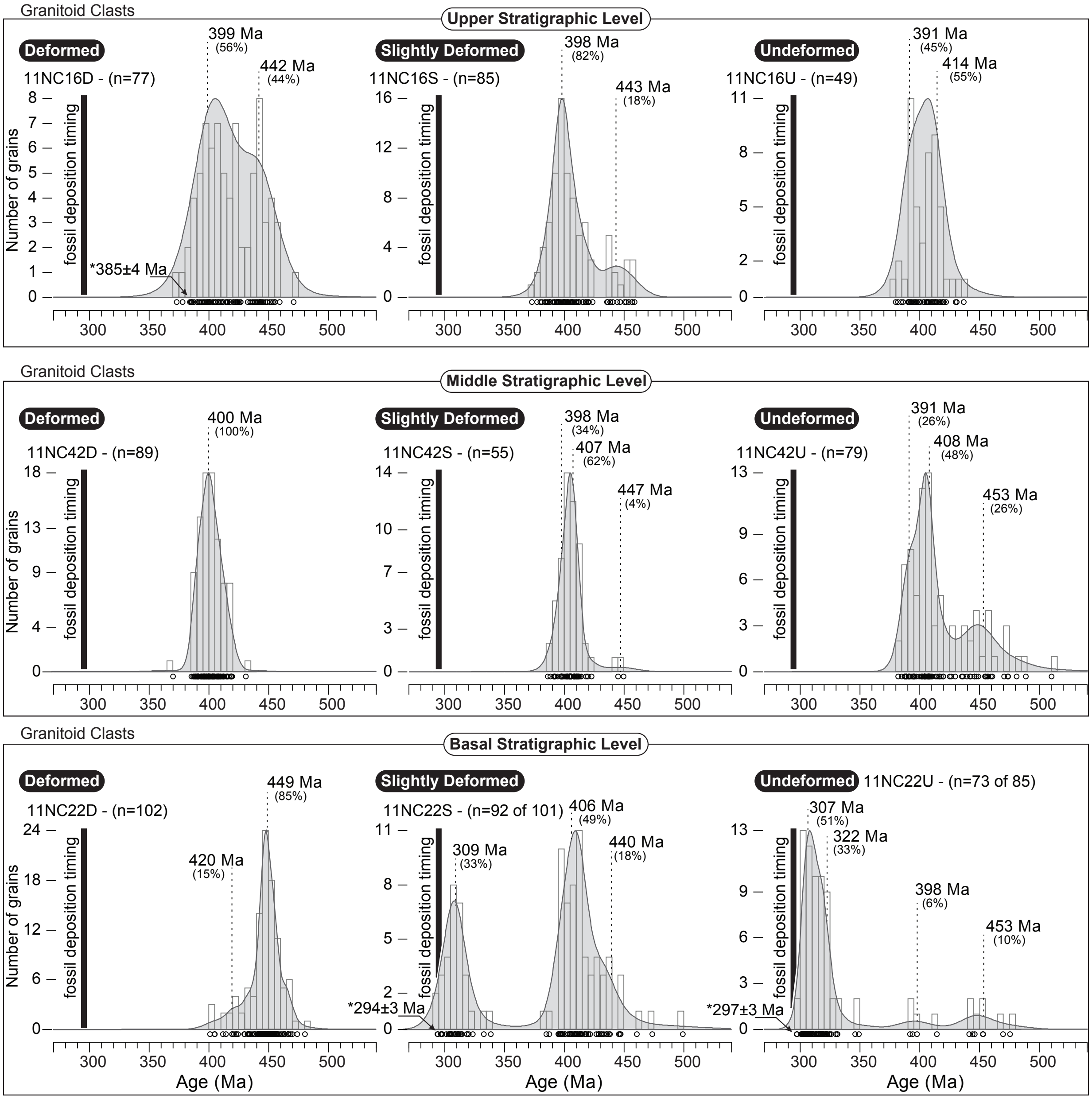

Figure 5.9: Array of paleozoic clast-detrital geochronology data kernel density estimate (KDE) (Sircombe and Hazelton, 2004) and histogram plots from across the Hongliuhe Formation stratigraphy. [*]Indicates youngest near-concordant zircon age of respective tectonization type.

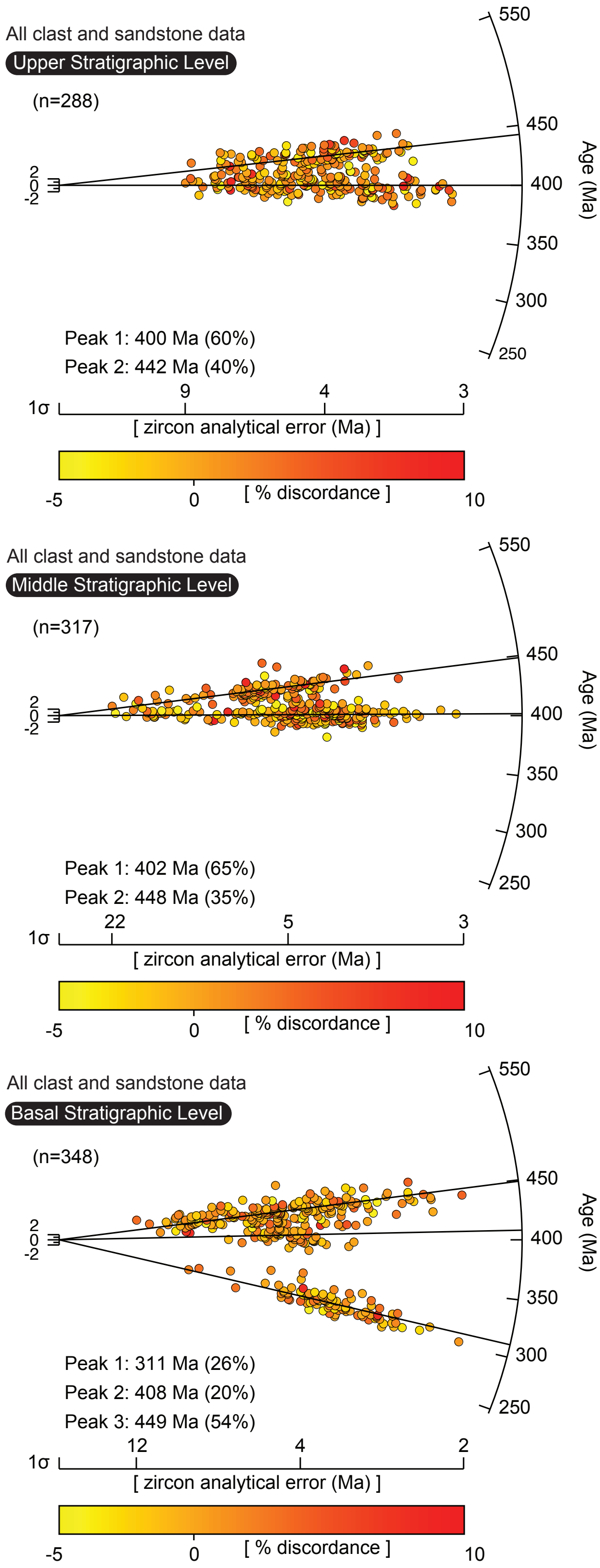

Figure 5.10: Radial plots (Galbraith, 1990) of zircon analytical measurement 1σ error amounts, with percent discordance indicated by color, versus magmatic ages of grains. Measurements from all samples are combined for each stratigraphic level.

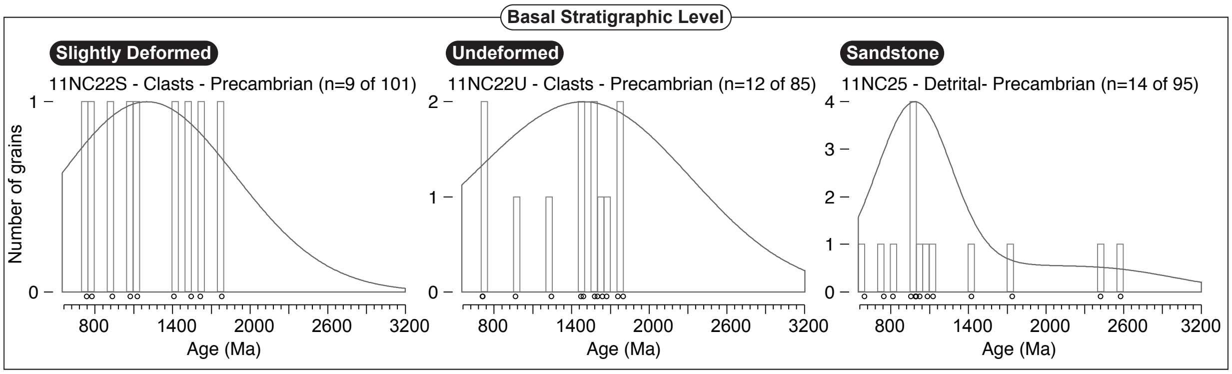

Figure 5.11: Precambrian clast and sandstone detrital geochronology data kernel density estime (KDE) (Sircombe and Hazelton, 2004) and histogram plots from all respective samples, as indicated.

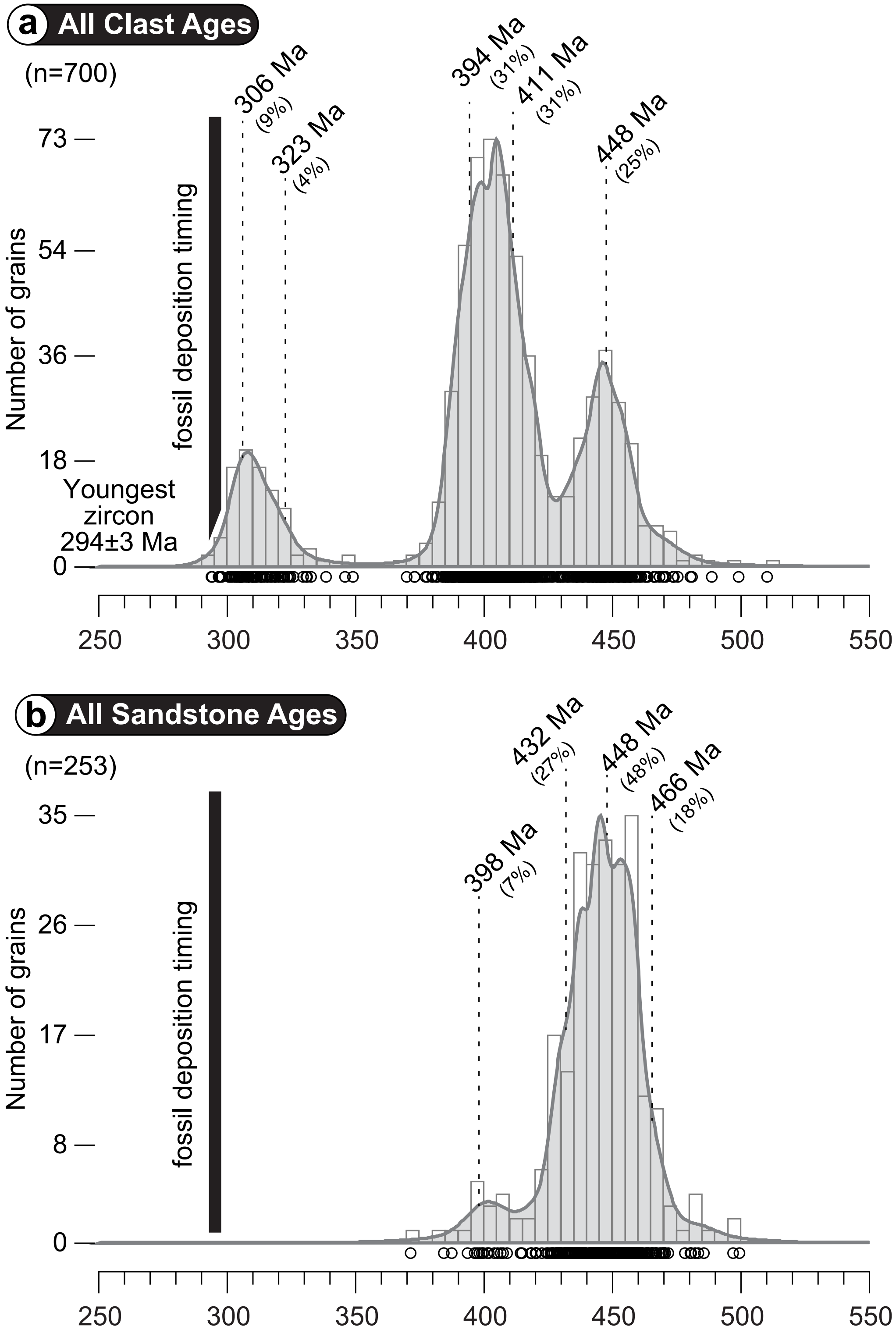

Figure 5.12: Compilation of all clast geochronology data compared to the compilation of all sandstone data.

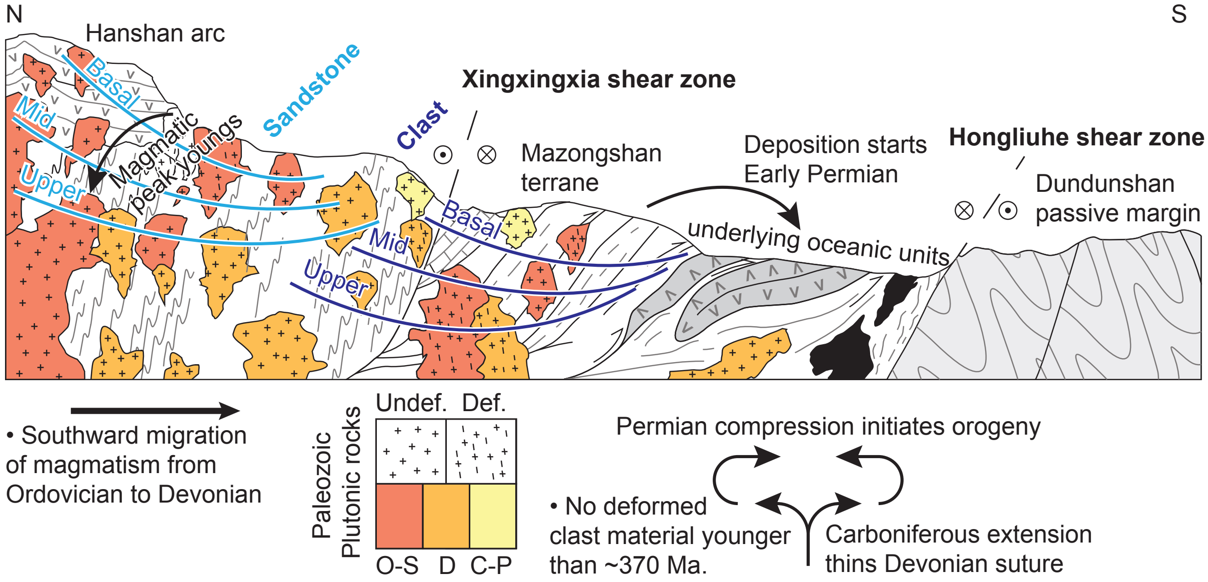

Figure 5.13: Schematic diagram showing proximal and distal provenances for the Hongliuhe Formation, within the tectonic setting of the region. The not-to-scale schematic cartoon cross-section, modified from Cleven et al. (2015), depicts the post-collision Hongliuhe suture in the Devonian-Carboniferous, prior to sedimentation of the Hongliuhe Formation. The light blue (sandstone) and dark blue (clast) lines labeled with Basal, Mid, and Upper refer to the potential material eroded during orogeny and unroofing of the provenance, for each of the respective stratigraphic levels. Key aspects of the signatures seen in the clast detrital geochronology results are displayed in simplified graphics of the plutonic bodies: color denotes age of plutons in the source or provenance, as inferred from the age spectra, (O-S = Ordovician-Silurian, D = Devonian, C-P = Carboniferous-Permian), and the degrees of tectonization are indicated with fill patterns.

Chapter 6

Summary of conclusions

6.1 Preliminary summary

This thesis has focused on elucidating the Paleozoic tectonomagmatic history of the central Beishan orogenic collage before terminal collision. In previous chapters the tectonic history of the Dundunshan, Hanshan, and Mazongshan terranes has been discussed, with particular reference to the proposed Hongliuhe suture that separates the Dundunshan and Hanshan/Mazongshan arcs (Fig. 5.3). Petrogenetic timing and characteristics of the Hongliuhe ophiolite indicate that the southern margin of the Mazongshan terrane is a suture zone. The kinematic evolution of the Hongliuhe and Xingxingxia ductile shear zones, and a series of subordinate faults in between, has been characterized (Fig. 4.2). The results indicate that oblique dextral convergence and collisional tectonics have played a more important role in the early Paleozoic Beishan history than previously considered. In this concluding chapter the main observations and interpretations from the thesis are summarized, and a cartoon of the Neoproterozoic–Late Paleozoic/Early Mesozoic tectonic history of the Beishan orogenic collage is reviewed.

6.2 Main conclusions

6.2.1 Paleozoic magmatic framework

- The combination of the Hanshan and Mazongshan terranes underwent a period of plutonism spanning the late Cambrian through Early Devonian, containing two main age peaks ca. 400 and 450 Ma. After a ca. 50 m.y. hiatus a minor period of plutonism occurred spanning the Carboniferous–Permian (Chapters 2 and 5).

- Magmatism likely migrated south from the Hanshan to Mazongshan terrane for the second peak of early Paleozoic plutonism outlined above (in the Silurian–Devonian, Chapter 5).

- The Mazongshan terrane experienced plutonism during periods of tectonism in the Silurian–Devonian, creating abundant syn-tectonic deformed plutonic bodies (Chapters 4 and 5).

- The Dundunshan terrane underwent a slighter later period of plutonism spanning the Ordovician through Late Devonian, containing two main peaks ca. 430 and 370 Ma, the second subordinate to the first. After a ca. 40 m.y. hiatus a minor period of plutonism occurred spanning the Permian–Early Triassic (Chapter 2).

6.2.2 Suturing processes within accretionary complexes

- Two significant subduction systems were operating in the early Paleozoic to create the early Beishan terranes, and our evidence indicates that their dynamics of subduction initiation and subsequent convergence may be linked, offset by 40-50 m.y. in all respects (Chapter 2).

- The Hanshan, Mazongshan and Dundunshan terranes underwent a staged collision and accretion event in the Paleozoic, first with the Hanshan/Mazongshan overriding the Dundunshan in a protracted collision, then the composite terrane colliding with (likely) the Dunhuang block approximately 40 m.y. later, by the end of the Late Devonian (Chapter 2).

- Oblique convergence and collision between the Hanshan/Mazongshan and Dundunshan terranes resulted in transpressive deformation structures seen in shear zones and formation-scale folding in the Mazongshan terrane (Chapter 4).

- The southern accretionary complex between the Dundunshan terrane from the Dunhuang block may have been separated apart by the Carboniferous development of the Liuyuan complex (Chapter 2). It is now largely covered in modern sediments, leaving the southern margin of the Dundunshan terrane lacking accretion-related structures and units.

- Orogeny was staged in the accretionary zones, and suture zones reactivated as inboard responses to outboard collisions, which resulted in overprinting of deformation (Chapters 4 and 5). The Hongliuhe shear zone represents the plate boundary between the Hanshan/Mazongshan terranes and Dundunshan terrane. It exhibits evidence of reactivation and late high-magnitude strike-slip translation and transpressive deformation (Chapter 4).

6.2.3 Ophiolitic rocks along the Hongliuhe suture

- Subduction rollback episodes played a large role in ophiolite formation in the central Beishan

- Two generations of ophiolite are represented within the Hongliuhe suture, aged Cambrian and Silurian to Early Devonian.

- The Hongliuhe ophiolite is a supra-subduction ophiolite, formed in an extensional arc-marginal environment in the Cambrian.

- The Tianhu volcanic sequences have known geochemistry (Pan et al., 2008) that correlates to portions of known geochemistry of the Huoshishan-Niujuanzi ophiolites (Tian et al., 2014), and both have a supra-subduction affinity. They are both Devonian in age (Chapter 2) and lie along strike from one another on the Tianhu shear zone (Chapter 4). This is the second generation of ophiolite in the Hongliuhe suture, emplaced in fault contact with the Hongliuhe ophiolite package and covered by Permian sedimentary rocks.

6.2.4 Early Paleozoic tectonism

- A period of dextral transpression affected the Mazongshan during the Silurian–Middle Devonian (Chapter 4). This timing correlates to the cessation of magmatism and start of a magmatic hiatus in the region (Chapters 2 and 5). We interpret the deformation to result from oblique convergence and collision.

- The timing of deformation and the kinematics correlate between the Xingxingxia and Tianhu shear zones. The Xingxingxia shear zone represents inboard strain partitioning localized at the backstop of the Mazongshan terrane; it is the boundary between the (Mazongshan) accretionary complex and the Hanshan terrane. The Tianhu shear zone represents the boundary between the Mazongshan terrane metasedimentary rocks and accreted oceanic units. It was oriented more orthogonal to the convergence direction in comparison to the Xingxingxia shear zone, and therefore accumulated more flattening strain and less shear strain. (Chapter 4).

6.2.5 Kinematics of ductile shear zones in the Mazongshan terrane

- The Xingxingxia ductile shear zone has a dextral sense of kinematics along its strike length, most dominantly in E-W oriented segments. This occurred during early Paleozoic regional deformation. The region between the Xingxingxia shear zone and the Tianhu shear zone exhibits penetrative ductile deformation in the form of large, sweeping dextral sigmoidal shapes. The Tianhu is interpreted to be dextral based on uncommon dextral kinematic indicators. The Hongliushu fault is largely obscured by modern sediments, but deformation in the supracrustal succession overlying the Hongliuhe ophiolite indicates it underwent dextral deformation (Chapter 4).

- The Hongliuhe shear zone exhibits dominant sinistral kinematics along its strike length, with rare indications of dextral deformation at the extreme margins. This occurred during late Paleozoic/early Mesozoic regional deformation. The region north of the Hongliuhe shear zone to the Hongliushu fault, involving the Yushishan fault array, underwent widespread sinistral penetrative ductile deformation and exhibits large, sweeping sinistral sigmoidal shapes (Chapter 4).

6.2.6 Evidence of affinities to Precambrian crustal blocks

- Paleozoic magmatism in the Beishan either incorporated, partially melted, or built through rocks with zircon age distributions peaking around 800, 950, 1100, 1400, 1600, 2550 and 3200 Ma (Chapters 2, 4, 5). This distribution of ages most closely represents the age distribution that exists in the Tarim craton.

6.2.7 New methods

- The variably tectonized conglomerate clast population dating technique (Chapter 4) provides an extra dimension of information over standard detrital geochronology. Age spectra relating to degrees of deformation in plutonic rocks can be used to infer tectonic processes and characterize events. Comparison to sandstone age spectra can provide a method for evaluating the effects of source proximity. The technique is particularly useful in highly tectonized regions, and in fault-bounded syn-orogenic deposits. Our application of the technique has established that the Hongliuhe Formation's provenance lies across the Xingxingxia shear zone, known to have had late strike-slip motion (Wang et al., 2010). This precludes the possibility that the magnitude of strike-slip motion is greater than the scale of the terranes.

6.3 Late Neoproterozoic to Early Paleozoic evolution of the Beishan

Synthesizing the data provided in this thesis with previously published data, interpretation, and models, a tectonic history outlining the stages of amalgamation of the Beishan orogenic collage can be constructed. The model included here (Fig. 6.1) focuses directly on the Beishan, and does not include interpretation concerning any lateral continuity with the Tianshan orogen or accretion involving the Siberian margin (such as the Southern Mongolian accretionary system). The components of the cartoon are not drawn to scale. All compass directions referred to are meant in a present-day reference frame.

After the assembly and subsequent breakup of the supercontinent Rodinia ca. 1100-950 Ma a series of pericratonic fragments were isolated in the Paleo-Asian ocean. The Hanshan block, the Huaniushan block, and the Tarim craton all share a distribution of Precambrian ages from continental material, reworked or incorporated crust, and inherited zircon, that are consistent with a shared history (Song et al., 2013c; Wang et al., 2014b; Chapters 2, 4, and 5). The Dunhuang block may similarly share a Precambrian history with the North China craton (Zhang et al., 2013b). There is minor evidence of magmatism during the Late Neoproterozoic (Chapter 2), and most rocks in the Beishan of this age are marginal sedimentary rocks, now metamorphosed. The earliest igneous record in the Beishan are the generation of Cambrian supra-subduction zone ophiolites associated with a subduction rollback event at the margin of an unknown arc or continent, possibly the Hanshan arc (Ao et al., 2012; Chapter 3; Fig. 6.1 A). We interpret that arc magmatism initiated along the southern margin of the Hanshan block in the Late Cambrian and peaked in the Ordovician, creating the Hanshan arc (Chapter 2). Arc magmatism initiated along the southern margin of the Huaniushan block 30-40 m.y. after the Hanshan, and peaked in the Ordovician, creating the Dundunshan arc (Fig. 6.1 B).

During the Silurian to Devonian, magmatism may have migrated into the forearc accretionary complex of the Hanshan terrane (Fig. 6.1 C; Chapter 5), giving the Mazongshan terrane an arc affinity in its plutonic rocks (Song et al., 2013b). Alternatively the second peak of magmatism in the Hanshan/Mazongshan terrane pair may represent a transition to collision and orogenesis. Penetrative ductile deformation in the Tianhu to Xingxingxia region was imparted during protracted oblique convergence and collision with the Dundunshan terrane during the Silurian–Middle Devonian (Fig. 6.1 C; Chapter 4). This event is likely responsible for emplacement of the Hongliuhe ophiolite. The geneses of the Huoshishan-Niujuanzi ophiolites and the Tianhu volcanic sequences, during the Early Devonian, is timed to be coincident with the collision (Tian et al., 2014). These events may have been triggered by slab-breakoff. Magmatism fully ceased in the Hanshan/Mazongshan terranes at the end of the Middle Devonian. Magmatism during the Devonian in the Dundunshan terrane is known to have migrated south (Guo et al., 2014) and include arc signatures (Mao et al., 2012a; Guo et al., 2014) transitioning to collisional

(Li et al., 2011) and intraplate (Zhao et al., 2007; Li et al., 2009b). Magmatism waned and finally ceased at the end of the Late Devonian in the Dundunshan terrane (Chapter 2). This is interpreted to have resulted from collision and accretion of the amalgamated arcs to the northern margin of the Dunhuang block (Fig. 6.1 C).

Post collision intraplate magmatism occurred in the Carboniferous and Permian in the Hanshan/Mazgonshan terranes, and in the Late Carboniferous to Triassic in the Dundunshan terrane (Su et al., 2011; Li et al., 2012; Zhu et al., 2012; Chapter 2). Regional extension accompanied this magmatism, largely localizing into the two suture zones (Fig. 6.1 D). Outboard collision of the Tarim forced inboard convergence, in the weak suture zones, emplacing small, isolated Carboniferous oceanic units (Mao et al., 2012b; Zheng et al., 2013) and initiating syn-orogenic sedimentation and fold-and-thrust belt deformation (Zhang and Cunningham, 2012; Tian et al., 2013; Cleven et al., 2015). Distributed strike-slip tectonics accompanied this, localizing sinistral strike-slip deformation with an unconstrained magnitude along the Hongliuhe suture (Chapter 4) and in segments with NE-SW orientations along the Xingxingxia shear zone (Wang et al., 2010).

6.4 Future directions

Many interpretations made from the research presented in this thesis may be improved by future work. Future directions that workers could take are outlined below.

- Considering the evidence of suturing and accretion within the Mazongshan terrane, it follows that similar structures, lithologies, and relationships should be sought along the southern margin of the Dundunshan terrane. We have noted that this region is largely covered in desert, meaning few researchers have attempted to work there and that there is considerable potential for new discoveries.
- The presence of both Cambrian and Devonian ophiolites along the Hongliuhe suture is a poorly understood phenomenon. Detailed work on this problem may be able to specify multiple accretion events within the timespan of the single event we have proposed.
- The continuity of structures between orogens in the southern CAOB, such as the Beishan and Tianshan, remains poorly constrained. Temporal and tectonic constraints on faulting in the regions linking CAOB orogens should be pursued to improve knowledge of the tectonic framework.

- Further development and refining of the variably tectonized clast detrital geochronology method is greatly encouraged. Workers may test if the method is effective in different settings, regions, or in older (or younger) orogens. Hafnium isotopic methods have great potential for use with the method, and may lead to exciting discoveries.

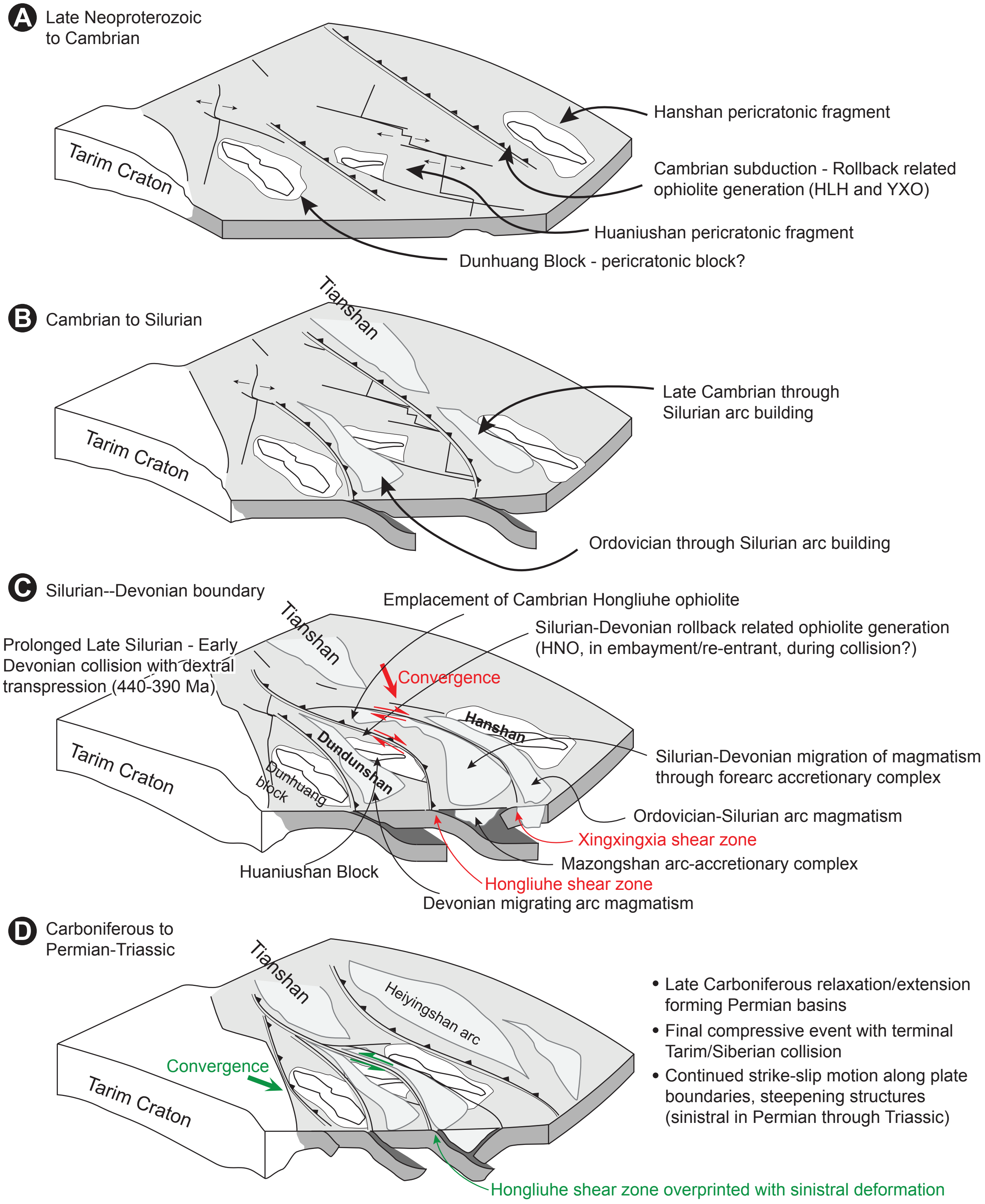

Figure 6.1: Tectonic model of the Paleozoic assembly of the Beishan.

Letters of copyright permission

Supplier	Elsevier Limited
Registered Company Number	1982084
Licensee	Nathan Cleven
License number	3793060192598
License date	January 20th, 2016
Licensed content publisher	Elsevier
Licensed content publication	Journal of Asian Earth Sciences
Licensed content title	Petrogenesis and implications for tectonic setting of Cambrian suprasubduction-zone ophiolitic rocks in the central Beishan orogenic collage, Northwest China
Licensed content author	Nathan Cleven, Shoufa Lin, Carl Guilmette, Wenjiao Xiao, Bill Davis
Licensed content date	December 1st, 2015
Licensed content volume number	113
Number of pages	22
Start Page	369
End Page	390
Type of Use	reuse in a thesis/dissertation
Portion	full article

References

Allen, M. B., A. M. C. Şengör, and B. A. Natal'in, 1995: Junggar, Turfan and Alakol basins as Late Permian to ?Early Triassic extensional structures in a sinistral shear zone in the Altaid orogenic collage, Central Asia. *Journal of the Geological Society, London*, **152**, 327–338.

Allen, M. B., B. F. Windley, and Z. Chi, 1992: Palaeozoic collisional tectonics and magmatism of the Chinese Tien Shan, central asia. *Tectonophysics*, **220**, 89–115.

Amato, J. M. and T. L. Pavlis, 2010: Detrital zircon ages from the Chugach terrane, southern Alaska, reveal multiple episodes of accretion and erosion in a subduction complex. *Geology*, **38 (5)**, 459–462.

Andersen, T., 2005: Detrital zircons as tracers of sedimentary provenance: limiting conditions from statistics and numerical simulation. *Chemical Geology*, **216 (3)**, 249–270.

Angen, J. J., C. R. Van Staal, S. Lin, J. L. Nelson, J. B. Mahoney, D. W. Davis, and W. C. McClelland, 2014: Kinematics and timing of shear zone deformation in the western Coast Belt: evidence for mid-Cretaceous orogen-parallel extension. *Journal of Structural Geology*, **68**, 273–299.

Anonymous, 1997: Geological Map of Tianshan and Adjacent Areas, 1:1,000,000. *Geology Publishing House*, (in Chinese).

Ao, S.-J., W.-J. Xiao, C.-M. Han, X.-H. Li, J.-F. Qu, J. Zhang, Q.-Q. Guo, and Z.-H. Tian, 2012: Cambrian to early Silurian ophiolite and accretionary processes in the Beishan collage, NW China: implications for the architecture of the Southern Altaids. *Geological Magazine*, **149 (04)**, 606–625.

Arai, S., 1992: Chemistry of chromian spinel in volcanic rocks as a potential guide to magma chemistry. *Mineralogical Magazine*, **56 (383)**, 173–184.

Barnes, S. J. and P. L. Roeder, 2001: The range of spinel compositions in terrestrial mafic and ultramafic rocks. *Journal of Petrology*, **42 (12)**, 2279–2302.

Bédard, J., 1999: Petrogenesis of boninites from the Betts Cove ophiolite, Newfoundland, Canada: identification of subducted source components. *Journal of Petrology*, **40 (12)**, 1853–1889.

Bernet, M., M. Zattin, J. I. Garver, M. T. Brandon, and J. A. Vance, 2001: Steady-state exhumation of the European Alps. *Geology*, **29 (1)**, 35–38.

Buckman, S. and J. C. Aitchison, 2004: Tectonic evolution of Palaeozoic terranes in West Junggar, Xinjiang, NW China. *Geological Society, London, Special Publications*, **226**, 101–129.

Carter, A. and C. Bristow, 2000: Detrital zircon geochronology: enhancing the quality of sedimentary source information through improved methodology and combined U–Pb and fission-track techniques. *Basin Research*, **12 (1)**, 47–57.

Cawood, P. A., C. Hawkesworth, and B. Dhuime, 2012: Detrital zircon record and tectonic setting. *Geology*, **40 (10)**, 875–878.

Charvet, J., L.-S. Shu, and S. Laurent-Charvet, 2007: Paleozoic structural and geodynamic evolution of eastern Tianshan (NW China): welding of the Tarim and Junggar plates. *Episodes: International Union of Geological Sciences*, **30 (3)**, 162–186.

Chen, B., B. Jahn, and W. Tian, 2009: Evolution of the Solonker suture zone: constraints from zircon U–Pb ages, Hf isotopic ratios and whole-rock Nd–Sr isotope compositions of subduction-and collision-related magmas and forearc sediments. *Journal of Asian Earth Sciences*, **34 (3)**, 245–257.

Chen, C.-M., H.-F. Lu, D. Jia, D.-S. Cai, and S.-M. Wu, 1999: Closing history of the southern Tianshan oceanic basin, western China: an oblique collisional orogeny. *Tectonophysics*, **302**, 23–40.

Choulet, F., M. Faure, D. Cluzel, Y. Chen, W. Lin, and B. Wang, 2012: From oblique accretion to transpression in the evolution of the Altaid collage: New insights from West Junggar, northwestern China. *Gondwana Research*, **21 (2)**, 530–547.

Cleven, N. R., S. Lin, and W.-J. Xiao, 2015: The Hongliuhe fold-and-thrust belt: evidence of terminal collision and suture-reactivation after the Early Permian in the Beishan orogenic collage, Northwest China. *Gondwana Research*, **27 (2)**, 796–810.

Coleman, R. G., 1989: Continental growth of northwest china. *Tectonics*, **8 (3)**, 621–635.

Condie, K. C., 2014: Growth of continental crust: a balance between preservation and recycling. *Mineralogical Magazine*, **78 (3)**, 623–637.

Constantin, M., 1999: Gabbroic intrusions and magmatic metasomatism in harzburgites from the Garrett transform fault: implications for the nature of the mantle–crust transition at fast-spreading ridges. *Contributions to Mineralogy and Petrology*, **136 (1-2)**, 111–130.

Constantin, M., R. Hékinian, D. Ackermand, and P. Stoffers, 1995: Mafic and ultramafic intrusions into upper mantle peridotites from fast spreading centers of the Easter Microplate (South East Pacific). *Mantle and lower crust exposed in oceanic ridges and in ophiolites*, Springer, 71–120.

Cousineau, P. A. and J. H. Bédard, 2000: Sedimentation in a subaqueous arc/back-arc setting: the Bobby Cove Formation, Snooks Arms Group, Newfoundland. *Precambrian Research*, **101 (2)**, 111–134.

Cunningham, D., 2013: Mountain building processes in intracontinental oblique deformation belts: Lessons from the Gobi Corridor, Central Asia. *Journal of Structural Geology*, **46**, 255–282.

Czeck, D. M. and P. J. Hudleston, 2003: Testing models for obliquely plunging lineations in transpression: a natural example and theoretical discussion. *Journal of Structural Geology*, **25 (6)**, 959–982.

Czeck, D. M. and P. J. Hudleston, 2004: Physical experiments of vertical transpression with localized nonvertical extrusion. *Journal of Structural Geology*, **26 (3)**, 573–581.

Dick, H. J. and T. Bullen, 1984: Chromian spinel as a petrogenetic indicator in abyssal and alpine-type peridotites and spatially associated lavas. *Contributions to Mineralogy and Petrology*, **86 (1)**, 54–76.

Dilek, Y. and H. Furnes, 2009: Structure and geochemistry of Tethyan ophiolites and their petrogenesis in subduction rollback systems. *Lithos*, **113 (1)**, 1–20.

Dilek, Y. and H. Furnes, 2011: Ophiolite genesis and global tectonics: Geochemical and tectonic fingerprinting of ancient oceanic lithosphere. *Geological Society of America Bulletin*, **123 (3-4)**, 387–411.

Dilek, Y., H. Furnes, and M. Shallo, 2008: Geochemistry of the Jurassic Mirdita Ophiolite (Albania) and the MORB to SSZ evolution of a marginal basin oceanic crust. *Lithos*, **100 (1)**, 174–209.

Dilek, Y. and P. Thy, 2009: Island arc tholeiite to boninitic melt evolution of the Cretaceous Kizildag (Turkey) ophiolite: model for multi-stage early arc–forearc magmatism in Tethyan subduction factories. *Lithos*, **113 (1)**, 68–87.

Dong, Y., G. Zhang, F. Neubauer, X. Liu, C. Hauzenberger, D. Zhou, and W. Li, 2011: Syn- and post-collisional granitoids in the Central Tianshan orogen: geochemistry, geochronology and implications for tectonic evolution. *Gondwana Research*, **20 (2)**, 568–581.

Dunkl, I., W. Frisch, J. Kuhlemann, and A. Brügel, 2009: Pebble population dating as an additional tool for provenance studies-examples from the Eastern Alps. *Geological Society, London, Special Publications*, **324 (1)**, 125–140.

Eizenhöfer, P. R., G. Zhao, J. Zhang, and M. Sun, 2014: Final closure of the Paleo-Asian Ocean along the Solonker Suture Zone: Constraints from geochronological and geochemical data of Permian volcanic and sedimentary rocks. *Tectonics*.

Fedo, C. M., K. N. Sircombe, and R. H. Rainbird, 2003: Detrital zircon analysis of the sedimentary record. *Reviews in Mineralogy and Geochemistry*, **53 (1)**, 277–303.

Galbraith, R. F., 1990: The radial plot: Graphical assessment of spread in ages. *International Journal of Radiation Applications and Instrumentation, Part D, Nuclear Tracks and Radiation Measurements*, **17 (3)**, 207 – 214.

Gao, J., R. Klemd, Q. Qian, X. Zhang, J. Li, T. Jiang, and Y. Yang, 2011: The collision between the Yili and Tarim blocks of the Southwestern Altaids: geochemical and age constraints of a leucogranite dike crosscutting the HP–LT metamorphic belt in the Chinese Tianshan Orogen. *Tectonophysics*, **499 (1)**, 118–131.

Gao, J., M.-S. Li, X.-C. Xiao, Y.-Q. Tang, and G.-Q. He, 1998: Paleozoic tectonic evolution of the Tianshan Orogen, northwestern China. *Tectonophysics*, **287**, 213–231.

Gehrels, G., 2011: Detrital zircon U-Pb geochronology: Current methods and new opportunities. *Tectonics of sedimentary basins: recent advances*, 45–62.

Guilmette, C., R. Hébert, C. Wang, and M. Villeneuve, 2009: Geochemistry and geochronology of the metamorphic sole underlying the Xigaze ophiolite, Yarlung Zangbo Suture Zone, south Tibet. *Lithos*, **112 (1)**, 149–162.

Guo, Q.-Q., W.-J. Xiao, Q. Hou, B. F. Windley, C.-M. Han, Z.-H. Tian, and D.-F. Song, 2014: Construction of Late Devonian Dundunshan arc in the Beishan orogen and its implication for tectonics of southern Central Asian Orogenic Belt. *Lithos*, **184-187**, 361–378.

Guo, Q.-Q., W.-J. Xiao, B. F. Windley, Q.-G. Mao, C.-M. Han, J.-F. Qu, S.-J. Ao, J.-L. Li, D.-F. Song, and Y. Yong, 2012: Provenance and tectonic settings of Permian turbidites from the Beishan Mountains, NW China: implications for the Late Paleozoic accretionary tectonics of the southern Altaids. *Journal of Asian Earth Sciences*, **49**, 54–68.

Harper, G. D., 2003: Tectonic implications of boninite, arc tholeiite, and MORB magma types in the Josephine Ophiolite, California-Oregon. *Geological Society, London, Special Publications*, **218 (1)**, 207–230.

He, Z.-Y., Z.-M. Zhang, K.-Q. Zong, W. Wang, and F. Yu, 2012: Zircon geochronology of Xingxingxia quartz dioritic gneisses: Implications for the tectonic evolution and Precambrian basement affinity of Chinese Tianshan orogenic belt. *Acta Petrologica Sinica*, **28 (6)**, 1857 – 1874 (In Chinese with English abstract).

He, Z.-Y., Z.-M. Zhang, K.-Q. Zong, H. Xiang, and R. Klemd, 2014a: Metamorphic P–T–t evolution of mafic HP granulites in the northeastern segment of the Tarim Craton (Dunhuang block): Evidence for early Paleozoic continental subduction. *Lithos*, **196**, 1–13.

He, Z.-Y., K.-Q. Zong, H.-Y. Jiang, H. Xiang, and Z.-M. Zhang, 2014b: Early Paleozoic tectonic evolution of the southern Beishan orogenic collage: Insights from the granitoids. *Acta Petrologica Sinica*, **30 (8)**, 2324–2338 (In Chinese with English abstract).

Hébert, R., R. Bezard, C. Guilmette, J. Dostal, C. Wang, and Z. Liu, 2012: The Indus–Yarlung Zangbo ophiolites from Nanga Parbat to Namche Barwa syntaxes, southern Tibet: first synthesis of petrology, geochemistry, and geochronology with incidences on geodynamic reconstructions of Neo-Tethys. *Gondwana Research*, **22 (2)**, 377–397.

Hébert, R., F. Huot, C. Wang, and Z. Liu, 2003: Yarlung Zangbo ophiolites (Southern Tibet) revisited: geodynamic implications from the mineral record. *Geological Society, London, Special Publications*, **218 (1)**, 165–190.

Hsü, K. J., 2003: Role of ophiolites in archipelago model of orogenesis. *Geological Society of America Special Paper*, **373**, 159–172.

Hsü, K. J., Y.-Y. Yao, J. Hao, P. Hsü, J.-L. Li, and Q.-C. Wang, 1994: Origin of Chinese Tianshan by Arc-Arc Collisions. *Eclogae Geologicae Helvetiae*, **87 (1)**, 265–292.

Hu, A.-Q., G.-J. Wei, B.-M. Jahn, J.-B. Zhang, W.-F. Deng, and L.-L. Chen, 2010: Formation of the 0.9 Ga Neoproterozoic granitoids in the Tianshan Orogen, NW China: Constraints from the SHRIMP zircon age determination and its tectonic significance. *Geochimica*, **39 (3)**, 197– 212 (In Chinese with English abstract).

Hu, A.-Q., G.-J. Wei, J.-B. Zhang, W.-F. Deng, and L.-L. Chen, 2007: SHRIMP U-Pb age for zicons of East Tianhu granitic gneiss and tectonic evolution significance from the eastern Tianshan mountains, Xinjiang, China. *Acta Petrologica Sinica*, **23 (8)**, 1795–1802 (In Chinese with English abstract).

Jahn, B.-M., F.-Y. Wu, and B. Chen, 2001: Growth of Asia in the Phanerozoic–Nd isotopic evidence. *Gondwana Research*, **4 (4)**, 640–642.

Jian, P., D. Liu, A. Kröner, B. F. Windley, Y. Shi, F. Zhang, G. Shi, L. Miao, W. Zhang, Q. Zhang, et al., 2008: Time scale of an early to mid-Paleozoic orogenic cycle of the long-lived Central Asian Orogenic Belt, Inner Mongolia of China: implications for continental growth. *Lithos*, **101 (3)**, 233–259.

Jian, P., D. Liu, A. Kröner, B. F. Windley, Y. Shi, W. Zhang, F. Zhang, L. Miao, L. Zhang, and D. Tomurhuu, 2010: Evolution of a Permian intraoceanic arc–trench system in the Solonker suture zone, Central Asian Orogenic Belt, China and Mongolia. *Lithos*, **118 (1)**, 169–190.

Jiang, D., 2007: Sustainable transpression: an examination of strain and kinematics in deforming zones with migrating boundaries. *Journal of Structural Geology*, **29 (12)**, 1984–2005.

Jiang, D., 2012: A general approach for modeling the motion of rigid and deformable ellipsoids in ductile flows. *Computers and Geosciences*.

Jiang, D., 2014: Structural geology meets micromechanics: A self-consistent model for the multiscale deformation and fabric development in Earth's ductile lithosphere. *Journal of Structural Geology*, **68**, 247–272.

Jiang, D., S. Lin, and P. F. Williams, 1998: Deformation path in high-strain zones, with reference to slip partitioning in transpressional plate-boundary regions. *Journal of Structural Geology*, **20 (8)**, 1105–1120.

Jiang, D. and P. F. Williams, 1998: High-strain zones: a unified model. *Journal of Structural Geology*, **20 (8)**, 1105–1120.

Kamenetsky, V. S., A. J. Crawford, S. Eggins, and R. Mühe, 1997: Phenocryst and melt inclusion chemistry of near-axis seamounts, Valu Fa Ridge, Lau Basin: insight into mantle wedge melting and the addition of subduction components. *Earth and Planetary Science Letters*, **151 (3)**, 205–223.

Kamenetsky, V. S., A. J. Crawford, and S. Meffre, 2001: Factors controlling chemistry of magmatic spinel: an empirical study of associated olivine, Cr-spinel and melt inclusions from primitive rocks. *Journal of Petrology*, **42 (4)**, 655–671.

Kelemen, P., K. Hanghøj, and A. Greene, 2003: One view of the geochemistry of subduction-related magmatic arcs, with an emphasis on primitive andesite and lower crust. *Treatise on geochemistry*, **3**, 593–659.

Kessler, L. and J. Bédard, 2000: Epiclastic volcanic debrites-evidence of flow transformations between avalanche and debris flow processes, Middle Ordovician, Baie Verte Peninsula, Newfoundland, Canada. *Precambrian Research*, **101 (2)**, 135–161.

Kokelaar, P., 1986: Magma-water interactions in subaqueous and emergent basaltic volcanism. *Bulletin of Volcanology*, **48 (5)**, 275–289.

Kröner, A., V. Kovach, E. Belousova, E. Hegner, R. Armstrong, A. Dolgopolova, R. Seltmann, D. Alexeiev, J. Hoffmann, J. Wong, et al., 2014: Reassessment of continental growth during the accretionary history of the Central Asian Orogenic Belt. *Gondwana Research*, **25 (1)**, 103–125.

Kröner, A., B. Windley, G. Badarch, O. Tomurtogoo, E. Hegner, B. Jahn, S. Gruschka, E. Khain, A. Demoux, and M. Wingate, 2007: Accretionary growth and crust formation in the Central Asian Orogenic Belt and comparison with the Arabian-Nubian shield. *Geological Society of America Memoirs*, **200**, 181–209.

Kuiper, Y. and D. Jiang, 2010: Kinematic of deformation constructed from deformed planar and linear elements: The method and its application. *Tectonophysics*, **492**, 175–191.

Kuiper, Y. D., S. Lin, and D. Jiang, 2011: Deformation partitioning in transpressional shear zones with an along-strike stretch component: An example from the Superior Boundary Zone, Manitoba, Canada. *Journal of Structural Geology*, **33 (3)**, 192–202.

Kusky, T. M., D. C. Bradley, and P. Haeussler, 1997: Progressive deformation of the Chugach accretionary complex, Alaska, during a Paleogene ridge-trench encounter. *Journal of Structural Geology*, **19 (2)**, 139–157.

Laurent-Charvet, S., J. Charvet, P. Monié, and L.-S. Shu, 2003: Late Paleozoic strike-slip shear zones in eastern central Asia (NW China): New structural and geochronological data. *Tectonics*, **22 (2)**, 1009.

Laurent-Charvet, S., J. Charvet, L.-S. Shu, R.-S. Ma, and H.-F. Lu, 2002: Palaeozoic late collisional strike-slip deformations in Tianshan and Altay, Eastern Xinjiang, NW China. *Terra-Nova*, **14**, 249–256.

Lehmann, J., K. Schulmann, O. Lexa, M. Corsini, A. Kröner, P. Štípská, D. Tomurhuu, and D. Otgonbator, 2010: Structural constraints on the evolution of the Central Asian Orogenic Belt in SW Mongolia. *American Journal of Science*, **310 (7)**, 575–628.

Lei, R.-X., C.-Z. Wu, L.-X. Gu, Z.-Z. Zhang, G.-X. Chi, and Y.-H. Jiang, 2011: Zircon U–Pb chronology and Hf isotope of the Xingxingxia granodiorite from the Central Tianshan zone (NW China): Implications for the tectonic evolution of the southern Altaids. *Gondwana Research*, **20**, 582 – 593.

Lei, R.-X., C.-Z. Wu, X. Qu, and L.-X. Gu, 2014: Geochronology, geochemistry and zircon Hf isotope compositions of the ore-bearing gneiss granite in the Tianhudong iron-molybdenum ore deposit in the Central Tianshan, West China: Implications for the Early Paleozoic tectonic evolution of Central Tianshan. *Journal of Jilin University (Earth Science Edition)*, **44 (5)**, 1540 – 1552 (In Chinese with English abstract).

Li, J.-B., X. Kang, T. Wang, W.-P. Li, and Y. Tong, 2006: Establishment of the Early Permian Hongliuhe Group in the Beishan area on the border region of Xinjian and Gansu, China. *Acta Petrologica Sinica*, **25 (4)**, 465–468 (in Chinese with English abstract).

Li, Q.-G., S.-W. Liu, B. Song, Y.-B. Wang, and Y.-Z. Chen, 2009a: Late Mesoproterozoic to Paleozoic tectonothermal events in the eastern segment of the Central Tianshan Tectonic Zone of Northwestern China: Constraints from SHRIMP zircon geochronology. *Earth Science Frontiers (China University of Geosciences, Beijing: Peking University*, **16 (2)**, 175–184 (In Chinese with English abstract).

Li, S., T. Wang, Y. Tong, D.-W. Hong, and Z.-X. Ouyang, 2009b: Identification of the Early Devonian Shuangfengshan A-type granites in Liuyuan area of Beishan and its implications to tectonic evolution. *Acta Petrologica et Mineralogica*, **28 (5)**, 407–422 (In Chinese with English abstract).

Li, S., T. Wang, S. A. Wilde, Y. Tong, D. Hong, and Q.-Q. Guo, 2012: Geochronology, petrogenesis and tectonic implications of Triassic granitoids from Beishan, NW China. *Lithos*, **134**, 123–145.

Li, W.-P., T. Wang, J.-B. Li, X. Kang, F.-S. Yu, Q.-J. Han, and Z.-P. Ma, 2001: The U-Pb age of zircon from Late Caledonian granitoids in Hongliuhe area, East Tianshan mountains, Northwest China and its geological implications. *Acta Geoscientia Sinica*, **22 (3)**, 231–235 (In Chinese with English abstract).

Li, X.-M., J.-Y. Yu, G.-Q. Wang, P. Wu, and Z.-Q. Zhou, 2011: LA-ICP-MS zircon U-Pb dating of Devonian Sangejing Formation and Dundunshan Group in Hongliuyuan, Beishan area, Gansu Province. *Geological Bulletin of China*, **30 (10)**, 1501– 1507 (In Chinese with English abstract).

Li, Y.-J., Z.-M. Wang, H.-R. Wu, Z.-B. Huang, Z.-J. Tan, and J.-C. Luo, 2002: Discovery of Radiolarian Fossils from the Aiketik Group at the Western End of the South Tianshan Mountains of China and Its Implications. *Acta Geologica Sinica*, **76 (2)**, 146–154.

Lin, S. and D. Jiang, 2001: Using along-strike variation in strain and kinematics to define the movement direction of curved transpressional shear zones: an example from northwestern Superior Province, Manitoba. *Geology*, **29 (9)**, 767–770.

Lin, S., D. Jiang, and P. F. Williams, 1998: Transpression (or transtension) zones of triclinic symmetry: Natural example and theoretical modeling. *Geological Society of London, Special Publications*, **135**, 41–57.

Liu, S., T. Qian, W. Li, G. Dou, and P. Wu, 2015: Oblique closure of the northeastern Paleo-Tethys in central China. *Tectonics*, **34 (3)**, 413–434.

Ludwig, K., 2003: User's manual for Isoplot 3.00 a geochronological toolkit for Excel. *Berkeley Geochronological Center Special Publication*, **4**, 71.

Ludwig, K. R., 1998: On the treatment of concordant uranium-lead ages. *Geochimica et Cosmochimica Acta*, **62 (4)**, 665–676.

Ma, X.-X., L.-S. Shu, B.-M. Jahn, W.-B. Zhu, and M. Faure, 2012: Precambrian tectonic evolution of Central Tianshan, NW China: constraints from U–Pb dating and in situ Hf isotopic analysis of detrital zircons. *Precambrian Research*, **222**, 450–473.

Ma, X.-X., L.-S. Shu, J. G. Meert, and J.-Y. Li, 2014: The paleozoic evolution of Central Tianshan: Geochemical and geochronological evidence. *Gondwana Research*, **25 (2)**, 797–819.

Mao, Q.-G., 2008: Paleozoic to Early Mesozoic Accretionary and Collisional Tectonics of the Beishan and Adjacent area, Northwest China. *PhD thesis, unpublished*, (In Chinese with English abstract).

Mao, Q.-G., W.-J. Xiao, T.-H. Fang, J.-B. Wang, C.-M. Han, M. Sun, and C. Yuan, 2012a: Late Ordovician to early Devonian adakites and Nb-enriched basalts in the Liuyuan area, Beishan, NW China: implications for early Paleozoic slab-melting and crustal growth in the southern Altaids. *Gondwana Research*, **22 (2)**, 534–553.

Mao, Q.-G., W.-J. Xiao, B. F. Windley, C.-M. Han, J.-F. Qu, S.-J. Ao, J. Zhang, and Q.-Q. Guo, 2012b: The Liuyuan complex in the Beishan, NW China: a Carboniferous–Permian ophiolitic fore-arc sliver in the southern Altaids. *Geological Magazine*, **149 (03)**, 483–506.

Mercier, J. C. and A. Nicolas, 1975: Textures and fabrics of upper-mantle peridotites as illustrated by xenoliths from basalts. *Journal of Petrology*, **16 (2)**, 454–487.

Metcalf, R. V. and J. W. Shervais, 2008: Suprasubduction-zone ophiolites: Is there really an ophiolite conundrum? *Geological Society of America, Special Papers*, **438**, 191.

Metzger, E. P., R. B. Miller, and G. D. Harper, 2002: Geochemistry and tectonic setting of the ophiolitic Ingalls complex, North Cascades, Washington: implications for correlations of Jurassic cordilleran ophiolites. *Journal of Geology*, **110 (5)**, 543–560.

Moecher, D. P. and S. D. Samson, 2006: Differential zircon fertility of source terranes and natural bias in the detrital zircon record: Implications for sedimentary provenance analysis. *Earth and Planetary Science Letters*, **247 (3)**, 252–266.

Pagé, P., J. H. Bédard, J.-M. Schroetter, and A. Tremblay, 2008: Mantle petrology and mineralogy of the Thetford Mines ophiolite complex. *Lithos*, **100 (1)**, 255–292.

Pagé, P., J. H. Bédard, and A. Tremblay, 2009: Geochemical variations in a depleted fore-arc mantle: The Ordovician Thetford Mines ophiolite. *Lithos*, **113 (1)**, 21–47.

Pan, J.-H., Z.-J. Guo, C. Liu, and Z.-H. Zhao, 2008: Geochronology, geochemistry and tectonic implications of Permian basalts in Hongliuhe area on the border between Xinjian and Gansu. *Acta Petrologica Sinica*, **24 (4)**, 793–802 (in Chinese with English abstract).

Passchier, C. and C. Simpson, 1986: Porphyroclast systems as kinematic indicators. *Journal of Structural Geology*, **8 (8)**, 831–843.

Pearce, J. A., 1996: A user's guide to basalt discrimination diagrams. *Trace element geochemistry of volcanic rocks: applications for massive sulphide exploration, Geological Association of Canada, Short Course Notes*, **12**, 79–113.

Pearce, J. A. and P. T. Robinson, 2010: The Troodos ophiolitic complex probably formed in a subduction initiation, slab edge setting. *Gondwana Research*, **18 (1)**, 60–81.

Pirajno, F., J.-W. Mao, Z.-C. Zhang, Z.-H. Zhang, and F.-M. Chai, 2002: The association of mafic-ultramafic intrusions and A-type magmatism in the Tian Shan and Altay orogens, NW China: Implications for geodynamic evolution and potential for the discovery of new ore deposits. *Journal of Asian Earth Sciences*, **32**, 165–183.

Qu, J.-F., W.-J. Xiao, B. F. Windley, C.-M. Han, Q.-G. Mao, S.-J. Ao, and J. Zhang, 2011: Ordovician eclogites from the Chinese Beishan: implications for the tectonic evolution of the southern Altaids. *Journal of Metamorphic Geology*, **29 (8)**, 803–820.

Rojas-Agramonte, Y., A. Kröner, A. Demoux, X. Xia, W. Wang, T. Donskaya, D. Liu, and M. Sun, 2011: Detrital and xenocrystic zircon ages from Neoproterozoic to Palaeozoic arc terranes of Mongolia: significance for the origin of crustal fragments in the Central Asian Orogenic Belt. *Gondwana Research*, **19 (3)**, 751–763.

Safonova, I., R. Seltmann, A. Kröner, D. Gladkochub, K. Schulmann, W.-J. Xiao, J. Kim, T. Komiya, and M. Sun, 2011: A new concept of continental construction in the Central Asian Orogenic Belt. *Episodes*, **34 (3)**, 186.

Schroetter, J.-M., P. Pagé, J. H. Bédard, A. Tremblay, and V. Bécu, 2003: Forearc extension and sea-floor spreading in the Thetford Mines ophiolite complex. *Geological Society, London, Special Publications*, **218**, 231–252.

Schulmann, K. and S. Paterson, 2011: Geodynamics: Asian continental growth. *Nature Geoscience*, **4 (12)**, 827–829.

Şengör, A. M. C. and B. A. Natal'in, 2007: *Magmatism and Metallogeny of the Altai and Adjacent Large Igneous Provinces with an Introductory Essay on the Altaids: Eduard Suess and the Altaids: what is in a name?* CERCAMS/NHM.

Şengör, A. M. C., B. A. Natal'in, and V. S. Burtman, 1993: Evolution of the Altaid tectonic collage and Palaeozoic crustal growth in Eurasia. *Nature*, **364**, 299–307.

Shi, Y.-R., P. Jian, A. Kröner, B.-M. Jahn, D.-Y. Liu, W. Zhang, and H.-D. Ma, 2014: Zircon ages and Hf isotopic compositions of plutonic rocks from the Central Tianshan (Xinjiang, northwest China) and their significance for early to mid-Palaeozoic crustal evolution. *International Geology Review*, **56 (11)**, 1413–1434.

Shu, L., J. Charvet, L. Guo, H. Lu, and S. Laurent-Charvet, 1999: A large-scale Palaeozoic dextral ductile strike-slip zone: the Aqqikkudug-Weiya Zone along the northern margin of the Central Tianshan belt, Xinjiang, NW China. *Acta Geologica Sinica*, **73 (2)**, 148–162.

Sircombe, K. and M. Hazelton, 2004: Comparison of detrital zircon age distributions by kernel functional estimation. *Sedimentary Geology*, **171 (1)**, 91–111.

Song, D.-F., W.-J. Xiao, C.-M. Han, J.-L. Li, J.-F. Qu, Q.-Q. Guo, L. Lin, and Z.-M. Wang, 2013a: Progressive accretionary tectonics of the Beishan orogenic collage, southern Altaids: insights from zircon U–Pb and Hf isotopic data of high-grade complexes. *Precambrian Research*, **227**, 368–388.

Song, D.-F., W.-J. Xiao, C.-M. Han, and Z.-H. Tian, 2013b: Geochronological and geochemical study of gneiss–schist complexes and associated granitoids, Beishan Orogen, southern Altaids. *International Geology Review*, **55 (14)**, 1705–1727.

Song, D.-F., W.-J. Xiao, C.-M. Han, and Z.-H. Tian, 2014: Polyphase deformation of a Paleozoic forearc-arc complex in the Beishan orogen, NW China. *Tectonophysics*, **632**, 224–243.

Song, D.-F., W.-J. Xiao, C.-M. Han, Z.-H. Tian, and Z.-M. Wang, 2013c: Provenance of metasedimentary rocks from the Beishan orogenic collage, southern Altaids: Constraints from detrital zircon U–Pb and Hf isotopic data. *Gondwana Research*, **24 (3)**, 1127–1151.

Spaggiari, C. V., D. R. Gray, and D. A. Foster, 2004: Ophiolite accretion in the Lachlan Orogen, southeastern Australia. *Journal of Structural Geology*, **26 (1)**, 87–112.

Stern, C. R. and M. J. De Wit, 2003: Rocas Verdes ophiolites, southernmost South America: remnants of progressive stages of development of oceanic-type crust in a continental margin back-arc basin. *Geological Society, London, Special Publications*, **218 (1)**, 665–683.

Stern, R., 1997: The GSC Sensitive High Resolution Ion Microprobe (SHRIMP): analytical techniques of zircon U-Th-Pb age determinations and performance evaluation. *Radiogenic age and isotope studies: Geological Survey of Canada, Report*, **10**.

Stern, R. A. and Y. Amelin, 2003: Assessment of errors in SIMS zircon U–Pb geochronology using a natural zircon standard and NIST SRM 610 glass. *Chemical Geology*, **197 (1)**, 111–142.

Su, B.-X., K.-Z. Qin, P. A. Sakyi, P.-P. Liu, D.-M. Tang, S. P. Malaviarachchi, Q.-H. Xiao, H. Sun, Y.-C. Dai, and H. Yan, 2011: Geochemistry and geochronology of acidic rocks in the Beishan region, NW China: petrogenesis and tectonic implications. *Journal of Asian Earth Sciences*, **41 (1)**, 31–43.

Sun, S.-S. and W. McDonough, 1989: Chemical and isotopic systematics of oceanic basalts: implications for mantle composition and processes. *Geological Society, London, Special Publications*, **42 (1)**, 313–345.

Tian, Z.-H., W.-J. Xiao, Y. Shan, B. Windley, C.-M. Han, J. Zhang, and D.-F. Song, 2013: Mega-fold interference patterns in the Beishan orogen (NW China) created by change in plate configuration during Permo-Triassic termination of the Altaids. *Journal of Structural Geology*, **52**, 119–135.

Tian, Z.-H., W.-J. Xiao, B. F. Windley, L. Lin, C.-M. Han, J. Zhang, B. Wan, S.-J. Ao, D.-F. Song, and J. Feng, 2014: Structure, age, and tectonic development of the Huoshishan–Niujuanzi ophiolitic mélange, Beishan, southernmost Altaids. *Gondwana Research*, **25 (2)**, 820–841.

Tikoff, B. and D. Greene, 1997: Stretching lineations in transpressional shear zones: an example from the Sierra Nevada Batholith, California. *Journal of Structural Geology*, **19 (1)**, 29–39.

Tomlinson, K., D. Davis, D. Stone, and T. Hart, 2003: U-Pb age and Nd isotopic evidence for crustal recycling and Archean terrane development in the south-central Wabigoon subprovince, Canada. *Contributions to Mineralogy and Petrology*, **144**, 684–702.

Trouw, R. A., C. W. Passchier, and D. J. Wiersma, 2009: Shear sense indicators. *Atlas of Mylonites-and related microstructures*, Springer, 141–239.

Van Staal, C., J. Dewey, C. Mac Niocaill, and W. McKerrow, 1998: The Cambrian-Silurian tectonic evolution of the northern Appalachians and British Caledonides: history of a complex, west and southwest Pacific-type segment of Iapetus. *Geological Society, London, Special Publications*, **143 (1)**, 197–242.

Vermeesch, P., 2004: How many grains are needed for a provenance study? *Earth and Planetary Science Letters*, **224 (3)**, 441–451.

Vermeesch, P., 2009: RadialPlotter: a Java application for fission track, luminescence and other radial plots. *Radiation Measurements*, **44 (4)**, 409–410.

Vermeesch, P., 2012: On the visualisation of detrital age distributions. *Chemical Geology*, **312-313**, 190–194.

von Eynatten, H. and I. Dunkl, 2012: Assessing the sediment factory: the role of single grain analysis. *Earth-Science Reviews*, **115 (1)**, 97–120.

Wang, B., D. Cluzel, L. Shu, M. Faure, J. Charvet, Y. Chen, S. Meffre, and K. De Jong, 2009: Evolution of calc-alkaline to alkaline magmatism through Carboniferous convergence to Permian transcurrent tectonics, western Chinese Tianshan. *International Journal of Earth Sciences*, **98 (6)**, 1275–1298.

Wang, B., L.-S. Shu, M. Faure, B.-M. Jahn, D. Cluzel, J. Charvet, S.-L. Chung, and S. Meffre, 2011: Paleozoic tectonics of the southern Chinese Tianshan: insights from structural, chronological and geochemical studies of the Heiyingshan ophiolitic mélange (NW China). *Tectonophysics*, **497 (1)**, 85–104.

Wang, T., D.-W. Hong, B.-M. Jahn, Y. Tong, Y.-B. Wang, B.-F. Han, and X.-X. Wang, 2006: Timing, petrogenesis, and setting of Paleozoic synorogenic intrusions from the Altai Mountains, Northwest China: implications for the tectonic evolution of an accretionary orogen. *The Journal of Geology*, **114 (6)**, 735–751.

Wang, Y., G. Sun, and J. Li, 2010: U-Pb (SHRIMP) and 40Ar/39Ar geochronological constraints on the evolution of the Xingxingxia shear zone, NW China: A Triassic segment of the Altyn Tagh fault system. *Geological Society of America Bulletin*, **122 (3/4)**, 487–505.

Wang, Z.-H., S. Sun, J.-L. Li, Q.-L. Hou, K.-Z. Qin, W.-J. Xiao, and J. Hao, 2003: Paleozoic tectonic evolution of the northern Xinjiang, China: Geochemical and geochronological constraints from the ophiolites. *Tectonics*, **22 (2)**, 1014.

Wang, Z.-M., C.-M. Han, W.-J. Xiao, W. Bo, P. A. Sakyi, S.-J. Ao, J.-E. Zhang, and D.-F. Song, 2014a: Petrology and geochronology of Paleoproterozoic garnet-bearing amphibolites from the Dunhuang Block, Eastern Tarim Craton. *Precambrian Research*, **255**, 163 – 180.

Wang, Z.-M., C.-M. Han, W.-J. Xiao, B.-X. Su, P.-A. Sakyi, D.-F. Song, and L.-N. Lin, 2014b: The petrogenesis and tectonic implications of the granitoid gneisses from Xingxingxia in the eastern segment of Central Tianshan. *Journal of Asian Earth Sciences*, **88**, 277 – 292.

Windley, B. F., D. Alexeiev, W.-J. Xiao, A. Kröner, and G. Badarch, 2007: Tectonic models for accretion of the Central Asian Orogenic Belt. *Journal of the Geological Society, London*, **164**, 31–47.

Windley, B. F., M. B. Allen, C. Zhang, Z.-Y. Zhao, and G.-R. Wang, 1990: Palaeozoic accretion and Cenozoic redeformation of the Chinese Tien Shan range, Central Asia. *Earth Planetary Science Letters*, **45**, 326–336.

Windley, B. F., A. Kröner, J.-H. Guo, G.-S. Qu, Y.-Y. Li, and C. Zhang, 2002: Neoproterozoic to Paleozoic geology of the Altai Orogen, NW China: New zircon age data and tectonic evolution. *Journal of Geology*, **110**, 719–737.

Xia, B., L.-F. Zhang, Y. Xia, and T. Bader, 2014: The tectonic evolution of the Tianshan Orogenic Belt: Evidence from U–Pb dating of detrital zircons from the Chinese southwestern Tianshan accretionary mélange. *Gondwana Research*, **25 (4)**, 1627–1643.

Xiao, W.-J., C.-M. Han, W. Liu, B. Wan, J. Zhang, S.-J. Ao, Z.-Y. Zhang, D.-F. Song, Z.-H. Tian, and J. Luo, 2014: How many sutures in the southern Central Asian Orogenic Belt: Insights from East Xinjiang–West Gansu (NW China)? *Geoscience Frontiers*, **5 (4)**, 525–536.

Xiao, W.-J., C.-M. Han, C. Yuan, M. Sun, S. Lin, H.-L. Chen, Z.-L. Li, J.-L. Li, and S. Sun, 2008: Middle Cambrian to Permian subduction-related accretionary orogenesis of Northern Xinjiang, NW China: Implications for the tectonic evolution of Central Asia. *Journal of Asian Earth Sciences*, **32**, 102–117.

Xiao, W.-J., Q.-G. Mao, B. F. Windley, C.-M. Han, J.-F. Qu, J.-E. Zhang, S.-J. Ao, Q.-Q. Guo, N. R. Cleven, S.-F. Lin, Y.-H. Shan, and J.-L. Li, 2010: Paleozoic multiple accretionary and collisional processes of the Beishan orogenic collage. *American Journal of Science*, **310 (10)**, 1553–1594.

Xiao, W.-J. and M. Santosh, 2014: The western Central Asian Orogenic Belt: A window to accretionary orogenesis and continental growth. *Gondwana Research*, **25 (4)**, 1429–1444.

Xiao, W.-J., B. F. Windley, M. B. Allen, and C.-M. Han, 2013: Paleozoic multiple accretionary and collisional tectonics of the Chinese Tianshan orogenic collage. *Gondwana Research*, **23 (4)**, 1316–1341.

Xiao, W.-J., B. F. Windley, G. Badarch, S. Sun, J. Li, K. Qin, and Z. Wang, 2004a: Paleozoic accretionary and convergent tectonics of the southern Altaids: implications for the growth of Central Asia. *Journal of the Geological Society, London*, **161**, 339–342.

Xiao, W.-J., B. F. Windley, J. Hao, and M.-G. Zhai, 2003: Accretion leading to collision and the Permian Solonker suture, Inner Mongolia, China: Termination of the Central Asian orogenic belt. *Tectonics*, **22 (6)**, 1069.

Xiao, W.-J., B. F. Windley, B.-C. Huang, C.-M. Han, C. Yuan, H.-L. Chen, M. Sun, S. Sun, and J.-L. Li, 2009a: End-Permian to mid-Triassic termination of the accretionary processes of the southern Altaids: implications for the geodynamic evolution, Phanerozoic continental growth, and metallogeny of Central Asia. *International Journal of Earth Sciences*, **98**, 1188–1217.

Xiao, W.-J., B. F. Windley, C. Yuan, M. Sun, C.-M. Han, S.-F. Lin, H.-L. Chen, Q.-R. Yan, D.-Y. Liu, K.-Z. Qin, J.-L. Li, and S. Sun, 2009b: Paleozoic multiple subduction-accretion processes of the southern Altaids. *American Journal of Science*, **309**, 221–270.

Xiao, W.-J., L. Zhang, K.-Z. Qin, S. Sun, and J.-L. Li, 2004b: Paleozoic accretionary and collisional tectonics of the eastern Tianshan (China): implications for the continental growth of Central Asia. *American Journal of Science*, **304**, 370–395.

Yakubchuk, A., 2004: Architecture and mineral deposit settings of the Altaid orogenic collage: a revised model. *Journal of Asian Earth Sciences*, **23**, 761–779.

Yang, T., Y. Wang, J. Li, and G. Sun, 2007: Vertical and horizontal strain partitioning of the Central Tianshan (NW China): evidence from structures and 40Ar/39 Ar geochronology. *Journal of Structural Geology*, **29 (10)**, 1605–1621.

Zhang, C., M.-G. Zhai, M. B. Allen, A. D. Saunders, G.-R. Wang, and X. Huang, 1993: Implications of Palaeozoic ophiolites from Western Junggar, NW China, for the tectonics of central Asia. *Journal of The Geological Society, London*, **150**, 551–561.

Zhang, C.-L., H.-B. Zou, H.-K. Li, and H.-Y. Wang, 2013a: Tectonic framework and evolution of the tarim block in nw china. *Gondwana Research*, **23 (4)**, 1306–1315.

Zhang, J. and D. Cunningham, 2012: Kilometer-scale refolded folds caused by strike-slip reversal and intraplate shortening in the Beishan region, China. *Tectonics*, **31 (3)**.

Zhang, J., G. Zhao, S. Li, M. Sun, S. A. Wilde, S. Liu, and C. Yin, 2009: Polyphase deformation of the Fuping Complex, Trans-North China Orogen: structures, SHRIMP U–Pb zircon ages and tectonic implications. *Journal of Structural Geology*, **31 (2)**, 177–193.

Zhang, J.-X., S.-Y. Yu, J.-H. Gong, H.-K. Li, and K.-J. Hou, 2013b: The latest Neoarchean–Paleoproterozoic evolution of the Dunhuang block, eastern Tarim craton, northwestern China: evidence from zircon U–Pb dating and Hf isotopic analyses. *Precambrian Research*, **226**, 21–42.

Zhang, Y.-Y. and Z.-J. Guo, 2008: Accurate constraint on formation and emplacement age of Hongliuhe ophiolite, boundary region between Xinjiang and Gansu Provinces and its tectonic implications. *Acta Petrologica Sinica*, **24 (4)**, 803–809 (in Chinese with English abstract).

Zhao, Z.-H., Z.-J. Guo, and Y. Wang, 2007: Geochronology, geochemical characteristics and tectonic implications of the granitoids from Liuyuan area, Beishan, Gansu province, Northwest China. *Acta Petrologica Sinica*, **23 (8)**, 1847–1860 (In Chinese with English abstract).

Zheng, R., T. Wu, W. Zhang, Q. Meng, and Z. Zhang, 2014: Geochronology and geochemistry of late Paleozoic magmatic rocks in the Yinwaxia area, Beishan: Implications for rift magmatism in the southern Central Asian Orogenic Belt. *Journal of Asian Earth Sciences*, **91**, 39–55.

Zheng, R., T. Wu, W. Zhang, C. Xu, and Q. Meng, 2013: Late Paleozoic subduction system in the southern Central Asian Orogenic Belt: Evidences from geochronology and geochemistry of the Xiaohuangshan ophiolite in the Beishan orogenic belt. *Journal of Asian Earth Sciences*, **62**, 463–475.

Zheng, Y., Q. Zhang, Y. Wang, R. Liu, S. Wang, G. Zuo, S. Wang, B. Lkaasuren, G. Badarch, and Z. Badamgarav, 1996: Great Jurassic thrust sheets in Beishan (North Mountains)–Gobi areas of China and southern Mongolia. *Journal of Structural Geology*, **18 (9)**, 1111–1126.

Zhou, H., 2014: The Xingxingxia region Late Proterozoic intrusive rocks and the Xingxingxia Complex: Constraining characteristics of the Central Tianshan block and the Late Paleozoic tectonic framework (title translated). *Master's Thesis, unpublished*, In Chinese with English abstract.

Zhu, J., X.-B. Lü, X.-F. Cao, Y.-L. Mo, and C. Chen, 2012: U-Pb zircon geochronology, geochemistry and kinetics of the Huaniushan A-type granite in Northwest China. *Chinese Journal of Geochemistry*, **31**, 85 – 94.

Appendices

Appendix A

Chapter 2 supplementary material

A.1 Igneous geochronology data tables

Spot Name	U (ppm)	^{232}Th/ ^{238}U	^{207}Pb/^{206}Pb	±1σ	^{206}Pb/^{238}U	±1σ (%)	^{207}Pb/^{206}Pb Age (Ma)	±1σ	^{207}Pb/^{235}Pb Age (Ma)	±1σ	^{206}Pb/^{238}Pb Age (Ma)	±1σ	% Discordant
Tonalite gneiss													
08NC05-8-3.1	265	na	0.05549	0.00051	0.06977	0.00043	440.5	22.4	460.6	4.9	464.6	3.8	-5.7
08NC05-8-1.1	103	na	0.05835	0.00104	0.07120	0.00059	547.6	39.9	480.4	7.9	466.5	4.3	15.4
08NC05-8-2.1	192	na	0.05530	0.00081	0.07094	0.00053	431.1	33.7	462.2	6.5	468.5	4.0	-9.0
08NC05-8-4.1	188	na	0.05478	0.00072	0.07035	0.00050	410.2	30.6	464.4	6.2	475.4	4.3	-16.5
Crystal lithic tuff													
11NC57I-7.1	626	0.32	0.05622	0.00086	0.05512	0.00040	415.6	39.4	402.7	6.9	400.5	4.1	3.8
11NC57I-8.1	289	0.52	0.05525	0.00115	0.05470	0.00045	392.5	49.0	401.4	8.1	402.9	4.1	-2.7
11NC57I-31.1	2057	0.43	0.05624	0.00059	0.05553	0.00105	428.3	31.1	409.6	8.5	406.2	8.3	5.3
11NC57I-21.1	809	0.45	0.05579	0.00060	0.05551	0.00031	415.6	28.4	408.4	5.2	407.1	3.5	2.1
11NC57I-2.1	159	0.32	0.05563	0.00142	0.05436	0.00050	413.1	58.0	408.3	9.6	407.5	4.5	1.4
11NC57I-3.1	907	0.32	0.05518	0.00059	0.05476	0.00045	404.5	29.0	407.1	5.6	407.6	4.1	-0.8
11NC57I-26.1	401	0.17	0.05567	0.00082	0.05690	0.00038	418.4	35.7	416.0	6.4	415.6	3.9	0.7
11NC57I-25.1	623	0.33	0.05649	0.00064	0.05654	0.00028	443.5	28.9	420.9	5.3	416.8	3.3	6.2

Table A.1: Igneous zircon U-Pb LA-ICPMS geochronology data.

Spot Name	U (ppm)	Th (ppm)	^{232}Th/ ^{238}U	comm 206 (%)	^{207}Pb/ ^{206}Pb	±1σ (%)	^{207}Pb/ ^{235}U	±1σ (%)	^{206}Pb/ ^{238}U	±1σ (%)	^{207}Pb/^{206}Pb Age (Ma)	±1σ	^{206}Pb/^{238}Pb Age (Ma)	±1σ	% Disc.
Crystal lithic tuff															
08NC03C-10.1	464	219	0.49	-0.02	0.05585	4.0839	0.54811	4.2250	0.07118	1.0828	452.8	90.7	443.3	9.1	0.7
08NC03C-7.1	397	293	0.76	0.30	0.05633	2.0164	0.55610	2.3383	0.07160	1.1840	471.9	44.6	445.8	9.4	4.4
08NC03C-16.1	421	263	0.65	0.11	0.05554	2.0982	0.54860	2.3479	0.07165	1.0536	440.3	46.7	446.1	9.1	-2.9
08NC03C-12.1	253	123	0.50	0.01	0.05713	3.8521	0.56529	4.0206	0.07176	1.1518	503.0	84.8	446.8	9.3	10.4
08NC03C-5.1	187	108	0.60	0.60	0.05382	2.8937	0.53319	3.0907	0.07185	1.0858	370.2	65.2	447.3	9.2	-23.8
08NC03C-14.1	292	128	0.45	0.35	0.05692	3.1742	0.56694	3.4056	0.07223	1.2338	495.0	70.0	449.6	9.6	8.3
08NC03C-6.1	284	123	0.45	0.10	0.05788	5.2333	0.58011	5.3492	0.07269	1.1073	531.5	114.6	452.4	9.3	14.4
08NC03C-20.1	285	91	0.33	0.33	0.05476	1.8520	0.54942	2.2274	0.07276	1.2375	409.0	41.4	452.8	9.6	-12.9
08NC03C-18.1	538	256	0.49	0.24	0.05465	1.7402	0.55010	2.0343	0.07300	1.0537	404.4	39.0	454.2	9.2	-14.7
08NC03C-15.1	385	162	0.43	-0.14	0.05637	2.2829	0.56867	2.5132	0.07316	1.0508	473.5	50.5	455.2	9.3	2.6
08NC03C-3.1	377	167	0.46	-0.11	0.05618	1.8295	0.56763	2.3523	0.07329	1.4787	465.7	40.5	455.9	10.3	0.8
08NC03C-13.1	374	221	0.61	0.18	0.05413	3.8073	0.54781	4.0265	0.07340	1.3103	382.9	85.6	456.6	9.9	-22.1
Ash layer in marble															
08NC04A-14.2	279	186	0.69	0.11	0.06258	1.2920	0.90345	1.9799	0.10470	1.5002	694.0	27.5	641.9	11.1	7.9
08NC04A-43.1	220	115	0.54	0.15	0.06275	1.5114	0.91934	2.1241	0.10626	1.4925	699.7	32.2	651.0	11.2	7.3
08NC04A-62.1	439	196	0.46	0.06	0.06260	0.9317	0.92918	1.7663	0.10766	1.5006	694.5	19.9	659.1	11.4	5.4
08NC04A-13.2	674	295	0.45	-0.03	0.06253	0.8452	0.93474	1.6912	0.10841	1.4649	692.4	18.0	663.5	11.3	4.4
08NC04A-16.2	95	46	0.51	3.01	0.06149	13.3165	0.92209	13.4214	0.10875	1.6746	656.6	285.6	665.5	12.4	-1.4
08NC04A-35.1	237	133	0.58	0.28	0.05925	1.8127	0.88895	2.3562	0.10881	1.5053	576.4	39.4	665.8	11.5	-16.3
08NC04A-34.1	448	216	0.50	0.00	0.06278	1.2092	0.94835	1.9119	0.10956	1.4809	700.7	25.7	670.2	11.5	4.6
08NC04A-45.1	272	174	0.66	0.07	0.06181	1.7888	0.93431	2.3258	0.10963	1.4865	667.6	38.3	670.6	11.5	-0.5
08NC04A-33.1	285	218	0.79	0.34	0.06102	1.6243	0.92300	2.2395	0.10970	1.5418	640.1	34.9	671.0	11.8	-5.1
08NC04A-64.1	898	495	0.57	0.06	0.06159	0.6485	0.93533	1.7149	0.11014	1.5875	660.0	13.9	673.6	12.1	-2.2
08NC04A-63.1	202	98	0.50	0.26	0.06273	1.4975	0.95467	2.2273	0.11038	1.6488	699.1	31.9	674.9	12.5	3.6
08NC04A-70.1	559	206	0.38	0.00	0.06253	1.2140	0.95227	1.9014	0.11045	1.4634	692.3	25.9	675.4	11.5	2.6
08NC04A-65.1	274	154	0.58	0.13	0.06163	1.2081	0.93888	1.9118	0.11048	1.4817	661.4	25.9	675.5	11.6	-2.3
08NC04A-69.1	261	159	0.63	-0.13	0.06415	1.1739	0.98296	2.0142	0.11114	1.6368	746.5	24.8	679.3	12.5	9.5
08NC04A-40.1	391	151	0.40	0.17	0.06206	1.4219	0.95393	2.0500	0.11148	1.4768	676.3	30.4	681.3	11.6	-0.8
08NC04A-44.1	436	162	0.38	0.11	0.06179	2.4485	0.95218	2.9766	0.11176	1.6927	666.9	52.4	683.0	12.8	-2.5
08NC04A-46.1	508	186	0.38	0.05	0.06300	0.9210	0.97502	1.8288	0.11225	1.5799	708.1	19.6	685.8	12.3	3.3
08NC04A-9.2	299	120	0.41	0.48	0.06061	2.3520	0.95487	2.7916	0.11427	1.5038	625.3	50.7	697.5	12.0	-12.2
08NC04A-36.1	927	509	0.57	0.04	0.06184	1.0719	0.97440	1.8618	0.11428	1.5222	668.6	22.9	697.5	12.1	-4.6

Table A.2: Igneous zircon U-Pb SHRIMP geochronology data.

Spot Name	U (ppm)	Th (ppm)	^{232}Th/ ^{238}U	comm 206 (%)	^{207}Pb/ ^{206}Pb	±1σ (%)	^{207}Pb/ ^{235}U	±1σ (%)	^{206}Pb/ ^{238}U	±1σ (%)	^{207}Pb/^{206}Pb Age (Ma)	±1σ	^{206}Pb/^{238}Pb Age (Ma)	±1σ	% Disc.
Undeformed dyke															
08NC01A-32.1	99	130	1.36	3.03	0.05137	9.0948	0.25229	9.2630	0.03562	1.7571	257.7	209.0	225.6	4.5	12.7
08NC01A-11.2	456	422	0.96	0.26	0.05083	4.8383	0.25199	5.0758	0.03596	1.5345	233.0	111.7	227.7	4.1	2.3
08NC01A-34.1	417	464	1.15	0.51	0.04997	13.3101	0.24835	13.4246	0.03605	1.7493	193.4	309.5	228.3	4.6	-18.4
08NC01A-12.2	713	566	0.82	0.14	0.05225	1.6408	0.26009	2.2043	0.03610	1.4719	296.4	37.4	228.6	4.0	23.3
08NC01A-29.1	753	805	1.11	0.59	0.04764	3.6568	0.23767	4.0859	0.03619	1.8228	81.2	86.8	229.1	4.7	-185.5
08NC01A-27.1	388	371	0.99	0.36	0.05022	4.1787	0.25590	4.4473	0.03696	1.5220	205.1	97.0	234.0	4.2	-14.3
08NC01A-33.1	609	573	0.97	0.30	0.04842	2.4831	0.24715	3.0650	0.03702	1.7968	120.0	58.5	234.3	4.8	-97.0
08NC01A-31.1	549	380	0.72	0.34	0.04922	2.1574	0.25180	2.6147	0.03710	1.4773	158.4	50.5	234.8	4.2	-49.2
08NC01A-17.2	659	969	1.52	-0.01	0.05131	3.2723	0.26301	3.5904	0.03718	1.4775	254.6	75.2	235.3	4.2	7.7
08NC01A-26.1	561	488	0.90	0.17	0.05289	1.7942	0.27175	2.3176	0.03726	1.4670	324.2	40.7	235.8	4.2	27.7
08NC01A-28.1	858	769	0.93	0.27	0.04891	2.2902	0.25138	2.7170	0.03728	1.4620	143.4	53.7	235.9	4.1	-65.7
08NC01A-15.2	826	1213	1.52	0.15	0.05103	3.9446	0.26340	4.2119	0.03744	1.4764	242.1	90.9	236.9	4.2	2.2
Pillow basalt															
09NC39G-1.2	1129	686	0.63	0.12	0.05537	0.8550	0.49123	1.8368	0.06434	1.6257	427.3	19.1	402.0	7.5	6.1
09NC39G-4.1	450	224	0.51	0.14	0.05525	1.8951	0.50370	2.4825	0.06612	1.6036	422.6	42.3	412.7	7.6	2.4
09NC39G-1.1	1294	363	0.29	0.14	0.05485	0.8554	0.52632	1.6895	0.06959	1.4570	406.2	19.1	433.7	7.5	-7.0

Table A.2: *continued*

A.2 Detrital geochronology data tables

Spot Name	U (ppm)	^{232}Th/ ^{238}U	^{207}Pb/^{206}Pb	±1σ	^{206}Pb/^{238}U	±1σ (%)	^{207}Pb/^{206}Pb Age (Ma)	±1σ	^{207}Pb/^{235}Pb Age (Ma)	±1σ	^{206}Pb/^{238}Pb Age (Ma)	±1σ	% Discordant
Dundunshan Group													
11NC60-26.2r	289	0.24	0.05701	0.00107	0.08570	0.00175	402.3	45.6	401.6	10.2	401.4	9.0	0.2
11NC60-24.2r	436	0.24	0.05707	0.00099	0.08916	0.00140	424.6	41.8	416.6	9.2	415.1	7.7	2.3
11NC60-58.1	514	0.29	0.05680	0.00179	0.04793	0.00117	427.3	72.2	420.9	14.3	419.7	10.4	1.8
11NC60-23.1	131	0.49	0.05698	0.00109	0.07776	0.00063	422.2	44.7	423.8	7.8	424.1	4.2	-0.4
11NC60-30.1c	452	0.37	0.05571	0.00077	0.06521	0.00054	423.7	34.1	427.2	6.5	427.8	4.4	-1.0
11NC60-38.1	123	0.92	0.05568	0.00226	0.06914	0.00078	426.9	90.4	428.7	15.3	429.1	5.9	-0.5
11NC60-29.2r	528	0.37	0.05571	0.00064	0.06608	0.00042	421.0	29.6	428.6	5.6	430.0	3.8	-2.2
11NC60-34.1	553	0.73	0.05555	0.00086	0.06455	0.00057	437.0	37.9	434.2	7.3	433.7	4.8	0.8
11NC60-14.1	362	0.52	0.05632	0.00072	0.06600	0.00049	446.5	30.4	436.0	5.8	434.1	3.8	2.9
11NC60-4.1c	662	0.66	0.05728	0.00075	0.08026	0.00059	455.4	34.9	437.7	6.9	434.4	4.7	4.8
11NC60-44.1	484	0.50	0.05556	0.00138	0.06955	0.00062	424.0	60.7	432.8	10.6	434.5	5.2	-2.5
11NC60-26.1c	192	0.36	0.05722	0.00094	0.07983	0.00061	426.8	38.8	433.7	7.1	435.0	4.2	-2.0
11NC60-5.1	411	0.48	0.05569	0.00077	0.06768	0.00043	420.6	33.1	432.7	6.0	435.0	3.5	-3.5
11NC60-49.1	214	0.36	0.05570	0.00184	0.07085	0.00090	432.0	74.5	436.4	13.1	437.3	6.0	-1.3
11NC60-45.1	204	0.49	0.05642	0.00186	0.07039	0.00060	441.9	76.2	438.7	13.1	438.1	5.1	0.9
11NC60-62.1	686	0.38	0.05607	0.00129	0.05148	0.00041	445.9	61.3	439.4	10.8	438.2	5.2	1.8
11NC60-61.1	622	0.39	0.05669	0.00118	0.05127	0.00044	452.0	57.5	440.9	10.4	438.8	5.4	3.0
11NC60-41.1	226	0.48	0.05572	0.00147	0.07065	0.00055	455.1	61.7	441.7	11.0	439.1	5.2	3.6
11NC60-6.1	436	0.58	0.05650	0.00067	0.06796	0.00039	451.9	29.2	441.5	5.5	439.5	3.4	2.8
11NC60-3.1	132	0.51	0.05572	0.00133	0.06868	0.00053	419.2	54.7	436.4	9.5	439.7	4.2	-5.0
11NC60-11.1	852	1.03	0.05610	0.00058	0.06793	0.00046	437.0	26.3	440.0	5.2	440.6	3.6	-0.8
11NC60-8.1	325	0.58	0.05631	0.00081	0.06756	0.00037	437.4	34.5	440.4	6.2	441.0	3.1	-0.9
11NC60-65.1	299	0.25	0.05606	0.00149	0.05120	0.00042	450.3	61.9	443.1	10.9	441.7	4.8	2.0
11NC60-16.1c	86	0.39	0.05831	0.00125	0.07957	0.00077	458.8	49.5	445.0	9.2	442.3	5.2	3.7
11NC60-68.1	115	0.38	0.05633	0.00323	0.05132	0.00066	442.9	127.6	442.4	21.8	442.3	6.6	0.1
11NC60-3.2r	416	0.39	0.05699	0.00081	0.08220	0.00054	428.9	35.3	440.7	6.6	443.0	4.1	-3.4
11NC60-29.1c	664	0.39	0.05676	0.00061	0.06778	0.00054	456.0	27.2	445.2	5.6	443.1	4.1	2.9
11NC60-31.1	406	0.30	0.05835	0.00067	0.08111	0.00058	450.6	29.6	444.6	6.0	443.4	4.2	1.6
11NC60-32.2r	307	0.33	0.05798	0.00082	0.08097	0.00063	445.5	35.8	444.2	6.9	444.0	4.4	0.3
11NC60-15.1	244	0.52	0.05631	0.00106	0.06681	0.00043	439.8	43.5	443.4	7.7	444.2	3.7	-1.0
11NC60-12.1	120	0.34	0.05873	0.00124	0.08062	0.00073	446.2	48.4	444.5	8.9	444.2	5.0	0.5
11NC60-3.1c	272	0.55	0.05745	0.00104	0.08277	0.00067	432.1	42.9	442.4	8.0	444.4	4.7	-2.9
11NC60-71.1	425	0.31	0.05685	0.00130	0.05143	0.00036	458.3	54.6	447.0	9.7	444.8	4.4	3.0
11NC60-4.2r	373	0.47	0.05670	0.00094	0.08191	0.00065	437.3	41.5	444.0	7.9	445.3	5.0	-1.9
11NC60-72.1c	222	0.25	0.05641	0.00159	0.05173	0.00042	425.8	64.4	442.3	11.2	445.5	4.5	-4.8
11NC60-13.1	212	0.51	0.05593	0.00096	0.06862	0.00047	437.5	39.5	444.4	7.2	445.7	3.9	-1.9

Table A.3: Detrital zircon U-Pb LA-ICPMS geochronology data.

Spot Name	U (ppm)	^{232}Th/ ^{238}U	^{207}Pb/^{206}Pb	±1σ	^{206}Pb/^{238}U	±1σ (%)	^{207}Pb/^{206}Pb Age (Ma)	±1σ	^{207}Pb/^{235}Pb Age (Ma)	±1σ	^{206}Pb/^{238}Pb Age (Ma)	±1σ	% Discordant
Dundunshan Group continued													
11NC60-8.2r	666	0.49	0.05640	0.00063	0.08205	0.00062	439.0	32.7	445.0	6.9	446.2	5.2	-1.7
11NC60-37.1c	66	0.32	0.05679	0.00222	0.07208	0.00090	454.3	86.1	448.2	15.2	447.0	6.2	1.7
11NC60-39.1	186	0.41	0.05586	0.00171	0.07210	0.00087	448.2	70.1	447.3	12.8	447.1	6.5	0.3
11NC60-63.1	578	0.48	0.05630	0.00106	0.05233	0.00038	459.1	48.8	449.2	8.9	447.3	4.6	2.7
11NC60-64.1	449	0.44	0.05604	0.00122	0.05208	0.00040	453.0	52.5	448.3	9.5	447.4	4.7	1.3
11NC60-46.1	196	0.36	0.05642	0.00198	0.07231	0.00065	436.0	79.2	445.9	13.7	447.8	5.0	-2.8
11NC60-70.1	215	0.45	0.05625	0.00199	0.05174	0.00048	446.8	80.6	447.9	14.0	448.1	5.1	-0.3
11NC60-25.1	489	0.42	0.05624	0.00074	0.06771	0.00043	434.5	32.1	446.0	6.0	448.2	3.6	-3.3
11NC60-5.1	271	0.36	0.05714	0.00106	0.08239	0.00068	444.1	44.0	447.8	8.2	448.5	4.7	-1.0
11NC60-26.1	403	0.33	0.05641	0.00066	0.06780	0.00040	437.0	28.7	446.7	5.4	448.6	3.3	-2.7
11NC60-12.1	280	0.74	0.05638	0.00080	0.06954	0.00054	454.9	33.4	449.6	6.5	448.6	4.2	1.4
11NC60-28.1	222	0.39	0.05668	0.00112	0.06833	0.00056	446.4	45.9	448.6	8.4	449.0	4.3	-0.6
11NC60-10.1	260	0.59	0.05626	0.00095	0.06899	0.00046	436.4	40.5	447.2	7.3	449.3	3.8	-3.1
11NC60-11.1	233	0.48	0.05880	0.00094	0.08170	0.00071	449.7	38.8	449.4	7.7	449.3	5.1	0.1
11NC60-32.1	364	0.56	0.05617	0.00078	0.06621	0.00055	441.6	34.8	448.2	6.9	449.5	4.6	-1.8
11NC60-25.1	578	0.45	0.05811	0.00063	0.08265	0.00053	457.3	29.4	450.9	6.0	449.6	4.3	1.7
11NC60-18.1	203	0.38	0.05797	0.00113	0.08157	0.00083	443.6	46.2	449.1	8.9	450.2	5.4	-1.5
11NC60-48.1	120	0.30	0.05677	0.00209	0.07320	0.00073	455.8	81.9	451.2	14.4	450.2	5.5	1.3
11NC60-27.1	337	0.34	0.05676	0.00070	0.06816	0.00045	447.1	31.0	450.0	6.0	450.6	3.8	-0.8
11NC60-17.1	177	0.34	0.05852	0.00104	0.08140	0.00068	465.7	41.5	453.2	7.9	450.7	4.7	3.3
11NC60-19.1	246	0.39	0.05757	0.00113	0.08219	0.00073	434.7	46.7	448.3	8.7	451.0	5.0	-3.9
11NC60-66.1	300	0.43	0.05615	0.00150	0.05239	0.00047	446.7	63.8	450.3	11.4	451.1	5.0	-1.0
11NC60-21.2c	415	0.37	0.05722	0.00080	0.09763	0.00118	450.8	36.4	451.0	8.9	451.1	7.9	-0.1
11NC60-27.1c	156	0.36	0.05885	0.00097	0.08297	0.00056	492.8	38.3	458.4	7.3	451.6	4.2	8.7
11NC60-22.1	208	0.31	0.05762	0.00092	0.08300	0.00063	453.2	38.3	452.0	7.3	451.8	4.4	0.3
11NC60-28.1r	344	0.41	0.05728	0.00084	0.08273	0.00066	447.4	35.5	451.2	7.0	451.9	4.5	-1.0
11NC60-10.1	147	0.31	0.05813	0.00114	0.08262	0.00059	448.6	46.3	451.7	8.6	452.3	4.8	-0.9
11NC60-2.1	203	0.54	0.05815	0.00103	0.08444	0.00071	445.4	42.1	451.5	8.0	452.7	4.9	-1.7
11NC60-60.1	440	0.34	0.05716	0.00136	0.05247	0.00040	455.7	58.4	453.5	10.5	453.1	4.8	0.6
11NC60-1.2c	724	0.41	0.05845	0.00062	0.08427	0.00065	457.8	27.6	453.9	6.0	453.2	4.7	1.0
11NC60-8.1c	1032	0.84	0.05770	0.00072	0.08328	0.00092	474.6	32.4	456.9	7.3	453.4	5.9	4.6
11NC60-2.1	314	0.64	0.05663	0.00094	0.07036	0.00053	450.8	38.9	453.5	7.3	454.0	4.1	-0.7
11NC60-1.1r	313	0.48	0.05888	0.00087	0.08442	0.00068	475.5	37.0	458.6	7.7	455.2	5.4	4.4
11NC60-21.1	230	0.30	0.05825	0.00083	0.08343	0.00062	475.8	34.8	458.7	6.9	455.3	4.4	4.5
11NC60-17.1	128	0.25	0.05703	0.00125	0.06853	0.00052	462.5	49.6	456.8	9.0	455.6	4.0	1.5
11NC60-24.1	292	0.27	0.05654	0.00086	0.06812	0.00045	455.1	36.1	455.6	6.8	455.7	3.9	-0.1

Table A.3: *continued*

Spot Name	U (ppm)	^{232}Th/ ^{238}U	^{207}Pb/^{206}Pb	±1σ	^{206}Pb/^{238}U	±1σ (%)	^{207}Pb/^{206}Pb Age (Ma)	±1σ	^{207}Pb/^{235}Pb Age (Ma)	±1σ	^{206}Pb/^{238}Pb Age (Ma)	±1σ	% Discordant
Dundunshan Group continued													
11NC60-33.1	291	0.60	0.05612	0.00101	0.06760	0.00059	449.4	42.3	454.9	8.1	456.0	4.7	-1.5
11NC60-9.2r	395	0.38	0.05802	0.00087	0.08358	0.00071	468.3	37.0	458.1	7.6	456.1	5.2	2.7
11NC60-18.1	195	0.30	0.05676	0.00083	0.06897	0.00045	452.3	35.1	455.4	6.7	456.1	3.9	-0.9
11NC60-14.1c	193	0.41	0.05833	0.00108	0.08225	0.00065	445.1	43.2	454.3	8.1	456.1	4.6	-2.6
11NC60-69.1	411	0.26	0.05675	0.00130	0.05286	0.00047	462.9	56.7	457.4	10.4	456.3	5.0	1.5
11NC60-30.2r	1377	0.55	0.05685	0.00049	0.06881	0.00039	465.4	23.6	458.1	5.0	456.6	3.6	1.9
11NC60-72.2r	451	0.39	0.05759	0.00115	0.05333	0.00036	456.5	48.2	456.8	8.9	456.9	4.5	-0.1
11NC60-16.2c	120	0.21	0.05730	0.00164	0.10273	0.00167	476.0	65.5	460.3	13.6	457.1	9.3	4.1
11NC60-28.2c	1050	0.66	0.05834	0.00052	0.08366	0.00063	493.8	27.7	463.6	6.2	457.5	4.8	7.6
11NC60-29.1	424	0.48	0.05766	0.00081	0.08365	0.00073	456.9	36.6	457.6	7.5	457.7	5.2	-0.2
11NC60-9.1	211	0.62	0.05673	0.00097	0.07013	0.00042	450.7	41.1	456.7	7.5	457.8	3.5	-1.6
11NC60-20.1	361	0.35	0.05786	0.00080	0.08373	0.00066	453.1	33.8	457.2	6.7	458.0	4.4	-1.1
11NC60-9.1c	473	0.59	0.05686	0.00097	0.08423	0.00078	447.6	43.2	456.4	8.7	458.2	5.9	-2.5
11NC60-34.2c	871	0.50	0.05787	0.00071	0.08300	0.00067	475.4	32.3	461.1	6.7	458.2	4.7	3.7
11NC60-34.1r	440	0.51	0.05793	0.00100	0.08316	0.00075	473.3	44.6	460.8	8.7	458.3	5.3	3.3
11NC60-30.1	305	0.33	0.05771	0.00091	0.08395	0.00066	442.4	38.3	456.1	7.4	458.8	4.5	-3.8
11NC60-32.1c	237	0.32	0.05875	0.00094	0.08403	0.00067	462.0	38.5	459.7	7.5	459.3	4.6	0.6
11NC60-59.1	322	0.32	0.05787	0.00165	0.05275	0.00106	468.9	66.2	461.6	13.8	460.1	9.6	1.9
11NC60-35.1	788	0.48	0.05741	0.00061	0.08343	0.00065	462.2	28.3	461.4	6.2	461.3	4.8	0.2
11NC60-1.1	329	0.81	0.05715	0.00100	0.07089	0.00051	466.7	41.5	462.3	7.8	461.4	4.1	1.2
11NC60-15.1c	172	0.34	0.05852	0.00099	0.08311	0.00056	460.0	40.1	461.4	7.7	461.7	4.5	-0.4
11NC60-7.1	213	0.31	0.05760	0.00105	0.08484	0.00074	456.0	43.2	461.2	8.4	462.2	5.1	-1.4
11NC60-15.2r	416	0.34	0.05803	0.00096	0.10220	0.00143	476.2	40.1	464.7	9.5	462.4	7.9	3.0
11NC60-55.1	401	0.43	0.05686	0.00177	0.05417	0.00184	467.8	73.2	463.5	18.0	462.7	15.6	1.1
11NC60-27.2r	298	0.34	0.05757	0.00082	0.08498	0.00071	453.5	34.3	461.5	7.0	463.1	4.8	-2.2
11NC60-20.1	297	0.33	0.05672	0.00080	0.06877	0.00032	464.0	33.6	463.4	6.4	463.3	3.5	0.2
11NC60-21.1	224	0.49	0.05635	0.00087	0.06805	0.00059	455.9	37.2	462.7	7.6	464.1	5.2	-1.9
11NC60-7.1	233	0.52	0.05657	0.00087	0.07138	0.00050	450.7	36.2	462.1	6.9	464.4	4.0	-3.1
11NC60-22.1	551	0.56	0.05641	0.00068	0.06810	0.00046	459.4	30.7	464.2	6.5	465.2	4.6	-1.3
11NC60-4.1	536	0.77	0.05724	0.00056	0.07307	0.00049	482.9	26.1	468.5	5.6	465.6	4.1	3.7
11NC60-16.1	402	0.35	0.05760	0.00057	0.06982	0.00042	484.1	25.8	469.4	5.4	466.3	3.7	3.8
11NC60-50.1c	253	0.65	0.05603	0.00167	0.07560	0.00162	464.1	68.9	466.2	14.5	466.7	10.1	-0.6
11NC60-36.1	77	0.28	0.05781	0.00149	0.08460	0.00071	458.2	57.4	465.8	10.6	467.3	4.8	-2.1
11NC60-23.1	399	0.39	0.05677	0.00076	0.06925	0.00042	469.0	32.0	468.1	6.3	467.9	3.9	0.2
11NC60-50.2r	234	0.60	0.05656	0.00142	0.07222	0.00129	488.1	59.4	482.4	12.7	481.3	8.9	1.4
11NC60-57.1	446	0.34	0.05864	0.00215	0.05820	0.00191	512.1	81.9	503.5	20.1	501.6	16.2	2.1

Table A.3: *continued*

Spot Name	U (ppm)	^{232}Th/ ^{238}U	^{207}Pb/^{206}Pb	±1σ	^{206}Pb/^{238}U	±1σ (%)	^{207}Pb/^{206}Pb Age (Ma)	±1σ	^{207}Pb/^{235}Pb Age (Ma)	±1σ	^{206}Pb/^{238}Pb Age (Ma)	±1σ	% Discordant
Mazongshan accretionary complex													
11NC57E-101.1	641	0.50	0.05445	0.00096	0.06635	0.00045	406.0	49.4	402.5	8.5	401.8	5.0	1.1
11NC57E-99.1	106	0.34	0.05546	0.00289	0.06848	0.00091	423.7	114.8	413.7	18.7	411.9	6.3	2.9
11NC57E-17.1	888	0.36	0.05605	0.00061	0.06267	0.00045	426.6	27.9	424.2	5.3	423.7	3.6	0.7
11NC57E-40.1	50	0.79	0.05602	0.00293	0.06569	0.00068	426.0	113.6	426.2	18.7	426.3	4.9	-0.1
11NC57E-26.1	90	0.27	0.05560	0.00150	0.06412	0.00058	431.9	61.1	427.5	10.4	426.7	4.6	1.2
11NC57E-39.1	307	0.40	0.05600	0.00112	0.06612	0.00051	434.0	46.6	429.0	8.1	428.1	4.0	1.4
11NC57E-35.1	93	0.45	0.05521	0.00136	0.06490	0.00046	427.5	55.5	428.9	9.3	429.2	3.6	-0.4
11NC57E-118.1	191	0.38	0.05479	0.00245	0.07072	0.00078	426.3	101.2	430.0	16.9	430.6	5.8	-1.0
11NC57E-2.1	2052	0.33	0.05609	0.00046	0.06498	0.00045	431.2	23.1	431.1	4.9	431.0	3.8	0.0
11NC57E-9.1	73	0.35	0.05623	0.00211	0.06581	0.00065	432.9	83.1	431.7	14.0	431.4	5.1	0.4
11NC57E-103.1	248	0.88	0.05528	0.00171	0.07054	0.00076	426.3	72.0	430.8	12.5	431.7	5.8	-1.3
11NC57E-22.1	244	0.24	0.05581	0.00114	0.06425	0.00047	438.1	47.4	433.1	8.3	432.2	3.9	1.4
11NC57E-88.1	130	0.59	0.05579	0.00184	0.07014	0.00071	439.4	73.6	434.2	12.6	433.3	5.0	1.4
11NC57E-85.1	220	0.30	0.05565	0.00179	0.07104	0.00062	434.8	72.5	434.4	12.4	434.3	4.8	0.1
11NC57E-38.1	596	0.88	0.05589	0.00068	0.06662	0.00043	441.4	30.6	435.6	5.7	434.4	3.5	1.6
11NC57E-42.1	777	0.29	0.05614	0.00056	0.06569	0.00041	436.7	27.2	435.1	5.4	434.8	3.8	0.5
11NC57E-76.1	70	0.45	0.05699	0.00194	0.07073	0.00075	464.8	75.9	439.8	13.2	435.1	5.3	6.6
11NC57E-7.1	220	0.20	0.05587	0.00072	0.06563	0.00045	419.2	31.4	432.6	6.0	435.1	4.0	-3.9
11NC57E-1.1	2722	0.33	0.05608	0.00044	0.06597	0.00040	432.7	25.0	434.8	5.2	435.2	4.0	-0.6
11NC57E-55.1	600	0.28	0.05547	0.00069	0.06478	0.00048	415.7	31.6	432.2	6.0	435.4	4.0	-4.9
11NC57E-31.1	346	0.60	0.05576	0.00072	0.06566	0.00043	432.8	32.2	435.3	6.0	435.8	3.7	-0.7
11NC57E-68.1	146	0.36	0.05512	0.00133	0.07171	0.00072	428.3	55.0	435.1	9.8	436.4	5.0	-2.0
11NC57E-41.1	1208	0.39	0.05620	0.00048	0.06663	0.00037	436.1	23.5	436.4	4.6	436.4	3.3	-0.1
11NC57E-36.1	789	0.28	0.05536	0.00044	0.06597	0.00040	438.8	24.4	436.9	4.9	436.5	3.6	0.5
11NC57E-84.1	171	0.34	0.05559	0.00203	0.07177	0.00073	445.0	82.4	439.4	14.2	438.4	5.6	1.5
11NC57E-53.1	136	0.30	0.05546	0.00199	0.06535	0.00067	430.7	79.4	437.2	13.5	438.4	5.0	-1.8
11NC57E-28.1	1167	0.25	0.05542	0.00045	0.06529	0.00045	432.1	24.1	437.6	5.1	438.6	3.9	-1.6
11NC57E-37.1	561	0.36	0.05546	0.00081	0.06679	0.00037	435.7	36.6	438.3	6.6	438.8	3.5	-0.7
11NC57E-13.1	341	0.20	0.05631	0.00072	0.06553	0.00044	436.0	31.5	438.4	5.9	438.9	3.7	-0.7
11NC57E-12.1	694	0.22	0.05614	0.00053	0.06608	0.00043	434.7	25.5	438.3	5.1	439.0	3.6	-1.0
11NC57E-98.1	392	0.40	0.05587	0.00126	0.07324	0.00052	425.3	55.3	437.3	9.6	439.6	4.5	-3.5
11NC57E-32.1	298	0.36	0.05610	0.00067	0.06652	0.00042	448.5	28.7	441.7	5.5	440.4	3.5	1.9
11NC57E-114.1r	132	0.34	0.05566	0.00219	0.07191	0.00074	426.6	88.1	438.7	15.1	441.0	5.5	-3.5
11NC57E-66.1	378	0.31	0.05589	0.00094	0.07177	0.00074	432.5	45.3	440.0	8.8	441.5	5.9	-2.1
11NC57E-86.1	171	0.41	0.05625	0.00197	0.07233	0.00076	446.1	78.3	442.7	13.7	442.1	5.6	0.9
11NC57E-16.1	334	0.38	0.05689	0.00085	0.06567	0.00044	448.5	36.7	443.4	6.7	442.4	3.7	1.4

Table A.3: *continued*

Spot Name	U (ppm)	^{232}Th/ ^{238}U	^{207}Pb/^{206}Pb	±1σ	^{206}Pb/^{238}U	±1σ (%)	^{207}Pb/^{206}Pb Age (Ma)	±1σ	^{207}Pb/^{235}Pb Age (Ma)	±1σ	^{206}Pb/^{238}Pb Age (Ma)	±1σ	% Discordant
Mazongshan accretionary complex continued													
11NC57E-57.1	558	0.56	0.05603	0.00083	0.06546	0.00032	439.3	37.2	442.1	6.7	442.7	3.5	-0.8
11NC57E-111.1	491	0.38	0.05692	0.00159	0.07284	0.00055	447.5	66.7	443.5	11.7	442.7	4.9	1.1
11NC57E-30.1	312	0.20	0.05601	0.00086	0.06610	0.00041	442.8	35.7	442.8	6.6	442.8	3.7	0.0
11NC57E-74.1	78	0.28	0.05611	0.00212	0.07252	0.00074	444.7	83.6	443.6	14.5	443.4	5.3	0.3
11NC57E-20.1	546	0.22	0.05588	0.00075	0.06543	0.00041	443.9	32.5	443.5	6.0	443.4	3.4	0.1
11NC57E-15.1	37	0.33	0.05686	0.00301	0.06610	0.00078	443.4	114.6	443.6	19.6	443.7	5.6	-0.1
11NC57E-105.1r	758	0.28	0.05649	0.00092	0.07237	0.00042	454.5	42.0	445.6	7.7	443.9	4.2	2.4
11NC57E-89.1	107	0.44	0.05559	0.00208	0.07163	0.00077	443.4	83.2	444.0	14.4	444.2	5.4	-0.2
11NC57E-62.1	277	0.37	0.05541	0.00106	0.07213	0.00054	432.2	45.4	442.3	8.2	444.2	4.3	-2.9
11NC57E-10.1	620	0.32	0.05653	0.00069	0.06779	0.00066	446.3	31.1	444.6	6.7	444.3	5.2	0.5
11NC57E-51.1	229	0.36	0.05561	0.00132	0.06597	0.00043	435.0	54.9	442.9	9.6	444.4	4.2	-2.2
11NC57E-4.1	963	0.33	0.05647	0.00057	0.06647	0.00051	442.2	25.8	444.2	5.5	444.6	4.2	-0.6
11NC57E-11.1	773	0.29	0.05652	0.00056	0.06742	0.00041	447.6	25.7	445.2	5.2	444.8	3.6	0.7
11NC57E-75.1	553	0.37	0.05657	0.00092	0.07260	0.00046	449.6	39.8	445.9	7.4	445.1	4.1	1.0
11NC57E-43.1	1237	0.15	0.05632	0.00039	0.06674	0.00041	449.3	22.2	446.2	4.9	445.6	3.9	0.9
11NC57E-3.1	140	0.57	0.05640	0.00157	0.06692	0.00061	441.3	62.3	445.0	11.0	445.7	4.7	-1.0
11NC57E-97.1r	788	0.23	0.05645	0.00090	0.07374	0.00052	439.9	40.8	444.9	7.6	445.9	4.4	-1.4
11NC57E-91.1	199	0.72	0.05530	0.00199	0.07206	0.00078	444.9	81.7	445.8	14.3	445.9	5.8	-0.2
11NC57E-70.1	36	0.32	0.05567	0.00251	0.07340	0.00095	463.7	98.4	448.9	17.2	446.0	6.1	4.0
11NC57E-64.1r	82	0.20	0.05623	0.00184	0.07255	0.00067	451.3	72.6	446.9	12.7	446.1	4.8	1.2
11NC57E-63.1	140	0.44	0.05603	0.00118	0.07259	0.00061	453.0	48.4	447.3	8.8	446.2	4.5	1.5
11NC57E-25.1	800	0.35	0.05623	0.00059	0.06760	0.00041	450.1	30.3	447.1	6.1	446.6	4.2	0.8
11NC57E-78.1	546	0.33	0.05607	0.00103	0.07310	0.00063	441.0	46.7	445.7	8.8	446.6	5.2	-1.3
11NC57E-21.1	308	0.36	0.05617	0.00088	0.06604	0.00057	455.6	37.5	448.6	7.2	447.2	4.4	1.9
11NC57E-8.1	436	0.18	0.05707	0.00068	0.06791	0.00052	466.1	29.2	450.3	6.0	447.3	4.3	4.2
11NC57E-113.1	377	0.33	0.05642	0.00154	0.07337	0.00048	435.6	63.5	445.5	11.0	447.4	4.2	-2.8
11NC57E-46.1	217	0.32	0.05651	0.00108	0.06682	0.00061	452.2	45.5	448.2	8.5	447.4	4.9	1.1
11NC57E-72.1	229	0.56	0.05565	0.00151	0.07339	0.00067	450.6	63.0	448.6	11.2	448.2	5.0	0.6
11NC57E-27.1	430	0.27	0.05601	0.00082	0.06717	0.00043	455.3	36.3	449.9	6.8	448.9	3.9	1.5
11NC57E-65.1	405	0.56	0.05659	0.00098	0.07276	0.00060	453.2	45.9	449.7	8.8	449.0	5.4	1.0
11NC57E-5.1	525	0.32	0.05661	0.00065	0.06725	0.00040	448.2	27.6	448.9	5.4	449.1	3.6	-0.2
11NC57E-33.1	337	0.69	0.05636	0.00069	0.06802	0.00046	461.1	29.0	451.1	5.7	449.1	3.7	2.7
11NC57E-23.1	442	0.26	0.05626	0.00075	0.06737	0.00042	452.0	33.4	449.6	6.3	449.1	3.8	0.7
11NC57E-59.1	1378	0.34	0.05662	0.00052	0.06638	0.00043	453.3	25.8	450.0	5.3	449.4	3.8	0.9
11NC57E-119.1	172	0.31	0.05547	0.00231	0.07438	0.00088	457.7	94.6	450.9	16.6	449.6	6.2	1.8
11NC57E-87.1	457	0.47	0.05632	0.00107	0.07324	0.00064	448.5	45.8	449.5	8.7	449.7	5.1	-0.3

Table A.3: *continued*

Spot Name	U (ppm)	^{232}Th/ ^{238}U	^{207}Pb/^{206}Pb	±1σ	^{206}Pb/^{238}U	±1σ (%)	^{207}Pb/^{206}Pb Age (Ma)	±1σ	^{207}Pb/^{235}Pb Age (Ma)	±1σ	^{206}Pb/^{238}Pb Age (Ma)	±1σ	% Discordant
Mazongshan accretionary complex continued													
11NC57E-14.1	708	0.15	0.05674	0.00057	0.06714	0.00048	445.7	26.3	449.2	5.3	449.8	3.8	-1.0
11NC57E-58.1	1049	0.60	0.05650	0.00062	0.06641	0.00043	453.3	30.3	450.5	6.0	449.9	4.0	0.8
11NC57E-69.1	19	0.63	0.05518	0.00395	0.07434	0.00138	444.1	152.6	449.5	26.8	450.5	8.5	-1.5
11NC57E-71.1	571	0.30	0.05554	0.00077	0.07402	0.00047	458.8	37.3	452.0	7.0	450.6	4.1	1.9
11NC57E-94.1	1538	0.35	0.05604	0.00084	0.07350	0.00052	452.9	41.6	451.3	8.0	451.0	4.8	0.5
11NC57E-60.1	1242	0.24	0.05673	0.00055	0.06672	0.00039	452.3	27.9	451.4	5.5	451.2	3.7	0.3
11NC57E-102.1	899	0.39	0.05575	0.00089	0.07438	0.00059	451.7	43.0	451.6	8.3	451.5	5.2	0.0
11NC57E-6.1	719	0.22	0.05691	0.00060	0.06779	0.00042	460.3	26.4	453.5	5.5	452.1	4.0	1.9
11NC57E-116.1	438	0.53	0.05618	0.00137	0.07285	0.00061	454.1	59.7	452.6	10.9	452.2	5.5	0.4
11NC57E-106.1	663	0.44	0.05651	0.00093	0.07379	0.00046	465.2	44.6	454.5	8.4	452.4	4.8	2.9
11NC57E-73.1	187	0.26	0.05599	0.00154	0.07413	0.00061	451.9	62.5	452.6	11.1	452.7	4.5	-0.2
11NC57E-24.1	2305	0.16	0.05664	0.00037	0.06860	0.00055	462.9	24.1	455.2	5.7	453.7	4.8	2.0
11NC57E-67.1	373	0.41	0.05590	0.00081	0.07429	0.00057	446.3	37.1	452.7	7.2	454.0	4.6	-1.8
11NC57E-56.1	267	0.30	0.05644	0.00109	0.06773	0.00054	454.9	44.9	455.8	8.3	456.0	4.3	-0.2
11NC57E-93.1	1668	0.44	0.05601	0.00074	0.07428	0.00052	463.1	42.5	458.1	8.4	457.2	5.4	1.3
11NC57E-19.1	1046	0.20	0.05646	0.00046	0.06762	0.00056	466.1	23.4	459.3	5.4	457.9	4.4	1.8
11NC57E-115.1	738	0.38	0.05572	0.00092	0.07400	0.00046	440.6	42.5	455.1	7.9	458.0	4.4	-4.1
11NC57E-108.1	521	0.46	0.05521	0.00128	0.07529	0.00067	461.3	57.9	464.0	10.8	464.5	5.5	-0.7
11NC57E-52.1	1109	0.27	0.05621	0.00056	0.06963	0.00051	468.9	27.7	466.9	6.1	466.5	4.6	0.5
11NC57E-117.1	1074	0.52	0.05637	0.00099	0.07595	0.00058	473.0	46.9	467.7	9.1	466.6	5.3	1.4
11NC57E-110.1	768	0.52	0.05654	0.00119	0.07685	0.00060	467.3	52.0	469.0	9.8	469.3	5.0	-0.4
11NC57E-47.1	762	0.47	0.05738	0.00081	0.07118	0.00063	474.3	34.2	477.2	7.2	477.8	4.9	-0.8
11NC57E-45.1	1460	0.20	0.05725	0.00044	0.07260	0.00042	490.3	24.6	484.0	5.5	482.7	4.1	1.6
Permian (?Triassic) – North of Liuyuan Complex													
11NC58-4.1	187	1.10	0.05100	0.00258	0.04323	0.00057	266.8	114.3	262.2	12.4	261.7	4.1	2.0
11NC58-70.1	231	0.66	0.05357	0.00153	0.04734	0.00054	254.2	66.6	264.1	7.5	265.2	3.5	-4.4
11NC58-22.1	183	0.40	0.05164	0.00219	0.04450	0.00057	260.5	98.9	266.3	10.9	266.9	4.0	-2.5
11NC58-24.1r	157	0.32	0.05298	0.00180	0.04997	0.00056	269.3	80.7	271.5	9.2	271.8	4.0	-0.9
11NC58-35.1	346	0.94	0.05311	0.00143	0.04968	0.00052	284.8	64.7	275.1	7.7	273.9	3.8	3.9
11NC58-22.1	41	1.01	0.05383	0.00278	0.05138	0.00079	267.4	115.5	274.3	13.1	275.1	4.7	-2.9
11NC58-10.1	457	0.61	0.05200	0.00165	0.04515	0.00044	268.0	77.7	274.9	8.9	275.7	3.7	-2.9
11NC58-12.1	1275	0.36	0.05366	0.00073	0.05077	0.00054	270.2	37.4	275.3	5.1	275.9	3.6	-2.1
11NC58-72.1	90	0.30	0.05390	0.00226	0.05027	0.00070	271.2	95.1	278.3	11.0	279.1	4.3	-3.0
11NC58-32.1	139	0.46	0.05237	0.00175	0.04876	0.00054	271.3	77.4	280.1	9.1	281.1	4.0	-3.7
11NC58-65.2r	103	0.49	0.05404	0.00213	0.05073	0.00063	298.3	88.9	285.7	10.6	284.2	4.1	4.8
11NC58-21.1	248	0.75	0.05470	0.00145	0.05408	0.00048	298.2	62.0	293.9	7.6	293.4	3.3	1.7

Table A.3: *continued*

Spot Name	U (ppm)	^{232}Th/ ^{238}U	^{207}Pb/^{206}Pb	±1σ	^{206}Pb/^{238}U	±1σ (%)	^{207}Pb/^{206}Pb Age (Ma)	±1σ	^{207}Pb/^{235}Pb Age (Ma)	±1σ	^{206}Pb/^{238}Pb Age (Ma)	±1σ	% Discordant
Permian (?Triassic) – North of Liuyuan Complex continued													
11NC58-69.1c	412	0.55	0.05451	0.00099	0.05337	0.00055	287.7	44.8	295.6	6.1	296.6	3.8	-3.2
11NC58-69.2r	1268	0.19	0.05462	0.00063	0.05341	0.00044	290.2	32.1	297.0	4.7	297.9	3.4	-2.7
11NC58-20.1	471	0.37	0.05241	0.00248	0.05445	0.00060	323.5	118.7	320.5	15.4	320.1	5.5	1.1
11NC58-48.1	190	0.58	0.05546	0.00121	0.06457	0.00057	356.4	51.4	355.6	7.7	355.4	4.0	0.3
11NC58-14.1	841	0.31	0.05162	0.00179	0.06182	0.00066	361.8	93.0	361.2	14.2	361.1	7.6	0.2
11NC58-55.1c	438	0.49	0.05502	0.00091	0.06611	0.00060	360.4	41.7	362.6	6.9	362.9	4.5	-0.7
11NC58-7.1	295	0.49	0.05350	0.00166	0.06063	0.00045	378.2	74.0	370.1	11.0	368.8	4.2	2.5
11NC58-8.1	438	0.26	0.05393	0.00150	0.06120	0.00052	382.8	66.6	373.8	10.1	372.4	4.3	2.8
11NC58-26.1	299	0.54	0.05501	0.00113	0.07001	0.00066	363.5	50.2	373.6	8.2	375.3	4.9	-3.3
11NC58-42.2r	713	0.11	0.05573	0.00092	0.08133	0.00119	397.8	42.4	389.3	8.5	387.8	6.8	2.6
11NC58-17.1	658	0.68	0.05651	0.00086	0.07515	0.00094	419.8	38.9	406.7	7.8	404.4	5.9	3.8
11NC58-66.1	479	0.57	0.05718	0.00090	0.07348	0.00067	425.5	39.6	408.2	7.4	405.1	5.1	4.9
11NC58-51.1c	192	0.65	0.05688	0.00161	0.07414	0.00065	398.0	65.7	406.1	10.8	407.5	5.1	-2.5
11NC58-58.1	244	0.48	0.05652	0.00107	0.07434	0.00074	396.7	44.9	407.6	7.9	409.5	4.8	-3.3
11NC58-19.1	460	1.52	0.05434	0.00159	0.07041	0.00062	409.2	85.4	411.0	14.1	411.3	6.6	-0.5
11NC58-16.1	174	0.73	0.05424	0.00247	0.06961	0.00093	409.8	102.8	413.0	16.9	413.5	6.7	-1.0
11NC58-53.1	68	0.70	0.05716	0.00209	0.07570	0.00096	411.0	81.5	414.1	13.7	414.6	6.2	-0.9
11NC58-62.1	78	0.85	0.05662	0.00257	0.07532	0.00100	416.2	101.0	415.6	16.7	415.4	6.6	0.2
11NC58-15.2r	856	0.52	0.05375	0.00110	0.07134	0.00060	424.2	58.5	420.3	10.6	419.6	6.5	1.1
11NC58-38.1	72	0.68	0.05814	0.00213	0.07666	0.00075	429.9	81.1	422.5	13.5	421.1	4.9	2.1
11NC58-17.1	95	0.70	0.05504	0.00356	0.07146	0.00123	418.2	141.4	423.4	23.6	424.4	8.0	-1.5
11NC58-37.1	1000	0.36	0.05310	0.00103	0.07066	0.00046	429.1	52.8	426.4	9.5	425.9	5.5	0.8
11NC58-49.1	476	0.51	0.05732	0.00073	0.07772	0.00088	427.2	32.6	426.1	6.9	425.9	5.6	0.3
11NC58-5.2c	1100	0.56	0.05670	0.00083	0.08734	0.00127	432.2	40.1	428.7	9.0	428.1	7.6	1.0
11NC58-5.1	330	1.10	0.05474	0.00160	0.07153	0.00069	432.2	67.4	429.7	11.6	429.2	5.3	0.7
11NC58-47.1	163	0.52	0.05646	0.00114	0.07914	0.00077	413.1	47.7	428.3	8.6	431.1	5.1	-4.5
11NC58-60.1	731	0.27	0.05772	0.00073	0.07848	0.00059	446.5	33.1	433.7	6.5	431.3	4.4	3.5
11NC58-51.2r	173	0.50	0.05744	0.00142	0.07882	0.00066	414.9	56.8	429.4	9.9	432.1	4.9	-4.3
11NC58-57.1r	655	0.36	0.05687	0.00081	0.07892	0.00063	424.3	35.2	431.4	6.7	432.8	4.5	-2.1
11NC58-52.1	658	0.54	0.05765	0.00055	0.07920	0.00079	417.9	27.4	431.3	6.4	433.8	5.6	-3.9
11NC58-24.1	211	0.23	0.05609	0.00201	0.07190	0.00068	451.0	81.7	436.8	14.0	434.1	5.3	3.9
11NC58-11.1r	563	0.36	0.05711	0.00106	0.08232	0.00085	426.2	44.4	436.6	8.4	438.6	5.4	-3.0
11NC58-28.1	219	0.90	0.05665	0.00137	0.08164	0.00090	432.1	56.5	438.3	10.5	439.5	6.1	-1.8
11NC58-30.1	288	0.56	0.05625	0.00129	0.08008	0.00079	423.9	56.0	440.3	10.5	443.5	6.4	-4.8
11NC58-25.1r	527	0.47	0.05683	0.00089	0.08229	0.00069	438.1	43.6	442.7	8.5	443.6	5.6	-1.3
11NC58-20.1	567	0.80	0.05804	0.00079	0.08152	0.00069	426.1	37.9	440.9	7.5	443.7	5.2	-4.3

Table A.3: *continued*

Spot Name	U (ppm)	^{232}Th/ ^{238}U	^{207}Pb/^{206}Pb	±1σ	^{206}Pb/^{238}U	±1σ (%)	^{207}Pb/^{206}Pb Age (Ma)	±1σ	^{207}Pb/^{235}Pb Age (Ma)	±1σ	^{206}Pb/^{238}Pb Age (Ma)	±1σ	% Discordant
Permian (?Triassic) – North of Liuyuan Complex continued													
11NC58-59.1	115	0.68	0.05741	0.00177	0.08089	0.00078	426.1	69.5	441.8	12.1	444.8	5.1	-4.5
11NC58-46.1	154	0.97	0.05728	0.00111	0.08210	0.00078	458.0	45.8	447.3	8.7	445.2	5.1	2.9
11NC58-43.1c	588	0.37	0.05695	0.00069	0.08117	0.00074	452.6	32.6	447.3	7.1	446.3	5.5	1.5
11NC58-36.1	269	0.49	0.05384	0.00190	0.07454	0.00091	455.9	83.2	448.2	15.2	446.7	7.6	2.1
11NC58-42.1c	170	0.93	0.05733	0.00132	0.08079	0.00074	441.7	53.6	446.1	9.9	446.9	5.6	-1.2
11NC58-9.1	348	0.58	0.05596	0.00130	0.07403	0.00072	452.1	58.8	448.8	10.8	448.1	5.8	0.9
11NC58-11.1r	857	0.23	0.05633	0.00094	0.07481	0.00058	443.6	45.9	447.4	8.6	448.2	5.0	-1.1
11NC58-44.1r	307	1.20	0.05619	0.00100	0.08266	0.00073	435.1	44.3	446.1	8.6	448.2	5.5	-3.1
11NC58-19.1	813	0.39	0.05830	0.00086	0.08268	0.00073	449.8	39.9	451.7	8.0	452.1	5.4	-0.5
11NC58-56.1	235	0.56	0.05694	0.00126	0.08282	0.00082	440.9	52.1	450.4	9.8	452.3	5.8	-2.7
11NC58-50.1	521	0.47	0.05777	0.00083	0.08268	0.00079	441.2	37.8	450.8	7.9	452.6	5.8	-2.7
11NC58-34.1	157	0.36	0.05558	0.00223	0.07505	0.00079	457.3	90.2	453.9	15.9	453.3	5.9	0.9
11NC58-68.1	173	0.56	0.05829	0.00116	0.08282	0.00081	448.7	46.8	452.9	9.0	453.8	5.5	-1.2
11NC58-64.1	63	0.33	0.05808	0.00212	0.08189	0.00107	464.7	80.7	457.2	14.8	455.7	6.8	2.0
11NC58-18.1	417	0.35	0.05808	0.00122	0.08487	0.00083	460.8	49.9	459.5	9.6	459.2	5.5	0.4
11NC58-37.1	104	1.01	0.05896	0.00131	0.08499	0.00090	468.3	51.1	464.5	9.9	463.8	5.7	1.0
11NC58-23.1	70	0.35	0.05681	0.00280	0.07794	0.00120	470.5	107.8	467.4	19.7	466.7	7.7	0.8
11NC58-44.2c	288	0.41	0.05743	0.00120	0.09950	0.00158	471.0	51.3	473.5	11.6	474.0	9.1	-0.7
11NC58-29.1	353	0.78	0.06686	0.00105	0.15098	0.00160	791.5	39.7	795.1	13.5	796.3	11.5	-0.6
11NC58-18.1	1478	0.07	0.06815	0.00063	0.14618	0.00095	886.3	41.6	847.9	13.6	833.4	9.7	6.4
11NC58-27.1	365	0.34	0.06772	0.00156	0.14609	0.00136	858.0	53.6	853.5	16.8	851.7	10.5	0.8
11NC58-2.1	329	0.34	0.06421	0.00086	0.17515	0.00164	928.8	33.4	916.2	12.7	911.0	11.3	2.0
11NC58-33.1	751	0.06	0.07150	0.00073	0.17282	0.00165	941.8	27.4	940.7	11.5	940.2	11.6	0.2
11NC58-10.1	263	1.21	0.07151	0.00102	0.18622	0.00176	921.7	33.2	939.3	12.7	946.8	11.4	-2.9
11NC58-1.1	251	0.72	0.07155	0.00121	0.16674	0.00140	982.8	39.9	965.2	14.3	957.5	10.5	2.8
11NC58-3.1	619	0.30	0.07046	0.00094	0.16760	0.00127	957.4	33.4	958.1	12.6	958.4	10.7	-0.1
11NC58-8.1c	61	2.11	0.07127	0.00179	0.18831	0.00198	923.2	52.7	952.4	17.9	965.1	11.7	-4.9
11NC58-8.2cr	354	0.38	0.07474	0.00099	0.21334	0.00322	1010.4	36.9	1009.1	17.0	1008.4	18.1	0.2
11NC58-23.1c	73	1.65	0.07727	0.00116	0.20679	0.00233	1057.9	33.6	1044.1	14.2	1037.6	13.4	2.1
11NC58-1.1	314	0.37	0.07557	0.00080	0.20506	0.00164	1134.9	27.1	1071.6	12.4	1040.8	12.3	9.0
11NC58-57.2c	296	0.36	0.07981	0.00138	0.25423	0.00368	1147.6	40.2	1140.2	18.7	1136.3	18.9	1.1
11NC58-67.1	367	0.82	0.08163	0.00084	0.22650	0.00244	1162.9	26.5	1167.7	13.5	1170.3	15.1	-0.7
11NC58-21.1	295	0.26	0.08831	0.00106	0.25237	0.00154	1393.9	40.8	1382.8	18.4	1375.7	14.8	1.5
11NC58-39.1	1523	0.79	0.09321	0.00066	0.27040	0.00242	1395.2	21.9	1386.7	12.7	1381.2	15.4	1.1
11NC58-11.2c	1093	0.23	0.08924	0.00084	0.24990	0.00144	1385.9	32.4	1383.9	15.4	1382.5	14.3	0.3
11NC58-61.1	533	0.69	0.09440	0.00073	0.27639	0.00228	1461.0	24.1	1426.6	13.6	1403.6	15.8	4.4

Table A.3: *continued*

Spot Name	U (ppm)	^{232}Th/ ^{238}U	^{207}Pb/^{206}Pb	±1σ	^{206}Pb/^{238}U	±1σ (%)	^{207}Pb/^{206}Pb Age (Ma)	±1σ	^{207}Pb/^{235}Pb Age (Ma)	±1σ	^{206}Pb/^{238}Pb Age (Ma)	±1σ	% Discordant
Permian (?Triassic) – North of Liuyuan Complex continued													
11NC58-31.1	1222	0.30	0.09061	0.00079	0.25582	0.00154	1424.0	42.1	1419.9	19.8	1417.2	17.4	0.5
11NC58-29.2r	1283	0.19	0.09126	0.00078	0.25840	0.00183	1436.6	33.7	1428.0	16.5	1422.3	15.8	1.1
11NC58-40.1	2647	0.21	0.09105	0.00057	0.25174	0.00163	1472.8	29.5	1442.8	14.8	1422.5	14.4	3.8
11NC58-6.1	671	0.31	0.09039	0.00082	0.25570	0.00162	1464.3	28.9	1440.1	14.4	1423.8	14.0	3.1
11NC58-45.1	588	0.51	0.09216	0.00082	0.28545	0.00242	1443.6	24.6	1433.7	13.8	1427.0	15.9	1.3
11NC58-39.1	1521	0.41	0.08979	0.00051	0.25669	0.00149	1448.3	25.4	1448.8	12.9	1449.1	13.1	-0.1
11NC58-71.1	1390	0.44	0.09356	0.00067	0.28398	0.00220	1423.5	21.7	1440.1	12.3	1451.3	14.5	-2.2
11NC58-9.1	268	0.12	0.10701	0.00094	0.35888	0.00389	1713.9	21.4	1715.9	15.1	1717.6	21.1	-0.2
11NC58-13.1	319	0.42	0.11498	0.00147	0.36740	0.00304	1919.4	39.1	1914.4	23.4	1909.8	26.9	0.6
11NC58-54.1	70	1.72	0.16746	0.00177	0.52986	0.00506	2479.8	21.6	2470.8	16.5	2459.9	25.3	1.0
11NC58-25.1	109	0.53	0.16701	0.00244	0.49407	0.00424	2531.0	34.2	2532.1	22.9	2533.6	28.7	-0.1
11NC58-36.1	266	0.28	0.19552	0.00144	0.58880	0.00541	2736.4	18.7	2700.2	16.0	2652.1	27.5	3.8
11NC58-25.2c	522	2.22	0.35091	0.00195	0.83935	0.00760	3678.2	16.8	3616.4	16.5	3505.8	34.0	6.1
11NC59-4.3r	89	0.25	0.05242	0.00178	0.05089	0.00108	251.8	79.3	246.1	9.2	245.5	5.7	2.6
11NC59-17.1	48	0.49	0.05311	0.00343	0.04718	0.00082	260.4	143.1	261.1	15.5	261.2	4.9	-0.3
11NC59-15.1	60	0.41	0.05349	0.00262	0.04823	0.00072	260.5	110.5	265.1	12.2	265.6	4.5	-2.0
11NC59-45.1	208	1.66	0.05269	0.00186	0.04869	0.00051	274.9	82.0	268.1	9.1	267.3	3.5	2.8
11NC59-27.1	55	0.70	0.05269	0.00244	0.04885	0.00066	257.1	105.2	266.3	11.6	267.3	4.1	-4.0
11NC59-8.1	102	0.34	0.05223	0.00195	0.03947	0.00049	262.5	85.0	267.2	9.4	267.7	3.6	-2.0
Triassic – South of Liuyuan Complex													
11NC59-7.1	26	0.53	0.05346	0.00330	0.04874	0.00098	266.9	137.4	272.4	15.7	273.1	5.8	-2.4
11NC59-22.1	55	0.56	0.05302	0.00297	0.04929	0.00096	265.7	125.6	272.4	14.4	273.1	5.6	-2.9
11NC59-5.1	1502	0.48	0.05303	0.00063	0.04958	0.00046	282.5	34.7	274.9	4.7	274.0	3.4	3.0
11NC59-44.1	448	0.70	0.05266	0.00108	0.04984	0.00046	281.0	49.5	275.4	6.0	274.7	3.1	2.3
11NC59-26.1	370	0.46	0.05166	0.00107	0.04182	0.00026	272.0	49.5	277.2	5.7	277.8	2.3	-2.2
11NC59-49.1c	404	0.39	0.05371	0.00118	0.04969	0.00037	281.4	53.3	280.0	6.4	279.9	3.0	0.5
11NC59-30.1	1851	0.63	0.05314	0.00064	0.05104	0.00048	279.4	36.9	280.3	5.1	280.4	3.7	-0.4
11NC59-19.1	794	0.44	0.05266	0.00095	0.04052	0.00026	278.6	46.2	280.5	5.5	280.7	2.7	-0.8
11NC59-49.2r	292	0.21	0.05449	0.00136	0.07391	0.00100	345.7	60.3	349.4	9.5	350.0	6.0	-1.3
11NC59-14.2r	419	0.22	0.05590	0.00096	0.06727	0.00053	359.2	42.2	366.4	6.7	367.6	3.9	-2.4
11NC59-36.1r	832	0.22	0.05545	0.00090	0.06804	0.00069	361.2	41.7	371.4	7.1	373.1	4.9	-3.4
11NC59-65.1	336	0.36	0.05560	0.00072	0.06930	0.00047	393.9	31.9	378.7	5.4	376.2	3.5	4.6
11NC59-20.1	277	0.38	0.05559	0.00135	0.05732	0.00047	394.5	56.2	394.5	8.9	394.5	3.9	0.0
11NC59-6.1	210	0.53	0.05641	0.00156	0.07334	0.00085	405.4	63.8	404.2	10.7	404.0	5.4	0.4
11NC59-43.1	153	0.86	0.05533	0.00173	0.07471	0.00076	399.8	70.7	407.9	11.6	409.4	5.0	-2.5
11NC59-67.1	155	0.51	0.05657	0.00098	0.07542	0.00068	412.7	41.1	411.5	7.4	411.2	4.7	0.4
11NC59-40.3r	380	0.14	0.05578	0.00091	0.08602	0.00132	398.7	43.6	409.5	9.3	411.4	7.8	-3.3

Table A.3: *continued*

Spot Name	U (ppm)	^{232}Th/ ^{238}U	^{207}Pb/^{206}Pb	±1σ	^{206}Pb/^{238}U	±1σ (%)	^{207}Pb/^{206}Pb Age (Ma)	±1σ	^{207}Pb/^{235}Pb Age (Ma)	±1σ	^{206}Pb/^{238}Pb Age (Ma)	±1σ	% Discordant
Triassic – South of Liuyuan Complex continued													
11NC59-2.1	532	0.12	0.05577	0.00090	0.06203	0.00029	417.9	38.3	413.8	6.3	413.0	2.8	1.2
11NC59-9.1	684	0.21	0.05573	0.00067	0.06131	0.00041	398.0	30.3	411.4	5.4	413.8	3.4	-4.1
11NC59-46.1	376	0.65	0.05595	0.00108	0.07599	0.00065	395.6	47.6	411.2	8.3	414.0	4.7	-4.8
11NC59-1.1	291	0.20	0.05606	0.00116	0.07632	0.00082	400.9	50.1	412.2	9.1	414.2	5.8	-3.4
11NC59-3.1c	155	0.51	0.05608	0.00154	0.07639	0.00090	400.9	63.8	413.7	11.0	416.0	6.0	-3.9
11NC59-32.1	1255	0.61	0.05623	0.00059	0.07632	0.00060	433.5	33.3	418.7	6.7	416.0	5.0	4.2
11NC59-24.2r	1399	0.79	0.05652	0.00061	0.07675	0.00069	418.6	33.2	417.5	6.7	417.3	5.2	0.3
11NC59-24.1	700	0.47	0.05497	0.00059	0.06281	0.00044	431.5	28.5	422.0	5.4	420.2	3.7	2.7
11NC59-12.1	124	0.41	0.05686	0.00172	0.07706	0.00070	417.3	68.3	420.3	11.4	420.9	4.8	-0.9
11NC59-66.1	145	0.40	0.05665	0.00085	0.07781	0.00068	425.6	36.2	422.0	6.9	421.3	4.7	1.1
11NC59-3.2r	444	0.21	0.05665	0.00080	0.07746	0.00072	429.4	37.5	423.0	7.3	421.9	5.3	1.8
11NC59-29.1	213	0.82	0.05716	0.00206	0.07753	0.00100	425.2	83.6	422.4	14.4	421.9	7.0	0.8
11NC59-26.1	280	0.17	0.05620	0.00123	0.07810	0.00067	412.0	51.9	420.6	9.0	422.2	4.7	-2.6
11NC59-12.1	2062	0.08	0.05574	0.00041	0.06237	0.00036	421.5	20.8	422.3	4.3	422.5	3.3	-0.2
11NC59-21.1	325	0.38	0.05681	0.00113	0.07707	0.00083	422.1	48.6	422.8	8.9	423.0	5.5	-0.2
11NC59-13.1	791	0.65	0.05685	0.00074	0.07764	0.00061	405.4	35.0	420.5	6.6	423.3	4.5	-4.6
11NC59-67.3cc	576	0.15	0.05664	0.00116	0.08792	0.00134	421.4	49.7	423.4	10.2	423.8	7.8	-0.6
11NC59-64.1r	702	0.32	0.05608	0.00058	0.07848	0.00068	423.0	28.1	423.8	5.9	424.0	4.6	-0.2
11NC59-25.1	456	0.52	0.05586	0.00073	0.06435	0.00049	470.2	32.4	431.5	6.1	424.3	3.8	10.0
11NC59-60.1	90	0.34	0.05744	0.00138	0.07768	0.00065	436.8	54.2	426.5	9.4	424.6	4.6	2.9
11NC59-21.1	809	0.43	0.05624	0.00064	0.06195	0.00042	413.7	30.1	424.4	5.6	426.3	3.7	-3.1
11NC59-71.1	196	0.70	0.05774	0.00175	0.07671	0.00071	418.3	71.0	425.2	12.0	426.5	5.2	-2.0
11NC59-23.1	1268	0.13	0.05571	0.00046	0.06324	0.00038	435.7	23.2	428.6	4.6	427.3	3.3	2.0
11NC59-31.1	225	0.39	0.05650	0.00161	0.07879	0.00085	436.9	67.1	428.8	11.8	427.3	6.0	2.3
11NC59-16.1	371	0.44	0.05695	0.00122	0.07850	0.00075	411.3	51.3	425.3	9.2	427.8	5.4	-4.2
11NC59-24.1c	778	0.23	0.05663	0.00080	0.07842	0.00062	418.2	38.9	426.4	7.4	427.9	5.0	-2.4
11NC59-62.1	695	0.74	0.05704	0.00056	0.07902	0.00061	449.4	25.4	432.2	5.4	429.0	4.2	4.7
11NC59-9.1	301	0.23	0.05709	0.00112	0.07793	0.00068	424.2	46.7	429.4	8.5	430.4	4.9	-1.5
11NC59-48.1	636	0.69	0.05716	0.00067	0.07786	0.00062	426.8	32.5	430.2	6.5	430.8	4.7	-1.0
11NC59-11.1	310	0.25	0.05655	0.00078	0.06377	0.00043	442.0	32.6	433.6	6.0	432.0	3.5	2.4
11NC59-7.1	1028	0.44	0.05634	0.00069	0.06510	0.00041	445.2	32.8	435.0	6.2	433.0	4.0	2.8
11NC59-63.2	204	0.47	0.05823	0.00151	0.08803	0.00116	425.3	61.1	432.4	12.0	433.7	8.3	-2.0
11NC59-4.1c	419	0.41	0.05691	0.00097	0.07993	0.00077	445.8	41.8	436.2	8.0	434.4	5.2	2.6
11NC59-13.1	323	0.16	0.05573	0.00102	0.06420	0.00047	435.1	42.1	435.3	7.5	435.3	3.9	0.0
11NC59-61.1c	327	0.53	0.05686	0.00082	0.08022	0.00062	432.0	34.7	435.9	6.7	436.6	4.5	-1.1
11NC59-55.1	697	0.59	0.05364	0.00088	0.07950	0.00068	443.6	44.5	439.0	8.2	438.2	4.7	1.3
11NC59-47.1	371	0.59	0.05704	0.00118	0.07998	0.00071	430.4	49.0	437.2	8.9	438.5	4.9	-2.0
11NC59-10.1	165	0.19	0.05687	0.00118	0.06490	0.00048	443.2	47.3	440.3	8.3	439.7	3.8	0.8

Table A.3: *continued*

Spot Name	U (ppm)	^{232}Th/ ^{238}U	^{207}Pb/^{206}Pb	±1σ	^{206}Pb/^{238}U	±1σ (%)	^{207}Pb/^{206}Pb Age (Ma)	±1σ	^{207}Pb/^{235}Pb Age (Ma)	±1σ	^{206}Pb/^{238}Pb Age (Ma)	±1σ	% Discordant
Triassic – South of Liuyuan Complex continued													
11NC59-4.2cr	556	0.34	0.05646	0.00077	0.08106	0.00074	434.2	36.8	439.0	7.4	439.9	5.2	-1.3
11NC59-64.3r	1997	0.10	0.05806	0.00058	0.08884	0.00141	450.1	31.3	441.8	9.2	440.2	9.1	2.3
11NC59-16.1	528	0.26	0.05583	0.00089	0.06457	0.00046	439.3	38.5	440.6	7.0	440.9	3.9	-0.4
11NC59-52.1	364	0.57	0.05601	0.00098	0.07987	0.00065	439.7	41.8	440.8	7.8	441.0	4.7	-0.3
11NC59-2.1	723	0.20	0.05713	0.00072	0.08132	0.00071	442.7	33.4	441.4	6.9	441.2	5.2	0.3
11NC59-4.1	2168	0.12	0.05654	0.00049	0.06615	0.00038	440.9	26.2	441.7	5.2	441.8	3.7	-0.2
11NC59-37.1	1202	0.93	0.05559	0.00060	0.08094	0.00057	423.3	31.4	438.9	6.3	441.9	4.5	-4.5
11NC59-35.1	489	0.88	0.05737	0.00136	0.08061	0.00068	440.5	56.8	442.4	10.3	442.8	5.5	-0.5
11NC59-14.1	739	0.35	0.05611	0.00055	0.06519	0.00034	452.6	24.9	444.4	4.8	442.9	3.1	2.2
11NC59-25.1	390	0.49	0.05705	0.00094	0.08257	0.00074	442.2	41.1	446.0	7.9	446.8	5.1	-1.1
11NC59-70.1	242	0.85	0.05789	0.00149	0.08161	0.00079	443.5	59.9	450.4	10.8	451.7	5.3	-1.9
11NC59-67.2c	931	0.06	0.05755	0.00081	0.09495	0.00121	451.7	38.4	461.5	9.5	463.5	8.4	-2.7
11NC59-56.1	2451	0.11	0.05664	0.00035	0.08467	0.00080	502.1	24.0	470.8	5.9	464.4	5.1	7.8
11NC59-64.2c	947	0.33	0.05876	0.00066	0.09422	0.00166	461.0	31.9	463.9	9.7	464.5	9.8	-0.8
11NC59-33.1r	2408	0.67	0.05856	0.00047	0.08966	0.00069	511.6	27.2	492.8	6.6	488.7	5.4	4.7
11NC59-20.1	23	0.90	0.06713	0.00340	0.14790	0.00262	784.9	104.5	787.9	29.7	788.9	14.4	-0.5
11NC59-1.1	389	0.06	0.06584	0.00060	0.12348	0.00078	784.9	22.6	791.8	7.4	794.3	6.1	-1.3
11NC59-38.2c	258	0.39	0.07146	0.00110	0.19434	0.00312	927.0	38.4	905.0	16.5	896.0	16.9	3.6
11NC59-15.1	316	0.39	0.07023	0.00055	0.13850	0.00092	933.6	20.9	916.3	8.1	909.2	7.3	2.8
11NC59-34.1	267	0.45	0.07215	0.00120	0.17640	0.00168	943.2	39.6	936.4	14.5	933.6	11.7	1.1
11NC59-5.1	374	0.22	0.07256	0.00069	0.14658	0.00096	978.9	24.5	950.3	9.3	938.0	7.8	4.5
11NC59-17.1	523	0.36	0.07101	0.00062	0.14380	0.00082	945.2	23.5	944.0	8.7	943.5	7.2	0.2
11NC59-11.1	1341	0.09	0.07443	0.00058	0.18496	0.00165	1000.9	22.8	978.8	10.6	968.9	11.4	3.4
11NC59-3.1	330	0.93	0.07201	0.00080	0.15204	0.00096	956.1	27.5	967.8	10.1	973.0	8.0	-1.9
11NC59-28.2r	756	0.28	0.07479	0.00073	0.18959	0.00211	990.0	32.5	987.0	14.2	985.7	14.4	0.5
11NC59-28.1c	128	0.66	0.07570	0.00139	0.19522	0.00214	1025.1	41.8	1014.9	16.1	1010.2	13.1	1.6
11NC59-40.1cr	519	0.35	0.07584	0.00080	0.20280	0.00177	1098.3	27.5	1067.0	11.9	1051.8	11.3	4.6
11NC59-18.1	217	0.36	0.07760	0.00107	0.17104	0.00135	1117.9	33.3	1111.0	13.4	1107.5	11.0	1.0
11NC59-40.2cc	120	0.73	0.08030	0.00131	0.24897	0.00319	1164.6	37.2	1133.8	17.2	1117.7	17.0	4.4
11NC59-53.1c	466	0.46	0.08774	0.00069	0.26338	0.00206	1411.7	22.3	1375.9	11.6	1353.0	12.4	4.6
11NC59-57.1r	660	0.32	0.08991	0.00066	0.26698	0.00225	1392.7	20.9	1372.7	11.7	1359.9	13.5	2.6
11NC59-27.1	301	0.47	0.10982	0.00069	0.29323	0.00173	1784.8	17.0	1759.6	10.4	1738.6	12.5	3.0
11NC59-68.2r	35	0.21	0.12821	0.00234	0.48688	0.01162	2033.2	36.9	2032.4	29.5	2031.7	46.2	0.1
11NC59-68.1	39	0.49	0.14463	0.00181	0.46174	0.00467	2234.9	24.6	2215.2	16.8	2193.9	22.6	2.2
11NC59-51.1	381	0.25	0.14233	0.00100	0.45945	0.00339	2202.4	16.9	2204.4	12.8	2206.5	19.5	-0.2
11NC59-36.2c	717	0.67	0.28259	0.00168	0.73422	0.00498	3326.9	19.0	3271.8	16.7	3182.7	30.6	5.5
11NC59-10.1	135	0.72	0.30904	0.00211	0.76505	0.00622	3475.4	16.5	3419.4	15.9	3324.5	31.7	5.6

Table A.3: *continued*

Appendix B

Chapter 3 supplementary material

B.1 Geochemistry data tables

B.1.1 Mineral chemistry analyses

Representative spinel analyses

Sample	HLH-036F – Detrital							HLH-104C – Granular						HLH-075A – Granular			
Spot	#02	#02	#03	#04	#07	#08	#16	#02	#03	#05	#06	#07	#10	#05	#05	#07	#12
Remarks	grain	corona												grain	corona		
SiO_2	0.08	0.19	0.06	0.07	0.08	0.20	0.14	0.02	0.01	0.03	0.26	0.03	0.03	0.05	0.06	0.05	0.00
TiO_2	2.73	0.04	3.04	2.91	3.16	0.93	0.23	0.32	0.37	0.28	0.25	0.29	0.26	0.49	1.98	0.50	0.70
Al_2O_3	20.44	0.07	17.37	18.09	24.09	14.25	17.61	22.32	18.54	16.48	22.92	20.00	22.97	17.03	1.26	15.14	14.23
Cr_2O_3	36.57	0.55	36.59	35.25	32.30	35.87	43.07	36.20	39.60	42.66	35.85	39.17	35.89	34.24	31.73	33.66	36.30
$Fe_2O_3{}^{calc}$	8.24	68.08	8.18	7.49	8.55	12.99	11.00	9.75	9.99	9.34	9.70	9.11	8.80	12.78	29.78	16.95	15.24
FeO^{total}	28.11	92.17	33.11	34.93	27.79	40.98	24.79	32.27	32.92	33.32	31.87	32.71	32.14	42.67	57.39	44.94	41.91
FeO^{calc}	20.70	30.91	25.75	28.18	20.10	29.30	14.89	23.50	23.93	24.92	23.14	24.52	24.22	31.17	30.59	29.69	28.20
NiO	0.14	0.06	0.13	0.18	0.19	0.11	0.10	0.16	0.12	0.06	0.10	0.12	0.10	0.09	0.05	0.18	0.16
MgO	11.00	0.03	7.25	5.41	12.16	1.76	13.04	7.76	7.11	6.33	8.09	6.94	7.36	1.66	0.21	2.70	3.65
CaO	0.01	0.01	0.03	0.01	0.00	0.02	0.01	0.00	0.00	0.00	0.00	0.00	0.09	0.00	0.00	0.05	0.02
MnO	0.00	0.05	0.00	0.18	0.00	2.06	0.00	0.46	0.33	0.27	0.34	0.35	0.22	0.66	1.86	0.59	0.59
CoO	0.03	0.00	0.02	0.00	0.03	0.13	0.03	0.07	0.11	0.05	0.06	0.04	0.01	0.00	0.00	0.08	0.05
ZnO	0.10	0.00	0.11	0.37	0.09	0.85	0.08	0.30	0.26	0.21	0.31	0.34	0.37	1.09	0.41	0.35	0.37
Na_2O	0.00	0.00	0.00	0.01	0.00	0.02	0.02	0.00	0.05	0.00	0.00	0.05	0.04	0.02	0.01	0.02	0.00
Total	100.03	99.98	98.53	98.15	100.76	98.48	100.22	100.85	100.41	100.62	101.02	100.95	100.36	99.27	97.93	99.94	99.51
Mg#	48.66	0.14	33.43	25.49	51.89	9.66	60.94	37.03	34.63	31.18	38.40	33.53	35.14	8.68	1.20	13.95	18.75
Cr#	54.54	84.91	58.56	56.66	47.35	62.80	62.13	52.10	58.90	63.46	51.21	56.78	51.17	57.43	94.41	59.86	63.11

Table B.1: Representative sample of spinel mineral chemistry analyses. ‘Total’ includes values from $Fe_2O_3{}^{calc}$ and FeO^{calc}. Fe^{2+} and Fe^{3+} amounts calculated from spinel stoichiometric ratios. Mg# $=100 \times$ Mg / (Mg + Fe^{+2}) (mol% values). Cr# $= 100 \times$ Cr / (Cr + Al) (mol% values).

Sample	HLH-075A – Granular			HLH-046B – Vermicular								HLH-051E – Vermicular				
Spot	#14	#14	#18	#01	#04	#04	#05	#08	#18	#19	#20	#02	#09	#14	#17	#17
Remarks	grain	corona			grain	corona									grain	corona
SiO_2	0.06	1.20	0.03	0.04	0.04	0.95	0.03	0.04	0.09	0.05	0.02	0.05	0.02	0.16	0.01	0.24
TiO_2	0.46	1.70	0.65	0.00	0.00	0.00	0.00	0.00	0.00	0.00	0.00	0.00	0.00	0.00	0.00	0.00
Al_2O_3	19.18	0.84	16.69	11.42	11.50	0.12	11.68	11.23	11.04	11.65	11.98	15.97	13.42	12.39	15.93	0.12
Cr_2O_3	37.90	17.77	35.90	56.63	54.72	6.89	56.89	56.31	56.98	56.77	55.29	49.68	54.11	55.25	49.78	1.52
$Fe_2O_3^{calc}$	10.00	45.81	14.13	2.46	3.96	63.69	2.94	3.27	2.79	2.51	3.44	4.45	3.85	3.63	4.49	66.89
FeO^{total}	34.06	70.12	38.93	22.77	25.57	84.71	21.94	23.67	22.57	22.22	23.40	25.43	22.53	21.43	24.74	90.63
FeO^{calc}	25.06	28.91	26.21	20.56	22.01	27.41	19.30	20.73	20.06	19.96	20.30	21.42	19.06	18.17	20.70	30.43
NiO	0.10	0.05	0.16	0.05	0.05	0.04	0.04	0.07	0.05	0.03	0.08	0.03	0.04	0.00	0.03	0.80
MgO	6.41	1.46	5.42	8.45	7.41	2.48	9.47	8.38	8.75	8.88	8.73	8.42	9.75	10.17	8.82	0.25
CaO	0.00	0.02	0.02	0.00	0.00	0.00	0.01	0.00	0.00	0.00	0.00	0.00	0.01	0.06	0.01	0.00
MnO	0.27	1.13	0.38	0.30	0.52	0.16	0.26	0.33	0.32	0.38	0.26	0.30	0.32	0.19	0.35	0.02
CoO	0.06	0.08	0.13	0.04	0.02	0.21	0.04	0.06	0.10	0.09	0.10	0.06	0.10	0.09	0.02	0.00
ZnO	0.24	0.19	0.30	0.36	0.45	0.02	0.12	0.35	0.35	0.32	0.29	0.35	0.17	0.27	0.30	0.00
Na_2O	0.02	0.03	0.00	0.00	0.03	0.04	0.00	0.00	0.00	0.00	0.00	0.00	0.03	0.00	0.00	0.02
Total	99.76	99.17	100.02	100.30	100.71	102.00	100.76	100.76	100.53	100.63	100.48	100.73	100.88	100.37	100.45	100.30
Mg#	31.33	8.27	26.95	42.28	37.51	13.90	46.66	41.87	43.73	44.21	43.38	41.19	47.70	49.94	43.17	1.42
Cr#	57.00	93.43	59.07	76.89	76.14	97.44	76.57	77.08	77.60	76.58	75.60	67.61	73.01	74.94	67.70	89.73

Table B.1: *continued*

Representative olivine analyses

Sample	HLH-077A				HLH-104C		HLH-042A					HLH-051E			
Spot	#01	#02	#15	#19	#01	#11	#03	#06	#08	#18	#20	#02	#03	#05	#09
SiO_2	41.35	40.72	41.05	41.19	40.69	40.37	39.74	39.43	39.91	39.62	39.52	40.63	41.49	40.27	34.68
TiO_2	0.00	0.01	0.00	0.00	0.02	0.00	0.02	0.00	0.01	0.00	0.01	0.00	0.00	0.00	0.00
Al_2O_3	0.01	0.00	0.01	0.00	0.00	0.02	0.01	0.00	0.01	0.01	0.00	0.00	0.00	0.00	0.00
Cr_2O_3	0.00	0.08	0.01	0.00	0.02	0.00	0.00	0.01	0.02	0.00	0.00	0.11	0.04	0.04	0.02
MgO	46.43	44.67	46.36	46.74	46.41	46.08	38.34	38.33	39.81	38.90	38.10	45.85	49.32	46.95	46.22
CaO	0.02	0.03	0.01	0.01	0.00	0.00	0.05	0.04	0.02	0.01	0.03	0.00	0.00	0.00	0.00
MnO	0.26	0.27	0.23	0.25	0.21	0.29	0.41	0.38	0.40	0.42	0.42	0.08	0.04	0.04	0.11
FeO	12.45	13.70	12.01	12.28	13.30	13.77	21.93	21.31	20.66	20.76	21.82	13.66	9.68	12.58	13.37
NiO	0.28	0.25	0.36	0.30	0.31	0.31	0.23	0.23	0.21	0.17	0.18	0.40	0.55	0.57	0.49
CoO	0.00	0.01	0.00	0.00	na	na	0.00	0.00	0.00	0.00	0.00	na	na	na	na
Na_2O	na	na	na	na	0.00	0.00	na	na	na	na	na	0.00	0.00	0.00	0.00
Total	100.80	99.74	100.04	100.77	100.96	100.85	100.72	99.72	101.04	99.90	100.06	100.73	101.11	100.45	94.89
Mg#	86.93	85.32	87.32	87.16	86.15	85.64	75.70	76.22	77.45	76.96	75.69	85.68	90.08	87.27	94.89

Table B.2: Representative sample of olivine mineral chemistry analyses. Mg# $=100 \times \text{Mg} / (\text{Mg} + \text{Fe}^{+2})$ (mol% values).

Representative clinopyroxene analyses

Sample	HLH-067C (Cpx)						HLH-077A (Cpx)					HLH-104C (Cpx)		
Spot	#03	#04	#08	#09	#14	#18	#01	#02	#05	#09	#11	#07	#08	#10
SiO_2	52.45	53.00	54.47	53.22	52.57	52.82	52.70	52.80	53.75	52.78	54.60	54.20	53.61	53.32
TiO_2	0.20	0.18	0.13	0.19	0.24	0.21	0.49	0.24	0.18	0.20	0.13	0.00	0.05	0.05
Al_2O_3	2.38	2.60	0.84	2.71	3.22	2.26	2.82	2.99	4.40	3.60	2.51	0.69	0.94	1.29
Cr_2O_3	0.93	1.15	0.18	1.17	0.84	0.87	1.20	1.18	0.62	1.22	0.83	0.00	0.06	0.26
$Fe_2O_3{}^{calc}$	0.32	1.81	0.62	0.06	1.06	2.23	1.71	1.05	-2.82	0.99	-0.70	2.64	2.66	2.71
FeO^{total}	3.06	3.05	2.82	3.10	4.52	3.90	3.67	3.69	3.80	3.23	4.07	2.78	3.10	3.02
MgO	16.28	19.47	17.22	16.67	18.86	19.13	17.38	17.00	20.77	17.05	21.58	18.34	17.94	17.80
CaO	23.42	20.62	24.62	23.36	19.31	20.61	22.09	22.04	13.06	22.24	16.50	24.63	24.31	24.25
FeO^{calc}	2.77	1.43	2.26	3.05	3.57	1.90	2.13	2.74	6.34	2.34	4.70	0.40	0.70	0.59
NiO	0.06	0.00	0.03	0.04	0.04	0.09	0.03	0.01	0.08	0.04	0.08	0.02	0.05	0.05
MnO	0.10	0.12	0.18	0.15	0.16	0.15	0.15	0.17	0.08	0.14	0.12	0.09	0.13	0.13
Na_2O	0.21	0.19	0.13	0.21	0.21	0.17	0.41	0.41	0.92	0.41	0.21	0.02	0.04	0.06
V_2O_3	0.04	0.02	0.01	0.03	0.06	0.05	0.05	0.06	-0.03	0.05	0.05	na	na	na
Total	99.16	100.58	100.68	100.84	100.12	100.49	101.16	100.70	97.35	101.06	100.61	101.02	100.49	100.49
Mg#	91.28	96.05	93.14	90.70	90.40	94.73	93.58	91.70	85.37	92.85	89.11	98.78	97.86	98.19
Cr#	20.68	22.91	12.65	22.49	14.84	20.51	22.17	20.99	8.68	18.49	18.13	0.00	3.92	11.72
En	46.97	55.49	47.59	47.40	54.28	54.64	50.45	49.44	61.60	49.64	59.82	50.56	50.11	50.06
Fs	4.49	2.28	3.50	4.86	5.77	3.04	3.46	4.48	10.56	3.82	7.31	0.63	1.10	0.92
Wo	48.55	42.23	48.91	47.74	39.95	42.32	46.09	46.08	27.84	46.53	32.87	48.81	48.79	49.02

Table B.3: Representative sample of clinopyroxene and orthopyroxene mineral chemistry analyses. 'Total' includes values from $Fe_2O_3{}^{calc}$ and FeO^{calc}. Fe^{2+} and Fe^{3+} amounts calculated from spinel stoichiometric ratios. Mg# =100 × Mg / (Mg + Fe^{+2}) (mol% values). Cr# = 100 × Cr / (Cr + Al) (mol% values). En: enstatite. Fs: ferrosilite. Wo:wollastonite.

Representative orthopyroxene analyses

Sample		HLH-077A (Opx)			HLH-104C (Opx)			
Spot	#12	#14	#15	#19	#02	#07	#08	#10
SiO_2	55.61	56.11	57.66	56.58	56.64	56.31	55.06	55.68
TiO_2	0.16	0.23	0.08	0.11	0.01	0.03	0.00	0.09
Al_2O_3	1.79	1.92	0.65	1.29	0.92	0.79	0.79	1.09
Cr_2O_3	1.00	0.63	0.06	0.13	0.15	0.01	0.06	0.19
$Fe_2O_3{}^{calc}$	0.81	0.87	0.51	1.02	1.93	2.77	4.57	2.65
FeO^{total}	7.86	8.13	7.97	8.17	8.79	9.01	8.79	8.65
MgO	32.00	32.19	33.74	33.36	33.53	33.59	33.78	33.23
CaO	1.59	1.72	0.81	0.59	0.53	0.51	0.47	0.68
FeO^{calc}	7.13	7.35	7.51	7.25	7.06	6.51	4.68	6.26
NiO	0.07	0.07	0.11	0.09	0.07	0.03	0.04	0.09
MnO	0.25	0.25	0.27	0.23	0.22	0.30	0.27	0.22
Na_2O	0.04	0.02	0.01	0.01	0.00	0.00	0.02	0.02
V_2O_3	0.03	-0.04	-0.04	0.03	na	na	na	na
Total	100.47	101.32	101.38	100.68	101.05	100.85	99.74	100.20
Mg#	88.89	88.65	88.90	89.13	89.44	90.19	92.78	90.44
Cr#	27.12	18.14	5.73	6.22	9.59	1.09	4.82	10.35
En	86.15	85.74	87.56	88.14	88.53	89.31	91.92	89.26
Fs	10.77	10.98	10.93	10.75	10.45	9.71	7.15	9.43
Wo	3.08	3.29	1.51	1.11	1.01	0.97	0.93	1.30

Table B.3: *continued*

B.1.2 Whole rock analyses

B.2 Igneous geochronology data tables

Sample Type	HLH·W05 Pyrocl.	HLH·081A Dacite	HLH·030A Andesite	HLH·036C Andesite	HLH·078B Andesite	HLH·061A Porph. And.	HLH·030A Bas. And.	HLH·046D Bas. And.	HLH·082C Bas. And.	HLH·116A Bas. And.	HLH·152A Bas. And.	HLH·51A Bas. And.	HLH·078A Bas. And.	HLH·101B Boninite
SiO_2	72.6	64.23	58.03	58.16	54.95	56.13	54.2	50.67	51.78	51.27	52.82	50.96	51.58	54.4
MgO	2.44	0.98	3.97	4.45	4.6	5.07	5.06	11.06	3.86	2.75	3.19	7.07	8.77	9.16
${Fe_2O_3}^T$	4	4.76	8.41	6.52	11.08	8.01	12.94	9.81	10.68	13.88	16.33	10.46	9.12	9.43
TiO_2	0.54	0.685	1.449	1.06	0.786	1	1.57	0.401	2.29	2.92	2.149	1.046	0.592	0.437
Al_2O_3	10.14	15.62	12.93	15.8	13.58	15.82	13.65	11.87	14	12.27	17.59	14.05	13.67	13.65
CaO	1.82	4.29	5.19	3.87	7.49	7.31	4.73	10.12	5.16	5.59	1.07	8.49	8.71	5.36
K_2O	2.22	1.94	0.29	3.69	0.27	1.39	0.19	1.41	1.15	1.82	4.8	0.26	0.29	0.33
Na_2O	3.1	3.94	5.4	5.07	3.43	3	3.72	1.85	4.43	3.58	0.91	1.91	3.32	4.49
MnO	0.06	0.046	0.109	0.08	0.147	0.12	0.15	0.161	0.167	0.19	0.059	0.125	0.153	0.162
P_2O_5	0.14	0.19	0.16	0.52	0.08	0.21	0.19	0.03	0.47	1.68	0.22	0.09	0.06	0.03
LOI	2.3	4.29	4.07	1.49	4.31	2.75	4.32	1.94	5.39	4.21	1.53	5.93	3.3	3.07
Total	99.37	101	100	100.71	100.7	100.81	100.7	99.33	99.38	100.16	100.7	100.4	99.58	100.5
Mg#	59	32.7	47.9	61.6	49.4	59.9	52.6	72.6	46	31.8	31.5	61.4	69.4	69.6
Cr	81	50	<20	64	30	131	25	510	50	13	150	120	270	170
Ni	24.3	20	<20	51.9	<20	56.9	12.8	130	<20	7.3	90	60	110	90
V	58.7	56	>370	155.3	403	144.8	370	266	280	94.1	179	255	256	242
La	37.81	21.3	3.47	45.81	3.95	28.39	5.2	1.35	31.8	94.41	23.7	8.34	2.34	0.8
Ce	78.57	40.1	9.79	99.44	9.92	59.64	14.11	3.92	69	217.48	51.6	18.9	6.13	2.45
Pr	8.828	4.55	1.61	12.571	1.54	7.084	2.234	0.65	8.92	27.099	6.59	2.5	0.92	0.42
Nd	32.42	17.7	8.91	51.57	7.67	27.71	11.37	3.29	37.8	109.57	27.8	10.8	4.59	2.28
Sm	6.263	3.41	2.83	10.188	2.32	6.009	3.744	1.23	8.04	21.981	6.78	3.08	1.4	0.93
Eu	1.082	0.929	1.11	2.721	0.918	1.467	1.215	0.441	2.23	4.942	1.98	0.84	0.437	0.361
Gd	5.255	3.04	3.86	7.853	2.77	5.77	4.803	1.54	7.7	20.147	6.84	3.75	1.85	1.44
Tb	0.796	0.46	0.7	0.958	0.47	0.9	0.839	0.28	1.24	2.984	1.12	0.67	0.34	0.27
Dy	4.725	2.68	4.62	4.873	3.08	5.655	5.859	2	6.73	17.607	6.24	4.28	2.25	1.89
Ho	0.934	0.57	1.02	0.835	0.71	1.145	1.278	0.44	1.39	3.483	1.23	0.86	0.51	0.44
Er	2.699	1.62	3	2.152	2.09	3.254	3.691	1.25	3.89	9.886	3.46	2.5	1.48	1.35
Tm	0.396	0.255	0.454	0.29	0.313	0.47	0.545	0.197	0.583	1.406	0.507	0.405	0.237	0.202
Yb	2.63	1.59	2.98	1.728	2.07	2.945	3.501	1.32	3.59	8.872	3.15	2.76	1.53	1.4
Lu	0.396	0.276	0.488	0.251	0.319	0.445	0.52	0.203	0.565	1.339	0.459	0.421	0.256	0.226
Y	25.29	15.8	27.6	22.75	19.4	29.96	32.11	11.7	38.6	91.76	30.4	25.6	13.8	12.2
Zr	241	168	57	195	39	192	76	19	218	1012	192	70	27	16
Hf	6.27	4.1	1.8	4.83	1.2	4.75	2.22	0.7	5.4	19.54	5.3	2.3	0.8	0.6
Nb	11.445	9.2	2.4	7.367	0.3	9.37	2.987	<0.2	9.5	49.709	16.1	8.2	1.6	<0.2
Ta	0.911	0.7	0.14	0.396	0.03	0.565	0.186	<0.01	0.58	2.641	1.06	0.71	0.12	0.03
Cs	4.381	4.9	0.7	1.38	<0.1	3.789	1.209	2.6	1.7	0.213	4.9	0.4	0.4	0.2
Rb	69.78	71	5	108.53	2	47.67	3.32	55	28	29.54	120	6	4	4
Ba	459.9	472	184	794.8	65	656.7	162.5	963	1068	886.4	1145	647	120	281
Th	20.589	5.14	0.35	12.885	0.21	6.329	0.476	0.1	5.84	7.802	6.05	6.15	0.07	<0.05
U	3.219	1.3	0.26	2.756	0.12	1.349	0.256	0.06	1.48	2.352	1.04	2.18	0.06	0.22
Sr	104.5	490	136	465.2	323	326.3	154.3	211	522	309.3	138	211	121	147

Table B.4: Ophiolite whole-rock geochemistry data tables. Mg# $=100 \times \mathrm{Mg} / (\mathrm{Mg} + \mathrm{Fe}^{+2})$ (mol% values). LOI = loss on ignition.

Sample	HLH·061C	HLH·051B	HLH·51C	HLH·51D	HLH·121D	HLH·052E	HLH·056C	HLH·081C	HLH·104A	HLH·099A	HLH·121E	HLH·122A	HLH·146	HLH·146A	HLH·053
Type	Basalt	Basalt	Basalt	Basalt	Bas. Picrite	Diabase	Diabase	Diabase	Diabase	Diabase	Diabase	Diabase	Diabase	Diabase	Diabase
SiO_2	48.23	40.53	47.67	44.97	48.29	50.28	52.82	50.08	46.04	48.7	51.45	50.77	52.67	51.19	51.13
MgO	6.17	4.9	5.26	6.68	13.2	3.83	7.52	4.43	6.78	6.9	6.08	7.25	7.66	8.08	5.74
$Fe_2O_3{}^T$	13.9	13.19	14.66	9.96	9.51	11.83	8.63	8.83	7.67	11.8	8.94	8.84	9.47	10.02	10.97
TiO_2	1.62	1.108	1.2	0.875	0.51	2.25	1.039	1.72	0.497	1.063	1.2	1.18	0.663	0.68	1.08
Al_2O_3	13.54	10.09	13.47	13.69	13.71	15.42	15.02	15.59	14.12	14.71	16.68	15.71	15.01	15.17	14.98
CaO	11.45	13.71	8.09	13.11	10.31	7.35	10.31	6.78	19.84	6.36	8.57	8.92	7.01	8.71	6.54
K_2O	0.4	0.05	0.16	0.06	0.28	0.74	0.75	1.44	1.16	0.44	0.73	1.04	0.16	0.46	0.61
Na_2O	2.88	3.25	3.3	1.53	1.3	5.32	2.28	4.61	0.53	3.72	3.1	2.9	4.92	3.87	3.86
MnO	0.19	0.193	0.149	0.169	0.16	0.15	0.142	0.117	0.201	0.184	0.15	0.14	0.163	0.18	0.1
P_2O_5	0.14	0.11	0.11	0.05	0.05	0.4	0.21	0.57	0.05	0.12	0.2	0.24	0.08	0.08	0.15
LOI	2.3	12.93	5.61	9.18	3.54	2.66	2.19	5	1.73	3.96	3.46	2.85	2.55	2.04	4.53
Total	100.81	100.1	99.68	100.3	100.86	100.22	100.9	99.17	98.62	97.96	100.56	99.83	100.4	100.47	99.68
Mg#	51.1	46.7	45.8	61.2	76.6	43.3	67.2	54.2	67.6	57.9	61.6	65.9	65.6	65.5	55.2
Cr	186	60	40	320	1110	5	170	240	140	30	151	191	40	57	30
Ni	100.1	40	40	100	363.4	3.8	<20	90	40	30	50.3	64.7	30	42	<20
V	347.5	250	328	250	237	193.4	221	210	201	315	157.2	185.1	272	284.8	352
La	7.25	4.51	9.81	4.09	1.83	32.14	22.8	47.3	2.09	2.85	13.43	20.03	3.8	2.61	4.69
Ce	18.8	11.2	20.9	9.63	4.95	71.13	48.2	102	5.64	7.93	30.23	48.53	9.51	7.07	11.7
Pr	2.778	1.61	2.67	1.38	0.776	8.9	5.99	13.3	0.89	1.31	3.978	6.592	1.37	1.1	1.76
Nd	13.42	7.87	11.6	6.51	3.91	37.32	24.8	53.3	4.51	7.02	17.3	27.79	6.66	5.72	8.54
Sm	4.039	2.1	3.21	1.92	1.308	8.426	5.41	9.8	1.35	2.36	4.142	6.006	1.87	1.889	2.58
Eu	1.442	0.754	0.954	0.764	0.453	2.251	1.39	2.95	0.644	0.846	1.396	1.661	0.653	0.711	0.955
Gd	4.902	2.52	3.83	2.37	1.705	8.376	4.91	7.97	1.75	3.18	4.458	5.443	2.33	2.546	3.26
Tb	0.786	0.46	0.7	0.41	0.309	1.308	0.75	1.07	0.31	0.59	0.708	0.794	0.43	0.459	0.58
Dy	5.099	2.78	4.37	2.57	2.178	8.061	4.4	5.79	2.08	3.88	4.531	4.778	2.76	3.153	3.92
Ho	1.011	0.57	0.97	0.52	0.469	1.638	0.89	1.1	0.49	0.84	0.918	0.958	0.62	0.68	0.83
Er	2.826	1.79	3.08	1.53	1.417	4.613	2.44	2.97	1.4	2.56	2.631	2.619	1.87	2.031	2.49
Tm	0.386	0.285	0.473	0.233	0.209	0.663	0.377	0.425	0.228	0.398	0.379	0.375	0.284	0.311	0.384
Yb	2.435	1.89	3.21	1.49	1.382	4.18	2.45	2.49	1.47	2.61	2.41	2.344	1.82	1.994	2.64
Lu	0.353	0.316	0.521	0.241	0.209	0.621	0.382	0.41	0.243	0.449	0.369	0.344	0.312	0.304	0.414
Y	26.05	17.1	27.7	14.9	12.23	42.86	24.7	28.8	13.8	24.2	24.08	24.64	16.9	18.23	23.2
Zr	103	49	79	42	26	269	123	187	22	41	120	134	34	34	50
Hf	2.71	1.3	2.3	1.3	0.73	6.69	3.2	4.6	0.7	1.3	3.04	3.37	1.1	1.03	1.5
Nb	6.442	4.4	6	3	1.185	14.629	6.5	7.5	0.2	1.2	5.757	6.478	0.8	1.379	2
Ta	0.41	0.29	0.38	0.26	0.075	0.884	0.38	0.43	0.04	0.08	0.353	0.365	0.07	0.091	0.14
Cs	1.25	<0.1	0.3	0.3	0.239	2.144	0.6	3.9	3.4	2.3	0.692	0.578	<0.1	0.145	1.1
Rb	10.49	<1	2	1	3.54	25.2	14	56	34	11	10.96	21.35	<1	4.27	9
Ba	198.5	17	150	29	15.9	1081.6	365	680	135	226	271.8	366.1	59	115.6	62
Th	0.923	0.38	2.22	0.33	0.168	6.757	4.87	6.6	<0.05	0.07	2.046	2.983	0.16	0.26	0.33
U	0.267	0.23	0.67	0.13	0.076	1.811	1.06	1.64	0.43	0.09	0.54	0.685	0.18	0.316	0.22
Sr	534.9	268	149	226	122.1	513.5	325	849	155	221	324.3	526	115	159.2	193

Table B.4: *continued*

Sample	HLH·066D	HLH·016	HLH·042B	HLH·044B	HLH·051G	HLH·052A	HLH·053	HLH·074D	HLH·085A	HLH·088	HLH·104D	HLH·108B	HLH·124B	HLH·051A	HLH·076C
Type	Diab. Picrite	Gabbro	Gabbro	Gabbro	Gabbro	Gabbro	Gabbro	Gabbro	Gabbro	Gabbro	Gabbro	Gabbro	Gabbro	Pyroxenite	Pyroxenite
SiO_2	45.91	39.88	47.88	45.15	44.02	41.24	47.15	47	45.87	44.77	48.08	47.06	47.76	51	44.82
MgO	18.49	7.46	4.89	12.8	9.67	6.08	8.83	8.7	11.13	11.88	13.43	12.57	8.68	11.63	10.38
$Fe_2O_3{}^T$	8.67	16.16	16.8	8.93	2.7	2.63	5.54	9.47	9.79	7.17	4.9	10.51	5.83	9.17	6.3
TiO_2	0.367	6.575	2.646	0.457	0.036	0.107	0.183	0.426	0.527	0.157	0.14	0.5	0.184	0.402	0.278
Al_2O_3	9.82	13.61	14.05	13.14	22.48	21.49	17.03	12.76	13.44	14	15.1	11.04	17.59	11.93	15.1
CaO	9.53	9.96	8.92	14.56	14.99	23.73	13.89	18.15	16.08	7.89	14.41	15.53	15.25	9.65	21.11
K_2O	0.04	0.68	0.99	0.08	0.22	0.04	0.91	0.03	0.13	1.8	0.95	0.08	0.17	0.72	0.02
Na_2O	0.87	1.8	2.77	0.54	1.8	0.09	1.82	0.29	0.61	1.34	0.85	0.78	1.26	3.09	0.38
MnO	0.152	0.269	0.269	0.127	0.045	0.043	0.11	0.162	0.169	0.147	0.1	0.18	0.115	0.166	0.119
P_2O_5	0.04	0.01	0.56	0.04	<0.01	0.01	<0.01	0.04	0.05	<0.01	0.01	0.03	<0.01	0.03	0.02
LOI	4.45	2.17	1.19	3.82	4.07	5.5	3.28	3.29	2.95	9.53	3.07	2.15	2.92	3.05	2.36
Total	98.34	98.57	101	99.66	100	101	98.73	100.3	100.8	98.7	101.03	100.42	99.76	100.8	100.9
Mg#	83.4	52.1	40.7	77.1	89.4	84.5	79	68.4	72.8	79.6	86.6	73.8	77.8	74.9	79.5
Cr	1770	20	40	640	1640	610	260	160	680	520	287	1135	670	710	350
Ni	560	50	<20	240	230	150	150	100	140	160	227.1	139.1	160	170	160
V	181	710	322	237	48	60	158	217	243	142	107.9	293.6	138	224	179
La	1.4	0.71	20.3	2	0.12	0.15	0.22	1.96	1.76	0.24	0.48	1.3	0.45	2.23	1.03
Ce	3.46	2.05	42	5.58	0.39	0.52	0.74	4.49	5.71	0.81	1.31	4.72	1.29	6.46	2.47
Pr	0.53	0.37	5.12	0.83	0.06	0.11	0.13	0.63	0.99	0.15	0.221	0.824	0.21	0.92	0.4
Nd	2.75	2.32	21.7	4.31	0.26	0.68	0.8	2.99	4.79	0.95	1.02	4.21	1.35	4.39	2.23
Sm	0.91	0.9	4.93	1.48	0.09	0.26	0.38	1	1.59	0.31	0.349	1.458	0.51	1.33	0.75
Eu	0.326	0.63	1.81	0.493	0.083	0.185	0.25	0.287	0.593	0.138	0.165	0.546	0.301	0.459	0.404
Gd	1.24	1.45	5.21	1.94	0.14	0.37	0.63	1.31	2.12	0.52	0.502	1.954	0.74	1.66	1
Tb	0.22	0.27	0.83	0.32	0.03	0.06	0.11	0.23	0.36	0.11	0.085	0.35	0.13	0.28	0.18
Dy	1.46	1.85	4.76	2.15	0.21	0.42	0.82	1.59	2.53	0.76	0.598	2.428	1	1.96	1.19
Ho	0.34	0.41	0.96	0.47	0.04	0.09	0.19	0.36	0.54	0.17	0.131	0.522	0.22	0.42	0.26
Er	0.98	1.18	2.63	1.37	0.12	0.28	0.57	1.12	1.61	0.5	0.372	1.588	0.64	1.24	0.79
Tm	0.156	0.172	0.373	0.224	0.019	0.047	0.091	0.178	0.231	0.078	0.054	0.235	0.1	0.181	0.126
Yb	1.04	1.17	2.46	1.49	0.12	0.32	0.55	1.18	1.55	0.54	0.348	1.497	0.61	1.24	0.74
Lu	0.158	0.196	0.387	0.243	0.023	0.05	0.096	0.197	0.257	0.091	0.052	0.228	0.098	0.223	0.125
Y	9.3	10.5	26.2	13.3	1.2	2.7	5.1	10.1	15.4	4.6	3.34	13.72	5.9	12	7.3
Zr	15	18	114	27	1	7	3	18	22	4	<6	17	4	24	7
Hf	0.5	0.7	3.2	0.9	<0.1	0.2	0.1	0.6	0.8	0.1	<0.14	0.64	0.2	0.8	0.2
Nb	0.6	4.9	8.9	<0.2	<0.2	<0.2	<0.2	1.2	<0.2	<0.2	0.211	0.176	<0.2	<0.2	<0.2
Ta	0.06	0.35	0.64	0.02	<0.01	<0.01	<0.01	0.1	<0.01	<0.01	<0.023	<0.023	<0.01	0.02	0.03
Cs	<0.1	0.8	0.6	<0.1	0.7	<0.1	0.6	0.2	0.2	4.3	2.318	0.054	0.6	0.6	<0.1
Rb	<1	9	30	<1	1	<1	14	<1	<1	59	33.05	0.75	2	9	<1
Ba	5	54	282	8	26	7	329	5	274	382	273.6	13.8	17	164	13
Th	<0.05	<0.05	2.72	0.18	<0.05	<0.05	<0.05	<0.05	<0.05	<0.05	0.041	0.055	<0.05	<0.05	<0.05
U	0.04	0.11	0.69	0.08	0.02	<0.01	0.12	0.06	0.02	<0.01	0.019	0.017	0.05	0.03	0.02
Sr	67	284	331	376	236	79	1126	39	182	129	398.1	94.3	288	155	2693

Table B.4: *continued*

Sample	HLH·042A	HLH·042A	HLH·046B	HLH·046F	HLH·047C	HLH·067C	HLH·071E	HLH·075A	HLH·076F	HLH·077A	HLH·079C	HLH·104C	HLH·021	HLH·113B	HLH·066B
Type	Peridotite	Peridotite	Peridotite	Peridotite	Peridotite	Peridotite	Peridotite	Peridotite	Peridotite	Peridotite	Peridotite	Peridotite	Peridotite	Peridotite	Dunite
SiO_2	47.39	46.64	35.29	40.06	44.35	42.27	31.43	39.98	48.2	42.23	38.51	41.55	40.12	46.19	40.59
MgO	20.76	20.49	40.11	40.41	26.87	31.28	40.86	25.76	21.42	31.06	37.56	30.13	40	21.69	32.25
$Fe_2O_3{}^T$	9.3	9.22	6.85	6.41	9.45	8.92	6.1	7.93	7.72	9.16	10.87	9.88	6.46	10.11	7.63
TiO_2	0.2	0.198	0.009	0.003	0.089	0.091	0.002	0.12	0.256	0.16	0.012	0.074	0.002	0.16	0.089
Al_2O_3	8.34	8.3	0.22	0.21	8.73	2.08	0.17	3.91	3.06	4.71	0.64	5.36	0.53	9.39	5.8
CaO	10.88	10.51	0.1	0.07	9	7.16	0.14	10.65	16.9	6.7	0.17	5.83	0.1	9.06	3.94
K_2O	0.08	0.08	<0.01	<0.01	0.03	<0.01	<0.01	0.01	0.01	0.02	0.01	0.03	<0.01	0.1	0.01
Na_2O	0.88	1.06	0.02	0.01	0.31	0.06	0.04	0.15	0.19	0.16	0.04	0.1	0.01	0.68	0.12
MnO	0.14	0.137	0.077	0.069	0.152	0.132	0.104	0.134	0.161	0.14	0.06	0.146	0.085	0.15	0.111
P_2O_5	0.01	0.01	<0.01	<0.01	<0.01	<0.01	<0.01	0.01	0.01	0.01	<0.01	<0.01	<0.01	0.01	<0.01
LOI	2.29	2.45	16.67	13.25	1.95	8.66	21.92	11.71	2.65	5.83	12.04	6.57	13.02	2.4	9.83
Total	100.27	99.11	99.35	100.5	100.9	100.7	100.8	100.4	100.6	100.18	99.92	99.68	100.3	99.95	100.4
Mg#	84	84	93.2	93.7	87	89.2	94	88.4	86.7	88.9	89.1	87.8	93.6	83.5	90.9
Cr	2987	2860	2080	2170	1630	3020	1730	2510	3100	3864	5550	2770	2500	2072	3930
Ni	696.4	650	2180	2210	840	1300	2120	1060	740	1459.9	1960	1340	2050	685.8	710
V	160.7	146	14	16	79	100	15	110	213	119.2	36	71	29	133.5	77
La	0.54	0.58	<0.05	<0.05	0.28	<0.05	<0.05	0.42	0.49	0.47	0.08	0.3	<0.05	0.61	0.07
Ce	1.47	1.46	<0.05	<0.05	0.64	0.26	<0.05	1.04	1.56	1.19	0.21	0.81	<0.05	1.55	0.3
Pr	0.254	0.25	<0.01	<0.01	0.09	0.07	<0.01	0.14	0.27	0.191	0.03	0.12	<0.01	0.246	0.06
Nd	1.36	1.33	<0.05	<0.05	0.52	0.43	<0.05	0.75	1.66	0.99	0.1	0.61	<0.05	1.17	0.31
Sm	0.577	0.47	<0.01	<0.01	0.19	0.18	<0.01	0.27	0.69	0.37	0.02	0.19	<0.01	0.43	0.16
Eu	0.256	0.247	<0.005	<0.005	0.112	0.051	<0.005	0.113	0.243	0.173	0.035	0.092	<0.005	0.175	0.074
Gd	0.848	0.74	0.02	<0.01	0.32	0.36	<0.01	0.38	0.99	0.576	0.02	0.28	0.01	0.612	0.24
Tb	0.159	0.14	<0.01	<0.01	0.06	0.06	<0.01	0.07	0.17	0.111	<0.01	0.05	<0.01	0.109	0.05
Dy	1.085	0.96	0.01	<0.01	0.45	0.38	<0.01	0.54	1.21	0.755	0.03	0.33	<0.01	0.789	0.38
Ho	0.249	0.21	<0.01	<0.01	0.1	0.08	<0.01	0.12	0.27	0.178	<0.01	0.07	<0.01	0.171	0.09
Er	0.705	0.67	0.01	<0.01	0.26	0.25	<0.01	0.35	0.82	0.522	0.03	0.23	<0.01	0.512	0.26
Tm	0.104	0.085	<0.005	<0.005	0.035	0.041	<0.005	0.05	0.124	0.078	<0.005	0.034	<0.005	0.072	0.044
Yb	0.664	0.63	0.01	<0.01	0.27	0.28	<0.01	0.36	0.68	0.511	0.03	0.22	0.01	0.496	0.3
Lu	0.099	0.098	<0.002	<0.002	0.052	0.047	<0.002	0.056	0.119	0.078	0.007	0.04	<0.002	0.074	0.049
Y	6.04	5.9	<0.5	<0.5	2.6	2.4	<0.5	3.2	7.1	4.35	<0.5	2.1	<0.5	4.44	2.5
Zr	7	6	<1	<1	4	1	<1	3	5	7	1	3	<1	9	3
Hf	0.25	0.2	<0.1	<0.1	0.1	<0.1	<0.1	<0.1	0.2	0.21	<0.1	<0.1	<0.1	0.25	0.1
Nb	0.094	<0.2	<0.2	<0.2	<0.2	<0.2	<0.2	<0.2	<0.2	0.225	<0.2	<0.2	<0.2	0.107	<0.2
Ta	<0.023	<0.01	0.03	<0.01	<0.01	<0.01	<0.01	<0.01	<0.01	<0.023	<0.01	<0.01	<0.01	<0.023	<0.01
Cs	0.191	0.2	<0.1	<0.1	0.4	0.1	9.5	0.4	<0.1	0.017	<0.1	0.1	<0.1	0.442	0.3
Rb	0.54	<1	<1	<1	<1	<1	<1	<1	<1	<0.23	<1	<1	<1	1.1	<1
Ba	5.6	8	3	4	5	<3	10	4	4	1.9	7	6	<3	7.9	3
Th	0.023	<0.05	<0.05	<0.05	<0.05	<0.05	<0.05	<0.05	<0.05	0.03	<0.05	<0.05	<0.05	0.076	<0.05
U	0.015	0.01	<0.01	<0.01	<0.01	0.01	<0.01	<0.01	0.04	0.017	0.05	0.03	0.12	0.031	<0.01
Sr	13.9	15	5	6	45	8	3	95	24	9.9	25	10	4	34.5	8

Table B.4: *continued*

Spot Name	U (ppm)	Th (ppm)	Th/U	comm 206 (%)	^{207}Pb/^{206}Pb	±1σ (%)	^{207}Pb/^{235}U	±1σ (%)	^{206}Pb/^{238}U	±1σ (%)	^{207}Pb/^{206}Pb Age (Ma)	±1σ	^{206}Pb/^{238}Pb Age (Ma)	±1σ
Gabbro														
HLH-124-1.1	283	217	0.79	-0.15	0.05775	2.111	0.67411	3.004	0.08465	2.138	520.5	46.3	523.8	10.7
HLH-124-2.1	103	29	0.29	0.35	0.05471	18.841	0.62845	19.003	0.08331	2.482	400.5	422.1	515.8	12.3
HLH-124-4.2	53	20	0.39	0.71	0.06043	8.370	0.69964	8.680	0.08397	2.301	619.1	180.6	519.8	11.5
HLH-124-10.1	160	78	0.50	0.38	0.05561	5.194	0.63665	5.703	0.08304	2.357	436.6	115.6	514.2	11.6
HLH-124-15.1	40	14	0.35	1.92	0.07179	13.739	0.84416	13.974	0.08528	2.554	980.1	279.9	527.6	12.9
HLH-124-14.1	101	52	0.53	0.96	0.05336	8.708	0.61465	8.990	0.08354	2.235	344.2	197.0	517.2	11.1
HLH-124-17.1	440	345	0.81	0.37	0.05532	2.636	0.64850	3.377	0.08502	2.111	425.2	58.8	526.0	10.6
HLH-124-18.1	87	36	0.42	-0.54	0.06717	7.872	0.77823	8.192	0.08403	2.267	843.0	163.8	520.1	11.3
HLH-124-20.1	48	18	0.40	1.53	0.05583	9.801	0.64286	10.092	0.08351	2.406	445.6	217.9	517.1	11.9
Tonalite														
HLH-094-1.1	406	253	0.64	0.09	0.05430	1.271	0.50989	2.216	0.06811	1.815	383.4	28.6	424.8	7.5
HLH-094-27.1	418	307	0.76	0.13	0.05493	1.475	0.51141	2.319	0.06752	1.790	409.4	33.0	421.2	7.3
HLH-094-5.1	862	551	0.66	0.00	0.05438	1.260	0.50538	2.185	0.06740	1.785	386.8	28.3	420.5	7.3
HLH-094-14.1	625	466	0.77	0.22	0.05354	1.338	0.49687	2.230	0.06730	1.783	351.9	30.2	419.9	7.3
HLH-094-29.1	1243	1116	0.93	-0.04	0.05511	0.830	0.51135	1.969	0.06730	1.786	416.6	18.5	419.9	7.3
HLH-094-9.1	690	527	0.79	-0.04	0.05484	1.091	0.50882	2.126	0.06730	1.825	405.6	24.4	419.8	7.4
HLH-094-24.1	789	623	0.82	0.13	0.05423	2.916	0.50302	3.424	0.06727	1.794	380.8	65.6	419.7	7.3
HLH-094-20.1	754	495	0.68	0.16	0.05430	1.327	0.50311	2.281	0.06720	1.855	383.5	29.8	419.3	7.5
HLH-094-13.1	485	365	0.78	0.19	0.05355	1.290	0.49372	2.208	0.06686	1.792	352.4	29.1	417.2	7.3
HLH-094-16.1	922	720	0.81	0.21	0.05375	1.372	0.49456	2.304	0.06673	1.851	360.7	31.0	416.4	7.5
HLH-094-2.1	555	459	0.85	0.27	0.05302	4.117	0.48769	4.495	0.06671	1.805	329.8	93.4	416.3	7.3
HLH-094-4.1	504	287	0.59	0.00	0.05608	1.125	0.51544	2.117	0.06665	1.793	455.7	25.0	416.0	7.2
HLH-094-18.1	752	617	0.85	0.08	0.05417	1.376	0.49646	2.254	0.06647	1.786	378.2	31.0	414.8	7.2
HLH-094-28.1	567	359	0.66	0.06	0.05607	3.185	0.51365	3.678	0.06644	1.840	455.3	70.7	414.6	7.4
HLH-094-6.1	917	649	0.73	0.06	0.05441	1.259	0.49791	2.182	0.06637	1.782	387.9	28.3	414.3	7.2
HLH-094-26.1	430	310	0.75	0.26	0.05475	1.655	0.49718	2.438	0.06586	1.791	401.9	37.1	411.2	7.2
HLH-094-32.1	354	215	0.63	0.21	0.05338	1.913	0.48076	2.625	0.06532	1.797	345.0	43.3	407.9	7.1
HLH-094-36.1	946	769	0.84	0.00	0.05555	1.669	0.49584	2.444	0.06474	1.786	434.2	37.2	404.4	7.0
HLH-094-22.1	399	288	0.74	0.18	0.05296	1.839	0.46768	2.599	0.06405	1.836	327.0	41.7	400.2	7.1
HLH-094-31.1	799	652	0.84	-0.04	0.05637	1.020	0.48989	2.063	0.06303	1.793	466.9	22.6	394.0	6.9

Table B.5: Zircon U-Pb SHRIMP geochronology data.

Appendix C

Chapter 4 supplementary material

C.1 Igneous geochronology data tables

Spot Name	U (ppm)	^{232}Th/ ^{238}U	^{207}Pb/^{206}Pb	±1σ	^{206}Pb/^{238}U	±1σ (%)	^{207}Pb/^{206}Pb Age (Ma)	±1σ	^{207}Pb/^{235}Pb Age (Ma)	±1σ	^{206}Pb/^{238}Pb Age (Ma)	±1σ	% Discordant
Xingxingxia fault hangingwall deformed dyke													
11NC39G-4.1	2839	0.27	0.06193	0.00157	0.03588	0.00030	595.0	65.7	271.7	8.4	235.7	4.1	61.5
11NC39G-12.1	2571	0.06	0.06641	0.00209	0.03490	0.00050	745.9	72.7	296.3	10.6	242.4	5.3	68.8
11NC39G-2.1	2863	0.04	0.05842	0.00160	0.03814	0.00057	490.2	68.0	267.8	8.7	243.1	4.8	51.4
11NC39G-8.1	3665	0.28	0.08400	0.00237	0.03832	0.00067	1252.4	66.9	383.0	13.4	255.2	6.1	81.2
11NC39G-17.1	2715	0.02	0.05855	0.00101	0.04925	0.00104	678.2	77.1	308.2	10.8	261.6	4.5	62.7
11NC39G-3.1	21043	0.02	0.06524	0.00059	0.04200	0.00052	720.5	41.9	324.3	7.8	271.8	5.3	63.6
11NC39G-6.2	2638	0.18	0.06343	0.00129	0.04718	0.00046	718.8	57.0	359.1	9.8	305.9	5.4	58.8
11NC39G-7.1	5468	0.01	0.05867	0.00132	0.04751	0.00061	530.2	61.3	338.7	9.8	311.4	5.9	42.3
11NC39G-4.2	4177	0.88	0.06936	0.00232	0.04823	0.00057	822.3	80.8	387.4	14.5	318.5	6.9	62.8
11NC39G-10.1	549	0.49	0.06251	0.00243	0.04962	0.00065	608.7	89.3	375.3	14.7	338.6	6.8	45.5
11NC39G-9.1	251	0.32	0.06142	0.00275	0.05122	0.00079	579.9	103.7	378.0	17.0	345.9	7.9	41.4
11NC39G-11.1	1299	0.61	0.05940	0.00160	0.05073	0.00045	487.5	69.5	367.9	11.6	349.2	6.9	29.1
11NC39G-4.1	101	0.14	0.05586	0.00137	0.07869	0.00085	395.3	55.9	395.6	9.3	395.7	5.0	-0.1
11NC39G-3.1	191	0.17	0.05596	0.00124	0.07741	0.00090	409.3	51.7	400.2	9.0	398.6	5.3	2.7
11NC39G-13.1	989	0.17	0.05603	0.00059	0.07853	0.00073	399.0	27.3	400.0	5.5	400.2	4.3	-0.3
Xingxingxia fault footwall deformed dyke													
11NC45-15.1c	1601	0.34	0.05603	0.00050	0.05516	0.00030	403.8	26.1	401.1	4.9	400.7	3.5	0.8
11NC45-7.1	697	0.32	0.05600	0.00062	0.05540	0.00041	430.0	30.2	411.1	5.8	407.7	4.1	5.3
11NC45-19.1	1537	0.13	0.05632	0.00063	0.08946	0.00066	404.0	30.8	408.3	6.0	409.1	4.6	-1.3
11NC45-17.1	766	0.31	0.05593	0.00064	0.05677	0.00034	421.5	30.9	413.5	5.6	412.1	3.6	2.3
11NC45-14.1	522	0.31	0.05626	0.00079	0.05642	0.00043	412.3	34.6	414.3	6.3	414.6	4.0	-0.6
11NC45-13.1	631	0.34	0.05668	0.00072	0.05577	0.00042	428.4	32.4	417.2	6.1	415.2	4.1	3.2
11NC45-16.1	475	0.30	0.05705	0.00090	0.05746	0.00041	458.4	37.9	421.9	6.8	415.3	3.8	9.7
11NC45-6.1	830	0.26	0.05574	0.00061	0.05661	0.00039	431.4	29.6	418.4	5.7	416.0	4.1	3.7
11NC45-12.1	630	0.10	0.05646	0.00065	0.05569	0.00037	417.5	30.0	417.8	5.7	417.9	3.9	-0.1
11NC45-20.1	538	0.04	0.05608	0.00076	0.05772	0.00041	414.1	34.9	418.1	6.4	418.9	4.0	-1.2
11NC45-3.2r	447	0.20	0.05571	0.00070	0.05684	0.00030	425.5	29.6	420.7	5.3	419.8	3.0	1.4

Table C.1: Zircon U-Pb LA-ICPMS geochronology data.

Spot Name	U (ppm)	^{232}Th/ ^{238}U	^{207}Pb/^{206}Pb	±1σ	^{206}Pb/^{238}U	±1σ (%)	^{207}Pb/^{206}Pb Age (Ma)	±1σ	^{207}Pb/^{235}Pb Age (Ma)	±1σ	^{206}Pb/^{238}Pb Age (Ma)	±1σ	% Discordant
Xingxingxia fault undeformed dyke													
11NC41-2.1	1073	0.49	0.05277	0.00080	0.04562	0.00045	260.5	40.5	267.7	5.1	268.5	3.4	-3.1
11NC41-16.1	955	0.49	0.05308	0.00035	0.04285	0.00034	283.1	17.3	271.0	2.8	269.5	2.3	4.9
11NC41-9.1	738	0.38	0.05304	0.00046	0.04336	0.00020	268.4	22.6	269.6	2.9	269.8	1.9	-0.5
11NC41-5.1	760	0.53	0.05315	0.00087	0.04540	0.00043	270.0	44.4	269.9	5.5	269.9	3.3	0.1
11NC41-10.1	530	0.41	0.05324	0.00042	0.04329	0.00021	278.6	19.9	270.8	2.6	269.9	1.8	3.2
11NC41-11.1	113	0.23	0.05304	0.00076	0.04323	0.00025	271.5	33.4	270.2	3.9	270.1	1.9	0.5
11NC41-18.1	147	0.28	0.05298	0.00070	0.04282	0.00032	271.3	31.4	270.2	3.9	270.1	2.3	0.4
11NC41-8.1	641	0.59	0.05313	0.00073	0.04543	0.00051	262.6	35.0	269.5	4.8	270.3	3.6	-3.0
11NC41-19.1	322	0.25	0.05308	0.00047	0.04272	0.00025	278.2	22.0	271.2	2.8	270.4	1.8	2.9
11NC41-14.1	531	0.32	0.05279	0.00040	0.04312	0.00029	275.9	20.0	271.5	2.8	271.0	2.1	1.8
11NC41-17.1	305	0.35	0.05322	0.00054	0.04312	0.00023	284.2	24.8	272.5	3.1	271.1	1.8	4.7
11NC41-3.1	417	0.39	0.05316	0.00146	0.04593	0.00043	277.5	65.3	271.9	7.4	271.3	3.1	2.3
11NC41-13.1	217	0.27	0.05296	0.00061	0.04324	0.00027	278.6	27.5	272.2	3.4	271.4	2.0	2.6
11NC41-12.1	265	0.16	0.05291	0.00053	0.04338	0.00031	271.6	24.2	271.9	3.2	271.9	2.2	-0.1
11NC41-6.1	226	0.28	0.05316	0.00176	0.04579	0.00052	262.4	76.5	270.9	8.7	271.9	3.5	-3.7
11NC41-15.1	250	0.26	0.05243	0.00074	0.04324	0.00024	259.9	33.9	270.7	3.9	272.0	1.9	-4.7
11NC41-7.1	103	0.30	0.05355	0.00178	0.04590	0.00049	271.6	76.1	272.2	8.7	272.3	3.5	-0.3
11NC41-4.1	625	0.48	0.05324	0.00124	0.04604	0.00049	281.3	58.2	273.7	7.0	272.9	3.6	3.1
Tianhu fault marginal deformed dyke													
11NC06B-8.1	568	0.60	0.05828	0.00089	0.05684	0.00045	429.1	41.6	428.3	8.0	428.1	5.4	0.2
11NC06B-6.2r	312	0.25	0.05750	0.00106	0.05881	0.00055	434.8	43.9	431.3	8.3	430.7	5.4	1.0
11NC06B-25.1	59	0.59	0.05689	0.00236	0.05755	0.00079	442.2	91.5	433.5	15.9	431.9	6.7	2.4
11NC06B-4.1	428	0.14	0.05592	0.00103	0.05847	0.00046	420.4	45.8	430.1	8.5	432.0	5.3	-2.9
11NC06B-5.1	108	0.39	0.05645	0.00213	0.05911	0.00065	431.4	83.6	433.0	14.3	433.3	5.8	-0.5
11NC06B-24.1	42	0.40	0.05645	0.00305	0.05746	0.00090	426.1	117.8	433.3	20.1	434.6	7.4	-2.1
11NC06B-1.1	183	0.37	0.05644	0.00150	0.05992	0.00051	442.3	61.2	436.3	10.8	435.2	5.3	1.7
11NC06B-2.1	165	0.35	0.05646	0.00174	0.05950	0.00061	446.0	69.5	437.3	12.2	435.6	5.6	2.4
11NC06B-15.1r	47	0.62	0.05611	0.00219	0.05908	0.00068	447.2	86.0	437.7	15.1	435.9	6.7	2.6
11NC06B-3.1	56	0.36	0.05590	0.00296	0.05922	0.00077	427.0	116.0	435.5	19.8	437.1	6.9	-2.5
11NC06B-14.1	312	0.39	0.05602	0.00089	0.05848	0.00040	426.7	38.8	435.9	7.5	437.7	5.1	-2.7
11NC06B-10.1	80	0.38	0.05816	0.00255	0.05721	0.00079	424.1	98.1	435.6	17.1	437.8	7.4	-3.3
11NC06B-6.1c	255	0.36	0.05701	0.00114	0.06050	0.00042	443.7	46.8	440.6	8.6	440.0	4.8	0.8
11NC06B-17.1	1148	0.30	0.05649	0.00044	0.06032	0.00034	475.0	24.2	445.8	5.9	440.2	5.1	7.6

Table C.1: *continued*

Spot Name	U (ppm)	^{232}Th/ ^{238}U	^{207}Pb/^{206}Pb	±1σ	^{206}Pb/^{238}U	±1σ (%)	^{207}Pb/^{206}Pb Age (Ma)	±1σ	^{207}Pb/^{235}Pb Age (Ma)	±1σ	^{206}Pb/^{238}Pb Age (Ma)	±1σ	% Discordant
Tianhu fault central deformed dyke													
11NC27-10.1	885	0.32	0.05770	0.00118	0.05816	0.00038	472.0	49.9	435.1	9.0	428.2	4.8	9.6
11NC27-8.2r	1030	0.25	0.05698	0.00073	0.05866	0.00043	431.4	36.0	429.9	7.0	429.6	4.9	0.4
11NC27-14.1	1380	0.22	0.05644	0.00061	0.05961	0.00045	405.5	35.7	426.3	7.2	430.1	5.4	-6.3
11NC27-15.1	1158	0.26	0.05723	0.00089	0.06009	0.00040	442.8	43.4	434.3	8.2	432.7	5.2	2.4
11NC27-4.1	196	0.54	0.05701	0.00116	0.06171	0.00090	443.8	47.4	434.5	9.8	432.7	7.4	2.6
11NC27-19.1	990	0.34	0.05690	0.00081	0.06162	0.00049	439.8	38.7	435.0	7.6	434.1	5.3	1.3
11NC27-7.1	791	0.26	0.05646	0.00078	0.06045	0.00038	452.2	37.8	437.2	7.5	434.4	5.3	4.1
11NC27-22.1	825	0.26	0.05719	0.00059	0.06134	0.00034	445.1	31.9	436.4	6.6	434.7	4.9	2.4
11NC27-20.1	657	0.25	0.05791	0.00086	0.06227	0.00044	463.9	38.9	440.8	7.6	436.4	5.0	6.1
11NC27-5.1	534	0.29	0.05661	0.00073	0.06216	0.00059	445.1	33.1	439.1	7.1	437.9	5.6	1.7
11NC27-11.1	1446	0.38	0.05739	0.00064	0.05966	0.00049	476.5	36.4	444.2	7.8	438.0	6.0	8.4
11NC27-1.1	648	0.32	0.05778	0.00069	0.06253	0.00078	467.1	32.0	444.3	7.8	440.0	6.8	6.0
11NC27-6.1	592	0.34	0.05659	0.00075	0.06230	0.00057	461.1	36.4	444.3	7.8	441.1	6.0	4.5
11NC27-2.1	545	0.29	0.05728	0.00086	0.06302	0.00049	444.6	36.4	442.4	7.3	442.0	5.1	0.6
11NC27-13.1	619	0.22	0.05715	0.00109	0.06105	0.00048	450.2	48.2	443.6	9.1	442.4	5.4	1.8
11NC27-16.1	1374	0.25	0.05630	0.00088	0.06176	0.00045	429.5	43.8	443.2	8.3	445.8	5.2	-3.9
11NC27-9.1	413	0.25	0.05805	0.00126	0.06065	0.00046	469.0	52.5	450.5	9.7	446.8	5.2	4.9
11NC27-17.2r	757	0.30	0.05606	0.00102	0.06236	0.00053	446.9	51.4	448.1	9.8	448.4	6.0	-0.3
11NC27-12.1	497	0.19	0.05637	0.00118	0.06159	0.00054	436.2	53.4	446.4	10.2	448.4	6.3	-2.9
Tianhu fault granite hosting dykes													
11NC28-3.1	975	0.48	0.05761	0.00058	0.05952	0.00027	481.3	26.3	445.6	5.0	438.7	3.0	9.1
11NC28-1.1	727	0.28	0.05607	0.00060	0.06026	0.00037	422.5	27.3	436.8	5.2	439.6	3.4	-4.2
11NC28-4.1	680	0.42	0.05610	0.00065	0.05963	0.00036	419.0	29.4	437.0	5.5	440.5	3.5	-5.3
11NC28-14.1	725	0.14	0.05746	0.00076	0.08022	0.00057	507.5	34.0	451.4	6.8	440.5	4.5	13.7
11NC28-6.1	502	0.54	0.05622	0.00081	0.06028	0.00039	419.4	35.6	438.9	6.5	442.6	3.6	-5.7
11NC28-17.1	1308	0.22	0.05994	0.00067	0.07952	0.00055	533.2	32.5	458.6	6.9	443.8	4.9	17.4

Table C.1: *continued*

Spot Name	U (ppm)	^{232}Th/ ^{238}U	^{207}Pb/^{206}Pb	±1σ	^{206}Pb/^{238}U	±1σ (%)	^{207}Pb/^{206}Pb Age (Ma)	±1σ	^{207}Pb/^{235}Pb Age (Ma)	±1σ	^{206}Pb/^{238}Pb Age (Ma)	±1σ	% Discordant
Hongliuhe fault marginal deformed dyke													
11NC49B-1.1	204	0.26	0.05457	0.00133	0.06727	0.00061	353.4	58.2	381.5	9.2	386.1	4.6	-9.5
11NC49B-15.1	79	0.25	0.05530	0.00075	0.06066	0.00050	378.6	30.8	388.0	5.3	389.5	3.4	-3.0
11NC49B-14.1	115	0.22	0.05555	0.00068	0.06114	0.00041	381.8	28.2	391.3	4.8	392.9	2.9	-3.0
11NC49B-20.1	47	0.20	0.05618	0.00160	0.06152	0.00052	409.2	63.3	395.4	9.9	393.1	3.6	4.1
11NC49B-9.1	342	0.18	0.05646	0.00045	0.06133	0.00031	410.7	19.7	395.7	3.6	393.1	2.4	4.4
11NC49B-9.2	389	0.18	0.05693	0.00121	0.06307	0.00062	384.5	52.5	392.1	9.0	393.4	5.5	-2.4
11NC49B-10.1	56	0.20	0.05616	0.00103	0.06163	0.00045	399.6	41.3	396.7	6.7	396.2	3.2	0.9
11NC49B-17.1	45	0.20	0.05546	0.00122	0.06213	0.00038	395.9	49.0	396.1	7.6	396.2	2.8	-0.1
11NC49B-3.1	169	0.25	0.05363	0.00199	0.06812	0.00069	363.7	85.6	391.9	13.2	396.7	5.0	-9.3
11NC49B-18.1	103	0.20	0.05541	0.00071	0.06249	0.00029	390.8	29.3	395.9	4.7	396.8	2.2	-1.6
11NC49B-16.1	107	0.16	0.05566	0.00066	0.06193	0.00038	399.9	27.3	397.4	4.7	397.0	2.8	0.7
Hongliuhe fault granite hosting deformed dyke													
11NC50-2.1	171	0.42	0.05463	0.00234	0.06690	0.00080	359.9	95.6	386.4	14.7	390.8	5.5	-8.9
11NC50-4.1	89	0.37	0.05784	0.00236	0.06762	0.00090	478.6	89.1	405.6	14.6	392.8	5.7	18.5
11NC50-19.1	490	0.33	0.05576	0.00047	0.06154	0.00033	389.6	21.5	392.7	3.8	393.3	2.6	-1.0
11NC50-16.1	382	0.10	0.05584	0.00040	0.06198	0.00041	394.1	17.4	394.1	3.6	394.1	2.9	0.0
11NC50-13.1	552	0.25	0.05600	0.00041	0.06232	0.00044	393.8	19.0	394.6	3.9	394.7	3.1	-0.2
11NC50-6.1	61	0.36	0.05308	0.00278	0.06849	0.00091	254.3	117.4	375.0	17.2	394.9	5.9	-57.0
11NC50-8.1	320	0.11	0.05365	0.00139	0.06903	0.00060	308.5	63.1	382.6	9.9	394.9	5.1	-28.9
11NC50-14.1	247	0.36	0.05599	0.00083	0.06260	0.00061	394.7	34.4	394.9	6.1	395.0	4.1	-0.1
11NC50-5.1	198	0.31	0.05930	0.00143	0.06815	0.00055	514.5	54.2	413.0	9.3	395.1	4.2	23.9
11NC50-11.1	599	0.24	0.05607	0.00045	0.06145	0.00056	401.8	19.2	396.2	4.3	395.2	3.8	1.7
11NC50-9.1	247	0.21	0.05735	0.00069	0.06247	0.00028	455.3	28.4	404.3	4.7	395.5	2.3	13.6
11NC50-17.1	196	0.24	0.05622	0.00056	0.06196	0.00036	410.7	23.3	397.8	4.2	395.6	2.7	3.8
11NC50-15.1	547	0.13	0.05603	0.00049	0.06248	0.00050	399.1	20.8	396.2	4.2	395.7	3.3	0.9
11NC50-3.1	119	0.32	0.05479	0.00169	0.06878	0.00079	376.9	70.8	396.7	11.5	400.1	5.5	-6.4
11NC50-1.1	100	0.26	0.05399	0.00294	0.06985	0.00116	303.7	121.3	392.7	18.8	408.0	7.3	-35.4

Table C.1: *continued*

Appendix D

Chapter 5 supplementary material

D.1 Procedures

D.1.1 Variably tectonized clast sampling methodology and strategy

- For each stratigraphic level two outcrops within 200 m along strike of each other were sought for sampling, both for sandstone and clast materials. This is done to accommodate for local variations in the coarse clastic material. Materials collected from the two outcrops were combined for each type of sample, to create only one detrital sample per type (undeformed clasts, slightly deformed clasts, deformed clasts, and sandstone), per stratigraphic level.

- Our clast sampling targeted granitoid clasts of all compositions and textures. An initial assessment, using a hand lens, of the modal abundances of plagioclase, K-feldspar, quartz and mafic grains was made in the field for granitoid classification. Clasts were numbered for reference, had their field-interpreted lithology (including composition and textures) noted, and were sorted by tectonization type in a cursory fashion at the outcrop. The sorting was refined in a camp setting after all sampling had been performed across the stratigraphy to ensure consistency of type discrimination between outcrops. Many lithotypes were found repetitively between outcrops and across the stratigraphy. The judgment of the authors and their experience with identifying deformed rocks were used for textural separation, visually differentiating among those with no foliation (undeformed), those with a definite foliation (deformed) and those with any visual cue of minor deformation without a fully developed foliation (slightly deformed). This slightly deformed population includes clasts that exhibit subtle or patchy deformation textures such as reduced grain size, a degree of mineral alignment, or the rounding of porphyroclastic grains. No L-tectonites were present in the clast populations of this study, though in future uses of the method they should be incorporated into the deformed population. No magmatic flow textures were identified. Fragments of most of the common lithotypes were collected for hand samples and thin section. Future users of these procedures may wish to preserve the numbered set of clasts and further refine the discrimination in a laboratory, given that microscopic analysis may allow for more specific criteria based on the degree of tectonic fabric development.

- A representative sample from each of the granitoid clast lithotypes with unique compositional and textural combinations (for example a K-feldspar megacrystic granite, or mylonitic tonalite) was selected for thin section. Thin section analysis was used to confirm the granitoid classification and to verify the degree of deformation. Deformation textures in deformed clasts include (but are not limited to) mylonitic textures, extensive dynamic recrystallization, mantling of porphyroclasts, rounding of porphyroclasts, mineral alteration (commonly sericitized plagioclase), and quartz and mica domain segregation. Slightly deformed clasts include patchy dynamic recrystallization, weak mantling of porphyroclasts, mineral alteration and limited to no quartz and mica domain segregation. Undeformed clasts exhibited primary granitoid textures, though some samples included intragranular and transgranular fracturing, rare small patches of dynamic recrystallization, and alteration of minerals. For future use of the variably tectonized clast dating method thin section analysis of clasts may be used to establish very specific criteria for classification of the level of deformation, such as the percentage or grain size of dynamically recrystallized quartz. This may be considered more robust by some, and would allow for correct classification of problematic textures such as primary magmatic mineral alignments.

- All sizes of clasts were sampled from the outcrops, except those less than approximately 5 cm in diameter. Each clast or clast fragment was trimmed, after sampling, to a uniform size of approximately 5 cm in diameter, and any matrix material adhering to the exterior of the clast was chipped away. After all sorting was completed all clast or clast fragments of the same tectonization type, per stratigraphic level, were bagged together and crushed for mineral separation as a single sample.

- Approximately 120-150 clasts were sampled per pair of outcrops at each stratigraphic level. In retrospect, more could have been taken; at the time of sampling we were improvising. We agree with the strategy of Dunkl et al. (2009) that "a minimum of 50 pieces [be sampled] for a representative [conglomeratic] pebble population". A general rule would be that more is better, to reduce the bias of any atypical clast material or unusually zircon-rich fragments. In addition, for this study we performed the sorting after sampling, to understand the natural distribution of tectonization amongst the clasts, which resulted in some clast populations being a statistically small set (eg. basal stratigraphic level, undeformed, $n_{clasts}=10$, Figs. 5.7 and 5.9). For future users of this method, a visual clast count of the exposed outcrop can be performed to provide the distribution of clast lithotypes. Preliminary sorting should be performed at the outcrops and sampling should aim to provide a minimum number of clasts per sample.

- Sandstone detrital samples were collected at each stratigraphic level as an essential addition. The outcrops sampled for this study included common interbeds of sandy material or sandstone beds only meters up or down section. An alternative would be to sample a sandy matrix of the conglomerate itself.

- This sampling procedure may be utilized in other ways than presented here, sampling for different lithologies or sorting based on different parameters, such as metamorphic grade/mineral assemblage, granitoid composition, geochemistry, metasedimentary rock type and tectonization, etc. Thin section textures may be used as parameters as well, such as sorting based on the increased degree of dynamic recrystalliztion of specific minerals or other microstructures.

D.1.2 LA-ICPMS analytical procedure

Uranium-lead zircon single-crystal geochronological analyses were performed for all detrital samples in this study, including nine clast populations and three sandstone samples. Zircon grains were separated from pulverized sample material using standard heavy liquid and magnetic separation techniques. Target grains were randomly selected and individually handpicked then mounted in an epoxy puck. The puck was ground to expose the zircon cores, then polished for laser ablation analyses.

Imaging of each mounted and polished target grain was performed with cathodoluminescence (CL) and electron backscatter (BSE) functions of a JEOL JSM6610-Lv scanning electron microscope (SEM). Images were used to identify internal zircon zonation, inherited cores, and the target regions. Uranium-lead isotopic analyses were performed on the laser ablation (LA) inductively coupled plasma mass spectrometer (ICPMS) apparatus at the Jack Satterly Geochronology Laboratory in the Department of Earth Sciences at the University of Toronto, Ontario, Canada. The analytical procedure utilizes a VG Series 2 Plasmaquad ICPMS in conjunction with a 75 l/s rotary pump for the expansion chamber (S-option), for the purpose of enhanced sensitivity. The laser ablation unit uses a 213 nm New Wave laser. Target zircon crystals were ablated with a beam diameter of 15, 25 or 30 μm at 10 Hz and 40% power. The He carrier gas was passed through a 25 ml mixing chamber to dampen signal instability from U heterogeneity in the sample. Time intervals of raw data collection for the selected elements and isotopes were chosen as follows: ^{88}Sr (10 ms), ^{206}Pb (30 ms), ^{207}Pb (40 ms), ^{232}Th (10 ms) and ^{238}U (20 ms). Sr was measured as a proxy for alteration or inclusions. Analyses with high Sr were rejected. A raster laser ablation pattern was applied to the surface of each target point prior to analytical measurement for the purpose of removing debris or impurities. Data acquisition was established over a 35 second ablation of the target zircon material, initiated after a 10 second reading of a basline signal. A fifty-second signal washout period was allowed to elapse between each data acquisition. Data reduction software authored and provided by D. Davis allowed for reduction and analysis of data. Analyses did not measure ^{204}Pb, and therefore no corrections were made for common lead. A single zircon standard was used in all analytical runs (DD85-17; 3002 ± 2 Ma), with standard grain analyses run bracketing sets of three or fewer sample acquisitions.

D.2 Detrital geochronology data tables

Spot Name	U (ppm)	^{232}Th/ ^{238}U	^{207}Pb/^{206}Pb	±1σ	^{206}Pb/^{238}U	±1σ (%)	^{207}Pb/^{206}Pb Age (Ma)	±1σ	^{207}Pb/^{235}Pb Age (Ma)	±1σ	^{206}Pb/^{238}Pb Age (Ma)	±1σ	% Discordant
Sandstone – Upper stratigraphic level													
11NC18-2.1	882	0.59	0.05508	0.00058	0.05117	0.00032	394.2	26.3	385.7	4.6	384.3	3.0	2.6
11NC18-6.1	49	1.09	0.05532	0.00237	0.05049	0.00059	383.1	94.7	386.9	14.5	387.5	4.9	-1.2
11NC18-30.1	887	0.51	0.05472	0.00063	0.05167	0.00031	390.0	31.2	395.4	5.3	396.3	3.1	-1.7
11NC18-7.1	224	1.09	0.05557	0.00093	0.05965	0.00047	385.6	39.4	395.6	6.6	397.3	3.8	-3.1
11NC18-9.1	184	0.91	0.05576	0.00145	0.05196	0.00044	408.3	59.5	399.8	9.6	398.3	4.2	2.5
11NC18-23.1	114	0.42	0.05520	0.00188	0.05208	0.00057	396.1	76.0	399.1	12.1	399.6	4.8	-0.9
11NC18-13.1	644	0.41	0.05558	0.00056	0.06103	0.00041	404.2	27.0	405.0	4.9	405.1	3.3	-0.2
11NC18-21.1	72	0.87	0.05553	0.00201	0.06171	0.00050	414.7	80.2	407.8	12.7	406.5	3.9	2.0
11NC18-47.1	487	0.39	0.05580	0.00088	0.05164	0.00038	421.8	39.7	409.6	6.8	407.4	3.7	3.5
11NC18-13.1	271	0.63	0.05661	0.00112	0.05220	0.00046	415.6	46.5	409.9	7.9	408.9	4.2	1.7
11NC18-51.1	80	0.40	0.05577	0.00278	0.05265	0.00091	415.7	109.8	414.5	18.2	414.3	7.4	0.4
11NC18-5.1	96	1.57	0.05627	0.00136	0.05510	0.00042	429.3	54.6	419.8	9.1	418.1	3.7	2.7
11NC18-17.1	454	0.33	0.05643	0.00088	0.05217	0.00060	399.5	36.8	415.4	7.1	418.3	5.2	-4.9
11NC18-44.1	317	0.62	0.05632	0.00109	0.05305	0.00040	421.8	46.0	422.3	7.9	422.4	3.8	-0.2
11NC18-57.1	99	1.18	0.05603	0.00191	0.05493	0.00092	438.0	75.5	427.0	13.5	425.0	7.2	3.1
11NC18-32.1	325	0.90	0.05577	0.00110	0.05568	0.00046	408.0	46.1	423.5	8.0	426.4	4.0	-4.7
11NC18-38.1	134	0.88	0.05544	0.00116	0.05499	0.00037	411.5	47.3	424.3	7.9	426.6	3.3	-3.8
11NC18-31.1	230	1.21	0.05618	0.00130	0.05609	0.00047	438.4	53.6	429.8	9.2	428.2	4.2	2.4
11NC18-37.1	102	0.64	0.05599	0.00139	0.05551	0.00051	432.5	55.2	428.9	9.5	428.2	4.4	1.0
11NC18-3.1	183	0.90	0.05606	0.00109	0.06694	0.00051	440.0	45.5	431.6	8.1	430.0	4.3	2.4
11NC18-35.1	332	0.70	0.05605	0.00098	0.05620	0.00039	412.1	41.3	427.7	7.2	430.6	3.7	-4.6
11NC18-67.1	108	1.01	0.05637	0.00196	0.05618	0.00055	443.1	76.6	433.0	13.0	431.1	4.7	2.8
11NC18-12.1	210	0.48	0.05659	0.00120	0.05581	0.00036	425.4	49.2	431.3	8.4	432.4	3.6	-1.7
11NC18-60.1	550	0.71	0.05641	0.00080	0.05676	0.00043	419.9	39.4	430.5	7.4	432.5	4.7	-3.1
11NC18-4.1	136	0.85	0.05589	0.00146	0.06669	0.00057	425.6	59.3	431.8	10.2	432.9	4.6	-1.8
11NC18-24.1	163	0.91	0.05659	0.00120	0.06623	0.00046	442.5	48.7	435.4	8.4	434.1	3.7	2.0
11NC18-39.1	53	0.24	0.05612	0.00219	0.05579	0.00058	440.0	85.4	435.9	14.5	435.1	4.8	1.2
11NC18-22.1	572	0.43	0.05672	0.00059	0.06642	0.00049	456.7	27.1	438.8	5.5	435.4	3.9	4.8
11NC18-24.1	147	0.71	0.05598	0.00143	0.05722	0.00050	433.1	58.1	435.2	10.1	435.5	4.5	-0.6
11NC18-36.1	210	0.53	0.05650	0.00133	0.05703	0.00057	440.5	53.7	436.5	9.6	435.8	4.9	1.1
11NC18-27.1	170	0.61	0.05591	0.00142	0.05661	0.00049	429.4	58.3	435.4	10.1	436.6	4.4	-1.7
11NC18-27.1	146	0.94	0.05641	0.00162	0.06612	0.00052	447.0	65.1	438.6	11.2	437.0	4.3	2.3
11NC18-26.1	121	0.59	0.05620	0.00159	0.05705	0.00056	443.2	63.5	438.2	11.0	437.3	4.7	1.4
11NC18-23.1	102	0.75	0.05649	0.00155	0.06675	0.00046	443.3	61.5	438.3	10.4	437.4	3.6	1.4
11NC18-4.1	106	1.40	0.05597	0.00123	0.05826	0.00053	425.6	50.1	435.6	8.9	437.5	4.6	-2.9
11NC18-8.1	1366	0.45	0.05669	0.00045	0.06565	0.00040	424.9	22.5	435.6	4.6	437.7	3.4	-3.1

Table D.1: Sandstone detrital zircon U-Pb LA-ICPMS geochronology data.

		^{232}Th/					^{207}Pb/^{206}Pb		^{207}Pb/^{235}Pb		^{206}Pb/^{238}Pb		%
Spot Name	U (ppm)	^{238}U	^{207}Pb/^{206}Pb	±1σ	^{206}Pb/^{238}U	±1σ (%)	Age (Ma)	±1σ	Age (Ma)	±1σ	Age (Ma)	±1σ	Discordant
Sandstone – Upper stratigraphic level continued													
11NC18-65.1	136	0.53	0.05617	0.00152	0.05623	0.00045	439.5	60.6	438.3	10.4	438.1	4.1	0.3
11NC18-2.1	371	0.48	0.05605	0.00083	0.06863	0.00048	440.1	34.7	438.7	6.5	438.5	3.9	0.4
11NC18-61.1	276	0.89	0.05743	0.00143	0.05706	0.00040	458.1	59.2	441.9	10.4	438.8	4.6	4.4
11NC18-1.1	412	0.61	0.05629	0.00064	0.06902	0.00050	450.4	27.7	440.7	5.6	438.9	4.0	2.7
11NC18-14.1	260	0.91	0.05635	0.00094	0.06627	0.00039	447.8	39.9	440.6	7.1	439.2	3.5	2.0
11NC18-7.1	864	0.69	0.05654	0.00066	0.05715	0.00038	429.0	30.3	437.8	5.8	439.4	3.7	-2.5
11NC18-5.1	405	0.43	0.05619	0.00069	0.06767	0.00050	430.2	29.7	439.9	5.8	441.7	4.0	-2.8
11NC18-6.1	143	0.92	0.05653	0.00109	0.06749	0.00047	436.5	44.0	442.2	7.8	443.2	3.9	-1.6
11NC18-69.1	534	0.44	0.05663	0.00089	0.05682	0.00044	440.2	40.7	443.0	7.5	443.6	4.2	-0.8
11NC18-19.1	207	0.53	0.05630	0.00108	0.06714	0.00056	448.0	43.8	444.3	8.0	443.6	4.3	1.0
11NC18-68.1	258	0.94	0.05657	0.00125	0.05737	0.00038	443.4	52.6	443.5	9.2	443.6	3.8	0.0
11NC18-33.1	1082	0.54	0.05695	0.00073	0.05787	0.00026	440.5	32.6	443.2	6.0	443.7	3.4	-0.8
11NC18-10.1	264	1.16	0.05622	0.00100	0.05797	0.00034	425.0	42.3	440.8	7.5	443.9	3.8	-4.6
11NC18-28.1	240	1.51	0.05640	0.00116	0.06728	0.00062	452.6	48.7	445.4	8.9	444.0	4.8	1.9
11NC18-26.1	226	1.18	0.05628	0.00125	0.06749	0.00046	436.6	50.8	443.2	8.8	444.5	3.7	-1.9
11NC18-16.1	497	0.42	0.05538	0.00103	0.06699	0.00059	429.5	45.7	442.2	8.5	444.6	4.9	-3.6
11NC18-70.1	658	0.08	0.05691	0.00074	0.05710	0.00034	453.2	33.3	447.2	6.2	446.0	3.4	1.6
11NC18-22.1	387	1.01	0.05705	0.00111	0.05812	0.00066	464.2	46.2	449.5	9.0	446.6	5.7	3.9
11NC18-20.1	170	0.30	0.05642	0.00115	0.06803	0.00051	451.6	46.2	448.6	8.3	448.0	3.9	0.8
11NC18-25.1	392	0.27	0.05673	0.00084	0.05891	0.00049	465.8	36.2	451.2	7.0	448.3	4.4	3.9
11NC18-56.1	174	0.73	0.05654	0.00117	0.05778	0.00089	459.0	46.9	450.6	9.8	448.9	7.0	2.3
11NC18-59.1	718	0.66	0.05652	0.00069	0.05897	0.00051	434.8	32.2	447.5	6.5	450.0	4.7	-3.6
11NC18-58.1	151	0.82	0.05664	0.00146	0.05883	0.00082	450.7	58.0	450.3	11.1	450.2	6.5	0.1
11NC18-63.1	513	0.38	0.05658	0.00098	0.05722	0.00040	443.8	42.7	449.6	7.9	450.8	4.3	-1.6
11NC18-49.1	397	0.77	0.05690	0.00081	0.05811	0.00046	476.1	35.5	456.9	7.0	453.1	4.4	5.0
11NC18-28.1	194	0.92	0.05680	0.00145	0.05892	0.00061	466.3	58.3	456.3	10.7	454.3	5.2	2.7
11NC18-18.1	435	0.31	0.05725	0.00072	0.06912	0.00056	491.5	30.5	463.4	6.3	457.7	4.3	7.1
11NC18-50.1	181	0.97	0.05649	0.00166	0.05858	0.00074	452.2	66.3	457.0	12.2	458.0	6.1	-1.3
11NC18-17.1	170	0.42	0.05664	0.00128	0.06913	0.00056	473.6	51.6	460.7	9.5	458.1	4.4	3.4
11NC18-46.1	363	0.63	0.05679	0.00130	0.05797	0.00048	451.2	55.6	456.9	10.1	458.1	4.8	-1.6
11NC18-40.1	123	0.72	0.05661	0.00160	0.05835	0.00066	453.3	62.9	457.5	11.5	458.3	5.5	-1.1
11NC18-48.1	1457	0.31	0.05685	0.00046	0.05871	0.00027	472.5	24.7	461.1	5.1	458.8	3.5	3.0
11NC18-43.1	151	1.50	0.05753	0.00186	0.05783	0.00052	468.2	71.5	460.5	12.7	459.0	4.6	2.0
11NC18-16.1	342	0.32	0.05766	0.00093	0.05783	0.00088	446.5	38.8	457.0	8.8	459.1	7.2	-2.9
11NC18-41.1	515	0.55	0.05720	0.00075	0.05838	0.00041	469.1	30.9	461.5	6.1	460.0	3.7	2.0
11NC18-12.1	128	0.63	0.05840	0.00118	0.06945	0.00055	496.0	46.3	466.3	8.6	460.3	4.1	7.4

Table D.1: *continued*

Spot Name	U (ppm)	^{232}Th/ ^{238}U	^{207}Pb/^{206}Pb	±1σ	^{206}Pb/^{238}U	±1σ (%)	^{207}Pb/^{206}Pb Age (Ma)	±1σ	^{207}Pb/^{235}Pb Age (Ma)	±1σ	^{206}Pb/^{238}Pb Age (Ma)	±1σ	% Discordant
Sandstone – Upper stratigraphic level continued													
11NC18-53.1	1827	0.85	0.05654	0.00058	0.05869	0.00073	449.4	28.9	459.4	7.0	461.4	6.1	-2.8
11NC18-14.1	153	1.44	0.05847	0.00143	0.05943	0.00071	483.7	55.0	468.3	10.6	465.1	5.8	4.0
11NC18-55.1	108	1.09	0.05704	0.00161	0.05962	0.00112	479.1	63.3	467.9	13.1	465.6	8.8	2.9
11NC18-15.1	702	1.23	0.05776	0.00069	0.05948	0.00059	452.8	30.6	464.8	6.7	467.2	5.2	-3.3
11NC18-20.1	115	0.66	0.05778	0.00170	0.05945	0.00082	471.0	65.3	469.8	12.6	469.6	6.8	0.3
11NC18-18.1	192	0.39	0.05864	0.00136	0.05949	0.00087	486.2	51.9	479.4	10.9	478.0	7.3	1.7
Sandstone – Middle stratigraphic level													
11NC47-42.1	1024	0.87	0.05567	0.00086	0.07102	0.00078	368.8	43.8	371.1	7.7	371.5	5.4	-0.8
11NC47-12.1	204	0.61	0.05611	0.00143	0.07897	0.00083	393.0	59.1	393.5	9.7	393.6	5.2	-0.2
11NC47-53.1	193	0.77	0.05628	0.00151	0.07460	0.00071	403.7	62.8	399.9	10.3	399.2	4.9	1.2
11NC47-5.1	242	0.62	0.05659	0.00128	0.07749	0.00087	404.9	53.8	401.8	9.2	401.2	5.3	0.9
11NC47-13.1	942	0.47	0.05439	0.00095	0.06157	0.00044	395.5	45.5	402.7	7.7	403.9	4.3	-2.2
11NC47-2.3r	605	0.00	0.05586	0.00117	0.08870	0.00161	425.0	51.3	416.4	10.9	414.9	8.7	2.5
11NC47-43.1	339	1.32	0.05643	0.00141	0.08078	0.00069	400.8	61.3	417.2	10.5	420.1	5.4	-5.0
11NC47-24.1	382	0.42	0.05674	0.00082	0.08358	0.00076	422.6	37.1	426.7	7.1	427.5	4.9	-1.2
11NC47-45.1	74	0.25	0.05588	0.00274	0.06756	0.00068	451.5	106.3	431.9	17.8	428.2	5.0	5.3
11NC47-16.1	440	0.20	0.05618	0.00109	0.06629	0.00051	445.7	46.1	431.5	8.3	428.9	4.6	3.9
11NC47-8.1r	102	0.44	0.05727	0.00219	0.08396	0.00106	446.8	84.8	432.2	14.7	429.5	6.3	4.0
11NC47-13.1	613	0.31	0.05729	0.00076	0.08659	0.00079	424.3	34.4	428.9	6.9	429.7	5.1	-1.3
11NC47-18.1	258	1.56	0.05675	0.00156	0.06755	0.00065	436.3	65.6	430.9	11.5	429.9	5.5	1.5
11NC47-10.1	67	0.37	0.05584	0.00166	0.06739	0.00065	444.7	66.0	433.4	11.3	431.3	4.6	3.1
11NC47-41.1	269	1.20	0.05763	0.00145	0.08240	0.00094	440.6	59.3	433.8	10.8	432.5	6.1	1.9
11NC47-20.1	258	0.87	0.05708	0.00134	0.08457	0.00076	431.1	54.3	433.2	9.7	433.6	5.1	-0.6
11NC47-22.1	335	0.71	0.05739	0.00108	0.08485	0.00099	449.8	46.4	436.7	9.2	434.2	6.4	3.6
11NC47-28.1	112	0.27	0.05701	0.00221	0.08357	0.00094	416.5	87.2	432.1	14.8	435.1	5.8	-4.6
11NC47-11.1	156	1.32	0.05789	0.00135	0.08702	0.00084	479.3	53.8	442.6	10.0	435.6	5.4	9.4
11NC47-64.1	376	0.29	0.05771	0.00090	0.08086	0.00069	444.8	37.8	437.7	7.4	436.4	5.0	2.0
11NC47-48.1	147	0.69	0.05739	0.00200	0.08331	0.00092	461.6	78.3	440.8	13.8	436.9	5.9	5.5
11NC47-38.1	355	0.34	0.05646	0.00109	0.06895	0.00046	453.3	46.9	440.1	8.4	437.6	4.3	3.6
11NC47-5.1	188	0.46	0.05701	0.00177	0.06666	0.00059	437.7	70.2	438.4	12.0	438.5	4.6	-0.2
11NC47-51.1	217	0.38	0.05721	0.00116	0.08290	0.00081	437.2	46.9	438.6	9.0	438.9	5.7	-0.4
11NC47-17.1	635	0.33	0.05593	0.00073	0.06856	0.00054	419.8	35.4	436.4	6.9	439.6	4.7	-4.9
11NC47-46.1	175	1.05	0.05542	0.00134	0.06977	0.00058	430.3	55.2	438.9	9.7	440.5	4.5	-2.5
11NC47-37.1	90	0.67	0.05740	0.00142	0.08512	0.00087	451.7	56.7	442.8	10.4	441.1	5.6	2.4
11NC47-19.1	138	0.63	0.05701	0.00187	0.08604	0.00090	424.4	73.6	438.5	12.9	441.2	5.8	-4.1

Table D.1: *continued*

Spot Name	U (ppm)	^{232}Th/ ^{238}U	^{207}Pb/^{206}Pb	±1σ	^{206}Pb/^{238}U	±1σ (%)	^{207}Pb/^{206}Pb Age (Ma)	±1σ	^{207}Pb/^{235}Pb Age (Ma)	±1σ	^{206}Pb/^{238}Pb Age (Ma)	±1σ	% Discordant
Sandstone – Middle stratigraphic level continued													
11NC47-71.1	416	0.34	0.05768	0.00117	0.08235	0.00068	453.1	50.2	443.4	9.5	441.5	5.7	2.7
11NC47-21.1	117	0.38	0.05737	0.00195	0.08626	0.00106	446.0	76.6	442.4	13.8	441.7	6.7	1.0
11NC47-40.1	584	0.25	0.05674	0.00075	0.06967	0.00037	466.0	33.1	446.1	6.1	442.2	3.5	5.3
11NC47-26.1	571	0.31	0.05777	0.00081	0.08595	0.00072	456.8	35.7	444.6	7.0	442.3	4.6	3.3
11NC47-57.1	136	0.84	0.05693	0.00164	0.08359	0.00086	442.7	66.0	442.3	12.0	442.3	6.2	0.1
11NC47-2.1cr	112	1.16	0.05703	0.00202	0.08729	0.00110	438.7	79.5	442.2	14.1	442.9	6.3	-1.0
11NC47-46.1	196	0.67	0.05781	0.00131	0.08412	0.00099	454.8	54.1	445.2	10.4	443.4	6.4	2.6
11NC47-60.1	145	0.28	0.05826	0.00146	0.08188	0.00087	460.5	58.0	446.4	10.8	443.7	5.9	3.8
11NC47-6.1	238	0.67	0.05762	0.00156	0.06766	0.00061	460.1	62.4	446.9	11.1	444.3	5.0	3.5
11NC47-20.1	418	0.60	0.05676	0.00132	0.06916	0.00063	428.0	55.8	441.7	10.1	444.4	5.3	-4.0
11NC47-2.1	206	0.80	0.05615	0.00179	0.06781	0.00062	430.7	72.1	442.5	12.5	444.8	4.9	-3.4
11NC47-35.1	879	0.71	0.05819	0.00095	0.08421	0.00081	429.2	47.4	442.3	9.3	444.8	6.4	-3.8
11NC47-68.1	71	0.20	0.05719	0.00211	0.08236	0.00094	462.9	81.7	448.4	14.6	445.5	6.3	3.9
11NC47-44.1	461	0.69	0.05795	0.00111	0.08533	0.00074	456.2	47.5	447.3	9.0	445.6	5.3	2.4
11NC47-67.1r	293	0.45	0.05699	0.00098	0.08278	0.00075	447.5	41.1	445.9	8.0	445.6	5.3	0.4
11NC47-35.1	1031	1.15	0.05654	0.00108	0.06996	0.00052	456.6	48.1	447.6	8.9	445.8	4.9	2.5
11NC47-9.1	522	1.07	0.05682	0.00082	0.08759	0.00085	450.5	39.1	447.0	8.2	446.3	6.1	1.0
11NC47-38.1	87	0.79	0.05830	0.00201	0.08536	0.00091	475.7	76.4	451.2	13.7	446.4	5.8	6.4
11NC47-44.1	338	0.22	0.05646	0.00122	0.07009	0.00050	474.8	51.2	451.1	9.2	446.4	4.1	6.2
11NC47-22.1	308	0.85	0.05713	0.00149	0.06911	0.00055	446.2	61.5	446.5	10.9	446.5	4.9	-0.1
11NC47-66.1	290	0.50	0.05728	0.00111	0.08339	0.00073	451.2	46.4	447.4	8.9	446.7	5.5	1.0
11NC47-26.1	210	1.03	0.05571	0.00176	0.06897	0.00061	445.1	70.7	446.6	12.3	446.9	4.7	-0.4
11NC47-33.1	698	0.91	0.05633	0.00090	0.06994	0.00047	440.6	42.6	446.4	8.0	447.5	4.7	-1.6
11NC47-47.1	171	0.56	0.05629	0.00139	0.07072	0.00062	462.9	56.7	450.2	10.3	447.8	4.9	3.4
11NC47-40.1	209	0.93	0.05840	0.00160	0.08476	0.00086	464.4	63.6	450.6	11.8	448.0	6.2	3.7
11NC47-48.1	152	0.26	0.05605	0.00197	0.07055	0.00073	450.9	80.0	448.6	14.2	448.2	6.0	0.6
11NC47-36.1	3305	0.06	0.05687	0.00052	0.07038	0.00038	472.0	34.5	452.3	7.1	448.4	5.0	5.2
11NC47-32.1	459	0.54	0.05678	0.00107	0.06985	0.00052	456.2	46.2	450.1	8.5	448.9	4.5	1.7
11NC47-72.1	300	0.95	0.05885	0.00125	0.08440	0.00081	490.9	51.0	455.9	9.9	449.0	5.9	8.8
11NC47-41.1	290	0.26	0.05719	0.00113	0.07041	0.00064	490.3	47.2	455.9	8.9	449.1	4.8	8.7
11NC47-15.1	141	0.72	0.05595	0.00164	0.06899	0.00072	454.6	66.0	450.6	11.9	449.8	5.7	1.1
11NC47-49.2r	611	0.32	0.05761	0.00075	0.08584	0.00073	466.5	32.9	453.0	6.9	450.3	5.1	3.6
11NC47-67.2c	639	0.27	0.05731	0.00100	0.09112	0.00142	449.8	47.4	450.9	10.6	451.1	8.6	-0.3
11NC47-69.1	149	0.54	0.05724	0.00155	0.08344	0.00096	460.6	61.6	452.8	11.6	451.3	6.5	2.1
11NC47-59.1	258	1.02	0.05791	0.00139	0.08420	0.00090	460.6	56.0	453.1	10.6	451.6	6.0	2.0
11NC47-27.1	589	0.43	0.05726	0.00102	0.06911	0.00052	495.4	43.0	459.1	8.2	451.9	4.6	9.1

Table D.1: *continued*

Spot Name	U (ppm)	^{232}Th/ ^{238}U	^{207}Pb/^{206}Pb	±1σ	^{206}Pb/^{238}U	±1σ (%)	^{207}Pb/^{206}Pb Age (Ma)	±1σ	^{207}Pb/^{235}Pb Age (Ma)	±1σ	^{206}Pb/^{238}Pb Age (Ma)	±1σ	% Discordant
Sandstone – Middle stratigraphic level continued													
11NC47-34.1	1508	0.18	0.05656	0.00073	0.07098	0.00041	454.9	37.7	452.4	7.3	451.9	4.6	0.7
11NC47-55.1	475	0.91	0.05736	0.00105	0.08530	0.00082	458.9	44.2	453.1	8.7	452.0	5.6	1.6
11NC47-56.1	279	0.46	0.05712	0.00122	0.08575	0.00096	454.9	51.1	452.7	10.1	452.3	6.6	0.6
11NC47-14.1	520	1.26	0.05571	0.00106	0.06930	0.00061	447.0	45.7	451.5	8.6	452.3	5.0	-1.2
11NC47-18.1	271	0.36	0.05797	0.00102	0.08858	0.00093	457.0	41.8	453.2	8.5	452.5	5.9	1.0
11NC47-42.1	1729	0.50	0.05598	0.00062	0.07058	0.00033	449.9	36.4	452.1	6.8	452.5	3.9	-0.6
11NC47-35.2c	159	0.25	0.05697	0.00148	0.09280	0.00159	457.2	60.7	453.3	12.7	452.6	9.2	1.0
11NC47-63.1	126	0.31	0.05776	0.00144	0.08352	0.00078	439.1	57.5	450.5	10.6	452.8	5.7	-3.2
11NC47-8.2c	365	0.35	0.05710	0.00094	0.09480	0.00123	473.2	41.9	456.4	9.6	453.1	7.7	4.4
11NC47-8.1	183	0.49	0.05716	0.00114	0.07032	0.00058	466.5	46.1	455.4	8.5	453.2	4.4	3.0
11NC47-31.1	656	0.46	0.05671	0.00115	0.07021	0.00056	450.9	49.6	452.8	9.1	453.2	4.8	-0.5
11NC47-2.2c	222	0.05	0.05673	0.00139	0.09634	0.00144	459.0	57.0	455.4	11.7	454.7	8.1	1.0
11NC47-62.1	85	0.61	0.05862	0.00165	0.08368	0.00070	467.7	63.6	457.2	11.6	455.2	5.4	2.8
11NC47-29.1	277	0.37	0.05781	0.00126	0.08729	0.00089	441.5	51.4	452.9	9.7	455.2	5.6	-3.2
11NC47-25.1	172	1.07	0.05604	0.00170	0.07100	0.00056	468.2	68.3	457.5	12.1	455.4	4.4	2.8
11NC47-28.1	156	0.81	0.05661	0.00169	0.06930	0.00069	456.5	67.6	455.6	12.2	455.4	5.5	0.2
11NC47-4.1	279	0.86	0.05757	0.00160	0.08820	0.00100	456.8	65.5	455.9	12.2	455.8	6.4	0.2
11NC47-7.1	139	0.75	0.05768	0.00152	0.08908	0.00094	442.0	60.4	453.7	11.2	455.9	5.8	-3.3
11NC47-1.1	222	0.97	0.05801	0.00116	0.09097	0.00097	471.4	48.1	458.7	9.5	456.2	6.0	3.3
11NC47-39.1	478	0.34	0.05649	0.00095	0.07235	0.00047	451.8	40.3	456.4	7.5	457.3	4.1	-1.3
11NC47-54.1r	1257	0.32	0.05764	0.00063	0.08601	0.00084	464.0	32.3	458.8	7.2	457.7	5.7	1.4
11NC47-58.1	261	0.60	0.05771	0.00131	0.08603	0.00105	462.9	52.6	458.7	10.4	457.9	6.6	1.1
11NC47-61.1	226	0.64	0.05822	0.00110	0.08473	0.00091	455.7	44.5	459.0	8.9	459.6	5.9	-0.9
11NC47-34.1	882	0.43	0.05934	0.00102	0.08696	0.00091	471.0	44.6	461.7	9.1	459.9	6.2	2.4
11NC47-29.1	1123	0.36	0.05687	0.00068	0.07062	0.00037	462.5	31.8	461.9	6.2	461.8	3.8	0.2
11NC47-30.1	764	0.73	0.05815	0.00087	0.07109	0.00038	507.6	38.9	470.4	7.5	462.8	4.1	9.2
11NC47-3.1	1198	0.35	0.05881	0.00065	0.09148	0.00095	512.1	34.8	475.7	8.0	468.2	6.3	8.9
11NC47-36.2c	804	0.16	0.05821	0.00079	0.09612	0.00131	494.4	37.1	475.5	9.2	471.6	8.0	4.8
11NC47-1.1	263	0.47	0.05773	0.00184	0.07446	0.00060	504.4	72.6	488.8	13.7	485.5	5.4	3.9
11NC47-16.1	709	0.28	0.05973	0.00080	0.09889	0.00081	521.2	35.5	503.4	8.0	499.5	5.8	4.3
Sandstone – Basal stratigraphic level													
11NC25-53.1c	499	0.75	0.05536	0.00078	0.05370	0.00071	398.7	32.8	401.4	6.7	401.9	5.5	-0.8
11NC25-44.1	352	0.28	0.05617	0.00076	0.05614	0.00036	444.8	32.0	424.1	5.7	420.4	3.2	5.7
11NC25-21.1	444	0.53	0.05714	0.00101	0.08789	0.00094	458.0	45.8	426.3	9.4	420.4	7.1	8.5
11NC25-22.1	750	0.76	0.05641	0.00064	0.05764	0.00035	422.0	31.2	424.0	5.7	424.4	3.5	-0.6

Table D.1: *continued*

Spot Name	U (ppm)	^{232}Th/ ^{238}U	^{207}Pb/^{206}Pb	±1σ	^{206}Pb/^{238}U	±1σ (%)	^{207}Pb/^{206}Pb Age (Ma)	±1σ	^{207}Pb/^{235}Pb Age (Ma)	±1σ	^{206}Pb/^{238}Pb Age (Ma)	±1σ	% Discordant
Sandstone – Basal stratigraphic level continued													
11NC25-22.1	473	0.76	0.05724	0.00103	0.08967	0.00099	461.4	46.6	431.4	9.7	425.9	7.3	8.0
11NC25-29.1	859	0.81	0.05725	0.00139	0.08432	0.00097	415.1	63.8	426.3	12.0	428.3	7.9	-3.3
11NC25-3.1	465	0.69	0.05623	0.00098	0.09267	0.00098	418.3	47.1	426.9	9.0	428.5	6.1	-2.5
11NC25-43.1	510	0.71	0.05600	0.00059	0.05736	0.00026	429.3	25.6	428.8	4.5	428.8	2.5	0.1
11NC25-40.1c	549	0.52	0.05730	0.00052	0.05718	0.00026	443.9	22.3	431.6	4.2	429.3	2.8	3.4
11NC25-17.1	536	0.42	0.05554	0.00055	0.05955	0.00040	411.0	25.2	426.7	4.9	429.6	3.6	-4.7
11NC25-64.1	524	0.61	0.05660	0.00082	0.05828	0.00033	441.2	35.2	433.3	6.3	431.8	3.3	2.2
11NC25-24.1	526	0.67	0.05622	0.00067	0.05857	0.00033	416.4	29.4	429.9	5.3	432.4	3.0	-4.0
11NC25-9.1	449	0.39	0.05643	0.00080	0.05856	0.00038	455.6	36.2	437.2	6.7	433.7	3.9	5.0
11NC25-61.1	962	0.89	0.05679	0.00069	0.05929	0.00055	420.5	31.0	431.8	6.4	433.9	4.8	-3.3
11NC25-24.1	347	1.14	0.05708	0.00159	0.08713	0.00106	444.4	66.2	437.7	12.4	436.4	7.4	1.8
11NC25-59.1	725	0.79	0.05730	0.00086	0.06028	0.00073	435.0	36.0	436.2	7.5	436.5	5.7	-0.4
11NC25-58.2r	500	0.68	0.05726	0.00067	0.06064	0.00078	442.9	29.6	438.6	6.9	437.8	6.0	1.2
11NC25-58.1c	484	0.61	0.05683	0.00086	0.06055	0.00059	438.7	35.8	438.3	7.0	438.2	4.8	0.1
11NC25-25.1	427	1.07	0.05697	0.00118	0.08731	0.00078	431.7	50.7	437.2	9.5	438.2	5.8	-1.6
11NC25-37.1	208	0.62	0.05682	0.00080	0.06077	0.00029	447.0	32.4	440.1	5.8	438.8	3.0	1.9
11NC25-71.1	298	0.51	0.05605	0.00096	0.05892	0.00042	430.8	40.7	437.6	7.3	438.9	3.8	-1.9
11NC25-6.1c	173	0.95	0.05703	0.00152	0.09172	0.00092	440.0	62.6	439.1	11.4	438.9	6.1	0.2
11NC25-30.1	707	0.65	0.05848	0.00141	0.08700	0.00097	447.1	62.0	442.2	11.7	441.3	7.1	1.3
11NC25-40.2r	642	0.23	0.05690	0.00047	0.05903	0.00027	434.9	20.6	440.7	4.0	441.8	2.6	-1.6
11NC25-27.1r	511	0.86	0.05717	0.00116	0.08764	0.00090	423.4	51.3	439.4	9.8	442.4	6.3	-4.7
11NC25-70.1	509	0.39	0.05700	0.00078	0.05895	0.00039	465.2	34.0	446.3	6.4	442.7	3.6	5.0
11NC25-38.1	289	0.68	0.05679	0.00074	0.06069	0.00032	436.6	29.8	442.7	5.4	443.9	3.0	-1.7
11NC25-23.2c	797	0.61	0.05706	0.00078	0.09060	0.00091	453.0	40.0	446.0	8.8	444.7	7.0	1.9
11NC25-9.1r	548	0.80	0.05716	0.00133	0.09146	0.00107	444.5	61.6	444.9	11.9	445.0	7.7	-0.1
11NC25-39.1	329	1.30	0.05708	0.00071	0.06014	0.00034	438.6	29.0	444.6	5.4	445.8	3.3	-1.7
11NC25-32.1	1082	1.01	0.05845	0.00107	0.08844	0.00096	450.4	55.3	447.2	10.7	446.5	6.8	0.9
11NC25-33.1	396	0.65	0.05743	0.00181	0.08883	0.00104	447.0	74.7	446.9	13.5	446.8	6.8	0.0
11NC25-65.1	837	0.87	0.05710	0.00066	0.05976	0.00036	460.5	29.3	449.1	5.6	446.9	3.5	3.0
11NC25-55.1	117	0.42	0.05677	0.00104	0.06072	0.00067	448.8	41.9	448.8	8.2	448.8	5.3	0.0
11NC25-51.1	484	1.24	0.05645	0.00070	0.06073	0.00065	451.3	29.9	449.3	6.6	448.9	5.3	0.5
11NC25-11.1	584	0.58	0.05680	0.00105	0.09268	0.00087	443.1	50.3	448.0	9.9	449.0	6.7	-1.4
11NC25-57.1r	557	0.84	0.05736	0.00060	0.06198	0.00060	471.9	27.3	453.0	6.2	449.2	5.1	5.0
11NC25-66.1	740	0.60	0.05708	0.00065	0.05980	0.00028	451.3	28.5	450.8	5.3	450.7	2.8	0.1
11NC25-60.1	353	0.70	0.05734	0.00093	0.06208	0.00067	439.2	38.1	449.3	7.7	451.3	5.3	-2.8
11NC25-20.2r	1307	0.19	0.05758	0.00066	0.09246	0.00084	475.4	32.3	455.9	7.5	452.0	6.3	5.1

Table D.1: *continued*

Spot Name	U (ppm)	^{232}Th/ ^{238}U	^{207}Pb/^{206}Pb	±1σ	^{206}Pb/^{238}U	±1σ (%)	^{207}Pb/^{206}Pb Age (Ma)	±1σ	^{207}Pb/^{235}Pb Age (Ma)	±1σ	^{206}Pb/^{238}Pb Age (Ma)	±1σ	% Discordant
Sandstone – Basal stratigraphic level continued													
11NC25-54.1	284	0.45	0.05676	0.00071	0.06068	0.00046	442.2	29.8	450.6	5.9	452.3	4.0	-2.4
11NC25-47.2r	640	0.50	0.05744	0.00081	0.06080	0.00053	459.2	33.2	454.2	6.7	453.2	4.5	1.4
11NC25-12.2r	1127	0.57	0.05642	0.00050	0.06260	0.00039	462.9	24.3	455.4	5.2	453.9	4.0	2.0
11NC25-63.1	417	0.66	0.05720	0.00087	0.06154	0.00056	456.3	36.0	454.5	7.2	454.1	4.7	0.5
11NC25-67.1	328	0.72	0.05790	0.00078	0.05987	0.00036	474.3	32.9	458.1	6.2	454.9	3.4	4.2
11NC25-28.1	798	0.74	0.05810	0.00129	0.08989	0.00108	461.9	58.9	456.1	12.1	455.0	8.5	1.6
11NC25-53.2r	299	0.39	0.05695	0.00071	0.06080	0.00054	452.2	29.6	454.6	6.2	455.0	4.5	-0.6
11NC25-12.1c	1298	1.05	0.05626	0.00052	0.06269	0.00029	457.4	25.1	456.0	5.1	455.8	3.6	0.4
11NC25-49.1	408	0.78	0.05705	0.00092	0.06170	0.00058	456.0	40.5	455.9	8.0	455.9	5.3	0.0
11NC25-46.1	212	0.35	0.05731	0.00104	0.06106	0.00056	475.4	40.8	459.5	7.9	456.3	4.5	4.2
11NC25-10.1	450	0.53	0.05762	0.00152	0.09407	0.00108	468.6	64.1	458.4	12.3	456.4	7.1	2.7
11NC25-1.1	397	0.54	0.05660	0.00089	0.06265	0.00074	462.7	37.5	457.5	8.0	456.5	6.0	1.4
11NC25-26.1	270	0.94	0.05755	0.00149	0.09091	0.00114	445.5	61.6	454.8	11.8	456.6	7.1	-2.6
11NC25-13.1	562	0.57	0.05636	0.00114	0.09332	0.00108	439.2	50.0	454.7	10.0	457.7	6.8	-4.4
11NC25-17.1	362	0.88	0.05715	0.00113	0.09228	0.00115	450.0	48.6	456.6	10.1	458.0	7.2	-1.8
11NC25-11.1	708	1.08	0.05636	0.00067	0.06277	0.00033	459.6	30.1	458.7	5.8	458.6	3.6	0.2
11NC25-12.1	345	0.66	0.05685	0.00133	0.09423	0.00107	455.2	58.6	458.1	11.5	458.7	7.3	-0.8
11NC25-56.1r	306	0.57	0.05745	0.00073	0.06272	0.00045	481.9	31.3	463.0	6.4	459.2	4.3	4.9
11NC25-56.2c	860	0.91	0.05602	0.00166	0.07676	0.00094	465.9	73.4	460.5	13.8	459.5	7.4	1.4
11NC25-27.2c	2015	1.21	0.05795	0.00064	0.09099	0.00097	454.9	35.9	458.8	8.4	459.6	7.0	-1.1
11NC25-52.1	288	0.58	0.05728	0.00061	0.06216	0.00067	483.8	25.7	464.9	6.3	461.0	5.4	4.9
11NC25-45.1	279	0.38	0.05722	0.00067	0.06174	0.00042	483.1	28.2	464.9	5.7	461.2	3.7	4.7
11NC25-15.2r	505	0.34	0.05649	0.00064	0.06376	0.00046	453.5	28.2	460.1	5.7	461.4	3.9	-1.8
11NC25-13.1	480	0.71	0.05678	0.00070	0.06379	0.00034	474.5	30.3	465.2	5.9	463.3	3.4	2.4
11NC25-16.1	506	0.80	0.05686	0.00067	0.06434	0.00039	465.8	28.9	463.8	5.7	463.5	3.6	0.5
11NC25-23.1	617	0.79	0.05720	0.00061	0.06307	0.00034	454.0	27.5	462.1	5.3	463.7	3.2	-2.2
11NC25-50.1	608	0.60	0.05686	0.00072	0.06280	0.00065	458.0	31.6	462.8	6.9	463.7	5.4	-1.3
11NC25-9.2c	885	1.04	0.05838	0.00104	0.09831	0.00134	460.6	48.6	463.8	10.9	464.4	8.7	-0.9
11NC25-19.1c	1018	0.01	0.05722	0.00045	0.06426	0.00033	477.7	19.9	467.4	4.2	465.3	3.1	2.7
11NC25-4.1	430	0.87	0.05718	0.00086	0.06097	0.00082	446.9	37.2	463.0	8.5	466.3	7.0	-4.5
11NC25-16.1c	276	0.97	0.05723	0.00145	0.09449	0.00119	465.2	58.5	466.5	11.6	466.8	7.0	-0.4
11NC25-57.2c	214	0.51	0.05657	0.00284	0.07808	0.00155	483.4	112.7	469.8	21.4	467.0	10.2	3.5
11NC25-20.1	881	0.19	0.05701	0.00048	0.06430	0.00035	457.1	23.0	466.9	4.7	468.9	3.2	-2.7
11NC25-10.1	698	1.12	0.05617	0.00069	0.06403	0.00043	450.7	32.7	466.6	6.6	469.8	4.4	-4.4
11NC25-19.2r	367	0.04	0.05758	0.00080	0.06464	0.00044	485.8	32.3	473.0	6.4	470.4	3.7	3.3

Table D.1: *continued*

Spot Name	U (ppm)	^{232}Th/ ^{238}U	^{207}Pb/^{206}Pb	±1σ	^{206}Pb/^{238}U	±1σ (%)	^{207}Pb/^{206}Pb Age (Ma)	±1σ	^{207}Pb/^{235}Pb Age (Ma)	±1σ	^{206}Pb/^{238}Pb Age (Ma)	±1σ	% Discordant
Sandstone – Basal stratigraphic level continued													
11NC25-14.1	326	0.66	0.05691	0.00130	0.09527	0.00134	464.4	54.8	469.4	11.5	470.4	8.0	-1.3
11NC25-8.1	1237	0.27	0.05853	0.00070	0.09904	0.00102	492.3	43.0	482.3	9.9	480.2	7.8	2.5
11NC25-48.2r	336	0.44	0.05848	0.00104	0.06500	0.00064	500.5	43.2	484.2	9.0	480.7	5.7	4.1
11NC25-48.1c	608	0.55	0.05798	0.00073	0.06500	0.00076	480.7	31.1	481.8	7.4	482.0	6.1	-0.3
11NC25-5.1	356	0.65	0.05769	0.00078	0.06395	0.00059	475.4	32.3	482.0	7.0	483.4	5.1	-1.7
11NC25-8.1	232	0.54	0.05769	0.00090	0.06733	0.00049	500.6	36.8	497.6	7.5	496.9	4.3	0.8
11NC25-7.1	428	0.90	0.06022	0.00065	0.08161	0.00056	590.5	25.9	596.7	6.6	598.3	4.8	-1.4
11NC25-42.1	69	1.04	0.06620	0.00124	0.10250	0.00086	783.0	40.2	755.7	11.4	746.5	6.5	4.9
11NC25-18.1	120	0.56	0.06720	0.00096	0.11664	0.00078	822.8	31.1	819.8	9.5	818.8	6.1	0.5
11NC25-19.1	64	0.26	0.07264	0.00219	0.19614	0.00281	965.7	63.3	960.0	22.3	957.5	15.8	0.9
11NC25-21.1	94	0.93	0.07460	0.00143	0.14144	0.00109	1020.5	41.9	1000.8	14.6	991.9	9.0	3.0
11NC25-69.1	830	0.21	0.07480	0.00042	0.13737	0.00073	1028.7	17.0	1005.1	7.0	994.3	6.4	3.6
11NC25-1.1	107	0.76	0.07384	0.00121	0.23050	0.00250	1011.2	37.6	1001.2	15.1	996.6	13.6	1.6
11NC25-2.1	33	0.79	0.07461	0.00295	0.23450	0.00373	1025.7	80.3	1023.9	28.5	1023.0	17.3	0.3
11NC25-4.1	55	0.88	0.07730	0.00221	0.24208	0.00261	1083.1	61.5	1083.4	22.8	1083.5	14.9	0.0
11NC25-2.1	383	0.29	0.07876	0.00076	0.16011	0.00173	1140.0	23.0	1132.0	11.7	1127.8	13.0	1.2
11NC25-41.1	29	0.87	0.09485	0.00178	0.20620	0.00190	1485.6	36.4	1449.1	16.8	1424.4	12.9	4.6
11NC25-7.1	268	0.31	0.11443	0.00106	0.39760	0.00362	1824.8	27.3	1778.3	17.3	1738.9	21.6	5.4
11NC25-5.1	125	0.99	0.17175	0.00163	0.59831	0.00693	2535.7	23.2	2484.2	18.8	2421.8	29.9	5.4
11NC25-62.1	189	0.42	0.18428	0.00181	0.41504	0.00455	2653.1	19.7	2619.2	16.5	2575.6	27.5	3.5

Table D.1: *continued*

Spot Name	U (ppm)	^{232}Th/ ^{238}U	^{207}Pb/^{206}Pb	±1σ	^{206}Pb/^{238}U	±1σ (%)	^{207}Pb/^{206}Pb Age (Ma)	±1σ	^{207}Pb/^{235}Pb Age (Ma)	±1σ	^{206}Pb/^{238}Pb Age (Ma)	±1σ	% Discordant
Upper stratigraphic level – Deformed clasts													
11NC16D-2.1	17	2.74	0.05549	0.00526	0.06800	0.00143	367.8	201.4	372.3	30.1	373.0	8.4	-1.4
11NC16D-6.1	48	0.93	0.05595	0.00263	0.06951	0.00091	381.7	104.5	378.5	15.8	378.0	5.7	1.0
11NC16D-20.1	390	0.64	0.05560	0.00096	0.07012	0.00068	385.2	43.4	384.2	7.6	384.0	5.0	0.3
11NC16D-56.1	802	0.43	0.05581	0.00048	0.05312	0.00025	393.9	24.9	386.3	4.9	385.0	3.9	2.3
11NC16D-32.1	728	0.54	0.05510	0.00058	0.05240	0.00036	388.3	26.9	385.6	5.0	385.2	3.7	0.8
11NC16D-27.1	919	0.50	0.05620	0.00091	0.07207	0.00084	391.0	41.5	386.6	7.7	385.9	5.6	1.3
11NC16D-54.1	1357	0.31	0.05497	0.00030	0.05224	0.00023	372.2	19.9	384.0	4.3	386.0	3.7	-3.8
11NC16D-31.1	1020	0.55	0.05543	0.00050	0.05242	0.00031	391.9	23.2	387.9	4.5	387.2	3.5	1.2
11NC16D-59.1	30	2.66	0.05540	0.00297	0.05467	0.00073	389.1	117.2	390.0	18.2	390.2	6.3	-0.3
11NC16D-57.1	84	1.24	0.05603	0.00120	0.05450	0.00040	402.5	50.0	392.1	8.3	390.4	4.5	3.1
11NC16D-80.1	925	0.44	0.05529	0.00053	0.05307	0.00029	402.2	27.3	393.5	5.2	392.0	3.8	2.6
11NC16D-28.1	706	0.72	0.05567	0.00055	0.05227	0.00034	399.9	25.0	394.0	5.0	393.0	3.9	1.8
11NC16D-77.1	687	0.48	0.05548	0.00061	0.05275	0.00026	407.4	28.1	396.2	5.4	394.3	4.1	3.3
11NC16D-71.1	702	0.40	0.05580	0.00054	0.05284	0.00025	416.8	28.5	398.6	5.3	395.5	3.7	5.3
11NC16D-8.1	67	2.08	0.05632	0.00201	0.07324	0.00095	410.8	79.9	398.1	13.1	396.0	6.1	3.7
11NC16D-10.1	46	1.11	0.05524	0.00241	0.06254	0.00072	403.2	96.2	397.8	15.2	396.9	5.7	1.6
11NC16D-12.1	480	0.46	0.05510	0.00071	0.06194	0.00052	404.0	32.2	398.7	6.0	397.8	4.3	1.6
11NC16D-22.1	55	1.21	0.05525	0.00196	0.06108	0.00079	400.1	79.1	398.7	13.0	398.5	6.2	0.4
11NC16D-1.1c	219	2.97	0.05611	0.00137	0.07200	0.00088	413.8	58.4	401.2	10.2	399.0	6.1	3.7
11NC16D-79.1	1046	0.50	0.05569	0.00052	0.05339	0.00023	403.5	25.3	400.0	4.7	399.4	3.4	1.0
11NC16D-66.1	24	2.04	0.05615	0.00241	0.05245	0.00072	423.2	94.0	403.7	15.3	400.2	6.2	5.6
11NC16D-25.1	34	1.35	0.05494	0.00233	0.05280	0.00050	405.3	93.1	401.1	14.8	400.3	5.3	1.3
11NC16D-46.1	64	1.80	0.05605	0.00244	0.05352	0.00054	407.6	95.6	401.7	15.1	400.7	5.0	1.7
11NC16D-16.1	971	0.39	0.05556	0.00052	0.06161	0.00051	418.7	28.3	403.7	5.9	401.1	4.8	4.3
11NC16D-21.1	38	0.83	0.05496	0.00256	0.06208	0.00067	403.8	102.4	403.3	16.3	403.3	5.6	0.1
11NC16D-41.1	488	0.36	0.05504	0.00057	0.05451	0.00027	413.9	27.6	405.1	5.5	403.5	4.2	2.6
11NC16D-76.1	35	1.37	0.05516	0.00261	0.05436	0.00063	402.1	103.6	404.6	16.6	405.1	6.1	-0.8
11NC16D-55.1	15	2.40	0.05621	0.00295	0.05551	0.00087	416.0	113.9	407.1	18.5	405.6	7.0	2.6
11NC16D-1.1r	60	1.56	0.05635	0.00263	0.07370	0.00097	412.7	102.9	406.7	16.7	405.7	6.2	1.8
11NC16D-7.1	40	1.53	0.05542	0.00248	0.06468	0.00083	412.6	98.2	408.3	16.0	407.5	6.3	1.3
11NC16D-29.1	41	1.96	0.05619	0.00197	0.05443	0.00058	414.6	77.5	408.7	12.7	407.7	5.2	1.7
11NC16D-38.1	69	1.75	0.05524	0.00221	0.05456	0.00051	411.0	88.0	409.1	14.1	408.7	4.8	0.6
11NC16D-44.1	29	1.80	0.05577	0.00246	0.05518	0.00066	417.6	96.6	410.9	15.7	409.7	5.6	2.0
11NC16D-62.1c	678	0.06	0.05564	0.00074	0.05465	0.00023	418.7	33.2	412.2	5.8	411.1	3.4	1.9
11NC16D-49.1	54	1.23	0.05627	0.00234	0.05542	0.00054	421.2	91.4	412.8	14.8	411.3	5.1	2.4
11NC16D-20.1	49	1.13	0.05513	0.00188	0.06333	0.00076	415.7	76.1	412.4	12.7	411.8	5.8	1.0

Table D.2: Clast detrital zircon U-Pb LA-ICPMS geochronology data.

Spot Name	U (ppm)	^{232}Th/ ^{238}U	^{207}Pb/^{206}Pb	±1σ	^{206}Pb/^{238}U	±1σ (%)	^{207}Pb/^{206}Pb Age (Ma)	±1σ	^{207}Pb/^{235}Pb Age (Ma)	±1σ	^{206}Pb/^{238}Pb Age (Ma)	±1σ	% Discordant
Upper stratigraphic level – Deformed clasts continued													
11NC16D-23.1	58	0.96	0.05625	0.00220	0.06319	0.00082	429.5	86.2	416.4	14.5	414.0	6.4	3.7
11NC16D-62.2r	66	1.21	0.05569	0.00221	0.05416	0.00057	418.4	87.4	415.4	14.3	414.9	5.2	0.9
11NC16D-14.1	49	2.06	0.05570	0.00208	0.06414	0.00070	423.9	82.8	416.6	13.7	415.3	5.3	2.1
11NC16D-48.1	22	3.28	0.05656	0.00359	0.05565	0.00086	424.0	137.0	417.0	22.6	415.7	7.5	2.0
11NC16D-72.1	18	2.10	0.05616	0.00315	0.05561	0.00080	428.8	121.2	418.9	20.0	417.1	6.5	2.8
11NC16D-40.1	33	1.24	0.05520	0.00275	0.05638	0.00077	418.8	108.3	418.1	17.9	417.9	6.4	0.2
11NC16D-70.1	11	1.44	0.05632	0.00422	0.05620	0.00113	439.2	159.6	423.3	26.8	420.4	8.9	4.4
11NC16D-23.2c	1145	0.42	0.05681	0.00058	0.07954	0.00088	430.9	34.4	422.5	7.5	420.9	6.2	2.4
11NC16D-9.1	28	1.37	0.05603	0.00277	0.06708	0.00108	433.5	108.0	424.0	18.4	422.3	7.6	2.7
11NC16D-28.1	687	0.44	0.05770	0.00126	0.07909	0.00080	459.5	53.6	428.2	10.0	422.4	6.1	8.3
11NC16D-5.1	391	0.34	0.05695	0.00089	0.07798	0.00086	414.6	40.5	422.1	7.9	423.5	5.7	-2.2
11NC16D-19.1	46	1.04	0.05516	0.00274	0.06512	0.00102	422.1	108.9	423.5	18.4	423.7	7.5	-0.4
11NC16D-7.1	506	0.37	0.05724	0.00072	0.07852	0.00067	439.8	32.8	426.8	6.5	424.4	4.7	3.6
11NC16D-23.1r	362	0.47	0.05641	0.00107	0.08000	0.00087	426.4	49.3	425.7	9.3	425.6	6.2	0.2
11NC16D-26.1	77	2.19	0.05608	0.00150	0.05647	0.00056	441.5	59.4	428.8	10.5	426.4	5.3	3.5
11NC16D-8.1	26	1.50	0.05608	0.00320	0.06873	0.00097	437.1	123.1	433.0	20.9	432.3	6.9	1.1
11NC16D-3.1	1411	0.06	0.05553	0.00071	0.07586	0.00058	446.9	39.6	436.4	8.4	434.4	6.6	2.9
11NC16D-3.1	270	0.59	0.05786	0.00095	0.08044	0.00081	450.7	40.3	438.6	8.2	436.4	5.8	3.3
11NC16D-30.1c	207	0.52	0.05726	0.00097	0.05863	0.00028	450.9	39.4	439.2	7.3	437.0	4.3	3.2
11NC16D-58.1	444	0.88	0.05701	0.00067	0.06153	0.00038	447.3	29.8	439.7	6.1	438.3	4.5	2.1
11NC16D-13.1	267	0.46	0.05688	0.00115	0.07875	0.00089	430.7	48.7	437.4	9.5	438.7	6.4	-1.9
11NC16D-1.1	449	0.32	0.05534	0.00110	0.07723	0.00069	436.1	47.3	439.4	8.8	440.0	5.2	-0.9
11NC16D-13.1	598	0.57	0.05657	0.00050	0.06829	0.00048	461.9	24.5	443.9	5.4	440.5	4.4	4.8
11NC16D-45.1	441	0.73	0.05724	0.00067	0.05937	0.00029	460.5	29.3	444.8	5.8	441.8	3.8	4.2
11NC16D-36.1	261	0.81	0.05617	0.00109	0.05864	0.00034	436.2	47.1	441.4	8.4	442.4	4.2	-1.5
11NC16D-78.1	514	0.54	0.05729	0.00064	0.05899	0.00030	465.3	28.2	446.2	5.7	442.5	4.0	5.1
11NC16D-10.1	252	0.52	0.05825	0.00124	0.08113	0.00107	482.5	49.1	449.1	10.0	442.7	6.9	8.5
11NC16D-30.2r	80	0.46	0.05701	0.00163	0.05997	0.00053	444.9	63.6	443.5	11.3	443.3	5.4	0.4
11NC16D-33.1	457	0.66	0.05682	0.00057	0.06033	0.00031	463.8	26.1	446.9	5.3	443.7	3.8	4.5
11NC16D-35.1	886	1.10	0.05649	0.00055	0.05925	0.00030	445.4	29.5	444.7	5.9	444.5	4.1	0.2
11NC16D-37.1	637	0.67	0.05656	0.00070	0.05933	0.00032	457.5	31.4	447.3	6.0	445.3	3.8	2.8
11NC16D-4.1	763	0.49	0.05586	0.00115	0.07666	0.00069	455.1	53.3	448.4	10.7	447.1	7.2	1.8
11NC16D-12.1	922	0.62	0.05760	0.00072	0.08081	0.00079	452.9	34.3	449.4	7.8	448.7	6.4	1.0
11NC16D-24.1	1869	0.04	0.05681	0.00051	0.06862	0.00055	441.1	26.5	449.2	6.6	450.8	5.9	-2.3
11NC16D-17.1	1032	0.31	0.05663	0.00046	0.06970	0.00058	469.0	24.9	455.1	6.0	452.4	5.2	3.7
11NC16D-18.1	693	0.47	0.05659	0.00062	0.06981	0.00058	475.7	30.7	457.2	6.9	453.5	5.6	4.8

Table D.2: *continued*

Spot Name	U (ppm)	^{232}Th/ ^{238}U	^{207}Pb/^{206}Pb	±1σ	^{206}Pb/^{238}U	±1σ (%)	^{207}Pb/^{206}Pb Age (Ma)	±1σ	^{207}Pb/^{235}Pb Age (Ma)	±1σ	^{206}Pb/^{238}Pb Age (Ma)	±1σ	% Discordant
Upper stratigraphic level – Deformed clasts continued													
11NC16D-50.1	219	0.78	0.05722	0.00081	0.06192	0.00037	466.9	34.2	456.9	6.7	454.9	4.3	2.7
11NC16D-15.1	266	0.52	0.05627	0.00085	0.07040	0.00054	442.6	38.1	453.1	7.6	455.1	5.2	-2.9
11NC16D-52.1	227	0.62	0.05755	0.00070	0.06185	0.00033	484.5	29.8	460.0	6.0	455.2	4.0	6.3
11NC16D-5.1	639	0.53	0.05623	0.00108	0.07747	0.00072	463.6	48.1	459.9	9.7	459.2	6.5	1.0
11NC16D-6.1	683	0.84	0.05641	0.00109	0.07811	0.00089	464.9	48.8	469.8	10.2	470.8	7.1	-1.3
Upper stratigraphic level – Slightly deformed clasts													
11NC16S-12.1	739	0.85	0.05422	0.00143	0.05873	0.00072	358.5	61.6	371.1	9.6	373.1	5.1	-4.2
11NC16S-61.1	508	0.27	0.05518	0.00076	0.05031	0.00034	400.6	34.1	380.6	5.7	377.3	3.5	6.0
11NC16S-8.1	207	0.49	0.05465	0.00077	0.06086	0.00042	377.9	34.5	379.6	5.7	379.9	3.5	-0.5
11NC16S-63.1	636	0.26	0.05391	0.00078	0.05014	0.00033	370.1	36.0	379.5	5.8	381.1	3.3	-3.1
11NC16S-53.1	1974	0.49	0.05494	0.00063	0.05086	0.00033	395.2	39.1	385.3	6.4	383.7	3.6	3.0
11NC16S-100.1c	1991	0.53	0.05484	0.00053	0.05138	0.00031	413.5	30.7	388.1	5.6	383.9	3.9	7.4
11NC16S-60.1	484	0.27	0.05476	0.00080	0.05112	0.00043	392.0	35.8	385.9	6.1	384.9	3.8	1.9
11NC16S-9.1	530	0.55	0.05541	0.00065	0.06160	0.00062	404.0	32.4	388.5	6.3	385.9	4.9	4.6
11NC16S-100.2r	397	0.36	0.05385	0.00114	0.05160	0.00039	391.4	52.2	387.3	8.4	386.6	4.3	1.3
11NC16S-10.1	1006	0.50	0.05479	0.00068	0.06145	0.00044	376.8	34.2	386.1	6.1	387.7	4.2	-3.0
11NC16S-11.1	886	0.68	0.05505	0.00076	0.06131	0.00054	390.0	35.4	388.2	6.3	387.9	4.2	0.6
11NC16S-58.1	299	0.42	0.05462	0.00115	0.05152	0.00037	402.8	50.1	390.2	7.9	388.1	3.6	3.8
11NC16S-65.1	443	0.37	0.05390	0.00092	0.05073	0.00031	389.8	42.6	388.3	6.8	388.1	3.4	0.4
11NC16S-95.1	660	0.60	0.05520	0.00076	0.05253	0.00031	397.7	34.2	391.7	5.7	390.7	3.2	1.8
11NC16S-1.1	409	0.40	0.05552	0.00077	0.06158	0.00046	407.4	33.5	393.9	5.9	391.6	3.8	4.0
11NC16S-87.1	768	0.48	0.05542	0.00060	0.05261	0.00029	388.4	27.5	391.4	4.7	391.9	3.0	-1.0
11NC16S-27.1	1237	0.65	0.05524	0.00073	0.06159	0.00047	390.7	35.1	391.9	6.2	392.1	4.2	-0.4
11NC16S-91.1	737	0.51	0.05517	0.00088	0.05128	0.00025	378.2	46.0	391.4	7.4	393.6	3.8	-4.2
11NC16S-67.1	922	0.35	0.05474	0.00069	0.05267	0.00032	404.9	31.4	395.3	5.4	393.7	3.3	2.8
11NC16S-36.1	1325	0.32	0.05527	0.00070	0.06103	0.00044	382.2	35.2	392.0	6.3	393.7	4.3	-3.1
11NC16S-70.1	661	0.27	0.05550	0.00066	0.05336	0.00039	418.9	31.1	397.9	5.6	394.3	3.7	6.1
11NC16S-1.1	592	0.46	0.05517	0.00077	0.06288	0.00078	389.1	34.0	394.1	6.8	394.9	5.4	-1.6
11NC16S-21.1	678	0.36	0.05527	0.00091	0.06033	0.00053	406.0	42.4	396.6	7.4	394.9	4.6	2.8
11NC16S-82.1	1217	0.77	0.05474	0.00059	0.05252	0.00034	381.0	31.3	393.1	5.4	395.2	3.4	-3.8
11NC16S-74.1	873	0.29	0.05505	0.00060	0.05288	0.00032	405.8	27.7	396.8	4.9	395.3	3.2	2.7
11NC16S-75.1	1204	0.51	0.05547	0.00049	0.05255	0.00030	421.9	24.1	399.2	4.4	395.3	3.0	6.5
11NC16S-64.1	421	0.28	0.05463	0.00103	0.05159	0.00033	414.8	46.1	398.2	7.5	395.3	3.5	4.8
11NC16S-34.1	629	0.41	0.05605	0.00092	0.06099	0.00047	414.3	41.2	398.2	7.0	395.5	4.0	4.7
11NC16S-72.1	769	0.22	0.05473	0.00068	0.05342	0.00032	389.5	31.0	394.8	5.3	395.7	3.1	-1.7
11NC16S-24.1	779	0.27	0.05502	0.00063	0.06168	0.00039	393.6	29.5	396.4	5.3	396.9	3.6	-0.9

Table D.2: *continued*

Spot Name	U (ppm)	^{232}Th/ ^{238}U	^{207}Pb/^{206}Pb	±1σ	^{206}Pb/^{238}U	±1σ (%)	^{207}Pb/^{206}Pb Age (Ma)	±1σ	^{207}Pb/^{235}Pb Age (Ma)	±1σ	^{206}Pb/^{238}Pb Age (Ma)	±1σ	% Discordant
Upper stratigraphic level – Slightly deformed clasts continued													
11NC16S-89.1	359	0.85	0.05600	0.00085	0.05309	0.00040	418.9	37.0	400.4	6.3	397.2	3.6	5.4
11NC16S-76.1	359	0.44	0.05517	0.00101	0.05269	0.00039	408.9	44.1	400.2	7.3	398.7	3.7	2.6
11NC16S-23.1	615	0.39	0.05515	0.00072	0.06170	0.00050	403.6	33.3	399.6	6.0	398.9	4.1	1.2
11NC16S-99.1	876	0.37	0.05557	0.00087	0.05311	0.00043	425.7	39.9	403.2	7.0	399.3	4.2	6.4
11NC16S-56.1	753	0.40	0.05549	0.00058	0.05402	0.00034	438.4	27.4	405.4	4.9	399.6	3.1	9.1
11NC16S-73.1	624	0.23	0.05585	0.00070	0.05389	0.00035	437.0	30.9	405.2	5.5	399.6	3.4	8.8
11NC16S-37.1	1874	0.49	0.05536	0.00067	0.06131	0.00043	400.9	35.4	399.9	6.3	399.7	4.2	0.3
11NC16S-92.1	1161	0.74	0.05546	0.00081	0.05215	0.00037	393.9	43.8	399.0	7.4	399.9	4.4	-1.5
11NC16S-33.1	2494	0.51	0.05525	0.00055	0.06120	0.00059	389.7	32.2	398.4	6.2	399.9	4.7	-2.7
11NC16S-3.1	1270	0.36	0.05574	0.00074	0.06283	0.00110	381.7	33.4	397.3	7.9	400.0	7.3	-5.0
11NC16S-93.1	367	0.52	0.05547	0.00105	0.05292	0.00038	401.3	47.0	400.5	7.7	400.3	3.8	0.3
11NC16S-90.1	459	0.77	0.05613	0.00086	0.05291	0.00040	420.7	39.8	403.7	6.8	400.7	3.9	4.9
11NC16S-16.1	1581	0.59	0.05462	0.00071	0.06200	0.00053	386.8	34.3	399.1	6.3	401.3	4.5	-3.8
11NC16S-83.1	839	0.86	0.05552	0.00077	0.05367	0.00028	404.0	36.1	402.2	6.0	401.9	3.1	0.5
11NC16S-51.1	776	0.28	0.05441	0.00090	0.06153	0.00042	397.7	41.1	401.7	6.9	402.3	3.8	-1.2
11NC16S-26.1	1010	0.57	0.05603	0.00063	0.06190	0.00053	419.1	29.6	405.3	5.8	402.9	4.3	4.0
11NC16S-14.1	578	0.49	0.05494	0.00084	0.06304	0.00057	402.6	38.0	403.0	6.8	403.1	4.3	-0.1
11NC16S-31.1	793	0.41	0.05474	0.00083	0.06121	0.00044	403.6	39.6	403.5	6.8	403.4	3.8	0.0
11NC16S-18.1	471	0.39	0.05615	0.00117	0.06182	0.00056	421.0	49.1	407.2	8.5	404.8	4.7	4.0
11NC16S-3.1	1149	0.28	0.05546	0.00062	0.06353	0.00063	422.7	31.6	408.0	6.3	405.4	4.8	4.2
11NC16S-59.1	1624	0.48	0.05529	0.00039	0.05377	0.00030	421.9	24.1	408.4	4.6	406.1	3.3	3.9
11NC16S-17.1	911	0.50	0.05585	0.00081	0.06246	0.00059	422.9	35.8	408.9	6.7	406.5	4.6	4.0
11NC16S-85.1	553	0.61	0.05604	0.00101	0.05424	0.00042	409.7	43.3	407.0	7.4	406.5	4.1	0.8
11NC16S-38.1	1207	0.33	0.05490	0.00082	0.06172	0.00048	397.7	44.5	405.3	7.8	406.7	4.9	-2.3
11NC16S-45.1	996	0.42	0.05433	0.00092	0.06205	0.00053	403.5	44.5	406.8	7.8	407.4	4.6	-1.0
11NC16S-55.1	472	0.38	0.05583	0.00069	0.05519	0.00038	444.9	32.1	413.7	5.7	408.2	3.4	8.5
11NC16S-52.1	204	1.55	0.05496	0.00157	0.06259	0.00059	420.4	65.1	411.2	10.7	409.5	4.3	2.7
11NC16S-32.1	707	0.49	0.05478	0.00084	0.06226	0.00057	391.6	41.5	407.3	7.4	410.0	4.7	-4.9
11NC16S-30.1	1127	0.38	0.05477	0.00090	0.06228	0.00047	418.0	42.9	411.6	7.4	410.5	4.2	1.9
11NC16S-20.1	707	0.60	0.05593	0.00101	0.06281	0.00059	421.1	43.5	413.0	7.8	411.6	4.7	2.3
11NC16S-79.1	1152	0.56	0.05584	0.00082	0.05407	0.00036	429.9	39.9	414.9	7.1	412.2	4.2	4.3
11NC16S-50.1	1047	0.28	0.05435	0.00070	0.06333	0.00045	407.6	35.0	411.7	6.4	412.4	4.2	-1.2
11NC16S-29.1	1733	0.47	0.05524	0.00061	0.06381	0.00064	430.5	33.3	417.7	6.6	415.4	5.0	3.6
11NC16S-49.1	483	0.29	0.05451	0.00102	0.06402	0.00065	426.6	44.9	417.5	8.1	415.8	4.8	2.6
11NC16S-41.1	1226	0.32	0.05576	0.00069	0.06292	0.00040	429.8	34.3	419.6	6.3	417.8	4.0	2.9
11NC16S-19.1	1469	0.63	0.05628	0.00071	0.06364	0.00065	423.4	32.8	418.7	6.7	417.8	5.2	1.4

Table D.2: *continued*

Spot Name	U (ppm)	^{232}Th/ ^{238}U	^{207}Pb/^{206}Pb	±1σ	^{206}Pb/^{238}U	±1σ (%)	^{207}Pb/^{206}Pb Age (Ma)	±1σ	^{207}Pb/^{235}Pb Age (Ma)	±1σ	^{206}Pb/^{238}Pb Age (Ma)	±1σ	% Discordant
Upper stratigraphic level – Slightly deformed clasts continued													
11NC16S-42.1	1123	0.29	0.05508	0.00067	0.06316	0.00043	402.5	33.5	415.9	6.1	418.3	4.0	-4.1
11NC16S-43.1	882	0.38	0.05570	0.00098	0.06349	0.00054	433.4	43.5	421.9	7.8	419.8	4.5	3.2
11NC16S-39.1	1284	0.29	0.05519	0.00084	0.06316	0.00055	418.6	44.8	419.8	8.2	420.1	5.2	-0.4
11NC16S-46.1	596	0.49	0.05458	0.00096	0.06446	0.00061	427.1	43.6	421.7	7.9	420.7	4.7	1.6
11NC16S-88.1	66	0.56	0.05642	0.00163	0.05723	0.00054	433.4	64.3	425.2	10.9	423.7	4.5	2.3
11NC16S-103.1	2213	0.69	0.05619	0.00056	0.05671	0.00027	474.1	33.4	441.8	6.5	435.6	4.3	8.4
11NC16S-6.1	41	0.48	0.05603	0.00143	0.07015	0.00061	445.6	56.7	437.6	9.9	436.1	4.4	2.2
11NC16S-94.1	169	0.64	0.05611	0.00144	0.05861	0.00045	434.1	58.5	436.0	10.0	436.3	4.2	-0.5
11NC16S-84.1	831	0.78	0.05681	0.00075	0.05867	0.00036	447.6	33.3	439.9	6.2	438.4	3.6	2.1
11NC16S-102.1	362	0.54	0.05536	0.00126	0.05759	0.00042	456.3	56.1	441.4	10.1	438.6	5.0	4.0
11NC16S-104.2r	239	0.39	0.05566	0.00133	0.05762	0.00037	420.8	55.3	437.3	9.5	440.5	3.9	-4.8
11NC16S-97.1	832	0.56	0.05631	0.00072	0.05896	0.00035	428.5	35.8	441.9	6.8	444.4	4.2	-3.9
11NC16S-77.1	529	0.52	0.05691	0.00090	0.05885	0.00045	475.6	39.4	451.5	7.5	446.8	4.3	6.3
11NC16S-96.1	594	0.57	0.05727	0.00085	0.06033	0.00045	473.0	36.6	454.2	7.1	450.6	4.2	4.9
11NC16S-22.1	976	0.64	0.05675	0.00068	0.06982	0.00062	471.9	33.7	455.1	7.1	451.8	5.2	4.4
11NC16S-47.1	590	0.66	0.05504	0.00106	0.07006	0.00063	459.7	46.9	454.8	8.8	453.8	4.8	1.3
11NC16S-54.1	69	0.57	0.05618	0.00242	0.06142	0.00076	451.9	95.4	455.8	16.9	456.6	6.0	-1.1
11NC16S-78.1	414	0.90	0.05662	0.00117	0.06018	0.00044	462.4	49.0	457.8	9.0	456.9	4.3	1.2
11NC16S-104.1c	197	0.29	0.05648	0.00158	0.05997	0.00050	469.6	63.9	460.6	11.5	458.8	4.8	2.4
Upper stratigraphic level – Undeformed clasts													
11NC16U-46.1	64	0.79	0.05455	0.00216	0.05247	0.00042	379.6	87.5	379.7	13.0	379.8	3.9	0.0
11NC16U-4.1	1283	0.27	0.05626	0.00051	0.07194	0.00059	389.7	26.9	382.7	5.4	381.5	4.5	2.2
11NC16U-6.1	121	1.73	0.05555	0.00163	0.07313	0.00079	384.1	66.7	384.3	10.7	384.3	5.4	-0.1
11NC16U-1.1	219	1.94	0.05638	0.00166	0.07188	0.00081	386.7	68.4	385.9	11.2	385.7	6.0	0.3
11NC16U-20.1	87	2.45	0.05567	0.00214	0.07156	0.00117	372.0	87.3	387.4	14.2	390.0	7.4	-5.0
11NC16U-28.1	330	0.52	0.05467	0.00079	0.05485	0.00061	380.8	34.6	388.8	6.7	390.1	5.2	-2.5
11NC16U-23.1	61	1.77	0.05629	0.00262	0.07152	0.00095	429.3	103.2	396.1	16.6	390.5	6.8	9.3
11NC16U-19.1	247	1.75	0.05673	0.00115	0.07174	0.00080	406.1	49.8	392.8	8.8	390.6	5.8	4.0
11NC16U-3.1	147	1.33	0.05664	0.00142	0.07320	0.00082	394.8	58.1	391.2	9.7	390.6	5.5	1.1
11NC16U-2.1	510	0.24	0.05447	0.00108	0.06511	0.00061	384.9	51.3	390.0	8.9	390.9	5.8	-1.6
11NC16U-11.1	341	0.52	0.05715	0.00087	0.07159	0.00069	391.9	37.2	391.2	7.1	391.0	5.3	0.2
11NC16U-17.1	555	0.46	0.05618	0.00077	0.07195	0.00065	392.8	35.9	392.3	6.8	392.2	5.1	0.1
11NC16U-48.1	441	0.52	0.05543	0.00078	0.05426	0.00030	401.0	35.6	393.6	6.2	392.3	3.8	2.2
11NC16U-2.1	168	0.88	0.05702	0.00160	0.07348	0.00092	410.8	64.2	395.7	10.8	393.1	6.0	4.5
11NC16U-8.1r	621	0.33	0.05613	0.00077	0.07331	0.00072	420.3	34.3	398.2	6.7	394.4	5.1	6.4
11NC16U-16.1	111	0.86	0.05453	0.00285	0.06648	0.00099	405.6	116.3	397.0	18.6	395.5	7.4	2.6

Table D.2: *continued*

Spot Name	U (ppm)	^{232}Th/ ^{238}U	^{207}Pb/^{206}Pb	±1σ	^{206}Pb/^{238}U	±1σ (%)	^{207}Pb/^{206}Pb Age (Ma)	±1σ	^{207}Pb/^{235}Pb Age (Ma)	±1σ	^{206}Pb/^{238}Pb Age (Ma)	±1σ	% Discordant
Upper stratigraphic level – Undeformed clasts continued													
11NC16U-16.1	35	1.17	0.05626	0.00293	0.07227	0.00099	391.6	114.4	395.4	18.0	396.1	6.5	-1.2
11NC16U-26.1	25	1.79	0.05640	0.00337	0.07316	0.00137	409.8	129.4	398.5	20.9	396.6	8.2	3.3
11NC16U-38.1	19	2.61	0.05495	0.00439	0.05487	0.00089	405.4	170.3	398.7	26.8	397.5	6.9	2.0
11NC16U-30.1	393	0.57	0.05498	0.00086	0.05557	0.00038	408.3	40.5	400.5	7.3	399.1	4.7	2.3
11NC16U-21.1	285	1.09	0.05602	0.00135	0.07334	0.00075	398.7	57.0	400.0	9.8	400.2	5.7	-0.4
11NC16U-52.1	76	0.58	0.05500	0.00221	0.05556	0.00062	395.0	89.1	401.8	14.2	403.0	5.3	-2.1
11NC16U-15.1	96	1.05	0.05656	0.00191	0.07333	0.00078	394.8	75.6	402.3	12.2	403.6	5.3	-2.3
11NC16U-31.1	193	1.00	0.05476	0.00164	0.05615	0.00055	402.1	68.9	405.1	11.4	405.6	5.5	-0.9
11NC16U-15.1	109	0.73	0.05394	0.00249	0.06844	0.00101	396.4	104.2	404.4	17.1	405.8	7.5	-2.4
11NC16U-50.1	129	1.46	0.05564	0.00157	0.05655	0.00043	412.7	63.7	407.4	10.3	406.4	4.1	1.6
11NC16U-51.1	177	1.12	0.05621	0.00140	0.05671	0.00053	440.7	56.9	411.8	9.6	406.6	4.7	8.0
11NC16U-22.1	54	1.08	0.05680	0.00304	0.06674	0.00132	414.0	118.4	408.2	19.9	407.2	9.3	1.7
11NC16U-1.1	221	0.44	0.05574	0.00175	0.06838	0.00079	447.7	72.6	414.4	12.7	408.5	6.8	9.0
11NC16U-33.1	139	1.38	0.05496	0.00119	0.05665	0.00051	400.9	50.1	408.4	8.5	409.7	4.6	-2.3
11NC16U-10.1	259	0.16	0.05554	0.00152	0.06716	0.00062	419.6	65.2	411.6	11.3	410.2	6.1	2.3
11NC16U-18.1	66	1.09	0.05553	0.00319	0.06770	0.00118	407.9	125.9	409.9	20.8	410.2	8.4	-0.6
11NC16U-44.1	173	2.61	0.05496	0.00108	0.05731	0.00034	416.3	45.8	412.0	7.9	411.2	4.4	1.3
11NC16U-27.1	164	2.00	0.05603	0.00087	0.05857	0.00043	423.3	36.4	413.4	6.7	411.6	4.3	2.8
11NC16U-47.1	121	1.29	0.05546	0.00121	0.05715	0.00038	409.6	49.6	412.1	8.3	412.6	3.8	-0.7
11NC16U-11.1	37	1.18	0.05518	0.00328	0.06781	0.00134	414.9	129.2	413.1	21.5	412.8	8.8	0.5
11NC16U-40.1	47	0.74	0.05493	0.00203	0.05680	0.00053	396.2	81.7	410.3	13.2	412.8	4.8	-4.3
11NC16U-42.1	230	2.12	0.05477	0.00127	0.05769	0.00047	410.5	55.0	413.4	9.9	413.9	6.1	-0.8
11NC16U-17.1	230	2.63	0.05534	0.00158	0.06909	0.00078	419.3	66.9	415.2	11.6	414.4	6.3	1.2
11NC16U-32.1	181	1.56	0.05525	0.00127	0.05762	0.00053	417.1	53.2	416.3	9.2	416.2	4.9	0.2
11NC16U-13.1	100	2.51	0.05515	0.00231	0.06945	0.00093	436.9	93.1	420.2	15.7	417.2	6.5	4.7
11NC16U-39.1	159	2.37	0.05513	0.00098	0.05758	0.00039	403.1	41.5	416.3	7.2	418.7	4.0	-4.0
11NC16U-8.1	148	1.21	0.05465	0.00205	0.06887	0.00066	413.7	84.7	418.6	14.1	419.5	5.8	-1.4
11NC16U-13.1c	646	0.38	0.05800	0.00069	0.07653	0.00078	418.2	29.5	419.6	6.4	419.9	5.4	-0.4
11NC16U-53.1	91	1.21	0.05570	0.00197	0.05744	0.00055	420.9	78.7	421.7	13.0	421.8	4.9	-0.2
11NC16U-49.1	383	2.59	0.05632	0.00084	0.05978	0.00047	434.7	37.0	430.7	7.1	429.9	4.8	1.1
11NC16U-54.1	158	1.91	0.05590	0.00157	0.05786	0.00054	426.7	64.0	430.0	11.1	430.6	5.2	-1.0
11NC16U-34.1	77	1.82	0.05578	0.00165	0.06060	0.00051	436.1	66.4	436.5	11.5	436.5	4.8	-0.1
Middle stratigraphic level – Deformed clasts													
11NC42D-13.1	580	0.46	0.05498	0.00083	0.06682	0.00063	356.7	37.8	368.1	6.4	370.0	4.4	-3.8
11NC42D-1.1	933	0.36	0.05423	0.00068	0.04697	0.00031	375.8	36.4	384.0	6.1	385.3	3.9	-2.6
11NC42D-42.1	1505	0.40	0.05538	0.00089	0.04733	0.00030	412.4	47.7	390.5	8.1	386.8	4.9	6.4

Table D.2: *continued*

Spot Name	U (ppm)	^{232}Th/ ^{238}U	^{207}Pb/^{206}Pb	±1σ	^{206}Pb/^{238}U	±1σ (%)	^{207}Pb/^{206}Pb Age (Ma)	±1σ	^{207}Pb/^{235}Pb Age (Ma)	±1σ	^{206}Pb/^{238}Pb Age (Ma)	±1σ	% Discordant
Middle stratigraphic level – Deformed clasts continued													
11NC42D-9.1	775	0.40	0.05563	0.00102	0.04749	0.00029	382.8	48.3	386.3	8.0	386.9	4.6	-1.1
11NC42D-10.1	683	0.32	0.05575	0.00108	0.04715	0.00033	384.2	50.0	387.3	8.3	387.8	4.7	-1.0
11NC42D-25.1	941	0.45	0.05458	0.00083	0.04742	0.00034	383.8	44.6	387.5	7.6	388.2	4.8	-1.2
11NC42D-4.1	968	0.62	0.05463	0.00070	0.04744	0.00031	385.6	37.0	387.9	6.6	388.3	4.5	-0.7
11NC42D-6.1	880	0.35	0.05522	0.00096	0.04771	0.00037	391.2	48.8	389.0	8.3	388.6	5.1	0.7
11NC42D-9.1	799	0.44	0.05563	0.00055	0.07072	0.00056	394.9	25.8	390.2	5.1	389.4	4.0	1.4
11NC42D-19.1	1133	0.49	0.05579	0.00070	0.06679	0.00049	403.9	33.7	392.0	6.1	390.0	4.1	3.6
11NC42D-24.1	2577	0.64	0.05487	0.00058	0.04740	0.00025	386.2	37.6	389.5	6.7	390.0	4.6	-1.0
11NC42D-26.1	473	0.47	0.05435	0.00163	0.04759	0.00036	373.6	70.2	387.8	10.9	390.2	4.4	-4.6
11NC42D-16.1	2011	0.83	0.05593	0.00050	0.06697	0.00043	376.9	28.1	388.8	5.3	390.8	4.0	-3.8
11NC42D-12.1	1490	0.62	0.05585	0.00054	0.07045	0.00051	405.4	28.1	392.9	5.4	390.8	4.1	3.7
11NC42D-30.1	761	0.29	0.05546	0.00107	0.04772	0.00033	397.4	48.6	392.1	7.9	391.2	4.0	1.6
11NC42D-3.1	564	0.40	0.05593	0.00075	0.06764	0.00062	384.9	33.8	390.4	6.2	391.3	4.5	-1.7
11NC42D-49.1	1253	0.49	0.05639	0.00132	0.04550	0.00098	383.1	61.1	390.3	11.9	391.5	9.2	-2.3
11NC42D-23.1	1466	0.96	0.05553	0.00053	0.06683	0.00045	410.5	26.2	395.5	4.9	392.9	3.5	4.4
11NC42D-5.1	657	0.34	0.05494	0.00090	0.04816	0.00032	389.3	43.7	392.5	7.4	393.1	4.4	-1.0
11NC42D-2.1	417	0.32	0.05517	0.00104	0.04800	0.00033	415.3	46.2	396.8	7.7	393.6	4.0	5.4
11NC42D-11.1	795	0.60	0.05496	0.00067	0.07097	0.00053	378.2	32.4	391.4	5.9	393.6	4.2	-4.2
11NC42D-8.1	928	0.39	0.05595	0.00100	0.04847	0.00036	401.2	46.9	395.3	8.0	394.3	4.7	1.8
11NC42D-20.1	295	0.32	0.05576	0.00125	0.06773	0.00050	408.7	51.9	396.9	8.4	394.9	3.9	3.5
11NC42D-38.1	631	0.62	0.05578	0.00069	0.06702	0.00044	412.7	32.2	397.5	5.8	394.9	3.9	4.4
11NC42D-32.1	1325	0.52	0.05563	0.00095	0.04828	0.00033	388.4	46.3	394.2	7.9	395.1	4.8	-1.8
11NC42D-41.1	1958	0.58	0.05476	0.00076	0.04826	0.00030	407.4	45.0	397.4	7.8	395.7	4.9	2.9
11NC42D-13.1	633	0.23	0.05538	0.00223	0.04738	0.00209	387.4	92.0	394.5	20.0	395.8	17.3	-2.2
11NC42D-40.1	1637	0.65	0.05445	0.00083	0.04793	0.00025	412.2	44.2	398.6	7.4	396.2	4.1	4.0
11NC42D-18.1	1504	0.41	0.05588	0.00065	0.06787	0.00049	392.5	32.3	395.7	5.9	396.3	4.2	-1.0
11NC42D-22.1	938	0.50	0.05575	0.00107	0.04751	0.00043	401.9	52.0	397.2	9.0	396.4	5.5	1.4
11NC42D-15.1	1154	0.86	0.05637	0.00077	0.06816	0.00046	400.4	36.0	397.3	6.3	396.8	4.1	0.9
11NC42D-37.1	1134	0.53	0.05544	0.00072	0.06785	0.00046	414.3	35.3	399.9	6.5	397.4	4.4	4.2
11NC42D-26.1	712	0.59	0.05587	0.00056	0.06717	0.00054	400.3	26.0	398.0	5.1	397.6	3.9	0.7
11NC42D-22.1	529	0.59	0.05550	0.00081	0.06812	0.00054	410.5	37.5	399.6	6.6	397.7	4.1	3.2
11NC42D-56.1	968	0.50	0.05529	0.00104	0.04753	0.00032	403.2	52.5	399.0	9.0	398.2	5.3	1.3
11NC42D-3.1	540	0.29	0.05551	0.00085	0.04864	0.00029	429.7	40.6	403.3	7.2	398.7	4.4	7.4
11NC42D-51.1	932	0.41	0.05546	0.00179	0.04741	0.00141	390.8	76.9	397.9	15.5	399.1	12.4	-2.2
11NC42D-43.1	738	1.03	0.05635	0.00048	0.06640	0.00036	402.2	24.0	399.7	4.5	399.2	3.3	0.8
11NC42D-36.1	565	0.67	0.05498	0.00092	0.06857	0.00041	398.4	42.3	399.4	7.2	399.6	4.2	-0.3

Table D.2: *continued*

Spot Name	U (ppm)	^{232}Th/ ^{238}U	^{207}Pb/^{206}Pb	±1σ	^{206}Pb/^{238}U	±1σ (%)	^{207}Pb/^{206}Pb Age (Ma)	±1σ	^{207}Pb/^{235}Pb Age (Ma)	±1σ	^{206}Pb/^{238}Pb Age (Ma)	±1σ	% Discordant
Middle stratigraphic level – Deformed clasts continued													
11NC42D-35.1	1016	0.75	0.05522	0.00065	0.06855	0.00050	395.6	31.1	399.1	5.8	399.7	4.1	-1.1
11NC42D-28.1	1009	0.40	0.05657	0.00073	0.06752	0.00052	406.4	33.4	400.7	6.1	399.8	4.2	1.7
11NC42D-25.1	622	0.58	0.05550	0.00064	0.06735	0.00060	396.3	29.6	399.3	5.7	399.8	4.3	-0.9
11NC42D-54.1	2085	0.42	0.05448	0.00088	0.04805	0.00041	410.8	53.6	401.6	9.5	400.0	6.2	2.7
11NC42D-57.1	1284	0.51	0.05650	0.00110	0.04751	0.00029	412.7	52.5	402.0	9.0	400.1	5.2	3.1
11NC42D-31.1	1002	0.28	0.05633	0.00099	0.04892	0.00033	421.2	45.1	403.3	7.7	400.2	4.2	5.2
11NC42D-55.1	1215	0.42	0.05466	0.00090	0.04792	0.00033	397.9	48.8	399.9	8.5	400.2	5.2	-0.6
11NC42D-58.1	1863	0.72	0.05643	0.00083	0.04757	0.00031	391.2	42.7	399.9	7.6	401.4	4.9	-2.7
11NC42D-63.1	806	0.35	0.05399	0.00086	0.04852	0.00035	409.4	42.4	402.7	7.7	401.6	5.1	2.0
11NC42D-27.1	713	0.60	0.05563	0.00106	0.04894	0.00045	425.2	48.5	405.1	8.5	401.6	5.1	5.7
11NC42D-34.1	939	0.69	0.05612	0.00048	0.06903	0.00055	419.7	25.8	405.2	5.4	402.7	4.4	4.2
11NC42D-1.1	489	0.49	0.05667	0.00059	0.06897	0.00066	402.4	26.8	402.7	5.5	402.7	4.4	-0.1
11NC42D-29.1	2039	0.51	0.05567	0.00066	0.04916	0.00030	412.9	33.6	404.6	6.0	403.2	3.8	2.4
11NC42D-38.1	1241	0.47	0.05406	0.00105	0.04775	0.00033	410.6	53.2	404.3	8.9	403.2	4.7	1.9
11NC42D-16.1	781	0.43	0.05491	0.00102	0.04950	0.00075	392.4	49.8	401.7	9.7	403.3	7.4	-2.9
11NC42D-31.1	2895	0.78	0.05713	0.00046	0.06744	0.00041	431.3	31.4	407.5	6.0	403.3	4.4	6.7
11NC42D-62.1	1513	0.64	0.05404	0.00077	0.04801	0.00026	419.1	42.4	405.8	7.3	403.5	4.2	3.8
11NC42D-33.1	878	0.43	0.05594	0.00079	0.06866	0.00051	394.9	36.4	402.6	6.5	404.0	4.3	-2.4
11NC42D-44.1	715	0.51	0.05634	0.00070	0.06761	0.00044	400.7	31.3	403.8	5.6	404.3	3.6	-0.9
11NC42D-6.1	1068	0.64	0.05539	0.00059	0.07108	0.00058	386.8	29.8	402.0	5.9	404.6	4.6	-4.8
11NC42D-36.1	1606	0.46	0.05484	0.00105	0.04741	0.00037	401.9	58.2	404.2	10.0	404.6	5.9	-0.7
11NC42D-32.1	651	0.41	0.05628	0.00090	0.06837	0.00058	403.2	40.5	405.2	7.2	405.5	4.5	-0.6
11NC42D-30.1	1488	0.46	0.05691	0.00066	0.06783	0.00054	418.2	36.2	408.1	6.8	406.3	4.8	2.9
11NC42D-61.1	1495	0.48	0.05531	0.00091	0.04774	0.00039	421.3	46.8	408.7	8.2	406.5	4.9	3.6
11NC42D-34.1	1739	0.47	0.05478	0.00080	0.04815	0.00033	406.6	44.9	407.1	7.9	407.2	4.8	-0.2
11NC42D-39.1	1306	0.52	0.05415	0.00093	0.04891	0.00046	417.5	48.7	408.8	8.7	407.3	5.3	2.5
11NC42D-40.1	498	0.51	0.05639	0.00078	0.06823	0.00053	406.4	34.8	407.5	6.5	407.7	4.4	-0.3
11NC42D-43.1	2087	0.62	0.05551	0.00080	0.04979	0.00041	415.0	41.2	408.9	7.6	407.8	5.1	1.8
11NC42D-7.1	502	0.49	0.05618	0.00088	0.07106	0.00058	413.1	37.8	408.9	6.8	408.1	4.2	1.3
11NC42D-29.1	2004	0.75	0.05680	0.00051	0.06866	0.00043	414.5	27.8	409.6	5.4	408.7	3.9	1.4
11NC42D-24.1	732	0.61	0.05579	0.00054	0.06916	0.00055	419.7	26.4	410.4	5.3	408.8	4.1	2.7
11NC42D-41.1	556	0.56	0.05616	0.00078	0.06833	0.00053	396.8	33.7	407.7	6.1	409.7	4.0	-3.3
11NC42D-44.1	2484	0.41	0.05562	0.00093	0.04983	0.00090	417.0	45.4	410.8	9.9	409.7	8.3	1.8
11NC42D-23.1	920	0.52	0.05581	0.00092	0.04955	0.00034	414.4	45.1	410.7	8.0	410.0	4.8	1.1
11NC42D-4.1	338	0.39	0.05614	0.00091	0.07177	0.00060	402.8	38.8	409.9	7.0	411.2	4.4	-2.2
11NC42D-53.1	1830	0.82	0.05464	0.00127	0.04943	0.00108	411.1	64.7	411.7	13.1	411.8	10.2	-0.2

Table D.2: *continued*

Spot Name	U (ppm)	^{232}Th/ ^{238}U	^{207}Pb/^{206}Pb	±1σ	^{206}Pb/^{238}U	±1σ (%)	^{207}Pb/^{206}Pb Age (Ma)	±1σ	^{207}Pb/^{235}Pb Age (Ma)	±1σ	^{206}Pb/^{238}Pb Age (Ma)	±1σ	% Discordant
Middle stratigraphic level – Deformed clasts continued													
11NC42D-17.1	1126	0.41	0.05568	0.00151	0.05026	0.00133	407.5	65.7	411.4	13.8	412.1	11.2	-1.2
11NC42D-5.1	665	0.40	0.05649	0.00080	0.07256	0.00054	426.4	36.0	414.5	6.7	412.4	4.5	3.4
11NC42D-42.1	608	1.16	0.05642	0.00060	0.06859	0.00043	406.6	27.9	411.7	5.2	412.6	3.6	-1.5
11NC42D-2.1	965	0.64	0.05658	0.00061	0.07108	0.00056	400.0	28.5	412.1	5.6	414.2	4.3	-3.7
11NC42D-47.1	3642	0.81	0.05692	0.00122	0.04817	0.00145	405.4	62.7	413.3	14.6	414.7	13.2	-2.4
11NC42D-19.1	1635	0.64	0.05653	0.00146	0.04983	0.00153	412.1	66.0	414.9	14.9	415.3	13.0	-0.8
11NC42D-21.1	2924	1.04	0.05630	0.00096	0.04962	0.00113	410.1	48.4	414.6	11.3	415.5	10.2	-1.4
11NC42D-20.1	3321	0.66	0.05646	0.00108	0.04986	0.00123	412.9	50.8	415.9	11.9	416.5	10.7	-0.9
11NC42D-18.1	2019	0.50	0.05621	0.00150	0.05065	0.00148	412.4	67.3	417.2	14.8	418.1	12.5	-1.4
11NC42D-12.1	903	0.27	0.05606	0.00145	0.05011	0.00113	399.8	62.9	415.6	12.7	418.4	9.9	-4.8
11NC42D-14.1	791	0.30	0.05623	0.00150	0.05074	0.00160	435.1	63.0	421.2	15.0	418.6	13.3	3.9
11NC42D-37.1	2919	0.54	0.05476	0.00062	0.04939	0.00026	419.3	40.8	418.8	7.4	418.8	4.7	0.1
11NC42D-8.1	710	0.80	0.05616	0.00070	0.07244	0.00048	407.0	31.8	417.6	5.9	419.5	3.9	-3.2
11NC42D-50.1	1440	0.80	0.05765	0.00154	0.05064	0.00181	441.8	65.8	432.5	16.9	430.8	15.7	2.6
Middle stratigraphic level – Slightly deformed clasts													
11NC42S-46.1	193	0.83	0.05370	0.00286	0.06254	0.00091	377.1	119.6	384.8	18.4	386.1	6.7	-2.4
11NC42S-26.1	3379	0.62	0.05777	0.00083	0.08122	0.00134	429.4	41.1	394.2	8.9	388.2	7.5	9.9
11NC42S-29.1	725	0.31	0.05444	0.00104	0.06228	0.00037	387.5	48.0	390.9	7.7	391.5	3.9	-1.1
11NC42S-50.1	289	0.49	0.05523	0.00144	0.06389	0.00052	406.8	62.3	393.7	9.9	391.5	4.3	3.9
11NC42S-31.1	1893	0.67	0.05681	0.00057	0.08271	0.00116	390.9	35.4	391.7	8.0	391.8	7.2	-0.2
11NC42S-25.1	1123	0.48	0.05414	0.00078	0.06436	0.00040	408.3	39.9	394.8	6.9	392.5	4.2	4.0
11NC42S-61.1	842	0.49	0.05450	0.00075	0.06462	0.00040	396.5	36.5	394.9	6.3	394.6	3.9	0.5
11NC42S-66.1	832	0.38	0.05487	0.00070	0.06442	0.00037	393.5	33.5	396.6	5.7	397.1	3.4	-0.9
11NC42S-42.1	757	0.38	0.05410	0.00097	0.06359	0.00036	402.3	45.8	397.9	7.6	397.1	4.1	1.3
11NC42S-39.1	1428	0.57	0.05446	0.00097	0.06424	0.00039	387.3	49.5	395.8	8.3	397.3	4.8	-2.6
11NC42S-70.1	1322	0.41	0.05521	0.00076	0.06385	0.00037	411.7	37.9	399.5	6.7	397.4	4.2	3.6
11NC42S-19.1	865	0.63	0.05551	0.00085	0.06166	0.00034	381.4	44.5	395.5	7.3	397.9	3.9	-4.4
11NC42S-27.1	772	0.48	0.05404	0.00104	0.06427	0.00046	416.4	50.4	400.9	8.5	398.2	4.6	4.5
11NC42S-30.1	1019	0.39	0.05566	0.00103	0.06321	0.00045	411.4	47.1	400.2	8.0	398.2	4.4	3.3
11NC42S-49.1	959	0.56	0.05475	0.00062	0.06512	0.00045	396.7	32.4	398.6	5.8	399.0	3.9	-0.6
11NC42S-26.1	1005	0.68	0.05418	0.00091	0.06510	0.00045	416.0	43.7	402.4	7.5	400.0	4.2	4.0
11NC42S-6.1	723	0.63	0.05541	0.00097	0.06245	0.00045	386.2	42.6	398.7	7.3	400.8	4.3	-3.9
11NC42S-52.1	903	0.49	0.05564	0.00118	0.06526	0.00052	405.0	56.7	402.0	9.4	401.4	4.9	0.9
11NC42S-9.1	569	0.78	0.05578	0.00073	0.06255	0.00033	396.7	31.5	401.2	5.3	401.9	3.0	-1.3
11NC42S-21.1	680	0.54	0.05553	0.00073	0.06334	0.00039	396.2	34.1	401.4	5.8	402.3	3.3	-1.6

Table D.2: *continued*

Spot Name	U (ppm)	^{232}Th/ ^{238}U	^{207}Pb/^{206}Pb	±1σ	^{206}Pb/^{238}U	±1σ (%)	^{207}Pb/^{206}Pb Age (Ma)	±1σ	^{207}Pb/^{235}Pb Age (Ma)	±1σ	^{206}Pb/^{238}Pb Age (Ma)	±1σ	% Discordant
Middle stratigraphic level – Slightly deformed clasts continued													
11NC42S-1.1	916	0.37	0.05552	0.00072	0.06334	0.00061	386.6	36.3	400.1	6.7	402.4	4.8	-4.2
11NC42S-20.1	605	0.65	0.05581	0.00085	0.06288	0.00040	400.8	40.1	402.2	6.7	402.5	3.5	-0.4
11NC42S-44.1	1074	0.37	0.05457	0.00081	0.06523	0.00042	419.2	39.8	406.2	7.0	403.9	4.1	3.8
11NC42S-58.1	573	0.36	0.05459	0.00100	0.06467	0.00062	428.5	46.5	407.6	8.3	403.9	5.1	5.9
11NC42S-67.1	907	0.37	0.05520	0.00076	0.06532	0.00045	402.4	34.7	403.8	6.1	404.0	3.7	-0.4
11NC42S-22.1	561	0.66	0.05543	0.00073	0.06367	0.00042	392.5	34.5	402.9	5.9	404.7	3.5	-3.2
11NC42S-48.1	2523	0.95	0.05380	0.00090	0.06464	0.00046	402.4	59.7	404.4	10.1	404.8	5.7	-0.6
11NC42S-23.1	1646	0.71	0.05592	0.00044	0.06325	0.00041	404.9	27.7	404.9	5.2	404.8	3.7	0.0
11NC42S-11.1	762	0.52	0.05553	0.00071	0.06220	0.00040	399.2	32.4	404.0	5.6	404.9	3.4	-1.5
11NC42S-69.1	999	0.51	0.05499	0.00074	0.06507	0.00047	394.2	37.3	403.4	6.8	405.0	4.6	-2.8
11NC42S-5.1	1014	0.76	0.05585	0.00066	0.06326	0.00054	401.8	30.0	405.0	5.8	405.6	4.3	-1.0
11NC42S-57.1	1055	0.45	0.05437	0.00082	0.06452	0.00043	409.6	40.8	406.2	7.1	405.6	4.3	1.0
11NC42S-56.1	2221	0.29	0.05519	0.00060	0.06473	0.00042	424.8	30.6	408.8	5.7	405.9	3.9	4.6
11NC42S-10.1	1164	0.43	0.05582	0.00054	0.06279	0.00036	403.7	25.3	405.6	4.6	406.0	3.1	-0.6
11NC42S-16.1	1081	0.46	0.05522	0.00055	0.06438	0.00045	412.4	27.4	408.6	5.3	408.0	3.9	1.1
11NC42S-41.1	1959	0.41	0.05546	0.00061	0.06565	0.00039	443.6	33.6	413.4	6.3	408.0	4.2	8.3
11NC42S-14.1	628	0.54	0.05505	0.00070	0.06341	0.00045	408.2	32.5	408.1	5.9	408.1	3.8	0.0
11NC42S-24.1	765	0.73	0.05586	0.00079	0.06340	0.00042	395.7	42.3	406.6	7.4	408.5	4.5	-3.3
11NC42S-12.1	696	0.43	0.05574	0.00086	0.06240	0.00051	415.3	39.6	409.7	7.1	408.8	4.4	1.6
11NC42S-15.1	343	0.62	0.05480	0.00096	0.06428	0.00044	404.8	41.6	408.2	7.1	408.8	3.8	-1.0
11NC42S-36.1	1822	0.67	0.05494	0.00071	0.06512	0.00048	424.5	41.6	412.0	7.6	409.8	5.0	3.6
11NC42S-47.1	1963	0.64	0.05468	0.00083	0.06604	0.00041	428.0	48.6	412.8	8.5	410.1	4.8	4.3
11NC42S-17.1	297	0.52	0.05558	0.00131	0.06421	0.00055	410.3	56.0	410.3	9.3	410.3	4.4	0.0
11NC42S-43.1	1006	0.94	0.05440	0.00077	0.06598	0.00045	420.8	38.5	412.3	7.0	410.8	4.4	2.5
11NC42S-33.1	1281	0.63	0.05583	0.00099	0.06372	0.00041	396.2	50.3	408.9	9.0	411.1	5.8	-3.9
11NC42S-28.1	1218	0.59	0.05481	0.00074	0.06573	0.00041	428.1	40.2	413.8	7.3	411.3	4.6	4.1
11NC42S-34.1	2182	0.72	0.05533	0.00074	0.06407	0.00039	398.0	44.0	409.8	8.2	411.9	5.8	-3.6
11NC42S-37.1	3937	0.56	0.05484	0.00041	0.06638	0.00046	428.6	34.4	414.6	6.7	412.1	4.8	4.0
11NC42S-35.1	1439	0.62	0.05484	0.00094	0.06492	0.00050	399.2	47.2	410.8	8.4	412.8	5.3	-3.5
11NC42S-72.1	673	0.32	0.05508	0.00095	0.06712	0.00057	422.9	42.8	415.5	7.6	414.1	4.5	2.2
11NC42S-2.1	642	0.53	0.05716	0.00082	0.06575	0.00060	450.9	35.7	423.3	6.8	418.3	4.5	7.5
11NC42S-32.1	2009	0.67	0.05656	0.00078	0.06557	0.00041	424.1	39.4	420.3	7.4	419.6	4.9	1.1
11NC42S-13.1	676	0.38	0.05550	0.00077	0.06498	0.00061	419.7	36.9	422.3	7.1	422.8	5.0	-0.8
11NC42S-60.1	106	0.69	0.05554	0.00203	0.07270	0.00091	449.0	81.3	445.6	14.4	444.9	6.4	1.0
11NC42S-4.1	49	1.57	0.05687	0.00235	0.07040	0.00093	440.0	90.6	447.9	16.0	449.5	6.4	-2.2

Table D.2: *continued*

Spot Name	U (ppm)	^{232}Th/ ^{238}U	^{207}Pb/^{206}Pb	±1σ	^{206}Pb/^{238}U	±1σ (%)	^{207}Pb/^{206}Pb Age (Ma)	±1σ	^{207}Pb/^{235}Pb Age (Ma)	±1σ	^{206}Pb/^{238}Pb Age (Ma)	±1σ	% Discordant
Middle stratigraphic level – Undeformed clasts													
11NC42U-42.1	547	0.62	0.05553	0.00179	0.04818	0.00050	399.4	76.3	384.4	12.0	381.9	5.3	4.5
11NC42U-76.1	569	0.55	0.05680	0.00142	0.04773	0.00045	397.2	61.8	386.6	9.9	384.9	4.9	3.2
11NC42U-46.1	1320	0.66	0.05517	0.00138	0.04901	0.00047	399.1	84.1	388.7	13.8	387.0	7.7	3.1
11NC42U-32.1	1126	1.00	0.05556	0.00157	0.04802	0.00044	384.8	76.8	386.9	12.0	387.3	5.5	-0.7
11NC42U-36.1	432	0.70	0.05301	0.00169	0.04919	0.00052	386.4	74.7	387.4	11.9	387.6	5.7	-0.3
11NC42U-41.1	630	0.39	0.05462	0.00120	0.04889	0.00039	373.5	54.1	385.9	8.6	388.0	4.4	-4.0
11NC42U-16.1	753	0.53	0.05549	0.00143	0.04856	0.00106	384.4	67.7	388.3	12.6	389.0	9.3	-1.2
11NC42U-34.1	582	0.74	0.05394	0.00159	0.04869	0.00057	387.7	72.6	388.8	11.7	389.0	6.0	-0.3
11NC42U-1.1	624	0.67	0.05622	0.00074	0.06675	0.00052	405.8	33.0	391.4	5.9	389.0	3.9	4.3
11NC42U-48.1	691	0.83	0.05489	0.00121	0.04903	0.00040	396.0	58.8	391.2	9.7	390.4	5.2	1.5
11NC42U-45.1	1470	0.79	0.05535	0.00126	0.04965	0.00050	396.3	80.8	391.7	13.5	390.9	7.9	1.4
11NC42U-4.1	519	0.62	0.05548	0.00079	0.06788	0.00050	387.1	35.0	390.6	6.0	391.2	3.7	-1.1
11NC42U-77.1	673	0.47	0.05620	0.00099	0.04884	0.00039	396.2	44.9	392.0	7.7	391.3	4.8	1.3
11NC42U-43.1	1199	1.00	0.05595	0.00126	0.04973	0.00034	410.1	60.6	395.2	9.9	392.7	5.0	4.4
11NC42U-17.1	1062	0.62	0.05555	0.00147	0.04931	0.00114	389.7	65.2	393.6	12.6	394.2	9.6	-1.2
11NC42U-62.1	569	0.79	0.05726	0.00142	0.04730	0.00145	400.6	58.8	395.4	13.6	394.5	12.2	1.6
11NC42U-35.1	974	1.01	0.05367	0.00095	0.04975	0.00036	395.3	47.3	394.6	8.0	394.5	4.6	0.2
11NC42U-14.1	2559	0.47	0.05653	0.00049	0.06574	0.00041	411.3	28.3	397.5	5.2	395.1	3.7	4.1
11NC42U-25.1	1157	0.47	0.05499	0.00162	0.04848	0.00159	402.4	71.3	396.6	15.5	395.7	13.3	1.7
11NC42U-15.1	676	0.48	0.05523	0.00176	0.04921	0.00147	392.2	79.3	395.3	15.7	395.8	12.3	-1.0
11NC42U-29.1	860	0.76	0.05478	0.00143	0.04886	0.00041	386.8	72.6	395.7	11.6	397.2	5.4	-2.8
11NC42U-6.1	621	0.54	0.05497	0.00131	0.04861	0.00043	431.2	60.5	404.1	10.2	399.3	5.2	7.6
11NC42U-15.1	797	0.53	0.05644	0.00073	0.06672	0.00046	415.8	34.6	403.2	6.3	401.0	4.2	3.7
11NC42U-9.1	1331	0.56	0.05603	0.00050	0.06745	0.00051	387.4	26.6	399.4	5.4	401.5	4.3	-3.7
11NC42U-5.1	1097	0.41	0.05568	0.00059	0.06939	0.00041	399.6	28.4	401.5	5.1	401.9	3.4	-0.6
11NC42U-66.1	384	0.34	0.05573	0.00116	0.04832	0.00058	395.8	51.6	401.3	9.2	402.3	6.0	-1.7
11NC42U-18.1	527	0.46	0.05566	0.00171	0.05056	0.00105	396.7	73.1	402.3	13.4	403.3	9.0	-1.7
11NC42U-9.1	1316	0.10	0.05472	0.00121	0.04900	0.00039	406.4	59.0	404.1	10.4	403.7	6.4	0.7
11NC42U-24.1	99	0.99	0.05561	0.00354	0.04955	0.00127	414.9	139.4	405.5	23.5	403.9	11.0	2.8
11NC42U-20.1	573	0.51	0.05617	0.00090	0.06591	0.00053	407.4	40.5	404.4	7.0	403.9	4.2	0.9
11NC42U-20.1	441	0.37	0.05539	0.00163	0.05014	0.00052	416.9	69.1	405.9	11.4	404.0	5.2	3.2
11NC42U-70.1	2039	0.66	0.05500	0.00072	0.04804	0.00035	409.6	49.3	404.9	9.3	404.0	6.6	1.4
11NC42U-71.1	599	0.36	0.05532	0.00118	0.04800	0.00035	404.5	56.2	404.4	9.6	404.3	5.4	0.1
11NC42U-31.1	3172	0.95	0.05635	0.00093	0.05015	0.00041	391.7	70.3	402.6	11.7	404.5	6.4	-3.4
11NC42U-3.1	521	0.84	0.05690	0.00076	0.07042	0.00054	437.1	32.9	410.1	6.0	405.3	3.9	7.5

Table D.2: *continued*

Spot Name	U (ppm)	^{232}Th/ ^{238}U	^{207}Pb/^{206}Pb	±1σ	^{206}Pb/^{238}U	±1σ (%)	^{207}Pb/^{206}Pb Age (Ma)	±1σ	^{207}Pb/^{235}Pb Age (Ma)	±1σ	^{206}Pb/^{238}Pb Age (Ma)	±1σ	% Discordant
Middle stratigraphic level – Undeformed clasts continued													
11NC42U-10.1	2326	0.52	0.05459	0.00092	0.04937	0.00041	401.0	50.2	405.5	9.4	406.3	6.6	-1.4
11NC42U-6.1	916	0.74	0.05553	0.00064	0.06982	0.00047	398.1	32.4	405.3	5.9	406.5	4.0	-2.2
11NC42U-28.1	1455	0.71	0.05423	0.00116	0.04994	0.00057	406.9	58.2	406.9	10.2	406.9	6.2	0.0
11NC42U-12.1	1426	0.44	0.05431	0.00087	0.04995	0.00040	408.2	46.2	407.3	8.4	407.1	5.6	0.3
11NC42U-33.1	726	0.81	0.05507	0.00195	0.05064	0.00059	390.3	86.1	404.7	14.1	407.3	6.4	-4.5
11NC42U-11.1	390	0.44	0.05463	0.00197	0.04975	0.00055	411.9	83.7	408.1	13.9	407.4	6.4	1.1
11NC42U-72.1	387	0.50	0.05580	0.00120	0.04834	0.00052	405.6	54.8	407.4	9.6	407.8	5.8	-0.6
11NC42U-3.1	693	0.55	0.05498	0.00176	0.04881	0.00039	407.8	79.6	408.0	13.0	408.0	5.6	-0.1
11NC42U-7.1	1216	0.71	0.05619	0.00069	0.06981	0.00053	422.8	33.7	410.4	6.3	408.1	4.3	3.6
11NC42U-14.1	1410	0.73	0.05551	0.00154	0.05069	0.00154	424.3	67.7	410.9	15.0	408.5	12.7	3.9
11NC42U-69.1	1042	0.62	0.05575	0.00102	0.04879	0.00042	446.8	56.4	414.9	10.5	409.2	6.9	8.7
11NC42U-10.1	880	0.57	0.05653	0.00086	0.06899	0.00050	403.9	38.9	408.8	6.9	409.7	4.4	-1.5
11NC42U-22.1	1112	0.50	0.05512	0.00135	0.05040	0.00140	421.6	60.7	412.3	13.5	410.6	11.5	2.7
11NC42U-4.1	2326	0.57	0.05496	0.00081	0.04953	0.00035	404.2	49.8	411.8	8.8	413.2	5.4	-2.3
11NC42U-5.1	1449	0.59	0.05586	0.00104	0.05010	0.00038	453.6	50.9	420.4	9.0	414.4	5.0	8.9
11NC42U-64.1	622	0.52	0.05665	0.00216	0.05047	0.00253	399.7	87.4	413.5	21.9	415.9	20.6	-4.2
11NC42U-17.1	850	0.56	0.05649	0.00088	0.06801	0.00047	419.4	39.7	416.9	7.1	416.5	4.1	0.7
11NC42U-18.1	1326	0.58	0.05654	0.00068	0.06753	0.00045	418.8	36.4	417.7	6.7	417.5	4.4	0.3
11NC42U-61.1	1087	0.52	0.05740	0.00118	0.05000	0.00131	402.7	50.4	416.8	12.3	419.3	11.4	-4.3
11NC42U-2.1	1164	0.72	0.05508	0.00123	0.05057	0.00036	428.0	58.0	420.9	10.0	419.6	5.0	2.0
11NC42U-59.1	590	0.64	0.05621	0.00129	0.04979	0.00092	410.1	55.3	422.7	11.2	425.1	8.5	-3.8
11NC42U-1.1	947	0.58	0.05447	0.00099	0.05173	0.00050	419.4	50.4	425.2	9.3	426.2	6.0	-1.7
11NC42U-30.1	476	0.34	0.05737	0.00242	0.05312	0.00062	448.6	108.8	432.5	18.6	429.5	7.6	4.4
11NC42U-78.1	955	0.10	0.05644	0.00086	0.05480	0.00036	428.3	39.8	434.0	8.1	435.1	6.0	-1.6
11NC42U-56.1	1314	0.56	0.05544	0.00117	0.05201	0.00167	428.0	51.4	434.6	14.3	435.9	14.0	-1.9
11NC42U-8.1	761	0.71	0.05537	0.00143	0.05370	0.00045	442.0	63.1	439.9	11.4	439.5	6.0	0.6
11NC42U-40.1	266	0.21	0.05629	0.00185	0.05585	0.00064	452.6	74.9	443.7	13.4	441.9	6.3	2.4
11NC42U-27.1	433	0.95	0.05497	0.00189	0.05432	0.00124	453.7	79.7	444.2	15.9	442.4	10.7	2.6
11NC42U-7.1	253	0.39	0.05556	0.00253	0.05467	0.00098	459.1	102.5	447.7	18.7	445.5	9.0	3.0
11NC42U-39.1	196	0.35	0.05543	0.00212	0.05653	0.00060	448.3	86.0	446.4	15.1	446.0	6.1	0.5
11NC42U-12.1	797	0.46	0.05764	0.00078	0.07506	0.00055	441.6	39.4	446.4	7.6	447.3	4.8	-1.3
11NC42U-49.1	361	0.43	0.05641	0.00181	0.05621	0.00064	461.7	75.2	451.1	13.7	449.0	6.7	2.9
11NC42U-16.1	849	0.39	0.05748	0.00067	0.07515	0.00055	461.5	31.7	455.5	6.6	454.4	4.9	1.6
11NC42U-13.1	3497	0.96	0.05785	0.00046	0.07612	0.00044	454.8	31.3	455.0	6.4	455.1	4.5	0.0
11NC42U-19.1	2356	0.53	0.05782	0.00056	0.07404	0.00052	468.5	32.5	458.3	6.8	456.3	4.9	2.7
11NC42U-52.1	689	0.69	0.05632	0.00184	0.05676	0.00127	462.9	80.5	458.1	16.8	457.2	11.9	1.3

Table D.2: *continued*

Spot Name	U (ppm)	^{232}Th/ ^{238}U	^{207}Pb/^{206}Pb	±1σ	^{206}Pb/^{238}U	±1σ (%)	^{207}Pb/^{206}Pb Age (Ma)	±1σ	^{207}Pb/^{235}Pb Age (Ma)	±1σ	^{206}Pb/^{238}Pb Age (Ma)	±1σ	% Discordant
Middle stratigraphic level – Undeformed clasts continued													
11NC42U-8.1	1284	0.49	0.05740	0.00061	0.07899	0.00069	464.0	29.1	460.1	6.4	459.3	5.0	1.1
11NC42U-65.1	724	0.06	0.05728	0.00147	0.05585	0.00184	440.8	60.4	457.4	16.1	460.8	15.2	-4.7
11NC42U-54.1	967	0.40	0.05655	0.00202	0.05867	0.00278	481.9	83.0	472.3	23.2	470.3	22.0	2.5
11NC42U-26.1	1634	0.48	0.05672	0.00126	0.05832	0.00180	497.0	54.8	477.5	15.5	473.4	14.7	4.9
11NC42U-67.1	1221	0.10	0.05657	0.00072	0.05691	0.00039	457.0	37.5	470.9	7.9	473.8	5.7	-3.8
11NC42U-57.1	1404	0.02	0.05693	0.00127	0.05679	0.00137	491.6	56.0	482.8	14.1	480.9	12.2	2.3
11NC42U-58.1	621	0.31	0.05729	0.00107	0.05722	0.00114	481.2	49.6	487.3	12.3	488.6	10.6	-1.6
11NC42U-55.1	1588	0.07	0.05750	0.00187	0.06208	0.00221	503.7	72.7	508.9	19.9	510.1	18.0	-1.3
Basal stratigraphic level – Deformed clasts													
11NC22D-13.2	984	0.24	0.05638	0.00049	0.06429	0.00059	412.0	21.5	402.7	4.6	401.1	3.9	2.7
11NC22D-13.1	858	0.25	0.05651	0.00048	0.06522	0.00075	419.0	20.9	406.8	5.1	404.6	4.7	3.5
11NC22D-39.1	316	0.26	0.05576	0.00097	0.05544	0.00036	409.3	41.1	405.5	6.9	404.9	3.6	1.1
11NC22D-31.1	216	0.28	0.05549	0.00091	0.05536	0.00033	423.9	39.1	413.5	6.9	411.6	4.0	3.0
11NC22D-12.1	1086	0.22	0.05677	0.00034	0.06687	0.00058	432.8	15.3	417.0	4.0	414.2	3.7	4.4
11NC22D-38.1	265	0.28	0.05608	0.00100	0.05699	0.00047	423.6	41.9	420.0	7.4	419.3	4.2	1.0
11NC22D-22.1	315	0.37	0.05635	0.00051	0.06614	0.00038	431.3	22.0	421.2	4.3	419.3	3.1	2.9
11NC22D-23.1	552	0.30	0.05652	0.00041	0.06606	0.00046	427.6	18.0	422.0	4.0	420.9	3.3	1.6
11NC22D-26.1	543	0.27	0.05692	0.00050	0.06609	0.00041	424.6	21.5	423.0	4.2	422.7	3.0	0.5
11NC22D-40.1	184	0.53	0.05598	0.00086	0.05872	0.00034	424.8	36.2	423.2	6.5	422.9	3.8	0.5
11NC22D-7.1	392	0.66	0.05621	0.00101	0.07378	0.00067	408.1	43.6	421.9	7.9	424.5	4.8	-4.1
11NC22D-9.1	166	0.39	0.05609	0.00144	0.05763	0.00049	429.6	58.0	429.5	9.9	429.4	4.2	0.0
11NC22D-11.1	410	0.48	0.05602	0.00092	0.05760	0.00046	433.3	39.6	430.5	7.2	430.0	4.2	0.8
11NC22D-19.1	371	1.15	0.05581	0.00092	0.05896	0.00035	436.6	39.1	433.1	7.2	432.4	4.3	1.0
11NC22D-1.1	216	0.95	0.05600	0.00070	0.06093	0.00042	453.1	32.0	436.0	6.5	432.7	4.6	4.6
11NC22D-4.1	291	0.56	0.05608	0.00089	0.05749	0.00042	429.8	38.2	432.6	6.9	433.2	3.8	-0.8
11NC22D-6.1	375	0.98	0.05639	0.00099	0.07602	0.00060	436.8	42.9	434.2	7.9	433.8	4.7	0.7
11NC22D-16.1	303	0.96	0.05540	0.00100	0.05709	0.00036	415.7	43.2	431.4	7.6	434.4	3.8	-4.7
11NC22D-12.1	247	0.58	0.05616	0.00103	0.05807	0.00043	439.0	42.8	436.5	7.6	436.0	4.0	0.7
11NC22D-8.1	320	0.39	0.05640	0.00077	0.05862	0.00033	439.2	33.3	437.7	6.1	437.5	3.4	0.4
11NC22D-24.1	233	0.62	0.05628	0.00088	0.06081	0.00036	439.5	37.4	438.3	7.0	438.1	4.3	0.3
11NC22D-3.1	340	0.62	0.05607	0.00085	0.05830	0.00034	437.4	36.5	438.5	6.5	438.7	3.3	-0.3
11NC22D-9.2	723	0.57	0.05688	0.00042	0.06996	0.00075	443.6	18.1	440.8	5.0	440.3	4.8	0.8
11NC22D-5.2r	1915	0.19	0.05665	0.00050	0.05803	0.00026	441.1	27.7	441.0	5.3	440.9	3.4	0.0
11NC22D-11.1	428	0.47	0.05715	0.00039	0.07141	0.00034	450.9	17.1	442.6	3.6	441.0	2.7	2.3
11NC22D-18.1	915	0.83	0.05687	0.00036	0.07008	0.00025	442.4	17.3	441.5	3.5	441.3	2.5	0.3
11NC22D-16.1	1142	0.67	0.05751	0.00037	0.07014	0.00042	462.1	18.1	445.1	4.0	441.8	3.2	4.5

Table D.2: *continued*

Spot Name	U (ppm)	^{232}Th/ ^{238}U	^{207}Pb/^{206}Pb	±1σ	^{206}Pb/^{238}U	±1σ (%)	^{207}Pb/^{206}Pb Age (Ma)	±1σ	^{207}Pb/^{235}Pb Age (Ma)	±1σ	^{206}Pb/^{238}Pb Age (Ma)	±1σ	% Discordant
Basal stratigraphic level – Deformed clasts continued													
11NC22D-29.1	855	0.67	0.05752	0.00046	0.06967	0.00025	463.0	20.5	445.7	3.9	442.4	2.3	4.6
11NC22D-37.1	118	0.53	0.05632	0.00120	0.06049	0.00051	441.0	48.8	442.3	8.8	442.5	4.6	-0.3
11NC22D-14.1	316	0.70	0.05682	0.00090	0.06058	0.00035	449.5	37.4	444.1	6.9	443.0	3.8	1.5
11NC22D-19.1	768	0.63	0.05681	0.00049	0.07042	0.00024	447.0	21.5	443.9	4.1	443.3	2.5	0.9
11NC22D-15.1	739	0.50	0.05714	0.00052	0.07072	0.00051	444.2	23.1	443.7	4.8	443.6	3.6	0.2
11NC22D-13.1	438	0.67	0.05614	0.00081	0.05878	0.00033	438.6	34.9	443.0	6.4	443.8	3.7	-1.2
11NC22D-26.1	538	0.28	0.05600	0.00070	0.05826	0.00085	441.1	32.9	443.5	7.8	444.0	6.9	-0.7
11NC22D-21.1	895	0.80	0.05660	0.00029	0.07059	0.00023	447.1	14.7	444.8	3.3	444.3	2.7	0.6
11NC22D-16.1	328	0.68	0.05608	0.00092	0.06098	0.00048	431.3	38.3	442.7	7.2	444.9	4.3	-3.3
11NC22D-36.1	211	0.51	0.05640	0.00085	0.06088	0.00030	448.6	36.5	445.6	6.7	445.1	3.7	0.8
11NC22D-23.1	497	0.67	0.05646	0.00063	0.06184	0.00026	449.2	27.9	445.9	5.4	445.3	3.5	0.9
11NC22D-35.1	407	0.52	0.05640	0.00066	0.06073	0.00035	444.7	30.5	445.4	5.8	445.5	3.5	-0.2
11NC22D-17.1	448	0.79	0.05659	0.00047	0.07081	0.00039	429.1	20.8	443.1	4.2	445.8	2.9	-4.0
11NC22D-6.2r	316	0.50	0.05689	0.00094	0.05904	0.00033	450.2	39.5	446.6	7.1	445.8	3.4	1.0
11NC22D-14.1	332	0.43	0.05623	0.00082	0.05874	0.00043	444.4	35.3	446.0	6.8	446.3	4.2	-0.4
11NC22D-5.1	856	0.64	0.05681	0.00063	0.06269	0.00044	474.4	28.9	451.0	6.0	446.4	4.2	6.1
11NC22D-8.1	452	0.96	0.05782	0.00116	0.07715	0.00056	450.1	48.7	447.0	9.0	446.4	4.9	0.8
11NC22D-21.1	356	0.70	0.05725	0.00086	0.06169	0.00043	488.5	36.3	453.6	7.1	446.7	4.4	8.8
11NC22D-9.1	481	0.33	0.05720	0.00050	0.07107	0.00066	453.6	21.7	448.0	5.2	446.9	4.5	1.5
11NC22D-5.1c	825	1.01	0.05698	0.00069	0.05912	0.00028	459.7	30.8	449.0	5.7	447.0	3.1	2.9
11NC22D-9.3	278	0.52	0.05689	0.00052	0.07104	0.00046	446.4	21.6	447.0	4.5	447.1	3.3	-0.2
11NC22D-13.1	291	0.66	0.05688	0.00073	0.06101	0.00037	449.2	32.7	447.7	6.5	447.4	4.5	0.4
11NC22D-20.1	601	0.70	0.05715	0.00046	0.07113	0.00027	464.6	19.7	450.4	3.9	447.6	2.6	3.8
11NC22D-10.1	1558	0.34	0.05645	0.00042	0.06032	0.00031	447.1	23.1	447.7	4.8	447.8	3.5	-0.2
11NC22D-14.1	630	0.54	0.05726	0.00054	0.07176	0.00049	447.5	22.8	447.9	4.6	448.0	3.3	-0.1
11NC22D-27.1	517	1.11	0.05770	0.00045	0.07044	0.00039	455.8	20.2	449.4	4.2	448.2	3.1	1.7
11NC22D-30.1	722	0.70	0.05691	0.00043	0.07067	0.00031	445.8	20.4	448.2	4.0	448.6	2.7	-0.6
11NC22D-19.1	233	0.55	0.05577	0.00105	0.05871	0.00040	452.3	44.0	449.4	7.9	448.8	3.7	0.8
11NC22D-24.1	508	0.72	0.05749	0.00048	0.07025	0.00047	455.2	20.6	450.0	4.4	448.9	3.4	1.4
11NC22D-1.1	354	0.74	0.05746	0.00097	0.07626	0.00067	456.0	41.0	450.2	7.9	449.0	5.0	1.6
11NC22D-7.1	350	0.72	0.05668	0.00070	0.05981	0.00038	444.5	30.7	448.4	5.9	449.2	3.8	-1.1
11NC22D-6.1	347	0.70	0.05666	0.00074	0.06312	0.00041	455.4	33.1	450.8	6.7	449.9	4.6	1.2
11NC22D-5.1	171	0.87	0.05644	0.00128	0.07862	0.00075	457.2	52.9	451.1	9.9	449.9	5.5	1.6
11NC22D-4.1	345	0.84	0.05648	0.00105	0.07773	0.00060	456.2	45.0	451.1	8.4	450.1	4.7	1.4
11NC22D-22.1	466	0.54	0.05638	0.00092	0.06254	0.00040	449.3	39.2	450.0	7.4	450.1	4.3	-0.2
11NC22D-34.1	686	0.61	0.05672	0.00061	0.06117	0.00031	453.5	31.5	450.7	5.9	450.1	3.4	0.8

Table D.2: *continued*

Spot Name	U (ppm)	^{232}Th/ ^{238}U	^{207}Pb/^{206}Pb	±1σ	^{206}Pb/^{238}U	±1σ (%)	^{207}Pb/^{206}Pb Age (Ma)	±1σ	^{207}Pb/^{235}Pb Age (Ma)	±1σ	^{206}Pb/^{238}Pb Age (Ma)	±1σ	% Discordant
Basal stratigraphic level – Deformed clasts continued													
11NC22D-33.1	461	0.79	0.05672	0.00048	0.07173	0.00040	435.5	21.5	447.9	4.3	450.3	3.0	-3.5
11NC22D-25.1	177	0.68	0.05663	0.00118	0.06200	0.00042	449.5	48.0	450.8	8.8	451.1	4.6	-0.4
11NC22D-18.1	389	0.86	0.05667	0.00089	0.06148	0.00039	467.0	37.5	453.9	7.3	451.4	4.5	3.5
11NC22D-2.1	448	1.11	0.05656	0.00077	0.05987	0.00035	459.3	32.3	452.9	6.0	451.6	3.2	1.7
11NC22D-7.1	688	1.15	0.05665	0.00052	0.06284	0.00042	449.3	25.7	451.6	5.7	452.0	4.7	-0.6
11NC22D-9.1	467	0.87	0.05639	0.00066	0.06189	0.00040	454.2	30.0	452.6	5.9	452.3	3.8	0.4
11NC22D-32.1	472	1.00	0.05680	0.00047	0.07180	0.00035	441.6	20.9	450.6	4.1	452.3	2.7	-2.5
11NC22D-25.1	341	0.50	0.05831	0.00063	0.07068	0.00046	477.4	25.6	456.6	5.1	452.5	3.3	5.4
11NC22D-32.1	346	0.71	0.05652	0.00074	0.06114	0.00037	457.1	33.2	453.3	6.4	452.6	3.9	1.0
11NC22D-17.1	265	0.85	0.05613	0.00110	0.05954	0.00044	453.2	46.3	453.3	8.5	453.3	4.3	0.0
11NC22D-33.1	401	0.63	0.05639	0.00067	0.06138	0.00032	444.1	33.6	452.2	6.2	453.8	3.5	-2.3
11NC22D-28.1	916	0.89	0.05759	0.00037	0.07162	0.00032	459.0	18.1	455.0	3.8	454.2	2.8	1.1
11NC22D-2.1	454	0.72	0.05604	0.00071	0.06407	0.00036	460.2	32.1	455.3	6.3	454.4	3.9	1.3
11NC22D-8.1	462	0.54	0.05667	0.00071	0.06269	0.00039	457.7	30.9	454.9	6.1	454.4	3.9	0.8
11NC22D-6.1c	639	0.86	0.05711	0.00073	0.05991	0.00044	456.2	34.2	454.7	6.8	454.4	4.4	0.4
11NC22D-3.1	417	0.99	0.05678	0.00121	0.07771	0.00065	465.1	52.1	456.8	9.8	455.2	5.4	2.2
11NC22D-10.1	254	0.82	0.05639	0.00111	0.06189	0.00047	453.3	46.0	455.2	8.4	455.5	4.2	-0.5
11NC22D-26.1	430	0.63	0.05690	0.00075	0.06201	0.00042	459.6	32.4	456.5	6.4	455.9	4.2	0.8
11NC22D-1.1	632	0.98	0.05639	0.00072	0.06027	0.00034	455.2	31.2	456.0	5.8	456.1	3.2	-0.2
11NC22D-15.1	287	0.48	0.05711	0.00089	0.06268	0.00048	463.0	36.4	457.7	7.1	456.6	4.3	1.4
11NC22D-3.1	391	0.91	0.05574	0.00080	0.06440	0.00047	453.5	36.9	456.3	7.2	456.8	4.5	-0.8
11NC22D-28.1	518	0.67	0.05661	0.00067	0.06098	0.00037	454.6	31.7	456.5	6.2	456.9	4.0	-0.5
11NC22D-15.1	239	0.69	0.05647	0.00103	0.06018	0.00044	455.9	42.3	456.8	7.9	457.0	4.2	-0.2
11NC22D-27.1	777	0.79	0.05638	0.00096	0.06026	0.00095	447.7	40.4	455.9	9.1	457.5	7.4	-2.3
11NC22D-27.1	488	0.84	0.05681	0.00087	0.06169	0.00037	455.5	38.3	458.0	7.2	458.5	3.9	-0.7
11NC22D-20.1	344	0.74	0.05704	0.00060	0.06321	0.00039	482.7	26.8	463.7	5.7	459.9	4.2	4.9
11NC22D-12.1	519	0.92	0.05707	0.00067	0.06274	0.00040	462.6	30.7	461.4	6.5	461.2	4.7	0.3
11NC22D-30.1	268	0.66	0.05690	0.00069	0.06219	0.00043	480.2	30.1	465.6	6.5	462.6	4.8	3.8
11NC22D-21.1	224	0.59	0.05668	0.00117	0.06041	0.00078	468.0	47.3	463.6	9.5	462.7	6.2	1.2
11NC22D-31.1	672	0.57	0.05784	0.00049	0.07335	0.00031	485.1	22.0	467.1	4.4	463.5	2.7	4.6
11NC22D-29.1	425	0.55	0.05665	0.00057	0.06213	0.00032	463.0	26.6	463.6	5.5	463.7	3.8	-0.1
11NC22D-28.1	461	0.69	0.05702	0.00090	0.06158	0.00069	464.2	37.6	465.7	7.9	466.1	5.6	-0.4
11NC22D-23.1	309	0.62	0.05675	0.00117	0.06087	0.00084	452.5	48.0	463.9	9.9	466.2	6.8	-3.1
11NC22D-18.1	276	0.79	0.05643	0.00103	0.06119	0.00082	471.6	42.3	467.1	9.0	466.2	6.5	1.2
11NC22D-20.1	527	0.81	0.05656	0.00066	0.06100	0.00074	476.8	29.6	468.5	7.1	466.8	5.9	2.2
11NC22D-22.1	410	0.39	0.05682	0.00092	0.06114	0.00084	459.7	38.9	467.0	8.7	468.4	6.8	-2.0

Table D.2: *continued*

		^{232}Th/					^{207}Pb/^{206}Pb		^{207}Pb/^{235}Pb		^{206}Pb/^{238}Pb		%
Spot Name	U (ppm)	^{238}U	^{207}Pb/^{206}Pb	±1σ	^{206}Pb/^{238}U	±1σ (%)	Age (Ma)	±1σ	Age (Ma)	±1σ	Age (Ma)	±1σ	Discordant
Basal stratigraphic level – Deformed clasts continued													
11NC22D-2.1	214	0.62	0.05752	0.00156	0.07964	0.00073	474.4	63.0	470.6	11.9	469.8	5.8	1.0
11NC22D-24.1	317	0.73	0.05729	0.00120	0.06200	0.00102	482.5	48.2	475.4	10.7	473.9	8.0	1.8
11NC22D-25.1	733	0.94	0.05695	0.00095	0.06294	0.00095	478.2	40.8	479.8	9.5	480.2	7.7	-0.4
Basal stratigraphic level – Slightly deformed clasts													
11NC22S-20.1	140	0.98	0.05378	0.00152	0.05766	0.00054	294.6	65.9	293.9	8.1	293.8	3.4	0.3
11NC22S-63.1	195	0.76	0.05278	0.00094	0.03965	0.00039	282.9	43.0	293.0	5.8	294.2	3.7	-4.1
11NC22S-10.1	84	0.52	0.05380	0.00205	0.06025	0.00060	298.1	85.9	296.9	10.3	296.7	3.4	0.5
11NC22S-23.1	262	0.89	0.05404	0.00110	0.05673	0.00038	295.4	49.5	297.0	6.2	297.2	2.9	-0.6
11NC22S-16.1	96	0.53	0.05317	0.00142	0.04067	0.00034	287.7	62.1	296.8	7.7	297.9	3.5	-3.6
11NC22S-59.1	47	0.64	0.05369	0.00236	0.04121	0.00048	312.8	97.8	302.6	12.1	301.3	4.1	3.8
11NC22S-22.1	152	1.06	0.05415	0.00133	0.05853	0.00064	305.7	57.4	303.3	7.5	302.9	3.7	0.9
11NC22S-30.1	67	0.35	0.05460	0.00193	0.05732	0.00065	317.2	80.0	305.3	10.1	303.7	3.9	4.3
11NC22S-62.1	90	0.48	0.05325	0.00162	0.04149	0.00038	302.0	69.1	303.9	8.6	304.2	3.5	-0.7
11NC22S-48.1	117	0.39	0.05316	0.00196	0.04104	0.00040	304.7	83.6	305.1	10.4	305.1	3.6	-0.2
11NC22S-65.1	262	0.50	0.05293	0.00107	0.04096	0.00024	302.6	47.1	304.9	6.0	305.2	2.8	-0.9
11NC22S-67.1	56	1.02	0.05274	0.00198	0.04118	0.00039	301.2	84.9	305.1	10.5	305.6	3.7	-1.5
11NC22S-56.1	594	0.90	0.05322	0.00076	0.04191	0.00026	309.0	35.7	306.2	4.9	305.8	2.9	1.0
11NC22S-40.1	46	0.28	0.05342	0.00211	0.04155	0.00042	317.0	88.4	308.9	11.0	307.9	3.4	2.9
11NC22S-6.1	37	0.46	0.05323	0.00234	0.04235	0.00052	315.5	98.0	309.1	12.3	308.3	4.2	2.3
11NC22S-25.1	141	0.44	0.05343	0.00106	0.04165	0.00032	310.8	46.3	308.9	6.1	308.6	3.0	0.7
11NC22S-52.1	265	0.67	0.05234	0.00098	0.04232	0.00036	311.7	44.0	309.9	6.0	309.7	3.4	0.7
11NC22S-1.2r	339	0.65	0.05437	0.00088	0.06657	0.00042	309.1	38.5	310.5	5.1	310.7	2.5	-0.5
11NC22S-5.1	132	0.49	0.05296	0.00119	0.04268	0.00040	305.6	51.7	310.5	6.9	311.1	3.4	-1.9
11NC22S-13.1	160	0.60	0.05396	0.00114	0.06206	0.00065	308.3	49.4	311.1	6.7	311.4	3.6	-1.0
11NC22S-31.1	72	0.48	0.05406	0.00235	0.05815	0.00068	314.8	97.5	311.9	12.3	311.5	4.1	1.1
11NC22S-22.1	211	0.48	0.05432	0.00146	0.04187	0.00035	323.5	63.2	314.1	8.3	312.8	3.6	3.4
11NC22S-7.2r	338	0.54	0.05413	0.00133	0.06323	0.00112	321.2	59.8	314.6	9.6	313.7	7.1	2.4
11NC22S-28.2r	153	0.43	0.05399	0.00168	0.05935	0.00063	306.9	71.4	313.4	9.2	314.3	3.8	-2.5
11NC22S-6.1	260	1.02	0.05466	0.00098	0.06291	0.00044	320.4	42.7	318.6	6.0	318.4	3.4	0.7
11NC22S-11.1	242	0.44	0.05418	0.00114	0.06425	0.00062	324.0	49.7	319.1	6.8	318.4	3.5	1.8
11NC22S-12.1	228	0.83	0.05315	0.00120	0.04297	0.00029	316.9	53.5	319.6	7.0	319.9	3.0	-1.0
11NC22S-5.2r	1307	0.63	0.05478	0.00076	0.06551	0.00110	335.9	39.7	324.8	7.6	323.3	6.6	3.9
11NC22S-39.2r	516	0.25	0.05413	0.00061	0.04533	0.00028	332.4	29.3	332.5	4.6	332.6	3.1	-0.1
11NC22S-33.2r	205	0.57	0.05443	0.00109	0.04643	0.00039	337.1	48.6	338.4	7.1	338.6	3.8	-0.4
11NC22S-34.1	99	0.39	0.05539	0.00154	0.05314	0.00042	387.9	63.0	385.2	9.7	384.8	3.7	0.8
11NC22S-43.1	422	0.11	0.05451	0.00083	0.05333	0.00037	384.1	37.9	386.9	6.5	387.4	4.0	-0.9

Table D.2: *continued*

Spot Name	U (ppm)	^{232}Th/ ^{238}U	^{207}Pb/^{206}Pb	±1σ	^{206}Pb/^{238}U	±1σ (%)	^{207}Pb/^{206}Pb Age (Ma)	±1σ	^{207}Pb/^{235}Pb Age (Ma)	±1σ	^{206}Pb/^{238}Pb Age (Ma)	±1σ	% Discordant
Basal stratigraphic level – Slightly deformed clasts continued													
11NC22S-60.1	176	0.46	0.05567	0.00106	0.05493	0.00036	397.3	44.1	395.3	7.3	395.0	4.0	0.6
11NC22S-24.1	115	0.52	0.05677	0.00165	0.07517	0.00083	405.2	66.4	396.5	10.8	395.0	5.1	2.6
11NC22S-9.1	202	0.45	0.05623	0.00117	0.08150	0.00057	388.5	48.2	394.2	7.8	395.2	3.8	-1.8
11NC22S-58.1	731	0.65	0.05608	0.00052	0.05406	0.00032	408.1	25.9	397.7	5.0	395.9	3.8	3.1
11NC22S-42.1	177	0.31	0.05475	0.00103	0.05431	0.00037	391.9	43.6	396.3	7.1	397.0	3.5	-1.3
11NC22S-55.1	265	0.63	0.05528	0.00115	0.05535	0.00043	405.7	49.1	398.4	8.2	397.1	4.5	2.2
11NC22S-47.1	390	0.68	0.05539	0.00083	0.05406	0.00030	399.1	36.2	397.5	6.0	397.2	3.2	0.5
11NC22S-73.1	486	0.31	0.05517	0.00080	0.05565	0.00032	396.2	35.7	397.8	6.1	398.1	3.7	-0.5
11NC22S-31.1	129	0.46	0.05601	0.00136	0.05388	0.00037	406.1	54.8	399.3	8.8	398.1	3.9	2.0
11NC22S-46.1	218	0.53	0.05530	0.00107	0.05473	0.00041	402.3	45.1	399.4	7.4	398.8	3.7	0.9
11NC22S-37.1	288	0.68	0.05580	0.00087	0.05572	0.00033	399.5	37.3	400.2	6.4	400.3	3.7	-0.2
11NC22S-44.1	356	0.81	0.05512	0.00095	0.05541	0.00032	406.0	41.8	401.5	7.1	400.7	3.9	1.4
11NC22S-25.1	375	1.10	0.05655	0.00082	0.07684	0.00074	400.0	35.9	402.6	6.6	403.1	4.5	-0.8
11NC22S-21.1	236	0.55	0.05628	0.00120	0.05457	0.00033	403.8	51.3	404.1	8.4	404.2	4.0	-0.1
11NC22S-57.1	321	0.68	0.05577	0.00105	0.05532	0.00034	403.7	44.8	404.4	7.5	404.6	4.0	-0.2
11NC22S-20.1	321	0.54	0.05626	0.00111	0.05496	0.00043	411.1	46.2	405.6	7.7	404.6	4.0	1.6
11NC22S-69.1	372	0.53	0.05552	0.00082	0.05467	0.00033	406.8	40.0	405.2	7.0	404.9	4.3	0.5
11NC22S-53.1	380	0.54	0.05501	0.00092	0.05630	0.00041	417.8	39.2	407.6	6.9	405.8	4.0	3.0
11NC22S-50.1	245	0.53	0.05535	0.00125	0.05482	0.00035	405.4	54.0	406.1	9.0	406.2	4.6	-0.2
11NC22S-28.1	93	0.29	0.05557	0.00129	0.05458	0.00043	402.0	53.5	405.8	8.9	406.5	4.5	-1.2
11NC22S-36.1	92	0.52	0.05572	0.00122	0.05682	0.00043	410.1	49.7	408.3	8.2	408.0	3.8	0.5
11NC22S-5.1c	630	0.52	0.05698	0.00073	0.08232	0.00055	415.4	31.7	409.6	6.0	408.6	4.2	1.7
11NC22S-17.1	250	0.36	0.05597	0.00094	0.05623	0.00041	407.7	39.5	408.5	6.8	408.6	3.9	-0.2
11NC22S-51.2r	274	0.39	0.05529	0.00088	0.05568	0.00032	428.3	37.6	412.0	6.6	409.1	3.7	4.6
11NC22S-70.1	319	0.63	0.05543	0.00112	0.05562	0.00038	407.4	49.2	409.0	8.3	409.3	4.2	-0.5
11NC22S-10.1	638	0.69	0.05527	0.00065	0.05615	0.00037	430.2	31.1	413.4	6.1	410.4	4.4	4.8
11NC22S-2.1	143	0.43	0.05534	0.00123	0.05616	0.00046	413.8	50.2	411.1	8.5	410.6	4.2	0.8
11NC22S-51.1c	291	0.45	0.05484	0.00090	0.05583	0.00039	397.5	39.8	409.6	7.0	411.8	4.2	-3.7
11NC22S-30.1	159	0.45	0.05593	0.00099	0.05558	0.00043	411.2	40.9	412.5	7.2	412.7	4.3	-0.4
11NC22S-15.1	267	0.40	0.05593	0.00082	0.05660	0.00040	403.5	36.6	411.7	6.7	413.1	4.5	-2.5
11NC22S-29.1	127	0.34	0.05600	0.00121	0.05560	0.00040	416.6	49.1	413.8	8.3	413.3	4.0	0.8
11NC22S-68.1	161	0.54	0.05557	0.00109	0.05602	0.00045	414.0	46.7	413.5	8.1	413.4	4.4	0.2
11NC22S-26.1	246	0.43	0.05679	0.00112	0.07901	0.00060	413.2	46.7	413.6	8.0	413.6	4.1	-0.1
11NC22S-13.1	180	0.30	0.05584	0.00098	0.05603	0.00040	410.1	42.3	413.4	7.3	414.0	3.9	-1.0
11NC22S-12.1	251	0.75	0.05637	0.00085	0.08339	0.00065	414.8	36.8	414.3	6.6	414.3	4.0	0.1

Table D.2: *continued*

Spot Name	U (ppm)	^{232}Th/ ^{238}U	^{207}Pb/^{206}Pb	±1σ	^{206}Pb/^{238}U	±1σ (%)	^{207}Pb/^{206}Pb Age (Ma)	±1σ	^{207}Pb/^{235}Pb Age (Ma)	±1σ	^{206}Pb/^{238}Pb Age (Ma)	±1σ	% Discordant
Basal stratigraphic level – Slightly deformed clasts continued													
11NC22S-3.1	874	0.74	0.05693	0.00050	0.08816	0.00067	412.0	23.9	414.2	4.9	414.6	3.8	-0.7
11NC22S-49.1	309	0.61	0.05589	0.00134	0.05630	0.00042	416.0	56.6	416.7	9.7	416.8	4.9	-0.2
11NC22S-38.1	579	1.40	0.05689	0.00076	0.05810	0.00035	428.7	35.3	418.7	6.8	416.9	4.7	2.8
11NC22S-72.1	401	0.40	0.05556	0.00067	0.05816	0.00033	421.9	29.4	418.6	5.3	418.0	3.3	1.0
11NC22S-4.1	164	0.97	0.05563	0.00092	0.05774	0.00041	418.1	38.2	418.2	6.9	418.2	4.2	0.0
11NC22S-8.1	160	0.48	0.05534	0.00105	0.05808	0.00044	423.6	43.9	420.6	7.7	420.1	4.2	0.9
11NC22S-27.1r	364	0.85	0.05708	0.00097	0.08026	0.00067	429.5	41.1	421.6	7.4	420.1	4.4	2.3
11NC22S-41.1	125	0.35	0.05643	0.00092	0.05735	0.00041	457.3	37.4	427.1	6.7	421.5	3.6	8.1
11NC22S-66.1	237	0.87	0.05618	0.00074	0.05803	0.00034	442.6	32.1	429.3	6.1	426.8	4.1	3.7
11NC22S-21.1	490	0.52	0.05755	0.00074	0.08462	0.00067	448.4	33.6	431.7	6.5	428.6	4.4	4.6
11NC22S-27.2c	195	0.43	0.05744	0.00187	0.08934	0.00124	434.4	76.5	429.6	14.5	428.7	9.2	1.3
11NC22S-1.1	333	0.32	0.05562	0.00087	0.05852	0.00042	428.2	37.5	428.8	6.9	428.9	4.2	-0.2
11NC22S-3.1	143	0.61	0.05624	0.00095	0.05918	0.00049	447.1	39.0	433.1	7.4	430.5	4.7	3.8
11NC22S-4.1	168	0.64	0.05721	0.00098	0.08946	0.00071	423.6	39.7	430.2	7.2	431.4	4.3	-1.9
11NC22S-18.1	211	0.45	0.05740	0.00127	0.08468	0.00077	428.6	51.9	432.4	9.2	433.1	4.8	-1.1
11NC22S-24.1	754	1.12	0.05680	0.00057	0.05931	0.00034	439.0	25.6	435.7	5.1	435.1	3.6	0.9
11NC22S-23.1	97	0.57	0.05665	0.00140	0.05912	0.00057	425.7	56.4	434.0	9.9	435.6	4.9	-2.4
11NC22S-32.1	204	0.35	0.05633	0.00116	0.08135	0.00068	436.1	48.5	437.1	8.7	437.3	4.6	-0.3
11NC22S-35.1	350	0.37	0.05630	0.00064	0.06095	0.00036	435.8	27.8	437.7	5.3	438.1	3.4	-0.6
11NC22S-64.1	941	1.18	0.05696	0.00053	0.06025	0.00030	461.7	25.1	448.1	5.4	445.5	4.2	3.6
11NC22S-33.1c	618	0.99	0.05727	0.00064	0.06125	0.00043	445.0	30.8	446.2	6.4	446.5	4.7	-0.3
11NC22S-11.1	551	0.34	0.05626	0.00060	0.06100	0.00042	457.1	28.1	448.7	5.8	447.1	4.3	2.3
11NC22S-7.1	150	0.69	0.05645	0.00106	0.06403	0.00053	456.7	43.3	460.1	8.3	460.8	4.8	-0.9
11NC22S-15.1c	404	0.31	0.05867	0.00080	0.09444	0.00072	477.9	33.4	474.3	6.9	473.6	4.5	0.9
11NC22S-15.2r	733	0.19	0.05924	0.00091	0.10305	0.00203	518.5	40.2	502.5	12.3	499.0	12.0	3.9
11NC22S-19.1	571	0.61	0.06699	0.00054	0.14905	0.00112	769.6	22.8	746.5	7.7	738.8	6.8	4.2
11NC22S-39.1c	127	0.80	0.06697	0.00126	0.11076	0.00082	782.1	42.9	779.4	13.1	778.4	9.2	0.5
11NC22S-32.1	200	1.51	0.07208	0.00086	0.13317	0.00075	940.5	27.5	938.9	9.9	938.3	7.8	0.3
11NC22S-7.1c	131	0.56	0.07700	0.00093	0.22885	0.00182	1050.1	26.7	1066.7	11.3	1074.8	10.6	-2.6
11NC22S-9.1	114	0.33	0.07743	0.00085	0.16488	0.00134	1140.0	26.2	1133.2	12.2	1129.7	12.5	1.0
11NC22S-28.1c	203	0.45	0.09318	0.00090	0.29157	0.00284	1436.9	22.4	1422.5	12.5	1412.9	14.5	1.9
11NC22S-26.1	151	0.56	0.10308	0.00103	0.22899	0.00152	1652.2	21.3	1591.0	11.9	1545.2	12.8	7.3
11NC22S-54.1	216	0.57	0.10784	0.00075	0.24886	0.00118	1762.4	18.9	1681.1	11.7	1616.8	14.0	9.3
11NC22S-1.1c	59	0.27	0.11214	0.00126	0.42761	0.00382	1772.6	22.7	1778.4	13.9	1783.3	17.2	-0.7

Table D.2: *continued*

Spot Name	U (ppm)	^{232}Th/ ^{238}U	^{207}Pb/^{206}Pb	±1σ	^{206}Pb/^{238}U	±1σ (%)	^{207}Pb/^{206}Pb Age (Ma)	±1σ	^{207}Pb/^{235}Pb Age (Ma)	±1σ	^{206}Pb/^{238}Pb Age (Ma)	±1σ	% Discordant
Basal stratigraphic level – Undeformed clasts													
11NC22U-56.1	295	0.71	0.05405	0.00145	0.04078	0.00026	307.6	62.9	298.3	7.9	297.1	3.4	3.5
11NC22U-12.2	632	0.86	0.05479	0.00167	0.04781	0.00062	307.7	77.2	298.5	10.0	297.3	5.3	3.5
11NC22U-58.1	1199	0.78	0.05339	0.00092	0.04163	0.00032	309.1	45.5	301.7	6.4	300.7	4.0	2.8
11NC22U-53.2r	517	1.36	0.05349	0.00080	0.04036	0.00022	299.5	37.0	300.7	4.9	300.8	2.8	-0.5
11NC22U-32.1	124	0.45	0.05236	0.00140	0.04086	0.00033	296.4	61.7	301.0	7.6	301.6	2.9	-1.8
11NC22U-25.2	605	0.96	0.05404	0.00164	0.04876	0.00046	304.1	79.0	302.2	9.9	302.0	4.2	0.7
11NC22U-25.1	121	0.59	0.05302	0.00149	0.04160	0.00036	314.2	63.5	303.5	7.9	302.2	3.0	3.9
11NC22U-44.1	793	0.78	0.05320	0.00082	0.04124	0.00028	293.8	39.5	301.7	5.1	302.8	2.7	-3.1
11NC22U-48.1	838	0.72	0.05317	0.00091	0.04128	0.00022	306.7	43.0	303.6	5.4	303.1	2.3	1.2
11NC22U-12.1	134	0.35	0.05261	0.00170	0.04207	0.00037	311.4	73.7	304.5	9.1	303.6	3.1	2.6
11NC22U-10.1	118	0.35	0.05327	0.00141	0.03946	0.00035	314.1	61.1	305.0	7.7	303.8	3.1	3.4
11NC22U-21.1	159	0.42	0.05277	0.00138	0.04257	0.00041	311.4	60.0	305.5	7.6	304.7	3.3	2.2
11NC22U-11.2r	442	0.42	0.05220	0.00081	0.04300	0.00028	296.8	39.2	303.8	5.1	304.7	2.6	-2.7
11NC22U-59.1	1081	1.16	0.05292	0.00075	0.04221	0.00024	297.4	37.3	304.0	5.2	304.9	3.4	-2.6
11NC22U-28.1	219	1.03	0.05275	0.00134	0.04171	0.00031	298.5	58.9	304.2	7.4	305.0	2.9	-2.2
11NC22U-31.1	86	0.37	0.05276	0.00189	0.04152	0.00040	306.4	80.9	305.4	10.0	305.3	3.2	0.4
11NC22U-49.1	770	0.61	0.05377	0.00127	0.04138	0.00024	312.6	58.1	306.5	7.2	305.7	2.8	2.2
11NC22U-4.1	112	1.02	0.05229	0.00171	0.04240	0.00033	305.3	74.2	305.9	9.2	305.9	3.1	-0.2
11NC22U-17.1	216	0.90	0.05387	0.00120	0.05369	0.00049	313.0	51.9	307.2	6.8	306.5	3.3	2.1
11NC22U-16.1	694	0.86	0.05297	0.00068	0.05409	0.00043	308.2	34.9	307.4	5.0	307.2	3.2	0.3
11NC22U-13.1	166	0.37	0.05300	0.00133	0.04193	0.00036	315.7	57.9	308.2	7.3	307.3	2.9	2.7
11NC22U-24.1	156	1.00	0.05421	0.00166	0.04919	0.00044	311.7	70.1	308.6	8.8	308.2	3.2	1.1
11NC22U-15.1	813	0.78	0.05299	0.00080	0.05415	0.00041	318.2	43.5	309.4	6.1	308.3	3.7	3.2
11NC22U-22.1	318	0.70	0.05366	0.00132	0.04930	0.00032	314.0	58.1	309.1	7.4	308.5	2.9	1.8
11NC22U-6.1	202	0.62	0.05285	0.00129	0.04320	0.00035	307.8	58.0	309.3	7.5	309.5	3.3	-0.6
11NC22U-33.1	379	0.82	0.05322	0.00109	0.04190	0.00029	338.2	48.9	313.3	6.4	310.0	2.9	8.5
11NC22U-10.1	1497	0.80	0.05389	0.00065	0.05400	0.00038	319.6	34.6	311.1	5.0	310.0	3.2	3.1
11NC22U-3.1	81	0.36	0.05377	0.00171	0.04019	0.00048	316.5	72.4	310.8	9.4	310.1	4.1	2.1
11NC22U-46.1	174	0.71	0.05262	0.00155	0.04262	0.00039	304.7	67.6	309.6	8.5	310.2	3.2	-1.9
11NC22U-1.1	210	0.56	0.05306	0.00160	0.04370	0.00032	311.9	69.2	310.6	8.7	310.5	3.0	0.5
11NC22U-21.1	1140	1.02	0.05270	0.00086	0.04947	0.00036	318.3	44.0	311.6	6.1	310.8	3.6	2.4
11NC22U-57.1	842	1.17	0.05399	0.00074	0.04296	0.00032	315.4	38.9	311.8	5.9	311.4	4.1	1.3
11NC22U-64.1	774	0.73	0.05294	0.00092	0.04248	0.00026	313.0	45.2	313.0	6.2	313.0	3.5	0.0
11NC22U-29.1	145	0.52	0.05404	0.00148	0.05367	0.00051	317.0	62.8	313.6	8.2	313.1	3.5	1.3
11NC22U-3.1	347	0.55	0.05260	0.00079	0.04356	0.00028	317.1	36.2	313.7	5.0	313.2	2.8	1.3

Table D.2: *continued*

		^{232}Th/					^{207}Pb/^{206}Pb		^{207}Pb/^{235}Pb		^{206}Pb/^{238}Pb		%
Spot Name	U (ppm)	^{238}U	^{207}Pb/^{206}Pb	±1σ	^{206}Pb/^{238}U	±1σ (%)	Age (Ma)	±1σ	Age (Ma)	±1σ	Age (Ma)	±1σ	Discordant
Basal stratigraphic level – Undeformed clasts continued													
11NC22U-55.1	221	0.46	0.05440	0.00155	0.04294	0.00035	312.2	66.6	313.4	8.8	313.6	4.1	-0.5
11NC22U-37.1	299	0.52	0.05249	0.00172	0.04301	0.00039	317.3	75.9	314.7	9.7	314.4	3.5	0.9
11NC22U-40.1	241	0.77	0.05309	0.00107	0.04185	0.00031	313.7	46.7	315.1	6.1	315.3	2.8	-0.5
11NC22U-30.1	250	0.46	0.05353	0.00091	0.05414	0.00045	312.5	40.9	315.4	5.7	315.8	3.4	-1.1
11NC22U-26.1	324	0.49	0.05234	0.00181	0.04996	0.00043	309.2	81.7	315.0	10.4	315.8	3.7	-2.2
11NC22U-34.1	730	0.56	0.05247	0.00089	0.04271	0.00026	310.9	44.6	315.9	6.1	316.6	3.4	-1.9
11NC22U-5.1	94	0.36	0.05340	0.00201	0.04047	0.00044	316.3	84.5	316.7	10.8	316.8	3.7	-0.2
11NC22U-12.2r	131	0.34	0.05344	0.00138	0.04172	0.00029	327.9	58.5	318.4	7.5	317.1	2.7	3.4
11NC22U-26.1	84	0.51	0.05329	0.00186	0.04366	0.00040	322.9	78.2	318.1	10.0	317.4	3.2	1.7
11NC22U-35.1	188	0.68	0.05284	0.00140	0.04438	0.00044	322.2	60.7	319.0	8.1	318.6	3.7	1.2
11NC22U-45.1	482	0.98	0.05365	0.00121	0.04364	0.00033	331.0	52.7	320.2	6.9	318.8	2.9	3.8
11NC22U-13.1	227	0.79	0.05302	0.00103	0.04175	0.00047	311.8	45.2	318.2	6.4	319.1	3.9	-2.4
11NC22U-38.1	210	0.53	0.05268	0.00155	0.04312	0.00039	319.0	69.0	320.0	9.0	320.1	3.5	-0.4
11NC22U-14.1	308	0.35	0.05291	0.00165	0.05634	0.00060	321.1	74.5	320.8	10.0	320.8	4.5	0.1
11NC22U-36.1	218	0.67	0.05258	0.00159	0.04442	0.00040	316.2	69.1	321.0	9.0	321.6	3.4	-1.8
11NC22U-8.2	507	0.43	0.05465	0.00131	0.05585	0.00044	322.4	59.7	321.9	8.1	321.8	4.0	0.2
11NC22U-15.1	239	0.39	0.05346	0.00181	0.04180	0.00048	324.8	78.2	322.4	10.4	322.1	4.2	0.9
11NC22U-27.1	281	0.76	0.05485	0.00148	0.05510	0.00049	313.5	62.7	321.1	8.3	322.1	3.6	-2.8
11NC22U-41.1	83	0.62	0.05365	0.00183	0.04282	0.00043	318.4	76.7	321.8	10.0	322.2	3.5	-1.2
11NC22U-16.1	114	0.37	0.05339	0.00149	0.04379	0.00039	322.7	63.5	323.8	8.4	324.0	3.2	-0.4
11NC22U-62.1	324	0.62	0.05406	0.00160	0.04306	0.00031	353.9	69.4	328.2	9.4	324.5	3.8	8.5
11NC22U-51.1	250	1.56	0.05415	0.00130	0.04350	0.00032	336.5	56.2	327.1	7.5	325.8	3.0	3.3
11NC22U-14.1	174	0.58	0.05385	0.00133	0.04432	0.00039	339.2	56.5	330.7	7.7	329.5	3.2	2.9
11NC22U-14.1	102	0.61	0.05364	0.00217	0.04304	0.00068	336.1	90.6	331.6	12.5	330.9	5.4	1.6
11NC22U-19.1	93	0.46	0.05338	0.00208	0.04617	0.00043	337.6	86.8	331.9	11.5	331.1	3.4	2.0
11NC22U-50.1	98	0.79	0.05484	0.00254	0.04646	0.00051	351.5	104.1	346.6	14.4	345.8	4.4	1.7
11NC22U-5.1	114	1.00	0.05376	0.00158	0.04868	0.00045	357.4	66.8	350.0	9.5	348.9	3.8	2.4
11NC22U-4.1	754	0.20	0.05543	0.00078	0.05060	0.00031	393.3	34.8	392.0	5.8	391.8	3.2	0.4
11NC22U-25.1	1852	0.72	0.05587	0.00045	0.06312	0.00042	394.9	24.4	394.0	4.6	393.8	3.5	0.3
11NC22U-2.1	421	0.87	0.05483	0.00076	0.05601	0.00041	398.6	33.4	397.8	5.8	397.6	3.6	0.2
11NC22U-20.2	1562	0.53	0.05521	0.00067	0.06624	0.00046	426.1	35.2	415.9	6.5	414.1	4.3	2.9
11NC22U-23.2r	442	0.68	0.05596	0.00074	0.06137	0.00034	440.3	32.9	441.1	6.4	441.2	4.1	-0.2
11NC22U-23.1c	1146	0.80	0.05614	0.00060	0.06204	0.00036	449.8	28.3	444.8	5.8	443.9	4.2	1.4
11NC22U-1.1	709	0.44	0.05717	0.00072	0.05894	0.00028	451.6	32.5	446.9	5.9	446.0	3.2	1.3
11NC22U-11.1	228	0.73	0.05645	0.00095	0.05984	0.00042	445.9	38.8	451.6	7.2	452.8	3.8	-1.6
11NC22U-7.1	720	1.24	0.05760	0.00062	0.06439	0.00044	490.0	30.6	459.2	6.3	453.1	4.4	7.8

Table D.2: *continued*

		^{232}Th/					^{207}Pb/^{206}Pb		^{207}Pb/^{235}Pb		^{206}Pb/^{238}Pb		%
Spot Name	U (ppm)	^{238}U	^{207}Pb/^{206}Pb	±1σ	^{206}Pb/^{238}U	±1σ (%)	Age (Ma)	±1σ	Age (Ma)	±1σ	Age (Ma)	±1σ	Discordant
Basal stratigraphic level – Undeformed clasts continued													
11NC22U-24.1	505	0.48	0.05676	0.00074	0.06549	0.00032	469.4	30.8	469.6	6.0	469.6	3.5	0.0
11NC22U-63.1	1611	0.53	0.05677	0.00061	0.06385	0.00047	464.3	33.4	473.4	7.3	475.3	5.5	-2.5
11NC22U-13.1	746	0.59	0.06518	0.00066	0.12841	0.00110	773.9	29.3	724.4	9.4	708.5	7.8	8.9
11NC22U-30.1	291	0.44	0.06404	0.00073	0.10000	0.00056	729.0	26.9	715.8	7.6	711.5	5.2	2.5
11NC22U-31.1	175	0.93	0.07350	0.00094	0.17362	0.00134	994.4	29.1	973.0	11.1	963.5	9.4	3.3
11NC22U-21.2	1088	0.56	0.08611	0.00059	0.21364	0.00142	1321.9	23.8	1271.6	12.1	1242.0	12.8	6.6
11NC22U-20.1	351	0.47	0.09741	0.00067	0.22559	0.00155	1569.1	17.2	1511.6	9.9	1471.0	11.4	7.0
11NC22U-23.2	528	0.39	0.09751	0.00102	0.26386	0.00220	1529.9	38.4	1506.6	19.1	1490.1	17.6	2.9
11NC22U-9.1	1210	0.52	0.10458	0.00074	0.30217	0.00261	1654.8	25.4	1610.4	15.4	1576.7	18.6	5.3
11NC22U-8.1	1276	0.38	0.10150	0.00058	0.30847	0.00212	1593.7	20.2	1595.7	12.1	1597.2	14.8	-0.2
11NC22U-12.1	1043	0.59	0.10563	0.00051	0.31977	0.00251	1717.3	18.8	1672.1	12.4	1636.4	16.1	5.3
11NC22U-16.2	298	1.45	0.10666	0.00070	0.32823	0.00294	1720.1	16.8	1692.0	11.7	1669.4	16.0	3.3
11NC22U-19.1	454	1.14	0.11603	0.00069	0.34178	0.00217	1842.3	17.0	1794.8	11.1	1754.2	14.3	5.5
11NC22U-27.1	255	0.86	0.11401	0.00064	0.27720	0.00148	1849.3	13.6	1820.6	9.0	1795.6	11.7	3.3

Table D.2: *continued*

Location: Border region between Xinjiang autonomous region and Gansu province, Northwest China
Mapping Dates: Summers of 2008, 2009, and 2011
Publication Date: September, 2015
Author: Nathan Cleven
Association: University of Waterloo, Ontario, Canada
Contact (email): ncleven@uwaterloo.ca

Geology of the Hongliuhe suture and the Xingxingxia region, NW China

(Appendix E)

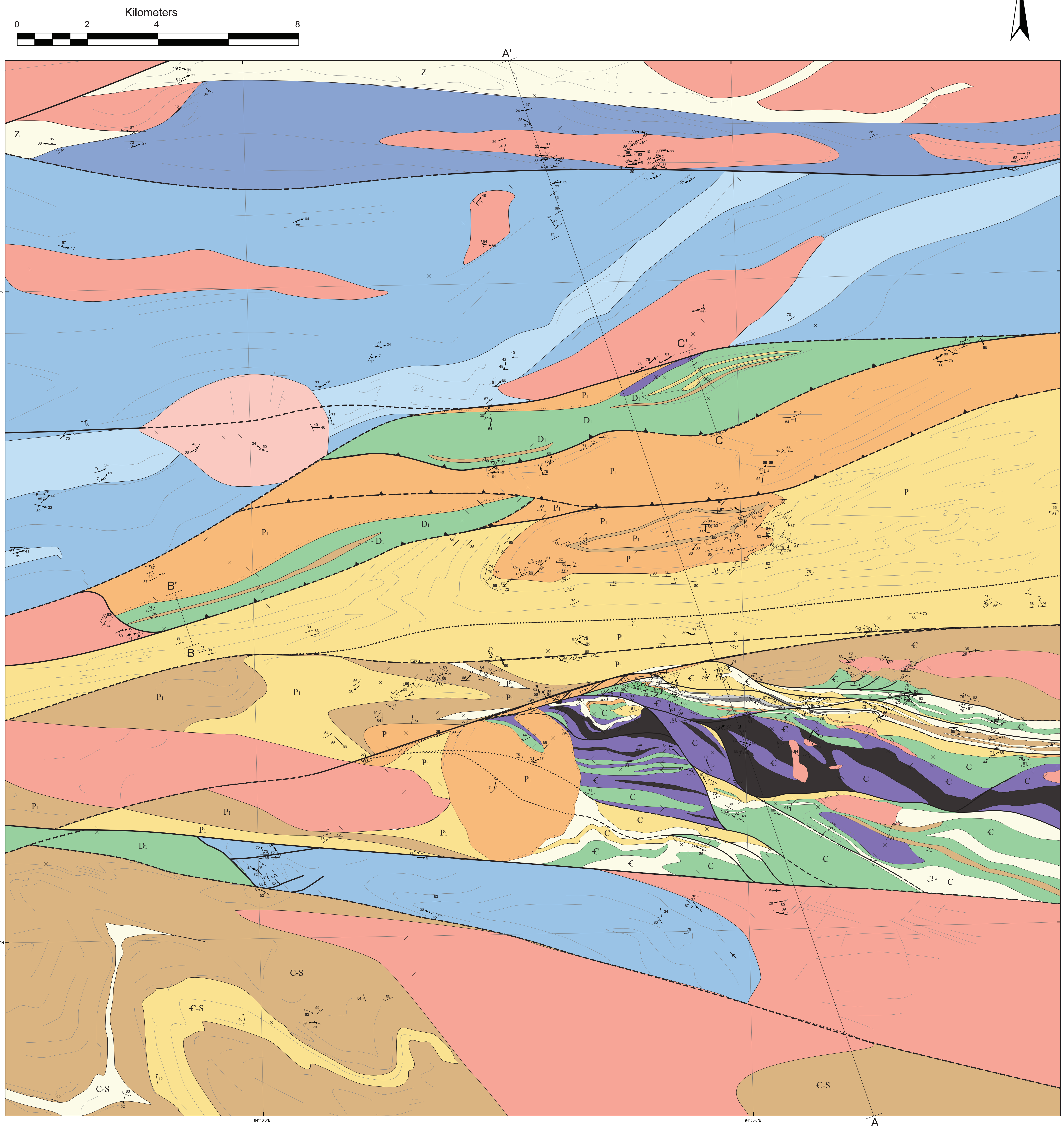

Lithology Legend

P1 Hongliuhe Formation (Zhesi Group)

- P1 **Limestone** - Beige to white limestone
- P1 **Siltstone** - grey to brown silty sandstones to sandy siltstones, rhythmically interbedded with sandstones and minor limestones
- P1 **Sandstone** - grey green to brown clast-supported lithic wackes, rhythmically interbedded with siltstones and minor limestones
- P1 **Conglomerate** - polymictic clast-supported conglomerates interbedded with pebbly lithic sandstones and sandy siltstones

D1 Tianhu volcanic sequences

Sedimentary

- D1 **Siltstone** - Brown to grey silstone with interbeds of siliceous tuff and chert
- D1 **Sandstone** - Grey-brown to green clast-supported lithic wacke

Igneous

- D1 **Volcanic** -Green to grey subaqueous basic volcanic flows with pillow structures, amygdules, porphytic textures and chloritic alteration
- D1 **Gabbro** - Black gabbro with layers of cumulate peridotite

Z-D (Age unknown) Upper greenschist-amphibolite grade metasedimentary rocks

- **Schist** - Grey quartz-biotite-garnet schist with tourmaline, epidote and staurolite and interlayers of marble
- **Quartzite** - White to rust-brown quartzite interlayered with marble and quartz-mica schist

Є-S Dundunshan passive margin sedimentary rocks

- Є-S **Limestone** - Light brown limestone with interbeds of siltstone
- Є-S **Siltstone** - Brown-grey siltstone with interbeds of limestone and sandstone
- Є-S **Sandstone** - Brown to grey muscovite bearing lithic wacke with interbeds of siltstone

Є Hongliuhe Ophiolite lithostratigraphy and associated supracrustal covering

Sedimentary

- **Chert** - Massive black chert
- **Chert** - White bedded chert with common black and grey laminae
- Є **Limestone** - White to buff and brown limestone and dolomite interlayered fine siliceous interlayering, commonly mylonitized with blebs of silica
- Є **Siltstone** - Grey to brown muscovite bearing siltstone
- Є **Sandstone** - Green to brown lithic wacke to lithic arenite, commonly volcaniclastic, with pebbly turbiditic graded bedding
- Є **Conglomerate** - Green polymictic volcaniclastic conglomerate

Igneous

- Є **Volcanic** - Green to grey intermediate to basic volcanic flow rocks with amygdaloidal and porphyritic textures, autoclastic breccias, interlayered with lenticular deposits of red chert, intruded by gabbro and diabase dykes
- Є **Gabbro** - Black plagioclase bearing fine to pegmatitic gabbro, occasionally mylonitized, intruded by diabase, gabbro and basalt dykes
- **Peridotite** - Black lherzolite and harzburgite with pyroxenite and rare dunite cumulate layers, occasional mylonitic and cataclastic textures, intruded by gabbro, diabase and basalt dykes

Z - Xingxingxia group metasedimentary rocks

- **Gneiss** - Grey quartz-biotite-garnet schist and paragneiss
- Z **Limestone** - Beige to white dolomitic limestone

Paleozoic felsic intrusive suites

- C-P **Granodiorite** - White granodiorite
- S-D **Granitoid** - Granite to tonalite compositions, occasionally with megacrystic k-feldspar phenocrysts

Structural Symbology Legend

- Inclined cumulate foliation
- Inclined bedding
- Vertical bedding
- Inclined cleavage foliation
- Vertical cleavage foliation
- Inclined schistosity/gneissosity
- Vertical schistosity/gneissosity
- Inclined protomylonite foliation
- Vertical protomylonite foliation
- Inclined mylonite foliation
- Vertical mylonite foliation
- Plunging mineral orientation, stretching or striation lineation
- Plunging hinge or intersection lineation
- × Outcrop location (without structural measurements)
- Approximate contact
- Unconformable contact
- Thrust fault
- Fault (known)
- Fault (approximate)
- Fault (inferred)

Geologic cross-section of the Xingxingxia to Hongliuhe regions

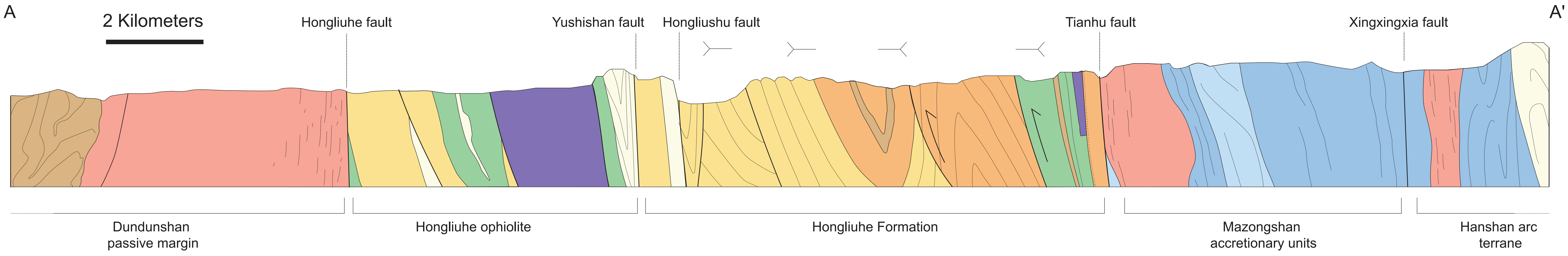

Tianhu volcanic sequences in cross-section

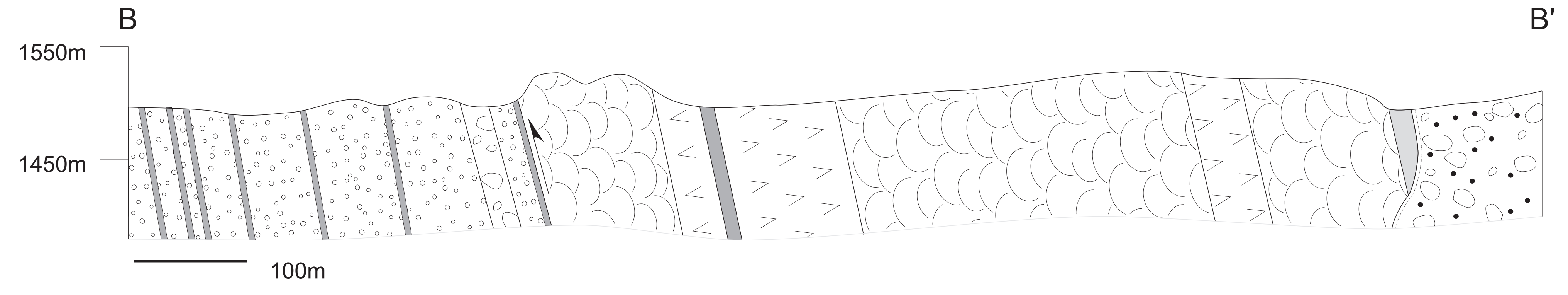

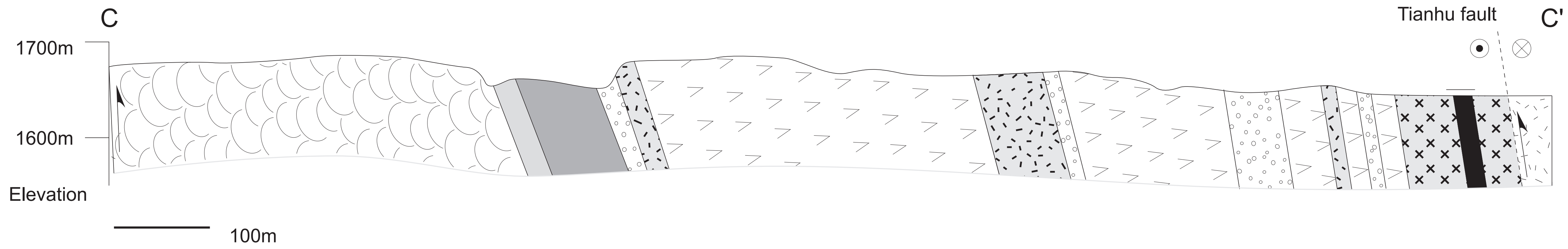

Detailed volcanic cross-section lithology legend

- Peridotite
- Gabbro
- Diabase
- Granite
- Basalt volcanic flow
- Basalt pillow flow
- Interlayered basalt/volcaniclastic and limestone
- Chert
- Limestone
- Limestone with sand interbeds
- Siltstone
- Sandstone
- Conglomerate